Investigations toward the accumulation, separation, mixing and detection of charged species using microfluidic electrophoresis

Untersuchungen zur Akkumulation, Separation, Mischung und Detektion von geladenen Spezies mittels mikrofluidischer Elektrophorese

Vom Fachbereich Maschinenbau an der Technischen Universität Darmstadt zur Erlangung des akademischen Grades eines Doktor-Ingenieurs (Dr.-Ing.) genehmigte Dissertation von Florian Gebhard aus Worms

Tag der Einreichung: 05.12.2023
Tag der Prüfung: 21.02.2024

1. Gutachten: Prof. Dr. Steffen Hardt
2. Gutachten: Prof. Dr. Moran Bercovici

Darmstadt - D 17

TECHNISCHE UNIVERSITÄT DARMSTADT

Nano- and Microfluidics

Investigations toward the accumulation, separation, mixing and detection of charged species using microfluidic electrophoresis
Untersuchungen zur Akkumulation, Separation, Mischung und Detektion von geladenen Spezies mittels mikrofluidischer Elektrophorese

Zur Erlangung des Grades eines Doktor-Ingenieurs (Dr.-Ing.) genehmigte Dissertation von Florian Gebhard

Tag der Einreichung: 05.12.2023
Tag der Prüfung: 21.02.2024

Darmstadt, Technische Universität Darmstadt

Erklärung laut Promotionsordnung

§ 8 Abs. 1 lit. d PromO

Ich versichere hiermit, dass zu einem vorherigen Zeitpunkt noch keine Promotion versucht wurde.

§ 9 Abs. 1 PromO

Ich versichere hiermit, dass die vorliegende Dissertation selbstständig und nur unter Verwendung der angegebenen Quellen verfasst wurde.

§ 9 Abs. 2 PromO

Die Arbeit hat bisher noch nicht zu Prüfungszwecken gedient.

Darmstadt, 05. Dezember 2022

F. Gebhard

Abstract

In microfluidics, a variety of electrophoretic techniques is used, for example to purify, focus, fractionate, detect or process bioparticles such as DNA molecules, proteins, cells or extracellular vesicles. Although there are many established methods - e.g. capillary electrophoresis, free-flow electrophoresis or isotachophoresis - there is still much potential for improvement and development of new approaches. Therefore, this thesis presents investigations toward the accumulation, separation, mixing and detection of charged species using microfluidic electrophoresis.

The first part deals with the electrophoretic transport of bioparticles in aqueous two-phase systems (ATPS) based on dextran and polyethylene glycol (PEG). In a first step, the interaction of two model proteins with the ATPS interface is investigated. Both proteins experience an interfacial transport resistance when they are transported from the dextran-rich phase to the PEG-rich phase. However, as this transport resistance is not equally pronounced for both proteins, they can be separated at the phase boundary. A similar principle is then applied to a solution containing both exosomes and proteins. While the exosomes are retained at the phase boundary, the proteins can cross over relatively easily. It should therefore be possible to purify exosomes in this way.

Next, the stability of the liquid-liquid phase boundary in an ATPS is studied. Especially at higher field strengths, instabilities occur that are presumably caused by Faradaic reactions at the electrodes. Only if these phenomena are prevented, it will be possible to study the actual influence of the electric field on the interface and to reliably perform separation processes.

The next part of this thesis focuses on sample detection using isotachophoresis (ITP), a special electrophoretic technique that allows to increase the local concentration of a sample by several orders of magnitude. A new approach is presented to lower the detection limit *via* signal processing by exploiting knowledge of the physics of electrophoretic sample transport and the imaging process. By cross-correlating pairs of noisy fluorescence images of an analyte focused by ITP, the electrophoretic velocity of the sample can be extracted in a first step even at low signal-to-noise ratios. Based on this velocity, a Galilean transformation is then performed on the entire set of images to align the fluorescence intensity distributions of the sample obtained from the individual images and generate a series of quasi-replicate measurements. Averaging over the transformed data significantly

reduces the noise superposing the raw images. In this way, the detection limit is lowered by approximately two orders of magnitude without any additional instrumentation.

Microfluidic ITP offers advantages not only in detecting low-concentration samples but also in significantly accelerating the reaction rate of chemical species by co-focusing reactants within a narrow sample zone. However, traditional ITP lacks the capability to control the reaction rate in real time. Therefore, a novel ITP mode is introduced that enables the temporal manipulation of the overlap of two ITP zones by applying an oscillating electric field. By adjusting the frequency and amplitude of the oscillation, it is possible to precisely control the time average of this overlap. This concept is demonstrated using two non-reactive fluorescent species. However, it is proposed that this approach can be applied to chemical reactions between ionic species focused by ITP, allowing for the direct control of the corresponding reaction rate by tuning the parameters of the oscillatory electric field.

Zusammenfassung

In der Mikrofluidik wird eine Vielzahl an elektrophoretischen Techniken angewendet, zum Beispiel um Biopartikel wie DNA-Moleküle, Proteine, Zellen oder extrazelluläre Vesikel aufzureinigen, zu fokussieren, zu fraktionieren, zu detektieren oder zu verarbeiten. Obwohl es viele etablierte Methoden gibt - z.B. Kapillarelektrophorese, Free-Flow Elektrophorese oder Isotachophorese - gibt es immer noch ein großes Potential für Verbesserungen und die Entwicklung neuer Ansätze. Deshalb werden in dieser Arbeit Untersuchungen zur Akkumulation, Separation, Mischung und Detektion von geladenen Spezies mittels mikrofluidischer Elektrophorese präsentiert.

Der erste Teil behandelt den elektrophoretischen Transport von Biopartikeln in wässrigen Zweiphasensystemen (englisch: *aqueous two-phase systems*, kurz: ATPS) auf Basis von Dextran und Polyethylenglycol (PEG). In einem ersten Schritt wird die Interaktion von zwei Modellproteinen mit der Grenzfläche des ATPS untersucht. Beide Proteine erfahren an der Grenzfläche einen Transportwiderstand, wenn sie von der Dextran-reichen Phase in die PEG-reiche Phase transportiert werden. Da dieser jedoch nicht für beide Proteine gleich stark ausgeprägt ist, können diese an der Phasengrenze separiert werden. Ein ähnliches Prinzip wird anschließend auf eine Lösung angewendet, die sowohl Exosomen als auch Proteine enthält. Während die Exosomen an der Phasengrenze zurückgehalten werden, können die Proteine relativ einfach passieren. Es sollte deshalb möglich sein, Exosomen auf diese Weise aufzureinigen.

Anschließend wird die Stabilität der flüssig-flüssig Phasengrenze in einem ATPS untersucht. Besonders bei hohen Feldstärken treten Instabilitäten auf, die vermutlich von Faradayschen Reaktionen an den Elektroden verursacht werden. Nur wenn diese Phänomene verhindert werden, wird es möglich sein, den eigentlichen Einfluss des elektrischen Feldes auf die Grenzfläche zu ermitteln und Trennoperationen zuverlässig durchzuführen.

Der nächste Teil dieser Arbeit fokussiert sich auf die Probendetektion mittels Isotachophorese (ITP), einer speziellen elektrophoretischen Technik, die es erlaubt, die lokale Konzentration einer Probe um mehrere Größenordnungen zu erhöhen. Ein neuer Ansatz wird präsentiert, mit dem es möglich ist, die Nachweisgrenze in der Signalverarbeitung zu verringern. Durch Kreuzkorrelation von Paaren verrauschter Fluoreszenzbilder eines mittels ITP aufkonzentrierten Analyten kann in einem ersten Schritt die elektrophoretische Geschwindigkeit der Probe auch bei geringen Signal-Rausch-Verhältnissen bestimmt wer-

den. Basierend auf dieser Geschwindigkeit wird anschließend eine Galilei-Transformation auf den gesamten Datensatz angewendet, um die Fluoreszenzintensitätsverteilungen der Probe aus den einzelnen Bildern auszurichten und eine Reihe von quasi-identischen Daten zu erzeugen. Das Rauschen, das die Rohdaten überlagert, kann durch Mittelung über diesen transformierten Datensatz reduziert werden. Auf diese Weise ist es möglich, die Nachweisgrenze ohne zusätzliche Messinstrumente um zwei Größenordnungen zu verringern.

Mikrofluidische ITP ist nicht nur von Vorteil bei der Detektion von Proben mit geringer Konzentration, sondern kann auch verwendet werden, um Reaktionen von chemischen Spezies signifikant zu beschleunigen, indem Reaktanten zusammen in einer engen Probenzone aufkonzentriert werden. In der traditionellen ITP ist fehlt es jedoch an Möglichkeiten, die Reaktionsrate in Echtzeit zu kontrollieren. Aus diesem Grund wird eine neue Variante der ITP eingeführt, die es erlaubt, die Überlappung von zwei ITP-Zonen mittels eines oszillierenden elektrischen Feldes temporär zu manipulieren. Durch Anpassung der Frequenz und der Amplitude der Oszillation ist es möglich, das zeitliche Mittel dieser Überlappung präzise zu kontrollieren. Dieses Konzept wird anhand zweier fluoreszierender Spezies, die nicht miteinander reagieren, demonstriert. Es liegt jedoch nahe, dass dieser Ansatz auch auf chemische Reaktionen zwischen ionischen Spezies, die durch ITP aufkonzentriert werden, angewendet werden kann, was die direkte Kontrolle der entsprechenden Reaktionsrate über die Einstellung der Parameter des oszillierenden elektrischen Feldes erlaubt.

Contents

Chapter 1

Introduction

”I am convinced that microfluidic technology will become a major theme in the analysis, and perhaps synthesis, of molecules: the advantages it offers are too compelling to let pass.” In a 2006 article on the past, present and future of microfluidics, George M. Whitesides, one of the pioneers in the field, used these words to emphasize the expectations he had for the benefits of microfluidic technologies, at least at the time [1]. Throughout the article, he highlights several areas where microfluidic approaches have been successfully applied: the handling of multiphase flow to generate and manipulate droplets (e.g. as compartments for fast organic reactions) and bubbles, cell biology, chemical synthesis, and - most prominent - microanalytical systems, especially for bioanalysis.

By the early 2000s, there were already a number of bioanalytical methods based on microfluidics. For example, in their 2002 paper, Beebe et al. reviewed microfluidics-based methods used for immunoassays, enzyme assays and DNA analysis [2]. In this context, microfluidic technology is used to mix and separate species, to purify analytes from contaminants, or to perform biochemical reactions and monitor reaction kinetics. They also highlight the use of microfluidics to culture, manipulate, sort and detect cells.

The impact of microfluidics on biomedical research was assessed in 2014 by Sackmann et al. [3]. They concluded that many microfluidic studies provided proof-of-concept and demonstrated the efficacy of a new approach. However, often these new approaches were not transferred to biomedical research because they were only minor improvements to established macroscale approaches. The authors argue that in some cases, however, microfluidic technologies may be superior to their competitors. For example, micro total analysis systems or lab-on-a-chip technology have the potential to replace or compensate for centralized laboratory infrastructure. In addition, microfluidic approaches allow the processing of very small sample volumes, often with short processing times, easy handling and high sensitivity. Finally, Sackmann et al. describe the use of microfluidics in organ-on-a-chip systems, which mimic organ functions and serve as a platform for drug development. These systems can help reduce the cost of research and development in the pharmaceutical industry.

The topic of organ-on-a-chip systems is also addressed in a 2022 issue of *Chemical Reviews* on microfluidics. In the editorial of the issue, Nunes and Stone list some further fields of application [4]. In addition to those mentioned above, they write that microfluidics can be used to fabricate microparticles, microfibers and porous materials, or to address energy and environmental challenges, for example through microfluidic electrochemical energy conversion. Although this list of possible applications mentioned in this chapter is not exhaustive, it provides a good introduction to the many ways in which microfluidic technology can be used.

Underlying all these applications are the physical phenomena that occur at the microscale. A good introduction to these effects is provided for example by Beebe et al. [2], Stone et al. [5], and Squires and Quake [6]. The latter two references also address electrokinetic transport processes in microfluidics. On the one hand, electric fields can be used to drive fluid flows *via* electro-osmosis. On the other hand, and of particular importance to this thesis, electric fields can also be applied to transport freely suspended charged particles relative to a liquid. This phenomenon is called electrophoresis and can in principle also be observed at the macroscopic level. However, in the last decades, a significant transfer of electrophoretic techniques and applications to microfluidic environments has taken place, for example in the form of capillary electrophoresis, free-flow electrophoresis or isotachophoresis [7–11]. The general reasons for this development are summarized in the book on capillary and microchip electrophoresis edited by Landers [7] or in the review on isotachophoresis by Ramachandran and Santiago [11]: Microfluidic systems allow the use of small sample volumes and usually provide easy optical access. In addition, microfluidics offers the possibility of implementing on-chip networks, which may be desirable in more sophisticated applications. Next, Joule heating can be rapidly mitigated *via* heat transfer on small length scales. These advantages make it attractive to perform electrophoretic processes in microfluidic devices. Although electrophoresis is already widely used in narrow capillaries and other microfluidic devices, e.g. for the purification, separation, processing or detection of biomolecules, there is still much potential for the development of new methods and the optimization of existing ones.

This thesis presents investigations toward the accumulation, separation, mixing and detection of charged species using microfluidic electrophoresis. The basics of electrokinetics in microfluidics are introduced in Chapter 2. Chapter 3 presents a study of the electrophoretic transport of proteins and exosomes across the liquid-liquid interface of an aqueous two-phase system (ATPS). It turns out that these bioparticles experience a transport resistance at the phase boundary that can be used to separate them. Next, Chapter 4 complements Chapter 3, since it deals with the stability of the liquid-liquid interface of an ATPS under the influence of an electric field. Based on the results, recommendations for measures to improve the reliability of separation processes in microfluidic ATPS will be formulated. This is followed by two chapters on the subject of isotachophoresis (ITP).

In Chapter 5, a novel post-processing scheme to detect ITP sample zones hidden in noise is suggested. Without the need for additional instrumentation, the detectability of low concentration samples is significantly improved. Chapter 6 demonstrates that oscillating ITP sample zones can be used to control the overlap of two co-focused species. By varying the amplitude and frequency of oscillation, the time-averaged overlap of the concentration profiles of the species can be adjusted. In principle, this could be used to control reaction rates between two reactive species. Finally, Chapter 7 contains some concluding remarks on the work presented.

Chapter 2

Fundamentals of electrokinetics in microfluidics

The purpose of this chapter is to provide an overview of the fundamentals of electrokinetics in microfluidics, as these are relevant in all of the subsequent chapters. Since there can be no discussion of transport phenomena in microfluidics without the basic equations of fluid dynamics, these are introduced first. Next, the occurrence of electric double layers at solid-liquid interfaces is explained. Electrophoresis and electro-osmosis, two electrokinetic phenomena, are then described, followed by a section on the Nernst-Planck equation. Finally, isotachophoresis (ITP), a specific electrophoretic technique, is introduced. The discussions below are based on the standard books by Bird et al. [12], Masliyah and Bhattacharjee [13] and Probstein [14], as well as on the review of the theory and application of ITP by Ramachandran and Santiago [11].

2.1 Basic equations of fluid dynamics

Two equations are particularly important for describing the fundamentals of fluid dynamics. First, the equation of continuity describes the conservation of mass at a fixed point in space. It is given by

$$\frac{\partial \rho}{\partial t} = -\nabla \cdot (\rho \vec{u}). \tag{2.1}$$

Here, ρ is the mass density, and $\vec{u}$ represents the velocity field in the fluid. The right hand side of the equation describes the transport of mass by convection. A special form of the equation of continuity is obtained for incompressible fluids where ρ is constant:

$$\nabla \cdot \vec{u} = 0. \tag{2.2}$$

Second, the Navier-Stokes equation describes the conservation of momentum. In its general form, it is

$$\frac{\partial \rho}{\partial t} = -\nabla \cdot (\rho \vec{u}\vec{u}) - \nabla P - \nabla \cdot \boldsymbol{\tau} + \vec{f}. \tag{2.3}$$

The first term on the right hand side describes the convective momentum inflow. The second and third terms represent the contribution of the pressure P and the viscous stress tensor $\boldsymbol{\tau}$. Last, $\vec{f}$ summarises the effect of external body forces, e.g. caused by gravitational or electric fields. Accounting for the equation of continuity and incorporating $-\nabla \cdot \boldsymbol{\tau} = \eta \Delta \vec{u}$, the Navier-Stokes equation can also be written as

$$\rho \left(\frac{\partial \vec{u}}{\partial t} + (\vec{u} \cdot \nabla)\vec{u} \right) = -\nabla P + \eta \Delta \vec{u} + \vec{f} \tag{2.4}$$

for incompressible Newtonian fluids with dynamic viscosity η. Microfluidic flows are characterised by a low ratio between inertial and viscous forces, expressed by the Reynolds number $\mathrm{Re} = \rho u l / \eta$ with characteristic velocity u and characteristic length scale l. Hence, the term on the left hand side of Equation 2.4 can be omitted, resulting in the linear Stokes equation

$$0 = -\nabla P + \eta \Delta \vec{u} + \vec{f}. \tag{2.5}$$

Derivations of the equations above are given for example by Bird et al. [12] and Probstein [14].

2.2 Electric double layers

Electric double layers (EDL) form at the interface between a liquid and another liquid, solid or gas in order to shield surface charges. Traditionally, electric double layers are discussed for the case of a solid in contact with an aqueous electrolyte solution. This approach will also be followed here. The origin of electric double layers in such systems is summarized by Masliyah and Bhattacharjee [13]: On the one hand, most solids exhibit a surface charge when in contact with an aqueous electrolyte solution. This can be caused, for example, by ionization of surface groups. If a surface contains acidic or basic groups, the surface charge can be adjusted *via* the pH of the solution. Charged surfaces can also occur when individual ions dissolve from crystal compounds according to their solubility in the aqueous medium. Besides, adsorption of surfactant ions onto the surface can also cause a net surface charge. On the other hand, ions in the electrolyte solution are either attracted or repelled by the surface charge. Ideas about the arrangement of electrolyte ions and about the resulting electrical potential distribution have evolved over time. Some of the most important milestones are described here.

The concept of electric double layers goes back to Helmholtz [15, 16]. According to him, when a charged electrode is immersed in an electrolyte solution, two layers of opposite polarity are formed: A layer of electrolyte ions covers the oppositely charged electrode surface. In his considerations, however, he did not take into account the diffusivity of ions in free solution. This gap was closed by Gouy and Chapman, who introduced, following the assumption of local thermodynamic equilibrium, a Boltzmann distribution to describe

the ion concentration profile in an electrolyte close to the interface to a solid surface [17, 18]. Following Masliyah's and Bhattacharjee's book [13] with some minor adjustments, this assumption can now be used to describe the ion distribution and correspondingly the potential distribution in an EDL: The concentration of a dissolved ion i can be written as

$$c_i = c_{i,0} \exp\left(\frac{-\nu_i e\varphi}{k_B \vartheta}\right), \tag{2.6}$$

where $c_{i,0}$ is the bulk concentration of the ion, ν_i the valence, e the elementary charge, φ the electrostatic potential, k_B the Boltzmann constant and ϑ the absolute temperature. According to this Boltzmann distribution, the concentration profile is determined by the potential energy of the ions. The charge density ρ_e is obtained by summing over all species weighted with their valence:

$$\rho_e = F \sum_{i=1}^{N} \nu_i c_i. \tag{2.7}$$

Here, F is the Faraday constant. The relationship between the charge density and the potential distribution is given by the Poisson equation

$$\Delta\varphi = -\frac{\rho_e}{\varepsilon} \tag{2.8}$$

with the dielectric permittivity ε. Evaluating this equation in one dimension with local variable x and inserting Equations 2.6 and 2.7 results in the Poisson-Boltzmann equation:

$$\frac{d^2\varphi}{dx^2} = -\frac{F}{\varepsilon} \sum_{i=1}^{N} \nu_i c_{i,0} \exp\left(\frac{-\nu_i e\varphi}{k_B \vartheta}\right). \tag{2.9}$$

A linearization leads to the Debye-Hückel approximation:

$$\frac{d^2\varphi}{dx^2} = -\frac{F^2 \sum_{i=1}^{N} \nu_i^2 c_{i,0}}{\varepsilon \hat{R} \vartheta} \varphi = \frac{\varphi}{\lambda_D^2}, \tag{2.10}$$

where $\hat{R} = F k_B / e$ is the universal gas constant. This simplification is permissible if the potential at the charged surface is small compared to the thermal potential $k_B\vartheta/e \approx 25\,\mathrm{mV}$. The Debye length

$$\lambda_D = \sqrt{\frac{\varepsilon \hat{R} \vartheta}{F^2 \sum_{i=1}^{N} \nu_i^2 c_{i,0}}} \tag{2.11}$$

is the characteristic thickness of the diffusive part of the EDL . Masliyah and Bhattacharjee stress that it only depends on the electrolyte solution (*via* the dielectric permittivity, the valence, and the ion concentrations), but not on the properties of the charged surface. Assuming a potential φ_0 at $x = 0$, corresponding to a charged wall, the solution to

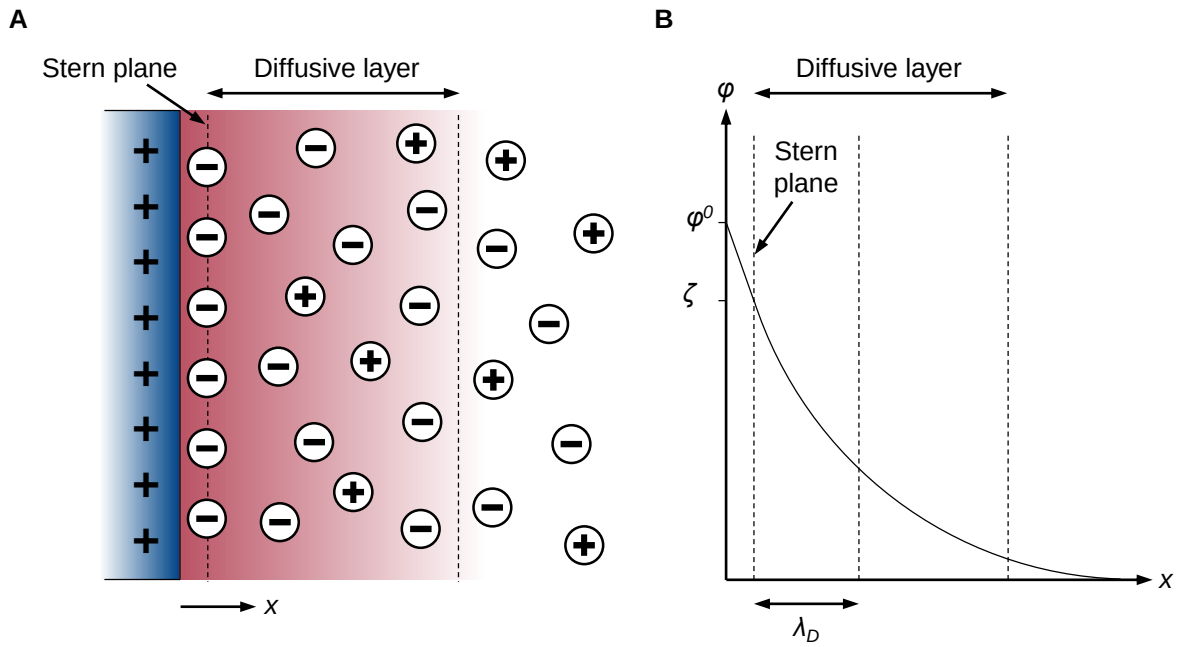

Figure 2.1: Schematic of the electric double layer occurring at the interface between a charged surface and an aqueous medium according to Stern. A) schematically shows the ion distribution in an aqueous phase adjacent to a charged surface. The red (blue) shading symbolizes the development of the net negative (positive) charge with increasing distance from the surface. B) schematically shows the corresponding potential distribution φ.

Equation 2.10 is given by

$$\varphi = \varphi_0 \exp\left(-\frac{x}{\lambda_D}\right). \tag{2.12}$$

The Gouy-Chapman theory of the EDL structure was later extended by Stern [19]. He assumed that some of the counterions in the electrolyte solution would adsorb on the charged surface, forming a layer of immobilized ions, later called the Stern layer, while others are distributed in a diffusive layer as predicted buy Gouy and Chapman. Across the Stern layer, the potential drop would be linear. Outside the Stern layer, it would then decrease non-linearly to a value of zero in accordance with the Gouy-Chapman theory. The ion distribution and the potential φ as a function of the distance from the charged surface are shown schematically in Figure 2.1. The potential at the Stern plane, marking the transition between Stern layer and diffusive layer, is referred to as ζ potential. When replacing φ_0 with ζ, Equation 2.12 describes the potential distribution in the diffusive layer. In their standard textbooks, Masliyah and Bhattacharjee [13] and Probstein [14] describe another layer (restricted by the shear plane) between the Stern layer and the diffusive layer. However, the potential drop across this additional layer is only marginal. Therefore, as in many accounts in the literature, it is omitted here. Note that in many other accounts of the EDL, the Stern layer is also omitted and φ_0 is equated with ζ. In general, ζ depends on both the charged surface and the electrolyte solution that participate in the formation of an EDL. The influence of solvent pH, temperature,

and counterion size, valence, and concentration on the ζ potential at polymer and glass surfaces, which are of relevance in the following, are extensively discussed by Kirby and Hasselbrink [20, 21]. They report ζ potential values on the order of 10^0 to 10^2 mV.

Since the publication of Stern's work in 1924, many other studies have been carried out on the strucutre of EDLs. For example, Grahame's 1947 article suggests an EDL structure with an inner Helmholtz plane, where ions are directly adsorped to the charged surface, and an outer Helmholtz plane, where ions with a solvation shell are located [22]. Trasatti investigated the effect of the nature of the metal at metal-electrolyte interfaces on the dielectric properties of the liquid [23]. The 2011 review by Gongadze et al. deals with a generalized Stern model that includes the effects of spatial variations of the electric permittivity [24]. However, it should be noted that this is by no means a comprehensive account of all developments in this field. This section is only intended to show the basic concepts of electric double layers.

2.3 Electrophoresis

Any particle carrying a charge q, e.g. ions and charged micro- or nanoparticles, experiences a force when exposed to an electric field:

$$\vec{F}_{el} = q\vec{E}. \tag{2.13}$$

In response, particles dissolved or suspended in a liquid are set into motion. This phenomenon is called electrophoresis. Again, Masliyah and Bhattacharjee give a basic description of this phenomenon [13], which is adapted here with a few minor adjustments. In the following, particles are assumed to be rigid and electrically non-conducting spheres.

The electrical force $\vec{F}_{el}$ on the particle is balanced by a drag force

$$\vec{F}_d = 6\pi\eta a\vec{u}, \tag{2.14}$$

where η, a, and $\vec{u}$ are the viscosity of the continuum fluid, the particle radius, and the particle velocity relative to the velocity of the continuum fluid, respectively. Equating these two forces and solving for $\vec{u}$ results in

$$\vec{u} = \frac{q}{6\pi\eta a}\vec{E}. \tag{2.15}$$

Accordingly, the direction of the particle movement will be determined by the orientation of the electric field and the sign of the particle charge. The ratio between the particle velocity and the local electric field is called electrophoretic mobility. In this very basic discription, it is given as

$$\mu = \frac{q}{6\pi\eta a}. \tag{2.16}$$

However, Masliyah and Bhattacharjee add that this is only a rough approximation and that in reality the situation in an electrolyte solution is more complex [13]. The charged particle will interact with the surrounding electrolyte ions. As a result, an EDL with a non-zero net charge is formed at the particle surface. This EDL will also experience an electrical body force, leading to a motion in the fluid immediately surrounding the particle. Depending on the ratio of the Debye length λ_D and the particle radius r, different equations for the electrophoretic mobility are obtained. For large EDL, i.e. $a/\lambda_D << 1$, the velocity field in the EDL can be determined by solving the Stokes equation with a source term that accounts for the force exerted on the EDL ions by the external electric field. The resulting retardation velocity has to be considered in the balance between the drag force and the electrical force on the particle. Eventually, an expression for the electrophoretic mobility that includes the zeta potential ζ, the dielectric permittivity ε, and the fluid viscosity η is obtained:

$$\mu = \frac{2}{3}\frac{\varepsilon\zeta}{\eta}. \tag{2.17}$$

Remarkably, in this limit the electrophoretic mobility is independent of the particle size. This solution was first published by Hückel [25]. It is valid in particular for organic liquids characterized by relatively large Debye lengths and under the assumption of a point-symmetric EDL, i.e. without considering deformation of the EDL by fluid movement around the particle. Likewise, an expression for μ is obtained for thin EDL, i.e. $a/\lambda_D >> 1$ [13]. Here, the description of the EDL around the particle can be simplified to the case of an EDL at a planar surface. Solving the Stokes equation together with the Poisson equation describing the potential distribution around the particle, the Helmholtz-Smoluchowski equation for the electrophoretic mobility results:

$$\mu = \frac{\varepsilon\zeta}{\eta}. \tag{2.18}$$

Again, this solution is independent of the particle size. However, Equations 2.17 and 2.18 are only valid for the two limiting cases $a/\lambda_D << 1$ and $a/\lambda_D >> 1$. For arbitrary ratios of the particle radius and the Debye length, an equation for the electrophoretic mobility was presented by Henry [26]:

$$\eta = \frac{2}{3}\frac{\varepsilon\zeta}{\eta} f\left(\frac{a}{\lambda_D}\right). \tag{2.19}$$

Here, Henry's function $f(a/\lambda_D)$ goes towards 1 for small values of a/λ_D and towards 1.5 for large values. However, it is only valid for small values of ζ. More elaborate expressions for μ are obtained when considering relaxation effects in the EDL as well as particle conductivity, shape, and concentration. It should be noted that the electrophoretic mobility

and the diffusivity of a species are related according to

$$\mu = \frac{\nu F}{\hat{R}\vartheta} D. \tag{2.20}$$

In the literature, this equation is usually called Nernst-Einstein relation [13, 14].*

Persat et al. extensively discuss the effect of the electrolyte solution pH on the electrophoretic mobility [27]. The dissociation and hence the charge of weak acids and bases are pH dependent. Accordingly, their electrophoretic mobilities are also affected by the electrolyte solution pH. An effective mobility considers all ionization states of a species X weighted with their molar fractions:

$$\mu_{\mathrm{X}} = \sum_{\nu} \mu^0_{\mathrm{X},\nu} \frac{c_{\mathrm{X},\nu}}{c_{\mathrm{X}}}. \tag{2.21}$$

Here, the superscript 0 refers to the fully ionized mobility of the corresponding ionization state. The different ionization states are indicated by the corresponding valence ν. The molar fractions $c_{\mathrm{X},\nu}/c_{\mathrm{X}}$ are strongly pH dependent. For example, the effective mobility μ_{A} for a divalent acid A with two pK_a values ($\mathrm{pK}_{\mathrm{A,\text{-}1}}$ and $\mathrm{pK}_{\mathrm{A,\text{-}2}}$) is

$$\mu_{\mathrm{A}} = \frac{\mu^0_{\mathrm{A,\text{-}1}} + \mu^0_{\mathrm{A,\text{-}2}} 10^{\mathrm{pH}-\mathrm{pK}_{\mathrm{A,\text{-}2}}}}{1 + 10^{\mathrm{pH}-\mathrm{pK}_{\mathrm{A,\text{-}2}}} + 10^{\mathrm{pK}_{\mathrm{A,\text{-}1}}-\mathrm{pH}}}. \tag{2.22}$$

Similar expressions can be found for effective mobilities of multivalent acids and bases. It is important to note that both the sign and the total value of the electrophoretic mobility, especially of bioparticles such as proteins, are strongly pH dependent, see for example [28].

Persat et al. continue to discuss the effects of ionic strength on electrophoretic mobilities [27]. The ionic strength is a measure of the ion concentrations in an electrolyte solution with different ionic speicies i. It is defined as

$$\mathcal{I} = \frac{1}{2} \sum_{i} \nu_i^2 c_i. \tag{2.23}$$

In the context of electrophoretic mobilities, it can be included to measure the deviation from the infinite dilution approximation. On the one hand, pK_a values are ionic strength dependent. On the other hand, the EDL around a charged particle is also affected by $\mathcal{I}$. In general, increasing $\mathcal{I}$ will reduce μ. Empirical expression for the ionic strength dependence of the electrophoretic mobility were for example presented by Friedl et al. [29] and Li et al. [30].

*Different notations of the Nernst-Einstein relation can be found in the literature. Depending on the definition of the electrophoretic mobility, it is often written as $\mu = FD/RT$. Here, however, the author follows the notation used by Masliyah and Bhattacharjee [13]. This also affects the definition of the Nernst-Planck equation (Equation 2.30) and the electrical conductivity (Equation 2.32).

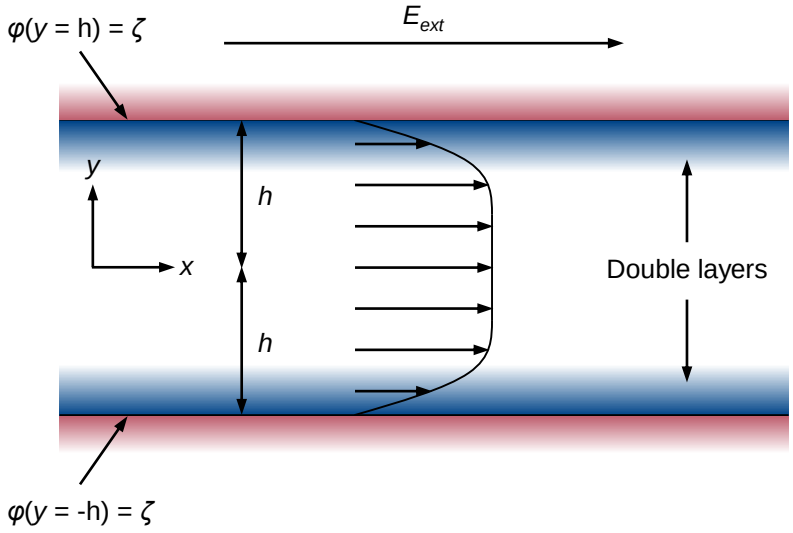

Figure 2.2: Schematic of the electro-osmotic flow in a slit microchannel formed by two parallel plates with negative surface charge. The red (blue) shading symbolises the distribution of the negative (positive) net charge density at the microchannel surface.

It should be noted that electrophoresis is often carried out in gels in many practical applications, e.g. in medical diagnostics. Here, the pore size and structure of the gel affects the electrophoretic mobility of a particle according to its size, which has been extensively discussed by Viovy [31]: In general, large particles are slowed down more strongly than small ones (which is not necessarily true for flexible DNA molecules). This usually facilitates size-based separation of particles. In the following, however, only the electrophoretic transport of biomolecules in free solution is of relevance.

2.4 Electro-osmosis

As briefly mentioned above, an external electric field will exert a force on the ions in an EDL at a solid-electrolyte surface. This results in a directed net ion migration towards the anode or cathode, respectively. Due to viscous drag, the bulk of the liquid will also be set into motion. Therefore, it is possible to establish a net transport of liquids in capillaries, microchannels or pores by applying an external electric field. This net flow is called electro-osmotic flow. A very general definition is given for example by Probstein, who writes that electro-osmosis is the transport of a liquid relative to a stationary charged surface driven by an external electric field [14]. Masliyah and Bhattacharjee present equations describing the very simple case of an electro-osmotic flow in a slit charged microchannel with negatively charged surfaces, see Figure 2.2, a scenario that is comparable to the experiments presented in the following chapters. They are briefly introduced here.

The potential distribution in the microchannel is given by a superposition of the potential distribution in the EDL at the channel surface and the applied external potential:

$$\varphi(x,y) = \varphi_{EDL}(y) + \varphi_0 - xE_{ext}. \tag{2.24}$$

Here, φ_0 is the value of the external potential at $x = 0$. The potential distribution in the EDL is obtained by solving the Poisson-Boltzmann equation in the Debye-Hückel approximation (see Equation 2.10) in an axisymmetric channel with height $2h$ and a wall potential equal to the ζ potential:

$$\varphi_{EDL}(y) = \zeta \frac{\cosh(y/\lambda_D)}{\cosh(h/\lambda_D)}. \tag{2.25}$$

Note that this equation is only valid in the case of negligible EDL overlap, i.e. $h/\lambda_D >> 1$. Accordingly, the charge density distribution in the EDL is given by

$$\rho_e = -\frac{\varepsilon}{\lambda_D^2}\varphi_{EDL} = -\frac{\varepsilon\zeta}{\lambda_D^2}\frac{\cosh(y/\lambda_D)}{\cosh(h/\lambda_D)}. \tag{2.26}$$

This expression can then be inserted into the Stokes equation (see Equation 2.5) with a source term accounting for the electric body force acting on the charges in the EDL caused by the external electric field. Gravitational forces can be neglected in flows on the micro scale. Assuming a fully developed flow, there is only a velocity component in the x direction, denoted as u_x. The equation of continuity dictates that u_x is only dependent on y. Hence, the Stokes equation can be written as

$$\eta\frac{\partial^2 u_x}{\partial y^2} = \frac{\partial P}{\partial x} - \rho_e\frac{\partial E_{ext}}{\partial x}. \tag{2.27}$$

Inserting Equations 2.24, 2.25 and 2.26 for ρ_e and φ results in

$$\eta\frac{\partial^2 u_x}{\partial y^2} = \frac{\partial P}{\partial x} + \frac{\varepsilon\zeta E_{ext}}{\lambda_D^2}\frac{\cosh(y/\lambda_D)}{\cosh(h/\lambda_D)}. \tag{2.28}$$

Exploiting the no-slip boundary condition at $y = h$ and $y = -h$ and axial symmetry at $y = 0$, the solution to this linear differential equation is a superposition of the solutions obtained for $E_{ext} = 0$ (purely pressure-driven flow) and $\partial P/\partial x = 0$ (purely electro-osmotic flow):

$$u_x(y) = \frac{h^2}{2\eta}\frac{\partial P}{\partial x}\left(\left(\frac{y}{h}\right)^2 - 1\right) + \frac{\varepsilon\zeta E_{ext}}{\eta}\left(\frac{\cosh(y/\lambda_D)}{\cosh(h/\lambda_D)} - 1\right). \tag{2.29}$$

For microchannels without an applied pressure gradient, the first term on the right hand side is omitted and a velocity profile as shown schematically in Figure 2.2 is obtained.

In many practical applications, EOF is undesirable and therefore needs to be suppressed. One way to do this is to add polyelectrolytes that cover the charged microchannel

walls and thereby reduce the surface potential. For example, polyvinylpyrrolidone (PVP) can be used to effectively reduce EOF occuring at negatively charged glass surfaces [32, 33].

2.5 The Nernst-Planck equation

The Nernst-Planck equation describes the ion flux in a solution, taking into account different driving forces. Introductions are given by Probstein [14] and Masliayah and Bhattacharjee [13], which serve as the basis for the following. In electrolyte solutions, there are several sources of ion movement: diffusion driven by concentration gradients, electrophoresis caused by electric fields, and convection of the bulk fluid. All three are combined in the Nernst-Planck equation, according to which the molar flux density $\vec{j}_i$ of an ionic species i is

$$\vec{j}_i = -D_i \nabla c_i - c_i \mu_i \nabla \varphi + c_i \vec{u}_b. \tag{2.30}$$

This notation of the equation is valid for sufficiently dilute solutions, where the diffusion tensor contains only terms on the diagonal and the molar average velocity is equal to the mass average velocity. In the third term on the right side, $\vec{u}_b$ is the velocity of the bulk fluid.

Based on the Nernst-Planck equations, the current density in an electrolyte system can be obtained by multiplying $\vec{j}_i$ with the valence ν_i and the Faraday constant F and then summing up over all ionic species:

$$\begin{aligned} \vec{i} &= F \sum_{i=1}^{N} \nu_i \vec{j}_i \\ &= -F \sum_{i=1}^{N} \nu_i D_i \nabla c_i - \kappa \nabla \varphi + F \vec{u} \sum_{i=1}^{N} \nu_i c_i. \end{aligned} \tag{2.31}$$

Here, it has been exploited that the electrical conductivity κ is determined by the concentrations, mobilities and valances of the different ionic species according to

$$\kappa = F \sum_{i=1}^{N} \nu_i c_i \mu_i. \tag{2.32}$$

Starting from the Nernst-Planck equation, Probstein also derives an equation that describes the conservation of a species i [14]:

$$\frac{\partial c_i}{\partial t} + \vec{u}_b \cdot \nabla c_i = D_i \Delta c_i + \mu_i \nabla \cdot (c_i \nabla \phi) \tag{2.33}$$

If species are consumed or produced in homogeneous reactions, a production rate R_i has to be added. Here, however, reactions between species are not considered.

2.6 Isotachophoresis

Isotachophoresis (ITP) is a specific electrophoretic technique that plays an important role in this thesis. Hence it will be discussed in detail. First, the basic principles of ITP will be explained, followed by a description of the physics behind ITP and how ITP enables sample focusing. In the last part of this section, the focus is on ITP based applications.

2.6.1 Basic principles of ITP

Many of the basic concepts in the following were taken from the extensive ITP review by Ramachandran and Santiago [11], which provides a very consistent view on the topic. Isotachophoresis uses a discontinuous electrolyte system, i.e. a system usually formed by two electrolytes with a common counterion, but different co-ions. The co-ions differ in their electrophoretic mobilities. One of the electrolytes has a co-ion with a higher magnitude of electrophoretic mobility, which is why it is referred to as the leading electrolyte (LE). Likewise, the trailing electrolyte (TE) has a co-ion with a lower magnitude of electrophoretic mobility. In its simplest form, ITP is carried out in a capillary connecting two buffer reservoirs, as shown schematically in Figure 2.3. Here, anionic ITP is depicted, i.e. ITP with anionic co-ions. At the beginning, the capillary and one of the reservoirs are filled with leading electrolyte, see the upper part of Figure 2.3.A. The trailing electrolyte is inserted into the remaining reservoir. Between TE and LE, a diffuse interface[†] is formed due to the co-ion (and counterion) concentrations gradients. When an electric field is applied *via* two electrodes placed in the reservoirs, all co-ions and counterions are electrophoretically transported towards the anode or cathode, respectively.

In narrow capillaries as shown in Figure 2.3, ITP can be treated as a 1D problem. Sufficiently far away from the interface, the electrical conductivity in the LE and TE, respectively, is locally uniform. The same is true for the electric field. Current conservation demands that

$$i = \kappa^{\mathrm{L}} E^{\mathrm{L}} = \kappa^{\mathrm{T}} E^{\mathrm{T}}. \tag{2.34}$$

The superscripts L and T refer to the LE and TE region, respectively. Accordingly, the electric field adjusts as shown schematically in Figure 2.3.B. More precisely, the electric field is distributed in such a way that the ITP condition

$$\mu_{\mathrm{L}}^{\mathrm{L}} E^{\mathrm{L}} = \mu_{\mathrm{T}}^{\mathrm{T}} E^{\mathrm{T}} = v_{\mathrm{ITP}} \tag{2.35}$$

is fulfilled. According to the ITP condition, LE co-ions in the LE zone (mobility $\mu_{\mathrm{L}}^{\mathrm{L}}$) and TE co-ions in the TE zone (mobility $\mu_{\mathrm{T}}^{\mathrm{T}}$) migrate at the same velocity, called the

[†]In the context of ITP, the term "interface" is not used in the sense of a phase boundary between immiscible phases.

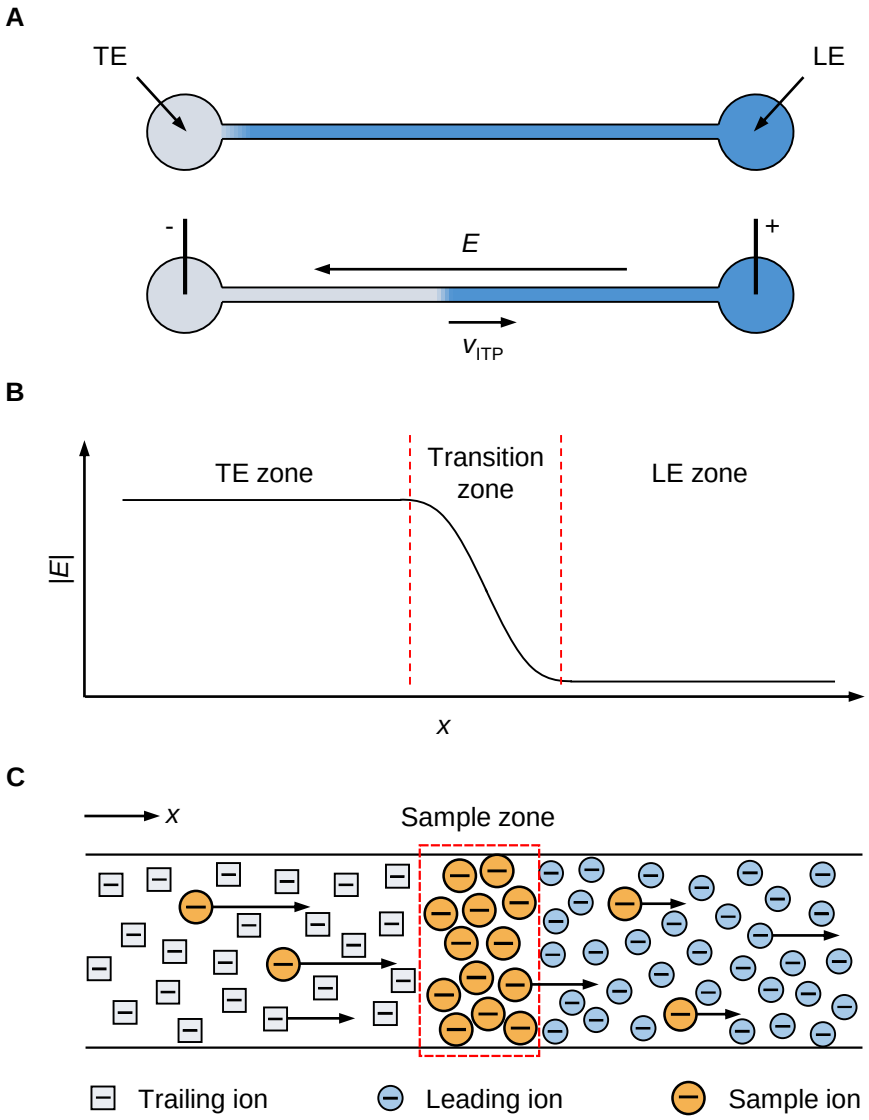

Figure 2.3: Schematic of anionic isotachophoresis in microchannels. A) shows a schematic of a simple microfluidic setup based on a narrow capillary that can be used for ITP experiments. During an ITP experiment, the electric field close to the interface is distributed as depicted in B). In C), the distribution of co-ions and sample ions is shown schematically. Sample ions can initially be dissolved in TE or LE. Alternatively, they can be introduced into a finite region between the two electrolytes.

isotachophoretic velocity v_{ITP}. The transition zone between LE and TE is characterized by a sharp electric field gradient. It moves with the same velocity v_{ITP}.

The electric field gradient can be used to focus a third species of intermediate electrophoretic mobility, for example a low concentration sample. The corresponding distribution of TE, LE and sample co-ions is depicted schematically in Figure 2.3.C. Sample ions in the TE zone have a higher speed than the TE co-ions and therefore they pass them until they reach the interface. Similarly, sample ions in the LE zone fall back behind the LE co-ions. Besides, TE and LE co-ions that have left their respective zones by diffusion

are transported back. In this way, the interface between TE and LE is self-sharpening, i.e. diffusive mixing of the two electrolytes is suppressed.

2.6.2 The physics behind ITP

This subsection explains the physics behind ITP. Following the approach of Ramachandran and Santiago [11] again, the basics are introduced by first focusing only on strong electrolytes. Hence, in a first step, a simple system with two co-ions and one counterion, all fully dissociated, will be considered. Later, a transfer to the case of weak electrolytes will be made. Note that in the following, the effects of ionic strength on ion mobilites are neglected, which is a valid assumption for rather low values of $\mathcal{I}$.

Ramachandran and Santiago extensively discuss the topic of charge neutrality in their review [11]. Apart from a mismatch between positive and negative charges at the ITP interface, net charge neutrality can generally be assumed. The ITP condition (Equation 2.35) follows accordingly: If the LE co-ions with high-magnitude electrophoretic mobility migrated faster than the TE co-ions, a gap with unbalanced counterions would form between the LE and TE zone. As a consequence, net charge neutrality would be violated. Instead, such imbalances are corrected on a very short time scale. Therefore, overall, LE and TE co-ions migrate at the same velocity. Using the approach of an ion concentration shock wave between co-ions of different mobility and concentration, Ramachandran and Santiago derive an equation for the electrophoretic velocity [11]:

$$v_{\mathrm{ITP}} = i\frac{\mu_{\mathrm{L}}^{\mathrm{L}}}{\kappa^{\mathrm{L}}} = i\frac{\mu_{\mathrm{T}}^{\mathrm{T}}}{\kappa^{\mathrm{T}}}. \tag{2.36}$$

In the case of strong electrolytes, the electrophoretic mobility is independent of the ion position in the ITP system. Therefore, the mobility superscripts (LE or TE) could be omitted. However, the above equation can also be used to estimate v_{ITP} in ITP systems based on weak electrolytes. In this case, $\mu_{\mathrm{L}}^{\mathrm{L}}$ and $\mu_{\mathrm{T}}^{\mathrm{T}}$ are effective mobilities as defined by Equation 2.21. Thus, they depend on the local pH and therefore on the ion position, which is indicated by the superscript. Insterting conservation of current (Equation 2.34) into Equation 2.36, the ITP condition (Equation 2.35) is obtained. Equations 2.35 and 2.36 reveal one important characteristic of ITP: If ITP is driven by a constant current, v_{ITP} and likewise E^{L} and E^{T} will generally remain constant over time. By contrast, if it is driven by a constant voltage, the electric field in the LE and TE zones is a function of the length of the respective zone, i.e. the position of the ITP interface. As the low conductivity TE replaces the high conductivity LE, the electric current decreases over time. In consequence, there is also a decrease in v_{ITP}.

As first shown by MacInnes and Longsworth, v_{ITP} can be used to predict the characteristic width of the interface between LE and TE [34]. Ramachandran and Santiago explain their result as follows [11]: For both LE and TE co-ions, an equation of conservation as

given by Equation 2.33 can be formulated at steady state in a frame of reference moving with the ITP interface and neglecting bulk flow. Combining these two equations and integrating with respect to the spatial coordinate (in the approximation of a 1D problem) leads to

$$L_{int} = \frac{\hat{R}\vartheta}{F v_{\mathrm{ITP}}} \frac{\mu_{\mathrm{L}}\mu_{\mathrm{T}}}{\mu_{\mathrm{L}} - \mu_{\mathrm{T}}}. \tag{2.37}$$

under the assumption that $\nu_{\mathrm{L}} = \nu_{\mathrm{T}}$. Accordingly, the width of the interface L_{int} scales inversely with the isotachophoretic velocity and hence also with current density and electric field, respectively. Hence, L_{int} stays constant in constant-current ITP, but increases over time in constant-voltage ITP. In Equation 2.37, the superscripts of the electrophoretic mobilities have been omitted to show that this approach is only valid in the case of fully dissociated strong electrolytes. For weak electrolytes, however, it still provides a useful estimate of the order of magnitude of the ITP interface width. In this case, effective mobilities have to be inserted. Typically, L_{int} is on the order of 10 µm.

Another characteristic of ITP can also be derived from species conservation [11]. When Equation 2.33 for one dimension is multiplied by the species valence ν_i, divided by the electrophoretic mobility μ_i and summed up over all species, it becomes

$$\frac{\partial}{\partial t}\left(\sum_i \frac{\nu_i c_i}{\mu_i}\right) = \frac{\partial}{\partial x}\left(\frac{\partial}{\partial x}\varphi \sum_i \nu_i c_i\right). \tag{2.38}$$

Here, bulk flow has again be neglected. Besides, sufficiently far away from the interface, there are no concentration gradients. Thus, diffusive species transport is also omitted. Considering charge neutrality, i.e. $\sum_i \nu_i c_i = 0$, the remaining term on the right side of Equation 2.38 also becomes zero. An integration with respect to t results in

$$\sum_i \frac{\nu_i c_i}{\mu_i} = w_{\mathrm{K}}(x). \tag{2.39}$$

On the right hand side of the equation, $w_{\mathrm{K}}(x)$ denotes a function that only depends on x. It is called the Kohlrausch regulating function, named after Friedrich Kohlrausch, who first derived it [35]. It bears some important consequences for the ion distribution in the different zones occurring during ITP. Since $w_{\mathrm{K}}(x)$ is independent of time, it is determined only by the initial conditions of an ITP process. For example, in the case depicted in Figure 2.3, a capillary is initially filled with LE. Accordingly, $w_{\mathrm{K}}(x)$ is given by

$$w_{\mathrm{K}}(x) = \frac{\nu_{\mathrm{L}} c_{\mathrm{L}}^{\mathrm{L}}}{\mu_{\mathrm{L}}} + \frac{\nu_{\mathrm{C}} c_{\mathrm{C}}^{\mathrm{L}}}{\mu_{\mathrm{C}}}, \tag{2.40}$$

where the index C denotes the counterion common to both LE and TE. When TE replaces LE, the concentration of TE ions in the TE zone can be determined according to

$$c_{\mathrm{T}}^{\mathrm{T}} = c_{\mathrm{L}}^{\mathrm{L}} \left(\frac{\nu_{\mathrm{L}} \mu_{\mathrm{T}}}{\nu_{\mathrm{T}} \mu_{\mathrm{L}}} \right) \left(\frac{\mu_{\mathrm{C}} - \mu_{\mathrm{L}}}{\mu_{\mathrm{C}} - \mu_{\mathrm{T}}} \right). \tag{2.41}$$

Remarkably, the concentration of TE co-ions in the TE zone $c_{\mathrm{T}}^{\mathrm{T}}$ is independent of and usually unequal to the initial concentrations of TE co-ions in the TE reservoir $c_{\mathrm{T}}^{\mathrm{T},0}$ (or, when different microchannel geometries are used, of the TE concentration in regions that are initially occupied by TE). Instead, it is proportional to the concentration of LE ions in the LE zone. In the literature, often the term "adjusted TE zone" is used to describe the difference in TE co-ion concentration between the TE reservoir (or regions that were initally occupied by TE) and the TE zone replacing the LE zone in the microchannel. Here, the superscript "T" always denotes the adjusted TE zone, whereas "T,0" refers to the initial TE concentration. The concentration of LE co-ions in the LE zone stays constant over time, i.e. $c_{\mathrm{L}}^{\mathrm{L}} = c_{\mathrm{L}}^{\mathrm{L},0}$.

In the literature, there is currently no generally applicable equivalent to the Kohlrausch regulating function for weak electrolytes. Only for the case of univalent species, i.e. with valence numbers ν of -1 and 0 or 0 and $+1$, respectively, Dismukes and Alberty [36] and Jovin [37] presented similar expressions. A discussion of their equations can be found in [38]. Dismukes and Alberty showed that

$$\sum_i \frac{c_i}{|\mu_{i,\pm 1}|} = w_{\mathrm{A}}(x). \tag{2.42}$$

In this equation, usually called Alberty function, c_i is the analytical concentration of a species and comprises both its ionized and neutral form, i.e. $c_i = \sum_\nu c_{i,\nu}$. Besides, $\mu_{i,\pm 1}$ is the mobility of either the cationic or anionic form of species i, respectively. Next, the Jovin function says that

$$\sum_i \nu_i c_i = w_{\mathrm{J}}(x), \tag{2.43}$$

i.e. the sum over all species i of the products of the total species concentration c_i and the corresponding valence of the ionized state is only a function of x, but not of time. The Jovin function looks similar to the electroneutratility condition, but is generally non-zero since c_i comprises also molecules in their neutral form. Again, Ramachandran and Santiago show how these equations can be derived from the species conservation equation (Equation 2.33) and how they can be used to determine the concentrations of TE co-ions and counterions in the TE zone [11]. Under the assumption that the electrophoretic mobilities of counterions as well as LE and TE co-ions are independent of the zone where

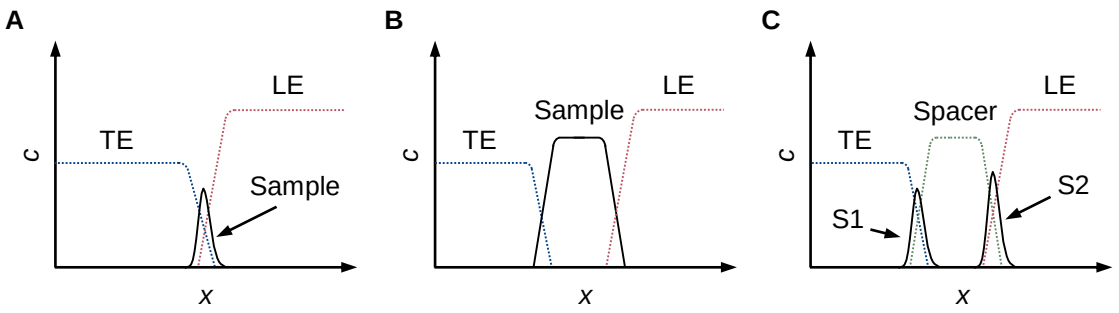

Figure 2.4: Schematic of concentration distributions of different species in different ITP modes. A) shows the concentration distribution of LE, TE, and sample in peak-mode ITP. B) shows the same species, but in plateau-mode ITP, where the sample forms its own plateau zone. In C) peak-mode ITP and plateau-mode ITP are combined: Two samples (S1 and S2) are separated by a spacer.

the corrsponding ions are located, they show that

$$c_{\mathrm{T}}^{\mathrm{T}} = c_{\mathrm{L}}^{\mathrm{L}} \frac{|\mu_{\mathrm{T}}|}{|\mu_{\mathrm{L}}|} \left(\frac{|\mu_{\mathrm{C}}| + |\mu_{\mathrm{L}}|}{|\mu_{\mathrm{C}}| + |\mu_{\mathrm{T}}|} \right). \tag{2.44}$$

For univalent strong electrolytes, Equation 2.41 and Equation 2.44 are identical. However, the authors also stress that the Alberty and Jovin functions are only valid for moderate and safe pH values, i.e. between 4 and 10 at buffer concentrations $> 10\,\mathrm{mM}$.

2.6.3 Sample focusing in ITP

Now that the basics of ITP have been outlined, this subsection will explain how it can be used to focus ionic species between the TE and LE zones. As before, this is first discussed for systems consisting only of strong electrolytes. Any species X with an intermediate electrophoretic mobility

$$|\mu_{\mathrm{T}}| < |\mu_{\mathrm{X}}| < |\mu_{\mathrm{L}}| \tag{2.45}$$

will be focused at the TE-LE interface [11]. For low initial amounts of X, its concentration distribution shows a peak that coincides with the electric field gradient between LE and TE, see Figure 2.4.A. Hence, this mode is called peak-mode ITP. Only at higher concentrations, X contributes significantly to the local electric field when focused. As a result, it forms a zone with a locally uniform electric field. Also, its concentration distribution is locally uniform (Figure 2.4.B), which is why this mode is called plateau-mode ITP. Theoretically, an arbitrary number of plateau zones can be formed between the TE and LE zones. Plateau-mode and peak-mode ITP can also be combined, for example to separate two low concentration samples with a third high concentration species acting as a spacer (Figure 2.4.C). Any plateau concentration can be determined *via* the Kohlrausch regulating function, see Equation 2.39.

Ramachandran and Santiago present similar conditions for the focusing of weak electrolyte species [11]. In this case, a species X will focus between LE and TE if the following condition for the effective mobilities is met:

$$|\mu_{\mathrm{X}}^{\mathrm{T}}| > |\mu_{\mathrm{T}}^{\mathrm{T}}| \quad \text{and} \quad |\mu_{\mathrm{X}}^{\mathrm{L}}| < |\mu_{\mathrm{L}}^{\mathrm{L}}|. \tag{2.46}$$

Again, a high concentration species will eventually form a plateau zone. Corresponding conditions can be derived for each interface between two plateaus or a plateau and the TE or LE zone, respectively.

The focusing of samples in peak-mode ITP is of particular importance in the work presented below. Therefore, some additional information on the accumulation dynamics and the sample distribution in peak-mode ITP is presented here. In 2008, Khurana and Santiago published their work on sample zone dynamics in peak-mode ITP [39]. There, they present an equation describing the accumulation rate of sample ions at the interface between TE and LE in constant-current ITP. If the sample S is initially dissolved in TE, there will be a continuous influx of sample ions from the TE reservoir into the sample zone. The number of focused sample ions per unit area n_{S} then increases over time according to

$$\frac{dn_{\mathrm{S}}}{dt} = (\mu_{\mathrm{S}}^{\mathrm{T}} E^{\mathrm{T}} - v_{\mathrm{ITP}}) c_{\mathrm{S}}^{\mathrm{T}}. \tag{2.47}$$

Integrating in time and using the relation $x = v_{\mathrm{ITP}} t$ for the position of the ITP interface leads to

$$n_{\mathrm{S}}(x) = \left(\frac{\mu_{\mathrm{S}}^{\mathrm{T}}}{\mu_{\mathrm{T}}^{\mathrm{T}}} - 1 \right) c_{\mathrm{S}}^{\mathrm{T}} x. \tag{2.48}$$

Note that $c_{\mathrm{S}}^{\mathrm{T}}$ is the sample concentration in the adjusted TE zone. Ramachandran and Santiago write that a similar equation is obtained if the sample is initially mixed with LE [11]. In this case, the number of focused sample ions per unit area would be

$$n_{\mathrm{S}}(x) = \left(1 - \frac{\mu_{\mathrm{S}}^{\mathrm{L}}}{\mu_{\mathrm{L}}^{\mathrm{L}}} \right) c_{\mathrm{S}}^{\mathrm{L}} x. \tag{2.49}$$

They also discuss how the accumulation rate changes if there is a bulk liquid flow caused by a pressure gradient and/or EOF. However, the equations derived by them are not presented here, as bulk flow plays only a minor role in the following ITP experiments. The above equations show that the sample accumulation depends on the initial placement of the sample ions. Depending on the electrophoretic mobilities of the different co-ions and the ratio between the initial TE ion concentration ($c_{\mathrm{T}}^{\mathrm{T},0}$) and the ion concentration in the adjusted TE zone ($c_{\mathrm{T}}^{\mathrm{T}}$), it is more effective to load the sample into either the TE or LE [40].

An analytical solution for the shape of the sample concentration distribution in peak-mode ITP is given by Rubin et al. [41]. Based on the Nernst-Planck equation, they

derive the concentration distributions of counterions and LE and TE co-ions, as well as the electric field distribution. These are then used to determine the sample concentration profile. The authors found that the exact solutions for the mentioned distributions involve hypergeometric functions. However, they also present a simplified approximate solution for the sample distribution, which, in dimensional form, is given by

$$c_{\mathrm{S}} = \frac{N_{\mathrm{S}}}{AL_{int}} \frac{\sin\left(\pi \frac{L_{int}}{L_{\mathrm{S}}}\right)}{\pi} \frac{\exp\left(\frac{x}{L_{\mathrm{S}}}\right)}{1+\exp\left(\frac{x}{L_{int}}\right)}. \tag{2.50}$$

Here, N_{S} is the total amount of focused sample ions. A is the channel cross-section. L_{int} and L_{S} are the characteristic widths of the ITP interface and the sample distribution, respectively. They both are obtained using Equation 2.37, only replacing μ_{L} by μ_{S} for L_{S}. *Via* L_{S}, the sample distribution depends on the sample mobility μ_{S}. Only if

$$\mu_{\mathrm{S}} = \frac{2\mu_{\mathrm{T}}\mu_{\mathrm{L}}}{\mu_{\mathrm{T}}+\mu_{\mathrm{L}}}, \tag{2.51}$$

the sample distribution is symmetric and can be approximated by a Gaussian distribution. Otherwise, it is asymmetric. The closer μ_{S} to μ_{L} or μ_{T}, the more the distribution tails into the LE or TE zone, respectively. Note that Equation 2.50 describes a cross-section-averaged distribution and is only valid as long as there is no pressure-driven flow or EOF that will disturb the sample distribution. These effects have been described in several publications (see for example [42–46]), but are not discussed here. Rubin et al. also studied the effect of asymmetric sample distributions on reaction kinetics [41]. They found that when two reactants with asymmetric concentration profiles are co-focused, the maximum reaction rate is not obtained for perfectly overlapping sample distributions. Instead, an optimum is obtained when the second reactant is more concentrated around the point of maximum concentration of the first.

2.6.4 ITP based applications

A prototype of ITP was presented in 1923 by Kendall and Crittenden, whose goal was to separate chlorine and lithium isotopes [47]. Since then, numerous applications of ITP have been proposed. The focus of this subsection will mainly be on the development over the last 15 years. The overview given here will not be comprehensive, but will focus on a few interesting applications.

In recent years, ITP has been widely used in different bioassays. For this reason, mainly nucleic acids [48–60] and proteins [61–65], but also bacterial cells [66, 67] and exosomes [68] have been accumulated. More examples of ITP-based nucleic acid and protein accumulation can be found in the reviews by Datinská et al. [69] and Khnouf and

Han [70]. In addition, it has also been demonstrated that ITP can be used to focus and transport polymer beads [71, 72] or emulsion droplets [73].

Depending on the experimental conditions, the local concentration of the focused sample in peak-mode ITP is increased by several orders of magnitude compared to the initial value [62, 74–78]. This can be exploited in the direct detection of fluorescent samples, where the strength of the measured signal increases with fluorophore concentration. Therefore, ITP allows to significantly improve the detectability of low concentration fluorescent samples, which has already been proven in the 1980s and early 1990s [79–83]. More recently, ITP has been combined with porous silicon optical biosensors and nanopore sensors for single molecule detection [58, 64, 84]. Sample molecules are focused and delivered to the sensors, whose sensitivity significantly increases with sample concentration. Here, too, the use of ITP improves the detectability of low concentration samples. Another main field of application of ITP is the purification of samples by separating them from contaminants. For example, Persat et al. have used ITP to isolate nucleic acids from blood lysate [85]. They have chosen the co-ion mobility of TE and LE in such a way that DNA molecules are concentrated at the ITP transition zone, while other components, mainly proteins, are left behind. Similarly, RNA molecules or proteins can be extracted or separated from lysed cells and other contaminants, see for example [48, 86–89]. Next, there is a large number of publications on ITP-based acceleration of reactions, usually between a target and a probe molecule. For example, in 2008 Park et al. and Kawabata et al. introduced an immunoassay based on the ITP-enhanced reaction between an α-fetoprotein and a corresponding antibody [90, 91]. In a 2008 conference paper, Persat and Santiago were the first to suggest applying ITP to DNA hybridization reactions [92], an idea that was adopted several times in the following years [48, 53, 93]. In 2012, Bercovici et al. came up with an approximate analytical model quantifying the impact of ITP sample focusing on reaction rates in hybridization reactions [54]. They report a 10,000-fold faster reaction compared to the standard reaction without ITP for reactant concentrations on the order of 100 pM. Since then, numerous bioanalytical assays based on ITP have been presented [67, 94–97]. All these examples are based on focusing at least one reactive species in a narrow ITP sample zone at some point during the protocol. Eid and Santiago have extensively reviewed the research on ITP applied to both homogeneous and heterogeneous biomolecular reactions [98]. Last, ITP can be used to preconcentrate sample molecules to increase the performance of a subsequent capillary electrophoresis-based separation process. A good introduction to this approach is given by Bahga and Santiago [94]. To summarise, peak-mode ITP is used to detect, purify, and pre-concentrate samples as well as to accelerate reactions. In many applications, two or more of these operations are combined.

This subsection on ITP-based applications is completed with a few remarks on microchannel design and different modes of operation. While most microchannels for ITP

are made from polymers or glass, there are also paper-, thread-, or fabric-based microfluidic devices for isotachophoretic species accumulation [50, 52, 59, 60, 68, 99, 100]. A very basic ITP setup was presented in Figure 2.3. If the sample is initially mixed with TE or LE (or both) and then inserted into the reservoirs, the sample is introduced *via* semi-infinite injection. During the ITP process, there will be a permanent influx of sample molecules into the sample zone. By contrast, in finite injection, the total amount of sample is initially loaded in a finite region between pure TE and LE zones. Usually, this can be achieved using branched microchannels. As a consequence, the concentration in the sample zone remains constant over time. The advantages and disadvantages of the two modes are discussed by Ramachandran and Santiago [11]. Using meandering microchannels increases the total length and hence, in accordance with Equations 2.48 and 2.49, the total amount of accumulated sample in semi-infinite injection. Positive effects on sample accumulation can also be achieved by creating a stationary ITP zone using counterflow caused by EOF or pressure-driven flow, see for example [59, 66, 75, 101].

Chapter 3

Interaction of bioparticles with phase boundaries in aqueous two-phase systems under electric fields

3.1 Summary

The electric field-driven transport of proteins and exosomes across the liquid–liquid interface in an aqueous two-phase system (ATPS) is studied in a microfluidic device using fluorescence microscopy. An ATPS containing polyethylene glycol (PEG) and dextran is employed. In a first step, bovine serum albumin (BSA) and bovine γ-globulins (BγG) are considered as model proteins. It is shown that both proteins, initially in the dextran-rich phase, accumulate at the liquid–liquid interface, preferably close to the three-phase contact line between the two liquid phases and the microchannel wall. It is in these regions where the proteins penetrate into the PEG-rich phase. The transport resistance of the liquid–liquid interface is higher for BγG than for BSA, such that a much larger molar flux of BSA into the PEG phase is observed. This opens up the opportunity of separating different protein species by utilizing differences in the transport resistance at the interface. A mathematical model is presented, accounting for adsorption and desorption processes at the liquid–liquid interface. The underlying theoretical concept is that of an electrostatic potential minimum formed by superposing the applied electric field and the field due to the Donnan potential at the interface. A fit of the model parameters to the experimental data results in good agreement between theory and experiments, thereby corroborating the underlying picture. Additionally, initial experiments on the interaction of exosomes with the phase boundary of an ATPS are presented. They suggest that the interface could also be used to separate exosomes from other particles with a lower transport resistance.

3.2 Contributions, funding and publications related to this project

The author of this dissertation began working on electric field-driven protein separation in microfluidic aqueous two-phase systems during his Master's thesis [102]. In this Master's thesis, the purification and separation of BSA and BγG at liquid-liquid interfaces of different ATPS was investigated using epifluorescence microscopy. Different pH values, ionic strengths, and electric field strengths were tested. Besides, a mathematical model describing the accumulation of the proteins at the interface was developed. The results indicated that it should in principle be possible to separate different proteins based on their different transport resistance at the phase boundary of the ATPS. During his PhD studies, the author continued his work on protein separation by doing experiments with the most promising combinations of pH value, ionic strength, and electric field strength. In addition to epifluorescence microscopy, confocal microscopy was used to gain further insights into the details of protein accumulation at the interface. The final results of this project were published in Soft Matter, a Journal of the Royal Society of Chemistry [103]. The author of this thesis contributed to the paper by fabricating the microfluidic devices, performing the experiments, as well as analyzing and visualizing the data. Johannes Hartmann advised the author of this thesis during the process of data acquisition and the evaluation of the results. Steffen Hardt conceived and directed the research. He also wrote the manuscript together with the author of this thesis. All contributors were involved in the design of the research. Some parts of the text of the Soft Matter article were directly inserted here, others were slightly adjusted. Most of the figures presented below were adapted from this article. The formatting and some symbols were adjusted to match the style of this thesis.* The raw fluorescence images obtained from the protein separation experiments and the Matlab code to evaluate them are freely available.† The initial research on the electric field-driven accumulation and purification of exosomes in microfluidic ATPS was funded by Merck KGaA.

3.3 Introduction

Aqueous two-phase systems find widespread applications in context with the separation and purification of biomolecules, especially proteins and DNA. In many cases, ATPS consist of two incompatible polymers that form two immiscible phases when a threshold concentration is exceeded. In thermodynamic equilibrium, many macromolecules prefer

*Reproduced from Soft Matter, 2021, 17, 3929-3936 with permission from the Royal Society of Chemistry.

†https://doi.org/10.48328/tudatalib-1078.

one of the phases over the other, i.e. they have a partition coefficient different from one, which is exploited in separation and purification protocols.

Of special relevance for the work reported in this chapter are processes in which species are separated based on the interfacial transport resistance in an ATPS. That is, when a molecule or particle crosses the interface, it experiences a transport resistance that is specific for the structure of the interface. Differences in transport resistance can be utilized for species separation. First indications that applying an electric field normal to the interface is key to tuning the transport resistance were found in experiments addressing protein partition in two-phase microflows under electric fields [104]. By contrast, in the absence of electric fields no significant transport resistance of the interface for proteins was found in a system consisting of polyethylene glycol (PEG) and dextran [105]. Later on, the transport resistance of the interface in an ATPS was utilized to achieve a size separation of DNA molecules [106, 107]. Here, the occurrence of an interfacial transport resistance is attributed to an electrostatic potential well that forms when the intrinsic electric field due to a back-to-back double layer at the liquid-liquid interface is superimposed by an external electric field [106], to be explained below.

Up to now, the molecular size separation based on the transport resistance of the liquid-liquid interface has only been demonstrated for DNA molecules. In that context, the physical processes governing the transport resistance are only beginning to be understood. The present work focuses on the transfer of proteins across the interface in an ATPS containing PEG and dextran. Protein separation and purification *via* partitioning over two phases is a classical application of ATPS [108, 109]. Here a different scheme for protein separation in ATPS is demonstrated, where instead of the properties of the bulk phases, the structure of the liquid-liquid interface plays a key role. Fluorescence microscopy is used to image the concentration fields of the proteins. The pathway through which the transfer from the dextran-rich to the PEG-rich phase occurs is studied. To progress the understanding of the underlying physical mechanisms, the mathematical model introduced in [102], accounting for the adsorption and desorption of proteins at the interface, is used to explain the experimental data.

Additionally, experiments with exosomes, a type of extracellular vesicles (EV), are carried out to explore possible further applications of electric field-driven separation processes in microfluidic ATPS. EVs are nanoparticles surrounded by a lipid bilayer that are released from cells [110]. Even though their function is not yet fully understood, it has already been found out that they are involved in communication between cells. Their characteristics, like their surface structure and their cargo, are specific to the cell from which they were secreted. That is why EVs can be used for diagnostic purposes. Therapeutic applications are also conceivable [111]. There are already a number of microfluidics-based approaches for the purification and size-separation of EVs [112, 113]. However, none of them are using the interface of ATPS as a transport barrier.

3.4 Theoretical background

Aqueous two-phase systems form when two incompatible species are combined in an aqueous solution above a critical concentration. Their discovery is usually attributed to Martinus Willem Beijerinck [114, 115]. In an 1896 article, he describes how a mixture of starch and gelatine separates into two phases. But it was not until the 1950s that Per-Åke Albertsson put ATPS to use by separating proteins and isolating cell walls from microorganisms [116, 117]. In the following, the fundamentals of ATPS are explained.

3.4.1 Thermodynamics of aqueous two-phase systems

As discussed in [118], the phase separation of an ATPS can be understood by considering the Gibbs free energy of mixing:

$$\Delta G_{mix} = \Delta H_{mix} - \vartheta \Delta S_{mix}. \tag{3.1}$$

Here, ΔH_{mix} is the enthalpy difference and ΔS_{mix} is the entropy difference between the mixed and the phase-separated state. Besides, ϑ is the absolute temperature of the system. The system will stay in a mixed state if $\Delta G_{mix} < 0$, i.e. when the entropic term is larger than the enthalpic term. Otherwise, two phases will form. In polymer-polymer ATPS for example, Hatti-Kaul summarizes, the driving force for the demixing process is the enthalpy associated with the interactions between the segments of the polymers which is opposed by the loss in entropy associated with the segregation of the polymers during phase separation [108].

The composition of the two phases can be predicted using phase diagrams, as schematically presented in Figure 3.1. In the phase diagram, a binodal curve separates the monophasic region from the biphasic region. The tie lines, which each connect two points on the binodal, determine the mass fractions ω_1 and ω_2 of the two incompatible components in the separated phases. For example, any mixture whose initial mass fractions lie on the line connecting points T and B will form two phases. The corresponding mass fractions in the top and bottom phase are then given by points T and B, respectively. At the critical point, marked with C, the tie line length is zero, resulting in two separate phases with equal composition. An extensive discussion of the interpretation of ATPS phase diagrams is given by Asenjo and Andrews [119]. To predict the equilibrium phase compositions, phase diagrams can either be derived from experimental data (see for example [120–122]) or from phase equilibrium calculations based on an estimation of the Gibbs free energy (see for example [123]). For the sake of completeness, it should be mentioned that the addition of significant amounts of biological feedstock for separation purposes may affect the phase equilibrium [124]. Besides, it is possible to create aque-

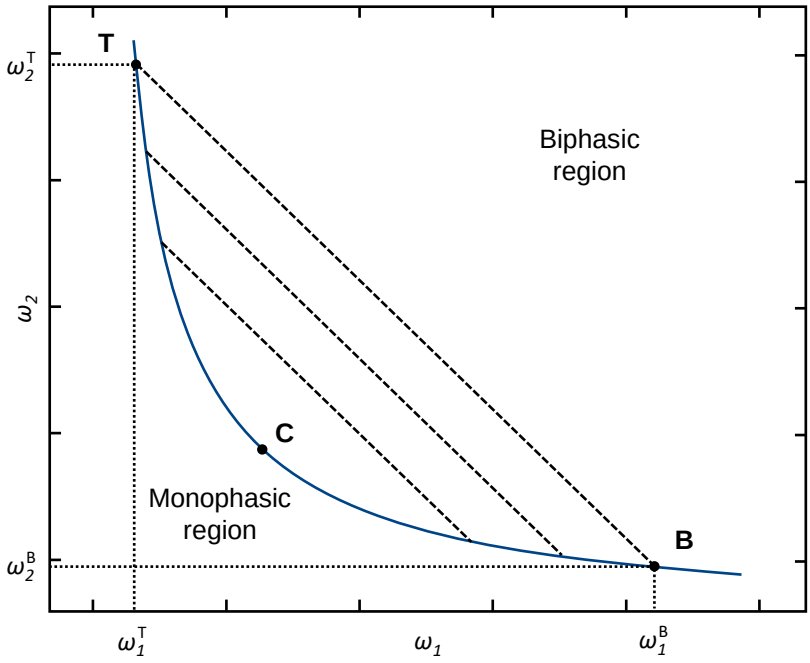

Figure 3.1: Schematic drawing of the phase diagram of an aqueous two-phase system. Here, ω_1 and ω_2 are the mass fractions of the two incompatible species. The binodal curve separates the monophasic from the biphasic region. The tie lines determine the mass fractions in the two separated phases. The indices T and B denote the top and bottom phase, respectively.

ous multi-phase systems with three or more phases by using more than two incompatible species [125–128].

Arsenjo and Andrews summarize the mechanism behind phase separation in ATPS for the most common cases of polymer-polymer and polymer-salt systems [119]. When incompatible polymers are mixed, they form large aggregates. Due steric exclusion, these aggregates tend to separate. Similarly, in polymer-salt systems, salts will capture a large amount of water, which will eventually lead to steric exclusion, too. Under the influence of gravity, the separated phases are stacked according to their densities, thereby forming a top and a bottom phase. In 2002, Arsenjo et al. showed that the separation rate of an ATPS based on polyethylene glycol (PEG) and phosphate salts depends on the densities and the viscosities of both phases as well as on their interfacial tension [129]. Interestingly, DC electric fields and decreased temperatures can be used to accelerate the separation process of certain ATPS [130–133]. As explained above, only mixtures with mass fractions of incompatible components higher than those defined by the binodal will separate. However, there are different ways of inducing phase separation in systems that do not initially phase separate. For example, Passos et al. showed that it is possible to design thermoreversible ionic liquid-based ATPS [134]. Upon increasing the temperature, the binodal curve is shifted towards lower mass fractions of the phase-forming components. Above a critical temperature, phase separation is triggered. When decreasing the temperature again, the system returns to its monophasic initial state. In this way, the

temperature dependence of the binodal is exploited. Similarly, thermoseparating polymers, i.e. polymers with reduced solubility above a critical temperature, can be used to thermally activate phase separation [135–137]. In another approach, phase separation is triggered by decreasing the water content of an ATPS mixture, for example by evaporation [138–140]. Reducing the mass fraction of water will go along with increased mass fractions of the incompatible components. Eventually, the binodal will be crossed and phase separation will occur. Already in 2013, Boreyko et al. published their work on reversible phase transitions *via* evaporation-induced dehydration and water rehydration [141].

In general, five different types of ATPS are known from the literature: polymer-polymer, polymer-salt, alcohol-salt, micellar, and ionic liquid-based ATPS [142]. Among these, polymer-polymer ATPS are most relevant for biological applications, especially those formed from dextran and polyethylene glycol (PEG). One of these systems formed from dextran and PEG will also be used below. The dextran rich (PEG rich) phase will be referred to as bottom (top) phase due to its higher (lower) density or simply as dextran (PEG) phase.

3.4.2 Interfacial tension of phase boundaries in ATPS

Compared to liquid-liquid two-phase systems with an organic and an aqueous phase, ATPS have a low interfacial tension. In their review on ATPS, Chao and Shum report values between 10^{-4} and 10^{-1} mN/m [115]. As systematically investigated by Liu et al., the interfacial tension increases with the total polymer concentration in polymer-polymer ATPS [143]. Some light has been shed on the composition of the interface of polymer-polymer ATPS by Tromp et al. [144]. Using the blob model and thereby taking into account excluded volume interactions, they found that with increasing incompatibility between the phase-forming polymers, the polymers are depleted from the interface. As a result, there is an excess of water at the liquid-liquid interface that is strongly dependent on the total polymer concentration. Later, Vis et al. studied the effect of polydispersity on the interfacial tension [145]. They used ATPS based on dextran and PEG molecules with a high molar mass. Replacing some of the high molar mass dextran with lower molar mass dextran, while keeping the tie line length in the phase diagram constant, reduced the interfacial tension. This was attributed to the displacement of the excess water at the interface mentioned above by the smaller polymer molecules.

Because of the low interfacial tension, Rayleigh-Plateau instabilities grow only slowly in ATPS. As a consequence, the formation of water-in-water jets is favored over the formation of droplets, as explained by Chao and Shum [115]. Still, emulsion droplets based on ATPS are often desired because of their high biocompatibility. Therefore, different methods for the formation of water-in-water droplets have been established [146–149].

3.4.3 Partitioning of ions in ATPS

Due to the different composition of the two phases of an ATPS, any ion, molecule or particle will have a different affinity for each of them. In the context of protein separation, Asenjo and Andrews summarize the main concept used to describe this difference in affinity [119]. In an ATPS in equilibrium, the concentrations of a species i will be different in the top and bottom phase (assuming the two phases are stacked according to their densities). The ratio of the concentrations is called partition coefficient:

$$K_i = \frac{c_i^{\mathrm{T}}}{c_i^{\mathrm{B}}}, \tag{3.2}$$

where the indices T and B denote the top and bottom phase, respectively. A value > 1 indicates that the species prefers the top phase and *vice versa*.

3.4.3.1 Partitioning of electrolytes and effects on the interfacial charge profile

In their 1998 paper, Pfenning et al. discuss the partitioning of electrolytes in aqueous two-phase systems [150]. They consider a salt of the form A^+B^-. On the one hand, the A^+ and B^- ions will each have individual partition coefficients (K_{A^+} and K_{B^-}). On the other hand, electroneutrality will force them to partition together. In the authors' interpretation, this will put the entire ATPS system under tension, manifesting itself in an electrostatic potential difference $\Delta\varphi$. Under the assumption that $K_{A^+} = K_{B^-}$, which is demanded by electroneutrality, the potential difference can be expressed as

$$\Delta\varphi = \frac{\hat{R}\vartheta}{(\nu_{B^-} - \nu_{A^+})F} \ln \frac{K^0_{B^-}}{K^0_{A^+}}. \tag{3.3}$$

Here, $\hat{R}$, ϑ, F, and ν_i are the universal gas constant, the absolute temperature, the Faraday constant, and the charge number of species i, respectively. K_i^0 describes the ratio of the activity coefficients of i in the top and bottom phase. It includes all interactions of i with the corresponding phase, including van der Waals forces, polar interactions, hydrogen bonding and ionic interactions, but excludes the interaction between i and $\Delta\varphi$. This macroscopic model is supported by Monte Carlo simulations of the ion distribution close to the interface. While the bulk phase remains electroneutral, the ion concentrations are slightly shifted at the phase boundary, resulting in a non-zero net charge density. Consequently, there is also a potential drop across the interface. An interfacial potential difference resulting from the unequal partitioning of ions over the two phases is also referred to as Donnan potential [151–153]. While Pfenning et al. provide a valuable contribution to the understanding of electrolyte partitioning in ATPS, they were not the first to address the issue of uneven ion distribution at liquid-liquid interfaces. As early as 1939, Verwey and Niessen applied the Gouy-Chapman model for solid-liquid interfaces

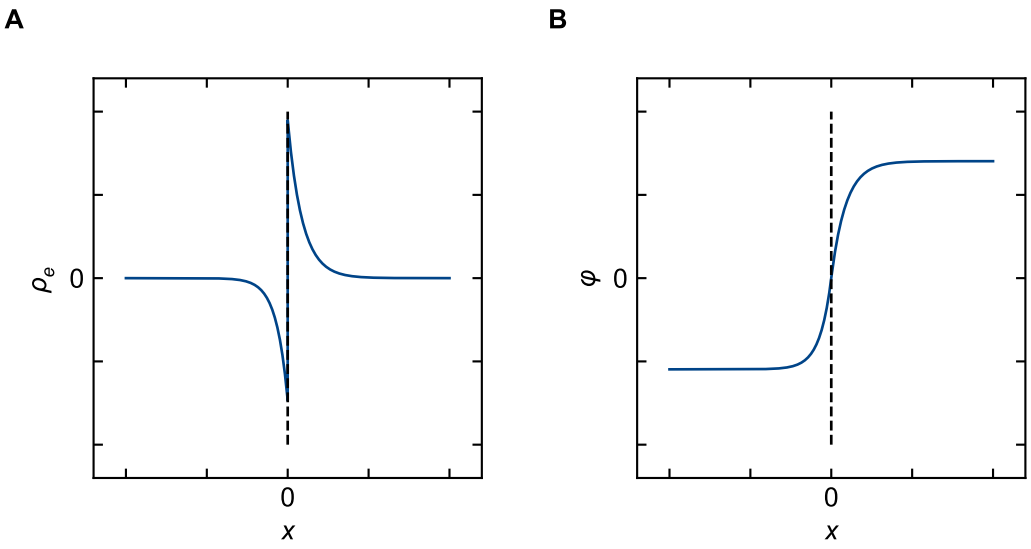

Figure 3.2: Schematic of the A) charge density and B) potential distributions close to the interface as described by Pfenning et al. [150] and Verwey and Niessen [154]. The black dashed line in both plots represents the interface of the ATPS.

(see Section 2.2) to systems with two liquid phases [154], thereby developing a first model for the charge and potential distribution at the phase boundary. In their article, they write that an electric double layer is formed with two diffusive layers, each falling into a liquid phase. These will henceforth be referred to as back-to-back double layers. A schematic of the charge density and potential distributions close to the interface as described by Pfenning et al. and Verwey and Niessen is depicted in Figure 3.2. It should be noted that this representation is only valid for the case of equilibrium, i.e. without an external electric field. Different contributions have been made to adept the Verwey-Niessen model, see for example [155–158]. Although these adapted models partly contradict each other, they all describe a potential drop and a polarization of the net charge distribution at the interface, too.

Hartounian et al. investigated the dependence of the potential drop $\Delta\varphi$ on the type of salt and the tie-line length of an ATPS based on PEG and dextran [159]. They combined models for ion-ion interactions, water-polymer interactions and ion-polymer interactions to calculate the activity coefficients of the salt ions in the different phases. The results show that the potential difference increases with the length of the tie-line and is significantly dependent on the type of salt. The values for $\Delta\varphi$ reported here range from 0 to 4 mV. This is in good agreement with the values measured in ATPS based on uncharged dextran and charged gelatin by Vis et al. [153]. They found that below the isoelectric point of gelatin, $\Delta\varphi$ varies between 0 and 8 mV. Above, values between 0 and −4 mV are obtained. Interestingly, based on the same type of ATPS, Vis et al. were able to show that the interfacial tension decreases with increasing $\Delta\varphi$ [160].

3.4.3.2 Partitioning of bioparticles applied in separation protocols

The uneven partitioning between the two phases can also be exploited for the separation of bioparticles. In the case of proteins, several properties of the ATPS/protein system contribute to the partitioning of biomolecules: top and bottom phase pH value, protein hydrophobicity, concentration of salts added and resulting electrical potential differences between the two phases, protein size (molecular weight) and surface area, biospecific affinities between proteins and ATPS polymers, and protein conformation [119]. If target proteins partition preferably into one phase and other biomolecules present in the ATPS system are predominantly found in the other phase, they can be separated. This has been demonstrated in several practical applications, see for example [161–165]. However, particle separation and purification in ATPS is not limited to proteins. Nucleic acids [166–168], cells [169–172] and viral particles [173–176] have also successfully been processed. Most recently, ATPS have also been used for the purification of extracellular vesicles [177–180].

3.4.4 Electrostatic potential distribution close to the interface under an external electric field

The potential distribution in Figure 3.2.B represents the equilibirum case, i.e. in an aqueous two-phase system without an external electric field. By contrast, in their 2011 paper, Hahn and Hardt present the potential distribution when an external electric field is applied [106]. They solved the Nernst-Planck equation for a system of two ions, in which one ion partitions unevenly between the two phases. The theory behind this is explained in detail in the non-peer-reviewed paper by Hardt and Baier [181]. In Figure 3.3, the results of this approach are shown schematically (based on the equations derived in [181]). The local minima and maxima formed near the interface are characteristic of the potential distribution in an ATPS with an external electric field. In consequence, a potential barrier is formed that might explain the accumulation of biomolecules like DNA and proteins at the interface, as explained below. As the external electric field strength increases, both the width of the potential well and the height of the potential barrier decrease. In this way, the interfacial transport resistance can be controlled *via* the external electric field.

3.4.5 Particle accumulation and separation at liquid-liquid interfaces of ATPS

So far, microfluidic ATPS systems have mainly been used for the generation of emulsion droplets and the separation of cells and biomolecules [115, 182, 183]. More recently, Přibyl and co-workers have proposed using microfluidic ATPS as a combined microreactor-microextractor system for the synthesis and purification of antibiotics [184–186]. Besides,

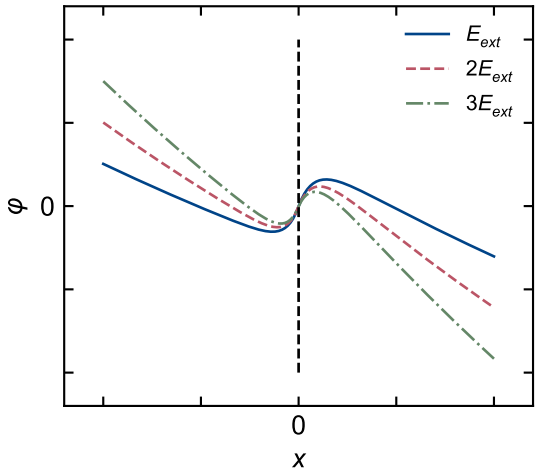

Figure 3.3: Schematic of the potential distribution close to the interface with an external electric field as described by Hahn and Hardt [106] and Hardt and Baier[181]. The black dashed line represents the interface of the ATPS. The different curves represent different strengths of the external electric field. The width of the potential well and the height of the potential barrier vary with the strength of the external electric field.

Han et al. presented their ATPS-based method to isolate EVs from small volumes of blood plasma in a microfluidic device [187]. However, the phase boundary of the ATPS is not used to support the purification process in any of these recent approaches.

As mentioned in the introduction of this chapter, Münchow et al. were the first to publish results on proteins experiencing a transport resistance at the interface of a microfluidic ATPS when transported with an electric field [104]. In their work, they are using an ATPS based on PEG and dextran. The different phases are injected into a microfluidic device to form co-flowing lamellae separated by an interface. Then, an electric field is applied, starting the transport of BSA molecules toward the phase boundary of the ATPS. When the protein is inserted into the PEG phase, the non-preferred phase, it crosses the interface unhindered. However, when inserted into the preferred dextran phase, it experiences a transport resistance up to a threshold electric field strength. Only when this threshold is exceeded, the proteins begin to penetrate into the adjacent phase. In a similar paper, Münchow et al. studied not only BSA, but also carbonic anhydrase and β-galactosidase [188]. They showed that all three proteins behave similarly when transported from the dextran phase across the interface. Even the threshold electric field strength to overcome the transport resistance is about the same. Therefore, they conclude that the transport resistance is not determined by the affinity of the proteins for the different phases, since the latter is different for BSA, carbonic anhydrase, and β-galactosidase.

In 2011, Hahn and Hardt presented their work on electric-field driven size-separation of DNA molecules at phase boundaries in microfluidic ATPS [106, 107]. In a microfluidic system similar to that used by Münchow et al., they accumulate DNA molecules of differ-

ent lengths at the interface of an ATPS with comparatively low electric field strengths. As the field strength is increased, smaller molecules detach earlier than larger ones. This allows the interface to be used as a size selective filter. The accumulation of DNA molecules is explained with the theory of a potential barrier at the interface [106] (as introduced in the previous subsection). This theory predicts that the width of the potential well and the height of the potential barrier at the interface decrease when the external electric field is increased. Hence, molecules trapped at the interface are more likely to escape at higher external electric field strengths. In their second paper, Hahn and Hardt show that the threshold electric field strength at which DNA molecules detach from the interface decreases roughly linear with their translational diffusivity [107]. This might explain why smaller molecules with a higher translational diffusivity detach earlier than larger ones. Summing up, the desorption process of DNA molecules (and also proteins) from the phase boundary can be described as a thermally activated escape from a metastable state [189]. In 2020, Hardt et al. published their work on the electric field-driven formation of clusters of DNA molecules attached to a liquid-liquid interface of an ATPS [190]. Hydrodynamic interactions between the molecules originating from the electro-osmotic flow due to the Debye layer around a molecule drive the formation of these patterns. Such clusters have already been observed by Hahn, who found that they depend on the type of salts used in the ATPS. He concluded that these inhomogeneous concentration distributions could have some disadvantages for studying fundamental issues at the boundary and also for possible applications [191].

Sinha et al. used the phase boundary of an ATPS to separate magnetic microspheres according to their size [192]. A magnetic field is used to transport the particles distributed in one phase towards the interface, where they are trapped as a liquid-liquid-solid three-phase contact line is formed. When the magnetic field strength is large enough to overcome the adhesion force, the particles get released and migrate into the adjacent phase. Similar to the findings above, smaller spheres detach earlier than larger ones when the distance between interface and magnet is decreased to increase the magnetic field strength. Although the exact mechanism of attachment and detachment remains to be elucidated, it is clear that the transport resistance in this case is caused by interfacial tension forces. The authors claim that it is most likely that line tension effects trigger particle detachment and are more relevant for smaller particles. Interfacial tension was also the dominant factor in the work of Li and Li, where polystyrene particles were transported across an ATPS liquid-liquid interface with a pulsed electric field [193]. Below a critical voltage, the particles were hindered from crossing the interface. However, by increasing the amplitude of the electrical pulse, the particles were able to penetrate the adjacent phase. The critical voltage depends on the direction of the particle transport (from the dextran phase to the PEG phase or *vice versa*) and on other experimental parameters such as ATPS composition, surfactant concentration and ionic strength. Irrespective of the direction of particle

transport, the critical voltage was lower for smaller particles. These findings were used in subsequent research to separate microparticles and microalgae cells of different sizes [194]. For completeness, Campos et al. reported on the electric-field driven transport of amino acids across the interface of an ATPS [195]. They found that at moderate electric field strengths, the molecules partially accumulate at the phase boundary. As soon as the external voltage is increased above a threshold value, the amino acids enter the adjacent phase. However, the authors do not offer any consistent explanation for their observation. Hence, it remains unclear if similar effects as described above are of relevance here.

3.5 Experiments and data processing

Here, the preparation of the ATPS and the samples used in the experiments is described. Besides, the experimental set-up and procedure are explained in detail. Last, the image processing methods used to study the temporal evolution of protein accumulation at the interface are presented.

3.5.1 ATPS preparation

To prepare the ATPS, 10.7 % (w/w) PEG 8,000 (Carl Roth) and 13.3 % (w/w) dextran 10,000 (Sigma Aldrich) are dissolved in a 10 mM N,N-bis[2-hydroxyethyl]-2-aminoethanesulfonic acid (BES) solution titrated with sodium hydroxide solution to a pH of 7 or 8, respectively. The ionic strength of the buffer is increased to 15 mM by adding NaCl. Subsequently, the ATPS components are mixed and the mixture is stored in a centrifuge tube at 5 °C for one hour, during which phase separation occurs. The top phase is rich in PEG, it will be referred to as PEG phase. It comprises approximately two third of the overall volume and is extracted with a syringe and a cannula. Afterwards, the interface between the dextran-rich phase, referred to as dextran phase, and the residue of the PEG phase is pierced with a second cannula. In this way, the bottom phase can be isolated. The viscosities of the two phases are $\eta_{\mathrm{PEG}} = 12.67\,\mathrm{cP}$ and $\eta_{\mathrm{dex}} = 21.89\,\mathrm{cP}$. Besides, the electric conductivities were determined to be $\kappa_{PEG} = 1.699\,\mathrm{mS/cm}$ and $\kappa_{dex} = 1.226\,\mathrm{mS/cm}$ in an ATPS based on a 10 mM BES buffer solution with pH = 8.

3.5.2 Sample preparation

Bovine serum albumin (BSA) Alexa Fluor 647 conjugate samples were purchased from Thermo Fisher Scientific. Bovine γ-globulins (BγG) were acquired from Sigma Aldrich and labeled with Alexa Fluor 488 reactive dye (Thermo Fisher Scientific). Both proteins are stored in phosphate-buffered saline (PBS) at pH = 7.4. Two different modes are investigated in the experiments with proteins. First BSA and BγG are observed separately. In a second series of experiments, they are combined and observed simultaneously. In

the latter case, 3.7 % (v/v) of both BSA and BγG dissolved in PBS are mixed with the dextran phase of the ATPS in a microcentrifuge tube. For the case that BSA and BγG are examined separately, one of the protein solutions is replaced by 3.7 % (v/v) pure PBS. Besides, 7.4 % (v/v) PBS is added to the PEG phase. Assuming a molecular weight of 66 kDa (150 kDa) for BSA (BγG), the total initial concentration in the dextran phase is 70.15 nmol/l (56.79 nmol/l). Measurements of the electrophoretic mobilities were carried out with a Zetasizer Nano ZS (Malvern Panalytical) at pH = 8. The resulting electrophoretic mobilities are: -1.61 ± 0.21 (BSA, dextran phase), -2.94 ± 0.30 (BSA, PEG phase), -1.26 ± 0.06 (BγG, dextran phase), -1.36 ± 0.021 (BγG, PEG phase). All values are given in units of $10^{-9}\,\mathrm{m^2/(Vs)}$.

In addition to experiments with BSA and BγG, some initial tests have been carried out with exosomes to see if the results obtained with proteins can be transferred to other types of bioparticles. To this end, exosomes in culture media were added to the dextran phase. Exosomes tagged with mNeongreen were provided by a collaborator from the Department of Biological and Medical Sciences at Oxford Brookes University, UK. They reported a size distribution ranging from 70 to 250 nm with a median size of approximately 110 nm. In a first experiment, the accumulation of exosomes at the interface was observed. Here, 40 µl of exosomes in culture media with a number concentration of $4.6 \cdot 10^{11}\,\mathrm{ml^{-1}}$ and 20 µl of PBS were dissolved in 1.5 ml of dextran phase. Hence, the final exosome concentration was $1.1 \cdot 10^{10}\,\mathrm{ml^{-1}}$. The ATPS was based on a 10 mM BES buffer with a pH of 8 an ionic strength of 15 mM. In a second set of experiments, the temporal evolution of the exosome concentration inside the bulk of the dextran and PEG phase was investigated. In this case, 60 µl of exosomes in culture media from a second batch with a number concentration of $5.1 \cdot 10^{11}\,\mathrm{ml^{-1}}$ were dissolved in 1.5 ml of dextran phase (ATPS based on a 10 mM BES buffer with a pH of 7 and an ionic strength of 15 mM). Accordingly, the final concentration was $1.9 \cdot 10^{10}\,\mathrm{ml^{-1}}$. In both cases, BSA served as reference molecule. It was added to the dextran phase together with the exosomes as described above. At the given buffer pH values, the exosomes, BSA and BγG have a negative surface charge.

3.5.3 Microfluidic device

Once the samples are prepared, the dextran phase and the PEG phase are introduced into a microchannel. Figure 3.4 shows a schematic drawing of the microfluidic device. The same design had already been used by Hahn and Hardt [106]. The system comprises two inlets through which the components of the ATPS are introduced. After each experiment, the liquids are withdrawn through the outlet. Two platinum electrodes serve as anode and cathode. They are dipped into two opposing buffer reservoirs. A comb-like structure of acrylamide gel bridges decouples them mechanically from the microchannel. Thereby, gas bubbles that form at the electrodes due to electrolysis are prevented from migrating into the channel. The channel has a length of 32 mm, a width of 8 mm and a height of 40 µm

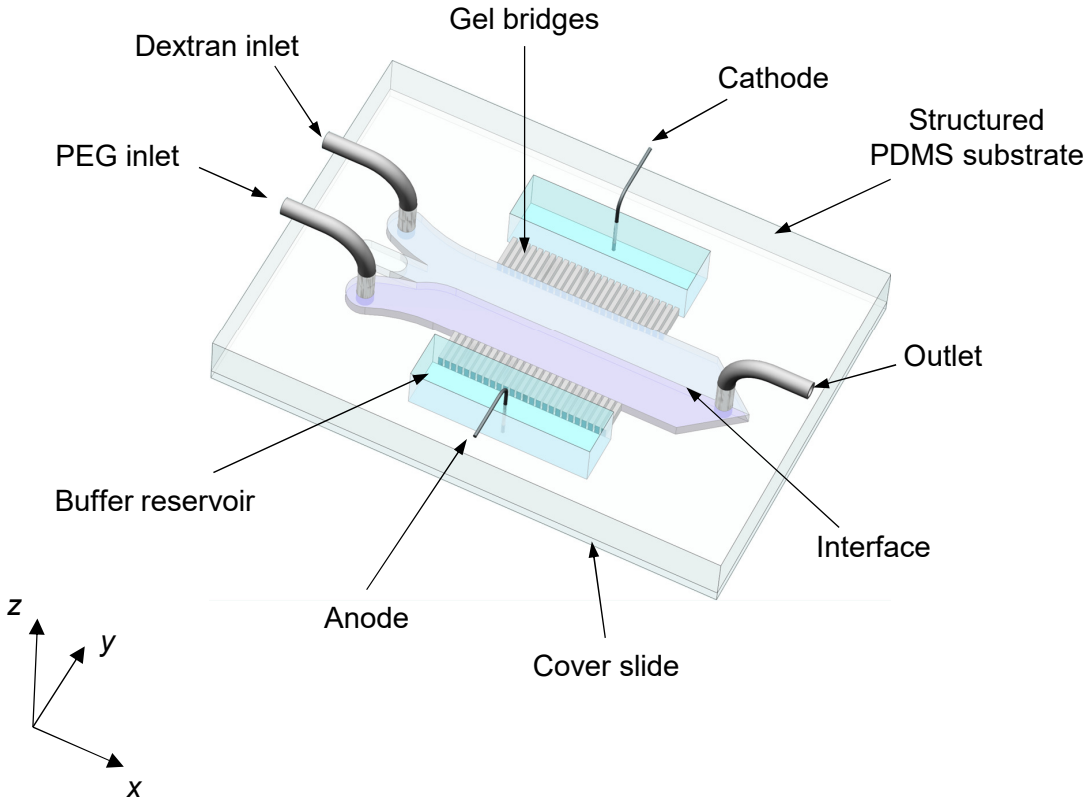

Figure 3.4: Schematic drawing of the microfluidic device used to study the electric field-induced behavior of different bioparticles (proteins and exosomes) at the interface of an ATPS. The particles were inserted together with the dextran phase. Reproduced from Soft Matter, 2021, 17, 3929-3936 with permission from the Royal Society of Chemistry.

in confocal microscopy experiments or 65 µm in epifluorescence microscopy experiments, respectively.

The soft lithography protocol was used to form the basic structures of the channel. PDMS and a curing agent were mixed at a ratio of 10:1, degassed for one hour, and poured on a SU-8 coated silicon wafer. Then the cast was cured for three hours at 85 °C. After cooling down, the buffer reservoirs, the outlet and two inlets were cut out at the intended positions. Plasma activation allowed to bond the cast to a glass cover slide of 0.13 to 0.16 mm thickness. Afterwards, the PDMS surfaces were silanized with a solution of 0.5 % (v/v) 3-(trimethoxysilyl)propyl methacrylate in 50 mM sodium acetate buffer at pH = 3.9 for 24 h. The gel bridges consisted of a solution of 30 g/l N,N'-methylenebisacrylamide, 30 g/l 2,2-dimethoxy-2-phenylacetophenone and 180 g/l acrylamide in isopropanol, which was inserted through the outlet hole. Next, the microchannel was covered with a simple lithography mask that spares the comb-like structure. Polymerization of the gel bridges and binding to the capillary walls was triggered by exposing the structure with UV light for 25 s with a Lightningcure LC8 UV light source (Hamamatsu). Before using the microfluidic chip, the gel bridges were dried carefully. Then, the whole device was filled with buffer and unlabeled BSA. In this way, BSA adsorbed to

the PDMS and glass surfaces and thereby prevented labeled proteins from attaching to the channel walls and disturbing the experimental results. Besides, the gel bridges were rendered conductive. Since the electric conductivity of the gel bridges is much higher than that of the PDMS walls, the electric field applied during experiments pointed in the y direction as indicated in Figure 3.4. Prior to introducing the ATPS, the channel was flushed with pure buffer solution to remove excess unlabeled BSA.

3.5.4 Experimental procedure

In a first step, the microfluidic chip was placed on the stage of a Nikon eclipse TI fluorescence microscope. The two liquid phases together with the proteins and exosomes, respectively, were injected with a syringe pump through PTFE tubings. By reducing the flow rate step by step, a stable interface formed and quiescent conditions were reached. The reservoirs were loaded with buffer and a DC electric field was applied between two platinum electrodes, using a TTi QL355TP voltage source (Thurlby Thandar Instruments).

In all experiments to investigate the interaction of BSA and BγG with the interface, the applied voltage was $U_{app} = 10\,\mathrm{V}$. The interface of the ATPS was examined using laser-scanning confocal microscopy as well as epifluorescence microscopy. In both cases, the fluorophores were excited with lasers of 488 and 639 nm wavelength and a power of 60 and 100 mW, respectively. In photobleaching tests over the time span of the experiments it was shown that no significant photobleaching of the fluorophores conjugated to the proteins occurs. All images were taken at a readout speed of 3 MHz and a bit depth of 16 bit (confocal microscopy) and 14 bit (epifluorescence microscopy), respectively. Confocal images were recorded with an Andor iXon Ultra 897 EMCCD camera and a Yokogawa CSU-X spinning disc unit through a Plan Fluor 20x objective (NA = 0.75). In this way, protein adsorption and desorption as well as the distribution of proteins over the interface could be monitored. The exposure time was kept at 200 ms. Every minute, a z-stack was recorded. In order to record the time evolution of the fluorescence intensity around the interface, epifluorescence microscopy was employed. All epifluorescence images were recorded at zero distance from the glass cover slide surface facing the microchannel. In this way, the three-phase contact line between the two liquids and the solid surface was within the focal plane, which is parallel to the x-y-plane in Fig. 1. Epifluorescence images were recorded with an Andor iXon+ 897 EMCCD camera with an exposure time of 200 ms through an S-Fluor 4x objective (Nikon, NA = 0.2). When BSA and BγG were examined separately (simultaneously), the frame rate was 4.96 fps (0.33 fps). Image acquisition starts as soon as the electric field is applied. Both microscope and cameras were controlled with Nikon's NIS-Elements software.

In experiments with exosomes, the applied voltage was $U_{app} = 30\,\mathrm{V}$. To investigate the accumulation of exosomes (and BSA as a reference) at the interface, epifluorescence

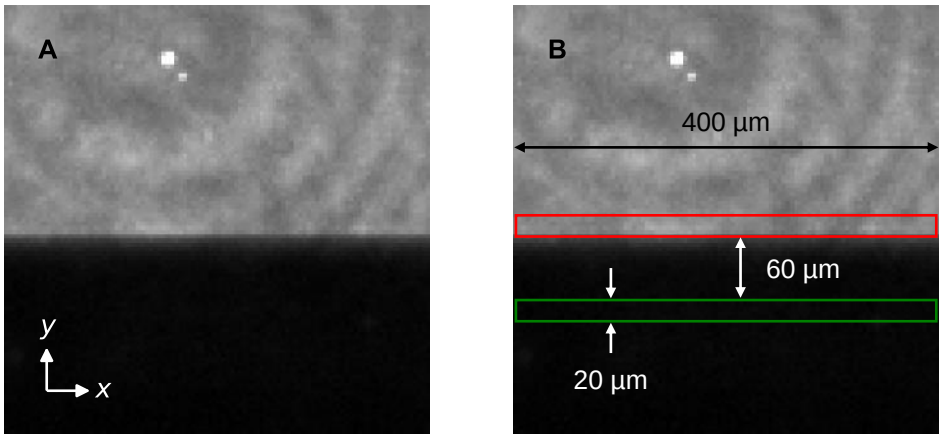

Figure 3.5: A) Epifluorescence image showing the interface between dextran and PEG phase at the beginning of an experiment. BγG is dissolved in the dextran phase, which leads to a high contrast between the two phases when excited with a wavelength of 488 nm. The two bright spots in the upper half of the image probably originate from impurities. To investigate the accumulation of BSA and BγG at the interface, a 400 µm long section of the interface is analyzed. To calculate the mean interfacial fluorescence intensity $I_{X,Y}$, the intensity values in a narrow region at the interface are averaged. The red rectangle in B) shows the range of pixels that are included. The green rectangle includes all pixels that are used to calculate a mean fluorescence intensity inside the PEG phase. This quantity is used to observe the protein penetration into the PEG phase.

images of the interface were recorded after $t = 30$ min. A wavelength of 488 nm (640 nm) was used to excite the exosomes (BSA). The exposure time was 500 ms. Here, an L Plan 50x objective (Nikon, NA = 0.45) was used. Otherwise, the camera settings and the positioning of the field of view were as described above. In a last variation of the experiments with ATPS, the electric field-induced development of the exosome (and BSA) concentration inside the dextran and PEG phase was investigated. To this end, fluorescence images of the bulk of the dextran and PEG phase were recorded at a distance of 1 mm from the interface before the experiment was started. These images served as reference since they represent the initial bulk concentration of exosomes (and BSA) in both phases. Then, after $t = 25$ min at $U_{app} = 30\,V$, fluorescence images of the bulk of both phases were recorded at distances of 1 and 2 mm from the interface, respectively. The same settings that were used to image the accumulation at the interface were applied here.

3.5.5 Data analysis

The post-processing of the epifluorescence images of BSA and BγG aims at quantifying the temporal evolution of the fluorescence intensity at the interface. The full image size is 512 px x 512 px. However, only a 400 µm long section of the interface was considered due to a rather inhomogeneous illumination of the images. An exemplary epifluorescence image (cropped to 100 px x 100 px) at the beginning of an experiment is shown in 3.5.A. MATLAB's built-in edge detection scheme allowed to localize the interface in a first step

by detecting sharp intensity gradients. The mean interfacial fluorescence intensity $I_{X,Y}$ was then determined by averaging over a narrow, 20 µm wide region, which comprises both the interface itself and the adjacent boundary region of the dextran phase as indicated in 3.5.B with a red rectangle.

To compare different series of measurements, the normalized fluorescence intensity I^* at the interface was calculated according to

$$I^*(t) = \frac{I_{X,Y}(t)}{I_{X,Y}(0)} \tag{3.4}$$

where $I_{X,Y}(t)$ is the mean interfacial fluorescence intensity at a time t while $I_{X,Y}(0)$ is the mean interfacial fluorescence intensity at the beginning of the respective experiment. The background fluorescence was subtracted from each image prior to calculating averaged or normalized fluorescence intensities. The penetration of proteins from the dextran into the PEG phase was evaluated by calculating $I^*(t)$ between distances of $\Delta y = 60\,\mu m$ and $\Delta y = 80\,\mu m$ from the interface inside the PEG phase, as indicated with the green rectangle in 3.5.B. In this case, normalization with $I_{X,Y}(0)$ was not possible since this quantity is zero after subtracting the background fluorescence intensity. Because of this, the averaged fluorescence intensity in the bulk of the dextran phase at the beginning of an experiment was used as reference value. Each experiment was carried out five times. All reported values of $I^*(t)$ are average values. For clarity of presentation, not all data points recorded during the experiments are displayed in Figure 3.9 and 3.10.

3.6 Results and discussion

As explained above, different experiments were carried out. First, the results obtained with confocal imaging of the distribution of proteins over the liquid-liquid interface will be shown. Then, the temporal evolution of the protein accumulation observed with epi-fluorescence microscopy will be analysed. Finally, the results of initial experiments with exosomes will be presented.

3.6.1 Distribution of proteins over the liquid-liquid interface

Here, the general trends in the spatiotemporal distribution of the proteins are reported. Figure 3.6 shows confocal images of a region enclosing the interface at pH = 8 and at different times t. For both types of proteins, the images indicate protein accumulation at the interface. As far as BSA is concerned, the interfacial fluorescence is most intense between $t = 4\,min$ and $t = 12\,min$ and declines afterwards. In the case of BγG, the intensity grows less rapidly but continuously until the end of the experiment.

In principle, the electrophoretic accumulation of charged species at or close to an interface between two electrolyte solutions can also occur when the species reach a phase

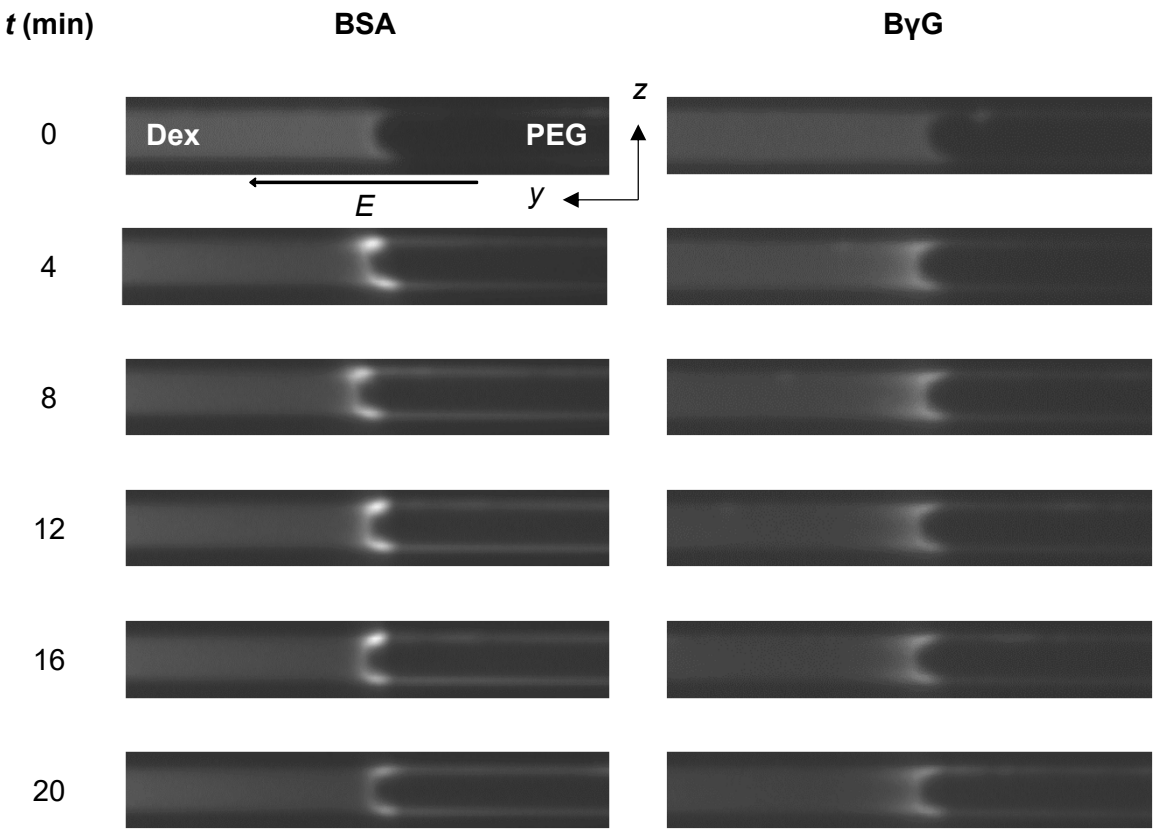

Figure 3.6: Confocal time-lapse images showing the evolution of the BSA and BγG concentration fields in a region enclosing the interface. The measurements were done at pH = 8. BSA and BγG were examined separately. Reproduced from Soft Matter, 2021, 17, 3929-3936 with permission from the Royal Society of Chemistry.

in which their electrophoretic transport is slower than at their starting point. The electrophoretic speed is given by the product of electrophoretic mobility and electric field strength, the latter being inversely proportional to the electric conductivity. To rule out such electrophoretic stacking as the dominant mechanism for protein accumulation at the interface between the dextran and the PEG phase, consider the case of BSA. Based on the values given in Subsection 3.5.2, the electrophoretic transport of BSA is by more than 30 % faster in the PEG phase than in the dextran phase. Hence, the BSA transport away from the interface is faster than the transport toward the interface, so an increase in fluorescence intensity can be attributed to protein adsorption at the interface. It suggests itself that a similar mechanism is at work for BγG. A decrease of the fluorescence intensity at the interface over time suggests that the rate of desorption from the interface exceeds the rate of adsorption. The series of images shown in Figure 3.6 already indicates that especially BSA mainly accumulates in the regions close to the three-phase contact lines between dextran phase, PEG phase and PDMS/glass wall. Besides, it is also at the three-phase contact line where the proteins preferably cross the interface.

Figures 3.7.A and B show the images at $t = 20\,\mathrm{min}$ with different contrast and brightness settings. Here it becomes obvious that also BγG accumulates mainly close to the

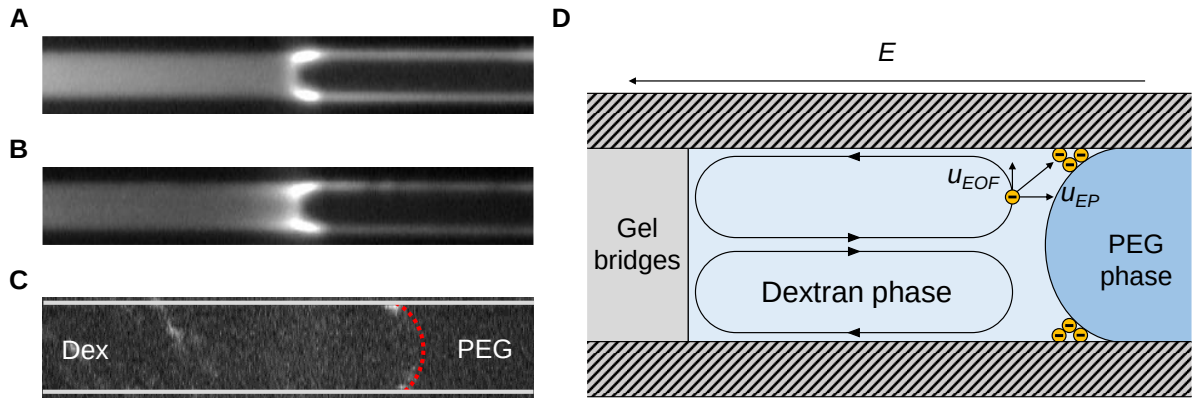

Figure 3.7: Contrast- and brightness-adjusted images of the fluorescence intensity of A) BSA and B) BγG in a region around the liquid–liquid interface, recorded at t = 20 min. In C), the accumulation of λ-DNA in a different ATPS with inversed interfacial curvature is shown[‡]. The gray lines mark the channel boundaries, the red dotted line represents the interface. D) shows a schematic of the flow pattern inside the dextran phase due to the combined actions of EOF and pressure-driven flow. A), B) and D) were reproduced from Soft Matter, 2021, 17, 3929-3936 with permission from the Royal Society of Chemistry.

three-phase contact line. When repeating the experiments with a sample of mixed proteins, no significant difference is observed between simultaneous and separate examination of BSA and BγG. To explain why protein accumulation preferably close to the three-phase contact lines is observed, the reader is referred to the schematic shown in Figure 3.7.D. Since both the glass and PDMS walls have a negative zeta potential at pH = 8 [20, 21], the electric field gives rise to an EOF. The diffuse part of the electric double layer has an excess of cations, which induces a flow along the walls away from the interface towards the gel bridges. However, in a closed container the net mass flow integrated over a plane spanned between the two channel walls needs to vanish, which happens because of an induced pressure-driven flow superposing the EOF. In total, this results in the recirculating flow pattern sketched in Figure 3.7.D. Taking into account that the proteins are mainly transported by advection and electrophoresis, in most of the regions inside the dextran phase they move towards the liquid-liquid interface. Once they arrive at the interface, most of them are not able to cross it, but slide along, driven by the combined action of the flow velocity and electrophoresis. They accumulate close to the three-phase contact lines. The streaks close to the walls inside the PEG phase visible in Figures 3.7.A and B indicate that the proteins cross the interface preferably at the contact lines. This can be explained by the large concentration in these regions and the stochastic nature of the detachment process, which is a key ingredient of the kinetic model presented further below.

With regard to the curvature of the interface, it seems likely that a molecule adsorbed at any location of the interface moves towards one of the three-phase contact lines. The applied electric field has a component parallel to the interface. As a result, molecules would migrate along the interface towards the contact lines. If this effect was the only reason for the preferred accumulation at the contact lines, inverting the curvature of the

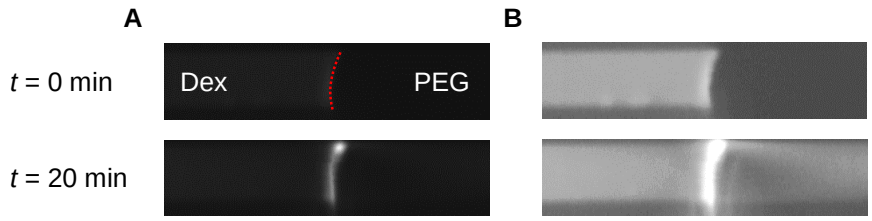

Figure 3.8: Confocal images showing the temporal evolution of the BSA concentration field in a region enclosing the interface of an ATPS with suppressed EOF at $t = 0\,\text{min}$ and $t = 20\,\text{min}$. A) shows the fluroescence intensity of BSA without adjustment of the image contrast or brightness. The red dotted line in the upper image marks the position of the interface. B) shows the contrast- and brightness-adjusted fluorescence intensity of BSA.

interface should suppress this accumulation. In earlier experiments with an ATPS based on dextran and PEG dissolved in 10 mM phosphate buffer at pH = 8.25, the curvature of the interface was inverted compared to what is shown in Figure 3.6, Figure 3.7.A and Figure 3.7.B. Still, the sample molecules, in this case λ-DNA, accumulated mainly at the three-phase contact lines, see Figure 3.7.C. The flow pattern caused by EOF as presented in Figure 3.7.D offers an explanation for this observation.

Additional experiments have been performed with 20 g/l of polyvinylpyrrolidone (PVP) added to both phases of the ATPS. PVP is a polyelectrolyte that suppresses the EOF by coating the PDMS and glass walls [32, 33]. The results of these additional experiments are shown in Figure 3.8, where fluorescence images from the beginning ($t = 0\,\text{min}$) and the end ($t = 20\,\text{min}$) are shown. With suppressed EOF, BSA accumulates more uniformly along the whole interface, as can be seen in Figure 3.8.A. Besides, the figure shows that PVP changes the contact angle between the interface and the PDMS and glass walls, respectively. However, the contact angle at the bottom glass wall changes more significantly than at the top PDMS wall, which suggests that coating with PVP is more efficient on glass than on PDMS. This could also explain the observation that BSA still mainly accumulates at the upper three-phase contact line, but not at the bottom one. The contrast- and brightness-adjusted images in Figure 3.8.B show that BSA no longer enters the PEG phase preferably at the three-phase contact line when EOF is suppressed. This observation can be interpreted as a confirmation of the hypothesis regarding the effects of EOF in the ATPS presented above. However, protein accumulation also occurs without EOF.

3.6.2 Experiments with separate protein samples

The previous section gave insights into the spatiotemporal distribution of the proteins. To quantify the differences between the two protein species with regard to their adsorption-desorption behavior, epifluorescence microscopy was used. In a first step, BSA and BγG were examined separately at different pH values, namely at pH = 7 and pH = 8. A variation of the pH value is motivated by the fact that important parameters such as

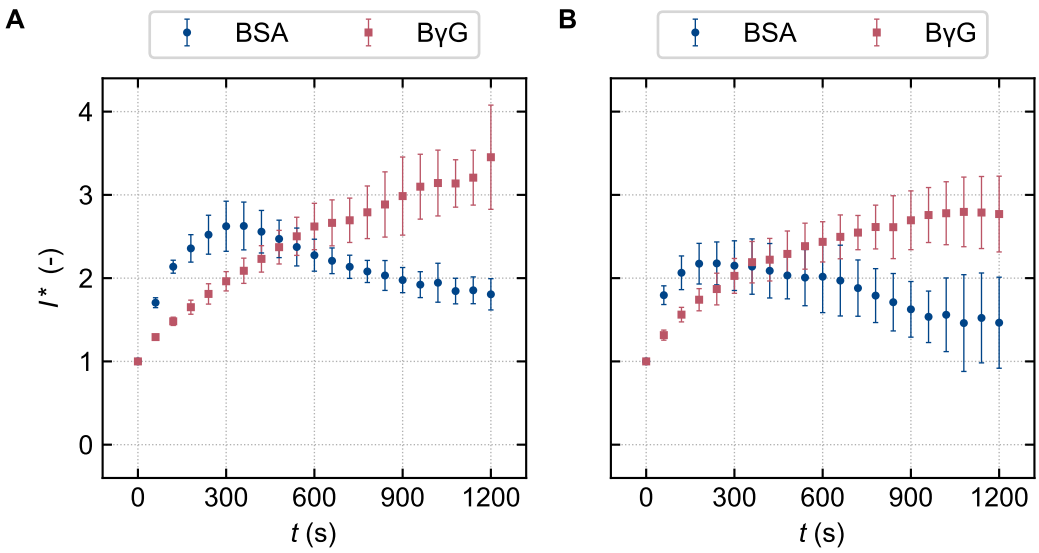

Figure 3.9: Normalized fluorescence intensity at the ATPS interface as a function of time. BSA and BγG were observed separately at A) pH = 7 and B)pH = 8. The data points represent the average over five measurements, with the error bars representing the standard deviation. Reproduced from Soft Matter, 2021, 17, 3929-3936 with permission from the Royal Society of Chemistry.

the electrophoretic mobility or the partition coefficient are pH-dependent. Figure 3.9 shows the respective results, plotted as the normalized fluorescence intensity at the ATPS interface as a function of time. Both at pH = 7 and 8, the normalized fluorescence intensity of BSA at the phase boundary rises sharply in the first 200 s after the electric field is applied. Subsequently, a plateau is reached, after which the intensity decreases. Hence, for a time span of about 600 s, the rate of BSA desorption from the interface exceeds the rate of BSA adsorption. Based on the error bars shown in both panels, which represent the standard deviation of the experiments, there is no significant difference between pH = 7 and pH = 8.

By contrast to the results obtained for BSA, BγG accumulates at the interface over the entire duration of the measurement. That is, adsorption dominates over desorption. As a result, significantly higher values of the normalized interfacial concentration are reached for BγG compared to BSA. At pH = 8, the fluorescence intensity reaches a plateau after $t \approx 1000$ s. Otherwise, no significant differences between the two pH values are found. Together, the results indicate that the transport resistance of the interface is significantly higher for BγG than for BSA: BSA is more easily able to cross the interface, while BγG accumulates over the entire duration of the experiments. This conclusion will be further corroborated in the next section.

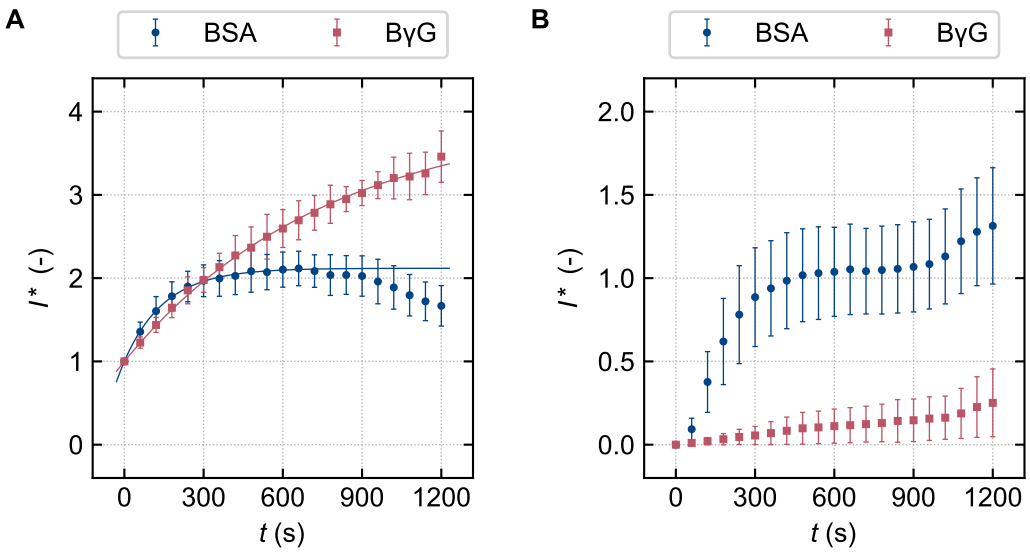

Figure 3.10: A) Normalized fluorescence intensity at the ATPS interface as a function of time with pH = 8. The symbols are experimental data, the lines are predictions by the model described in Subsection 3.6.4. B) Normalized fluorescence intensity between distances of 60 µm and 80 µm from the interface inside the PEG phase as a function of time. For both data sets the experiments were performed at pH = 8. BSA and BγG were observed simultaneously. The data points represent the average over five measurements, with the error bars representing the standard deviation. Reproduced from Soft Matter, 2021, 17, 3929-3936 with permission from the Royal Society of Chemistry.

3.6.3 Experiments with combined protein samples

Naturally, realistic scenarios for protein separation or purification deal with mixtures of different species. Therefore, experiments were conducted with samples containing both BSA and BγG. In this way, possible protein-protein interactions that would yield deviations from the results described in the previous section can be investigated. Figure 3.10.A is analogous to Figure 3.9.B. In the case of combined samples, the differences between BSA and BγG become somewhat more pronounced, i.e. the accumulation of BγG at the interface is even more distinct. However, there are no qualitative differences between the accumulation of proteins at the interface for the cases of separate and combined samples.

To get a realistic picture of how far this process would enable species separation, it is necessary to quantify the fraction that enters the PEG phase. By determining the averaged fluorescence intensity between distances of $\Delta y = 60\,\mu m$ and $\Delta y = 80\,\mu m$ from the interface inside the PEG phase, an indicator for the transfer into the PEG phase is obtained. Figure 3.10.B shows that, in the case of BSA, the normalized fluorescence increases rapidly at the beginning. At $t \approx 600\,s$ a plateau is reached. Afterwards, however, it starts rising again, which is only shortly after the normalized fluorescence intensity in Figure 3.10.A starts to decline. A possible explanation of this phenomenon will be given in the next section where the adsorption and desorption processes are described in a mathematical model. In contrast to BSA, the normalized fluorescence of BγG inside the

PEG phase rises only marginally. Therefore, BγG seems to desorb from the interface at a smaller extent than BSA, which reduces its mass flow across the interface. For comparison, the time evolution of the fluorescence intensity inside the PEG phase was also studied in the experiments in which BSA and BγG are kept separate. No significant differences compared to the results shown in Figure 3.10.B were found.

As a conclusion, it can be stated that the separation of BSA and BγG based on the transport resistance of the liquid-liquid interface is possible. Both molecules adsorb at the interface, but since BSA desorbs more easily than BγG, it is able to cross over into the PEG phase. Some details of the adsorption-desorption process will be discussed in the next section.

3.6.4 Model for the interaction of proteins with the liquid-liquid interface

As described above, the solution of the Nernst-Planck equation for a schematic liquid-liquid interface configuration as described by [106] yields the electrostatic potential distribution across the interface as a superposition of the Donnan potential and the potential of the applied electric field. When the applied electric field opposes that of the Donnan potential, a local minimum of the electrostatic potential is formed. Charged molecules can adsorb into this metastable state, but thermal fluctuations can let them jump over the potential energy barrier. This is a stochastic process, a thermally induced desorption from a metastable state. This adsorption-desorption kinetics is the likely reason for the accumulation of molecules at the interface.

Based on this picture, it is predicted that the accumulation of molecules is only achieved when the applied electric field opposes that of the Donnan potential, a situation sketched in Figure 3.3. By contrast, when both fields point into the same direction, no potential energy minimum is formed, and no accumulation at the interface should be observable. This was already confirmed in the experiments with DNA samples [106, 107] and the same is found in the experiments with proteins reported here. In other words: If proteins are inserted in the PEG phase and the electric field is reversed, the sample molecules pass the interface without experiencing any significant transport resistance.

In order to explain the results of the previous subsection, the mathematical model introduced in [102] is taken up and explained in detail here. First, the number of sample proteins per unit area adsorbed to the interface is defined as n_S, where all quantities refer to a specific protein species. The change of n_S over time can be described as

$$\frac{d}{dt} n_\mathrm{S} = j_a + j_d \tag{3.5}$$

where j_a is the molar flux of proteins from the dextran phase towards the interface, and j_d is the molar flux describing the desorption of proteins from the interface into the PEG

phase. In terms of the bulk protein concentration c_0, the electrophoretic mobility μ and the electric field strength E, j_a can be written as

$$j_a = c_0 \mu E. \tag{3.6}$$

This assumes that all molecules reaching the interface from the dextran phase end up in the potential energy minimum at the interface, a reasonable assumption given the reported shape of the electrostatic potential [106]. Adsorption to the interface from molecules already in the PEG phase via thermally activated hopping over the potential energy barrier is neglected, because in the experiments performed the protein concentration at the interface was always much higher than that in the adjacent PEG phase. This means that adsorption from the PEG phase can be neglected compared to desorption into the PEG phase.

Assuming thermally activated hopping, the molar flux away from the interface into the PEG phase is given by

$$j_d = -\alpha n_\mathrm{S} \tag{3.7}$$

with a rate constant α. The higher the energy barrier, the lower will be α. Inserting j_a and j_d into Equation 3.5 leads to a differential equation describing the dependence of n_S on t. Assuming the initial condition $n_\mathrm{S}(t = 0) = 0$, the solution is given by

$$n_\mathrm{S}(t) = \frac{c_0 \mu E}{\alpha} \left(1 - e^{-\alpha t}\right) = \frac{j_a}{\alpha} \left(1 - e^{-\alpha t}\right). \tag{3.8}$$

Assuming that the fluorescence intensity at the interface depends linearly on n_S, the normalized fluorescence intensity can be written as

$$I^*(t) = \frac{\beta}{\alpha} \left(1 - e^{-\alpha t}\right) + 1. \tag{3.9}$$

In this equation, β contains c_0, μ, E as well as two constants encoding the linear relationship between n and the fluorescence intensity at the interface.

According to this model, I^* increases monotonically and converges to $\beta/\alpha+1$. The best fits of the model to the experimental data for BSA and BγG are shown in Figure 3.10.A. Overall, a good agreement between the model and the experimental data is obtained, with one exception: For BSA the normalized fluorescence intensity decreases after a plateau is reached, a trend that is not captured by the model. Presumably, this is related to Faradaic reactions occurring at the electrodes. These reactions modify the chemical composition of the electrolyte solutions. The changes in the ionic concentrations need some time to travel from the buffer reservoirs into the microchannel and to the liquid-liquid interface. Since the structure of the back-to-back electric double layer at the interface depends on the ionic composition, the potential barrier and the rate constant of desorption α would also be affected. This possibly explains why the fluorescence intensity of BSA in

Protein	α ($10^{-3}\,s^{-1}$)	β ($10^{-3}\,s^{-1}$)	R^2
BSA	6.55 (6.21, 6.89)	7.37 (7.02, 7.62)	0.999
BγG	1.31 (1.20, 1.42)	3.88 (3.73, 4.03)	0.998

Table 3.1: Fit parameters with 95 % confidence bounds and coefficient of determination, based on the model of Equation 3.9.

the PEG phase (Figure 3.10.B) rises after $t = 600\,s$ while it declines at the interface (Figure 3.10.A). The approximate electrophoretic velocity of possible reaction products was estimated considering electrophoretic mobilities between 10^{-8} and $10^{-7}\,m^2/(Vs)$ and electric field strengths derived from the electric conductivities in the different segments of the microfluidic device. These calculations result in a time scale of ion transport from the buffer reservoirs to the interface that is of the same order of magnitude as the time scale on which a decrease of the interfacial fluorescence occurs for BSA. These findings corroborate the hypothesis formulated above. Similar effects of spontaneous desorption of molecules from the liquid-liquid interface after a certain time span were already observed in separation experiments with DNA [106].

Table 3.1 gives an overview of the fitting parameters α and β as well as of the coefficient of determination R^2. Remarkably, the rate constant α of BSA is approximately five times larger than that of BγG, translating to a higher rate of desorption. Ultimately, this leads to the conclusion that BSA has to overcome a lower energy barrier than BγG, i.e. it experiences a lower transport resistance at the interface. The differences in β can be attributed to different initial protein concentrations, electrophoretic mobilities and proportionality constants between concentration and fluorescence intensity.

Apart from the decrease in fluorescence intensity for BSA, it appears as if the model based on adsorption and desorption at the interface is able to describe the experimental data. This corroborates the picture of an electrostatic potential minimum at the liquid-liquid interface from which molecules can desorb [106], and offers an explanation of the transport resistance at the interface.

3.6.5 Accumulation of exosomes at the interface of an ATPS

The results above showed that phase boundaries in ATPS can be utilized for protein separation. The next step will be to investigate whether it is possible to extend the same separation process to other types of bioparticles. In particular, the interaction of exosomes with the interface will be studied on a qualitative level. Figure 3.11.A shows the exosome accumulation at the interface after 30 min with $U_{app} = 30\,V$. It can clearly be seen that a significant amount of exosomes is prevented from penetrating the adjacent PEG phase. However, some of the exosomes may have crossed over, as indicated by a few rather inconspicuous bright spots in the PEG phase. For reference, Figure 3.11.B

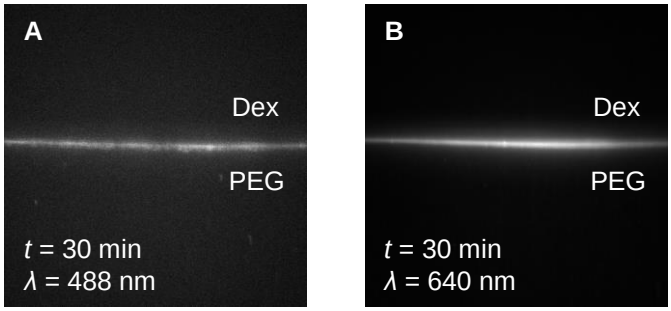

Figure 3.11: Accumulation of A) exosomes and B) BSA at the interface of an ATPS with $U_{app} = 30\,\mathrm{V}$ after 30 min.

shows the interaction of BSA with the phase boundary. Here, too, a significant amount is accumulated at the interface. However, it is not clear from this representation whether a significant proportion of the BSA has also entered the adjacent phase, which would be in line with the results presented above. To gain a better understanding of the extent to which exosomes and BSA pass through the interface, the particle distributions in the bulk of the two phases after 25 min are now compared to the initial state.

3.6.6 Development of the exosome and BSA distributions inside the bulk

Figure 3.12.A shows the distribution of exosomes at a distance of $d = 1\,\mathrm{mm}$ from the interface, i.e. inside the bulk of the dextran phase, at the beginning of an experiment. The EVs are visible as sparsely distributed bright spots. No electric field is applied that would shift the concentration field. Therefore, the distribution in this image is representative of the entire bulk of the dextran phase. In Figure 3.12.B, the exosome distribution at the same distance from the interface, but after 25 min with $U_{app} = 30\,\mathrm{V}$ is shown. The number of exosomes appears to be approximately the same as at the beginning of the experiment. By contrast, the exosome concentration is significantly lower at $d = 2\,\mathrm{mm}$, see Figure 3.12.C. Hence, most EVs have been removed from the bulk of the dextran phase at this distance from the interface. The bottom row of Figure 3.12 suggests that no exosomes have reached distances of $d = 1$ or 2 mm from the interface inside the bulk of the PEG phase after 25 min with $U_{app} = 30\,\mathrm{V}$. Together with the results shown in Figure 3.11.A, this indicates that most of the EVs get accumulated at the interface and do not penetrate the PEG phase. The exosomes that cross the interface are either insignificant in number or have a rather low electrophoretic mobility, which would keep them close to the interface.

Figure 3.13 illustrates the BSA concentrations in both the dextran and the PEG phase at $t = 0\,\mathrm{min}$ and $t = 25\,\mathrm{min}$. At the beginning of the experiment, BSA is homogeneously distributed in the bulk of the dextran phase (Figure 3.13.A). After 25 min with $U_{app} = 30\,\mathrm{V}$, however, BSA has been more or less removed from the bulk (Figure 3.13.B and C).

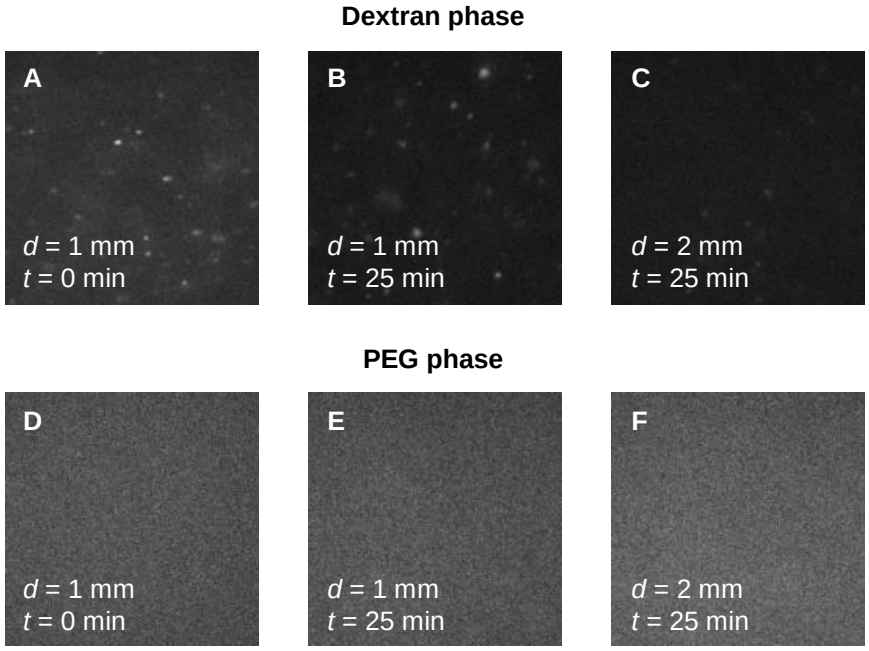

Figure 3.12: Temporal evolution of the exosome distribution in the bulk of the dextran phase (top row) and the PEG phase (bottom row). The distance from the phase boundary is given by d. All subfigures show a section of 200 x 200 px of the full image.

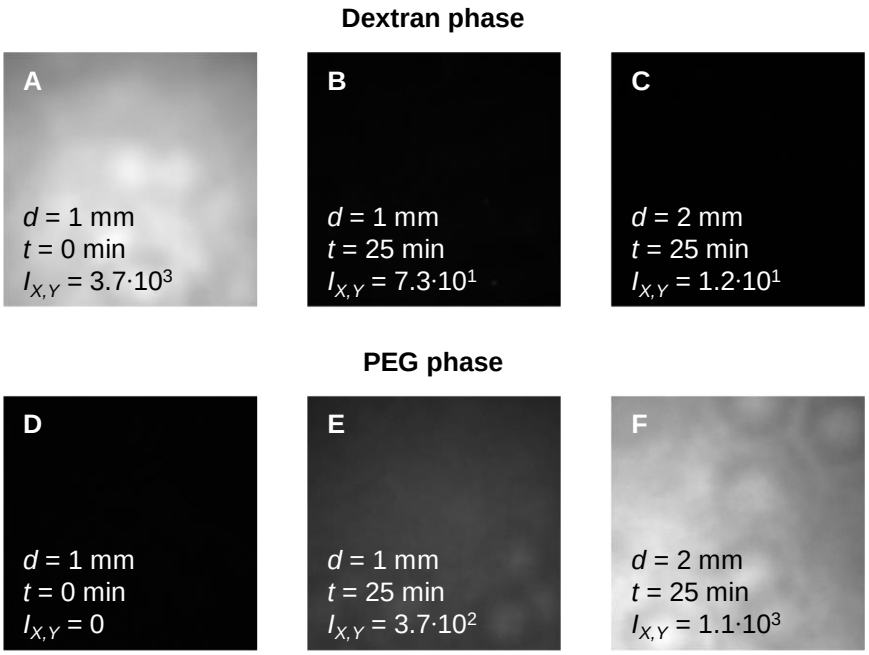

Figure 3.13: Temporal evolution of the BSA concentration in the bulk of the dextran phase (top row) and the PEG phase (bottom row). The distance from the phase boundary is given by d. All subfigures show a section of 200 x 200 px of the full image.

This is also supported by an analysis of the average fluorescence intensity $I_{X,Y}$. Compared to its initial value at $d = 1\,\text{mm}$, $I_{X,Y}$ is decreased by two orders of magnitude after 25 min both at $d = 1\,\text{mm}$ and $d = 2\,\text{mm}$. By contrast, the average fluorescence intensity rises significantly in the bulk of the PEG phase. Figure 3.13.D serves as a reference. Here, the fluorescence intensity is zero (after subtraction of the background fluorescence), since no fluorescent molecules are present. After 25 min, a significant amount of BSA has crossed the interface and migrated into the bulk. Hence, significantly higher values of $I_{X,Y}$ are obtained in Figures 3.13.E and F.

The results obtained with exosomes and BSA presented here are only preliminary. However, they already suggest that exosomes with a size distribution ranging from 70 to 250 nm (median size of approximately 110 nm) experience a higher transport resistance at the interface of the ATPS than BSA (stokes radius of 3.48 nm [196]). This could help to extract exosomes from complex mixtures containing proteins and other substances that cross the phase boundary more easily. However, this needs to be examined systematically in the future. Besides, the mechanism behind the accumulation of exosomes has to be further elucidated. For a detailed discussion of the adsorption behaviour of nanoparticles at liquid-liquid interfaces including the effects of surface tension, hydration of charged particles, interaction with electric fields and line tension, see [197].

3.6.7 Occurence of interfacial perturbations

In the experiments with exosomes and BSA, a relatively high voltage was applied. This led to the phenomenon described in Figure 3.14. The set of images underlying this figure is the same as in Figure 3.11, but evaluated at different times t. Only the images obtained with an excitation wavelength of 640 nm are shown. In subfigures A and B, the penetration of BSA into the bulk of the PEG phase can be observed. 180 s after the voltage has been applied, a wavefront[§] propagating in the positive y direction becomes visible. It seems to transport the BSA that has already entered the PEG phase back towards the interface. Likewise, the images obtained with an excitation wavelength of 488 nm (not shown here) show that the few exosomes that were able to cross the interface are also caught by the wavefront. Besides, at $t = 220\,\text{s}$ protein clusters are visible. A similar observation was made by Hardt et al. in experiments with DNA molecules at the interface of an ATPS [190]. Subfigures E and F show the collision of the wavefront with the ATPS phase boundary. It appears that the wavefront deforms the interface but does not cross it. Besides, the BSA molecules transported with the wavefront seem to re-adsorb to the interface. Afterwards, the phase boundary stabilizes again (subfigures G to I). No further wavefronts were observed. The experiment is continued for $\approx 2600\,\text{s}$, leading to the final results presented in Figure 3.11.

[§]The term "wavefront" was chosen for lack of a better description of the phenomenon.

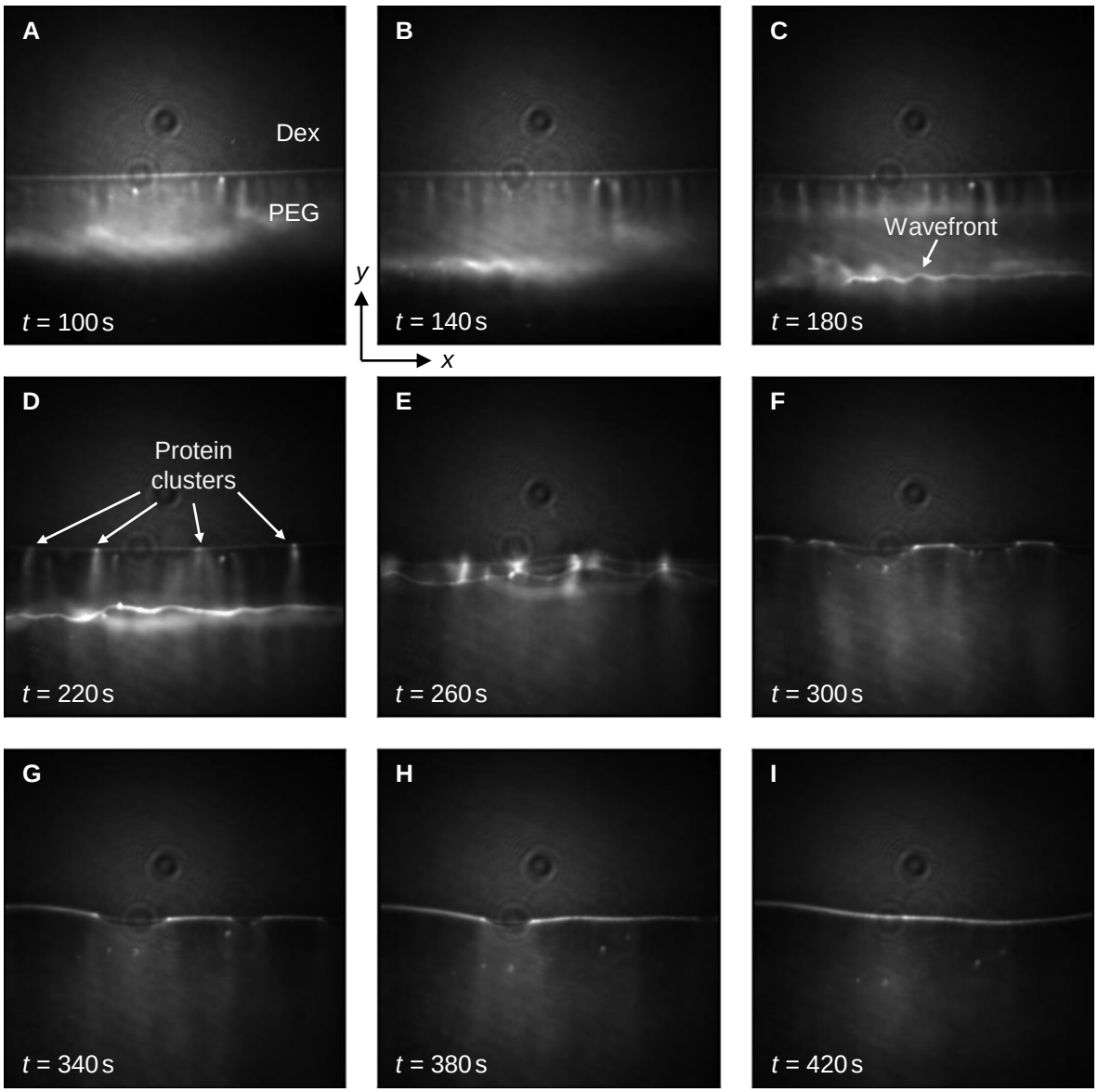

Figure 3.14: Interfacial perturbations caused by a wavefront of unknown origin. All images were obtained with an excitation wavelength of 640 nm. A) and B) show the penetration of BSA into the bulk of the PEG phase. In C), a wavefront propagating into the positive y direction is observed. In D), protein clusters are visible. When the wavefront reaches the ATPS interface, the phase boundary gets disturbed (E) and F)). Afterwards, the interface relaxes again (G) to I))

Similar observations were made in all experiments with exosomes and BSA. The author of this thesis also reported the occurrence of wavefronts at higher electric field strengths in his Master's thesis on protein separation [102]. So far, the origin of the wavefront is unknown. Faradaic reactions at the electrodes could be a possible source. Besides, it is not clear to which extend it affects the separation process. On the one hand, the wavefront deforms the interface as shown above. At higher field strengths, the perturbations might even increase. On the other hand, the results presented in Subsection 3.6.6 suggest that a successful separation may still be possible once the interface has stabilized again after

the collision with the wavefront. In the next chapter, similar phenomena are discussed in more detail.

3.7 Conclusions and Outlook

The electrophoretic transfer of proteins across the liquid-liquid interface in an aqueous to-phase system was studied in detail in a microfluidic device based on fluorescence microscopy. Two different proteins, BSA and BγG, in an ATPS containing polyethylene glycol and dextran were considered. For both proteins, a significant accumulation at the interface was found. The proteins, initially dissolved in the dextran phase, mainly accumulate close to the three-phase contact lines between the two aqueous phases and the solid surface. It is in these regions where the crossover into the PEG phase occurs. The accumulation of BγG at the liquid-liquid interface is significantly more pronounced than that of BSA. While the majority of BγG is still adsorbed at the interface, BSA already crosses over into the PEG phase. This allows a separation of the two proteins. A model for the interaction of the proteins with the liquid-liquid interface was developed that accounts for protein adsorption and desorption. The model is inspired by results on the electrostatic potential distribution across the interface: The superposition of the Donnan potential and the applied electric field creates a local potential minimum into which molecules can adsorb. Desorption occurs via a thermally activated process. Fitting the model parameters to the experimental data results in a good agreement between model and experiments. In this way, the rate constant for desorption of BSA is found to exceed that of BγG by about a factor of five. These results confirm the picture that the transport resistance of the interface is due to adsorption of molecules and their thermally-induced desorption from a metastable state.

It suggests itself that the electric field-induced interaction of proteins with ATPS interfaces can be used in separation and purification protocols. If the difference of desorption rate constants is high enough, it should be possible to separate different proteins contained in a sample. In addition, the initial experiments with exosomes suggest that it should be possible to separate EVs from other species. This process relies on principles very different from protein or exosome separation/purification based on their partitioning coefficients and should therefore enhance the spectrum of separation schemes. Besides, the interfacial transport resistance enables preconcentration and separation of charged sample molecules in one single step. For a practical implementation of such processes it will be necessary to withdraw the two phases from the microfluidic chip in a reliable and reproducible manner, which is a task to be addressed in future studies. A first attempt in this direction is described in Section A in the Appendix.

Chapter 4

Investigation of the stability of interfaces in aqueous two-phase systems

4.1 Summary

In order to reliably fractionate bioparticles at liquid-liquid interfaces in ATPS using electric fields, it is necessary to ensure that the phase boundary remains stable during the separation process. However, it is believed that depending on the volume flow rate $\dot{V}$ and the applied voltage U_{app}, i.e. the electric field strength, interfacial deformations occur, which would affect the separation process. A systematic investigation of the relationship between $\dot{V}$ and U_{app} on the one hand and the occurrence of interfacial instabilities on the other hand is therefore necessary. The experiments presented here contribute to this question. While the initial goal was to carry out a systematic parameter study, other effects were quickly discovered that need to be eliminated first: Particularly at higher field strengths, instabilities occur that are presumably caused by Faradaic reactions at the electrodes. Only if these effects are prevented, it will be possible to study the actual influence of the electric field on the interface and to perform reliable separation processes.

4.2 Contributions and publications related to this project

The experiments presented in this chapter were all carried out by Sonja Kemmerer under the author's supervision. The results were documented in her Bachelor's thesis [198]. Below, her most important findings are summarized. The figures were all created by the author of this thesis based on Kemmerer's experiments with her consent.

4.3 Introduction

Electric field-driven separation processes as described in the previous chapter are only feasible if the interface of the ATPS remains stable while the particles are accumulated and fractionated. However, Münchow et al. have already reported instabilities at interfaces in microfluidic ATPS that occur at high electric field strengths [104]. In the previous chapter, interfacial perturbations caused by a wavefront that may have originated from electrode reactions were observed. Besides, recent preliminary tests at the Institute for Nano- and Microfluidics have shown that high electric field strengths can lead to an emulsification of the ATPS, starting at the interface. Therefore, a more systematic investigation of electric field-induced interfacial instabilities in microfluidic ATPS is desirable.

Electric field-induced instabilities occurring in stratified flows have been extensively studied and used for mixing purposes in systems based both on aqueous solutions [199–202] and organic liquids [203, 204]. However, all these examples deal with fluid layers that are miscible. They do not form a sharp interface in the sense of a phase boundary. By contrast, Dehe and co-workers have investigated the deformation of the interface between an aqueous electrolyte solution and a dielectric organic phase under electric fields [205–207]. Compared to ATPS, such interfaces are characterized by a relatively high interfacial tension. Therefore, no conclusions can be drawn from these investigations about the stability of phase boundaries in ATPS. In their 2017 paper, Vobecká et al. discuss the electrophoretic transport of ATPS emulsion droplets [208]. Due to a non-zero net charge at the interface, ATPS emulsion droplets are set in motion by electric fields. Similarly, an electrostatic force at the interface between two co-flowing ATPS phases is expected to cause a displacement of the phase boundary and eventually lead to instabilities. To date, however, there has been no systematic investigation of such phenomena.

The work presented in this chapter contributes to close this gap. Originally, a parameter study was to be carried out to determine the influence of the volume flow rate and electric field strength on the occurrence of interfacial perturbations. Relatively quickly, however, it became apparent that the results were hardly reproducible. Faradaic reactions at the electrodes are a likely explanation for this. Further investigations suggest that the corresponding reaction products affect the stability of the interface. This has implications for further experiments on electric field-induced instabilities in ATPS, but also for the implementation of separation operations as described in the previous chapter.

4.4 Experiments

In this section, details on the experimental procedure are given, including the preparation of the ATPS from different buffer solutions, the design and fabrication of the microfluidic devices, and the experimental procedure.

4.4.1 ATPS preparation

Different buffer solutions were used to investigate a possible influence of salt type and concentration on electric-field induced instabilities at the interface. A first group of buffers was based on a 10 mM BES solution. One buffer out of this group was adjusted to pH = 7 with NaOH and to an ionic strength of $\mathcal{I} = 10\,\mathrm{mM}$ with NaCl. The second one had a pH of 8 and an ionic strength of 15 mM. Besides, 10 mM phosphate buffers (based on NaH_2PO_4) with pH = 7 and $\mathcal{I} = 20\,\mathrm{mM}$ or $\mathcal{I} = 30\,\mathrm{mM}$, respectively, were tested. Again, the pH was adjusted with NaOH and the ionic strength with NaCl.* The polymer concentrations and the ATPS preparation protocol were the same as in Subsection 3.5.1. In order to investigate the interface of the ATPS with epifluorescence microscopy, 0.923 % of the dextran are substituted by fluorescein isothiocyanate dextran 10,000 (Sigma-Aldrich), a fluorescent dextran derivative. It partitions unevenly between the two phases, resulting in a strongly fluorescing dextran phase and a weakly fluorescing PEG phase when excited with a laser. After separation of the ATPS, 0.1 % (w/v) PVP was added to each phase to suppress EOF.

4.4.2 Microfluidic devices

In total, three different microfluidic devices were used to investigate the occurance of interfacial perturbations. First, some experiments were carried out in devices as described in Subsection 3.5.3. Second, in a variation of these experiments, a slightly modified chip with two outlets instead of only one was used.† As this second chip design is not significantly different to the first, no schematic is provided for this modified version. Just as shown in Figure 3.4, a parallel flow of the two phases was created in this chip. Besides, a cross-shaped microchannel as schematically shown in Figure 4.1 was designed for further investigations. In this third chip, the dextran phase inlet and the PEG phase inlet are placed at opposite ends of the device. The interface is formed at the intersection of the different channel sections, as depicted in the inset of the figure. At each remaining end of the cross-shaped structure there is an outlet for the two phases. Electrode reservoirs are located close to the inlets separated from the main channel by gel bridges. They were filled with buffer solution. All sections of this device have a width of 500 µm and a depth of 150 µm. The distance between the two inlets is 2.4 cm, the distance between the outlets 2 cm. The devices were fabricated according to the protocol presented in Subsection 3.5.3.

*Further buffer solutions were tested in Sonja Kemmerer's Bachelor's thesis. However, only those buffer solutions are mentioned here that are necessary to explain the most important results presented in her thesis.

†The reasons behind this were of a pragmatic nature: After a few trials with the microfluidic chip from the previous chapter, the wafer that served as master structure broke. In order to be able to continue the experiments without delay, a quasi-equivalent chip design was used for which a wafer was available.

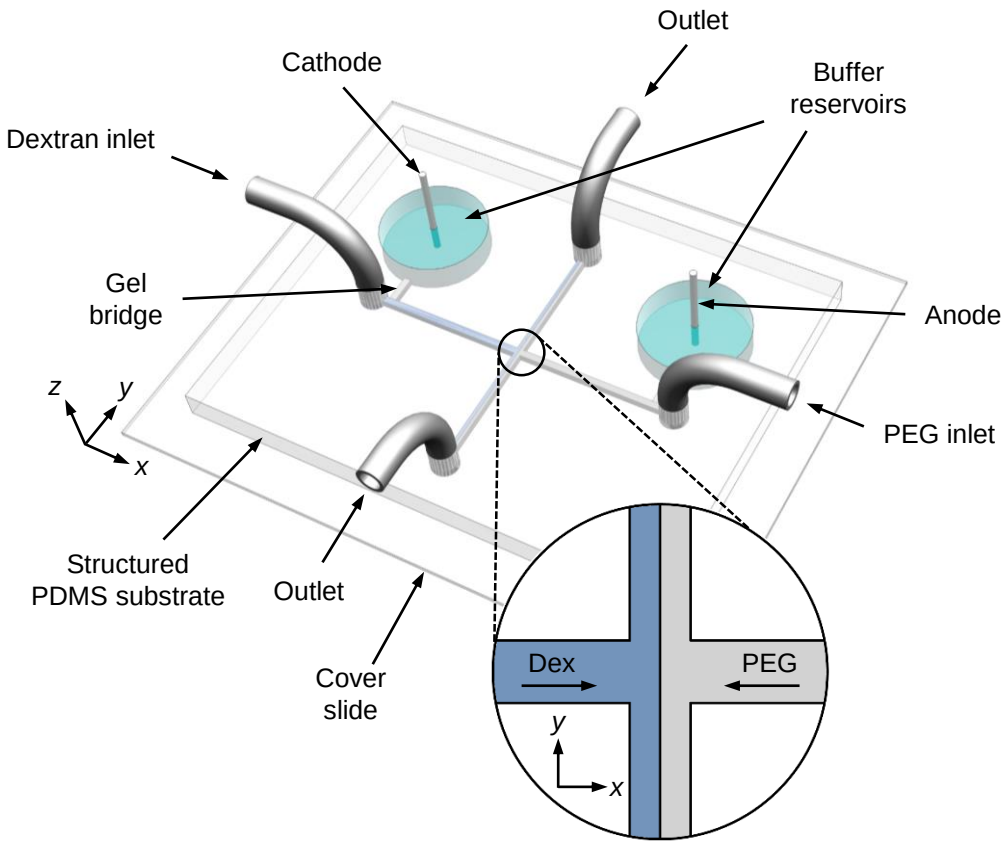

Figure 4.1: Schematic drawing of the cross-shaped microfluidic device used to study electric field-induced instabilities at the interface of an ATPS. The inset shows a schematic of the interface formed at the intersection of the four channel sections.

4.4.3 Experimental procedure

The microfluidic chip was placed on the stage of a Nikon eclipse TI fluorescence microscope. The two liquid phases were injected with a syringe pump through PTFE tubings. Initially, a high volume flow rate was used to prevent the formation of gas bubbles inside the microchannels. Then, the flow rate was reduced to a final value between 0.2 and 50 µl/min in both phases. Thus, in contrast to the previous experiments in Chapter 3, the interface was not studied under quiescent conditions, since in many practical applications flow-through operation is desirable, for example to separate the phases and analyze them offline. Subsequently, a voltage between 100 and 1000 V was applied using a TTi QL355TP voltage source (Thurlby Thandar Instruments).

Both bright-field and epifluorescence microscopy was used to study the deformation of the interface and connected phenomena. All images were recorded with an Andor iXon+ 897 EMCCD camera with an exposure time of 200 ms. The corresponding frame rate was ≈ 4.85 fps. Two different objectives were used, namely a Plan Apo 2x (Nikon, NA = 0.1) and a S Fluor 4x (Nikon, NA = 0.2) obejctive. In epifluorescence experiements, the fluorescent dextran was excited with a 488 nm laser.

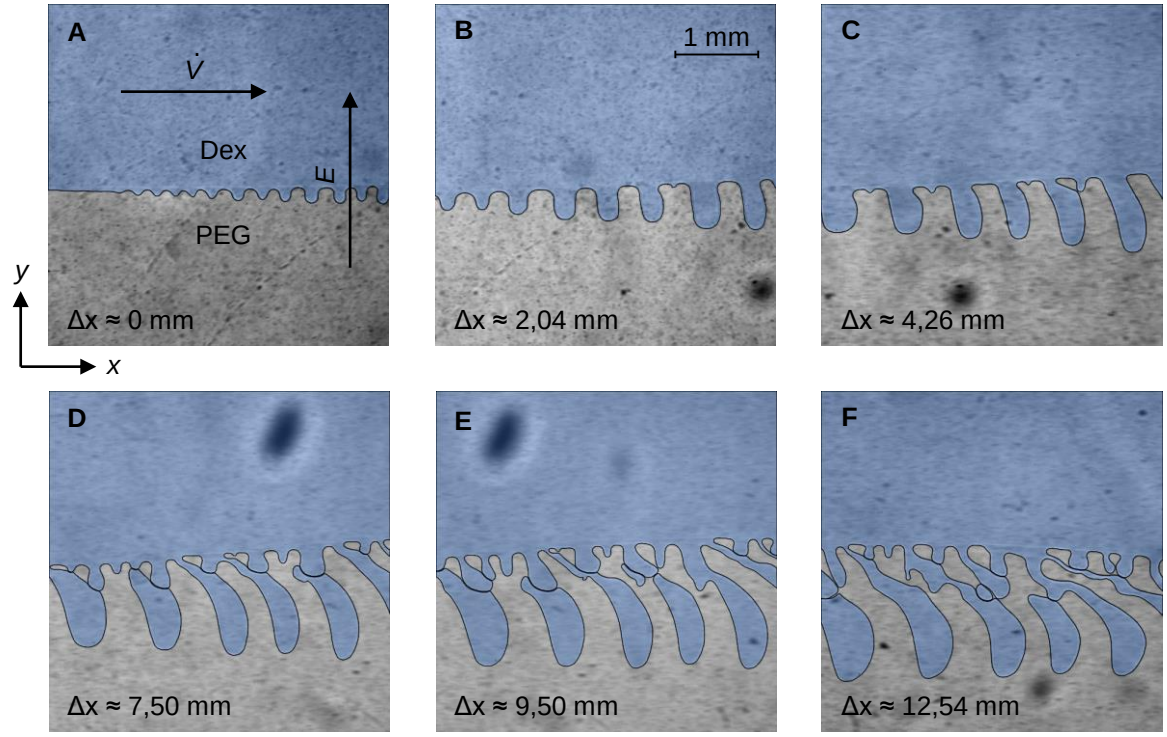

Figure 4.2: Bright-field microscopy images of the interfacial deformation in an ATPS under an electric field in a microfluidic device used for particle separation. The subfigures represent different distances from the inlet of the microfluidic device. For visualization purposes, the dextran phase has been colored in blue. The deformation intensifies with increasing distance from the inlet. A phosphate buffer with pH = 7 and $\mathcal{I} = 30\,\mathrm{mM}$ was used here. The flow rate was $\dot{V} = 10\,\mu\mathrm{l/min}$, the applied voltage $U_{app} = 500\,\mathrm{V}$. The images were recorded through a 2x objective and at different times.

4.5 Results and discussion

In this section, the results obtained with different experimental parameters will be presented. First, the findings from experiments in the "standard" microfluidic device for particle separation and in its modified version will be shown. Then, the focus will be on the interfacial deformation in the newly designed cross-shaped microchannel.

4.5.1 Experiments with devices for bioparticle separation

In a first step, interfacial instabilities in ATPS were studied in the microfluidic device as presented in the previous chapter. An exemplary result obtained with a flow rate of $10\,\mu\mathrm{l/min}$ and an applied voltage of $500\,\mathrm{V}$ is shown in Figure 4.2. Here, a phosphate buffer with pH = 7 and $\mathcal{I} = 30\,\mathrm{mM}$ was used. Close to the inlet (Figure 4.2.A), a wave-like deformation of the interface starts to form. In the first two subfigures, the amplitude and wavelength of the deformation grow with the distance Δx from the inlet. A wavelength between 400 and 500 µm can be measured in Figure 4.2.B. Further downstream (Figure 4.2.C), the deformation becomes more irregular. The "fingers" of the wave start to

deform. In Figure 4.2.D, some dextran droplets with a non-spherical shape have detached from the main phase. More droplets are formed with increasing Δx (Figure 4.2.E and F), leading to an emulsification of the two phases at the interface.

In the modified microfluidic device for particle separation with two outlets, the dependence of these instabilities on the flow rate ($\dot{V}$ between 0.2 and 50 µl/min) and the applied voltage (U_{app} between 100 and 1000 V) was systematically studied. However, the results were not reproducible, regardless of the buffer solution used. Therefore, it was not possible to find threshold voltages above which the interface begins to deform at a given flow rate. Only very general trends could be observed. First, the instabilities occur further downstream as the electric field strength is decreased. In Figure 4.2, the interfacial deformation begins close to the inlet. At lower field strengths, however, instabilities start in the center or close to the outlet. Second, it takes longer for instabilities to occur as the electric field strength decreases. At low applied voltages, it can take over a minute for the first deformations to become visible, whereas at high voltages they occur almost immediately. It was also observed that the gel bridges were damaged at higher electric field strengths, probably due to Joule heating. When cleaning the microchannel after applying high voltages, they broke easily.

In a variation of these experiments, some of the dextran was replaced by a fluorescent dextran derivative. Initially, the goal was to increase the contrast between the two phases by using epifluorescence microscopy. However, this variant also produced some other unexpected results. Figure 4.3 shows images taken in a section from the center of the microchannel, close to the gel bridges. The subfigures cover a period of ca. 10 s. Soon after the voltage is gradually increased to a value of $U_{app} = 400$ V, a "third phase" penetrates into the PEG phase, coming from the direction of the reservoirs, see Figure 4.3. It pushes through the gel bridges and propagates towards the interface. The term "third phase" was chosen due to a lack of deeper knowledge about the origin of the phenomenon. Faradaic reactions at the electrodes could be a possible source. However, the composition of this third phase remains unknown. It is not even clear whether it is a phase in the sense of a liquid that is not miscible with the dextran and PEG phases. Even when the electrode positions are swapped, the third phase is formed at the anode. Besides, it can be observed regardless of the buffer type. It seems plausible that the wavefront described at the end of the previous chapter is the result of the propagation of the third phase. In the next subsection, the connection between the third phase and the instabilities at the phase boundary will be examined in more detail.

4.5.2 Experiments with cross-shaped microchannels

Further investigations of electric field-driven interfacial instabilities in an ATPS were carried out in the cross-shaped microchannel. Again, different buffers, flow rates and electric field strengths were tested. As before, some parameter combinations led to perturba-

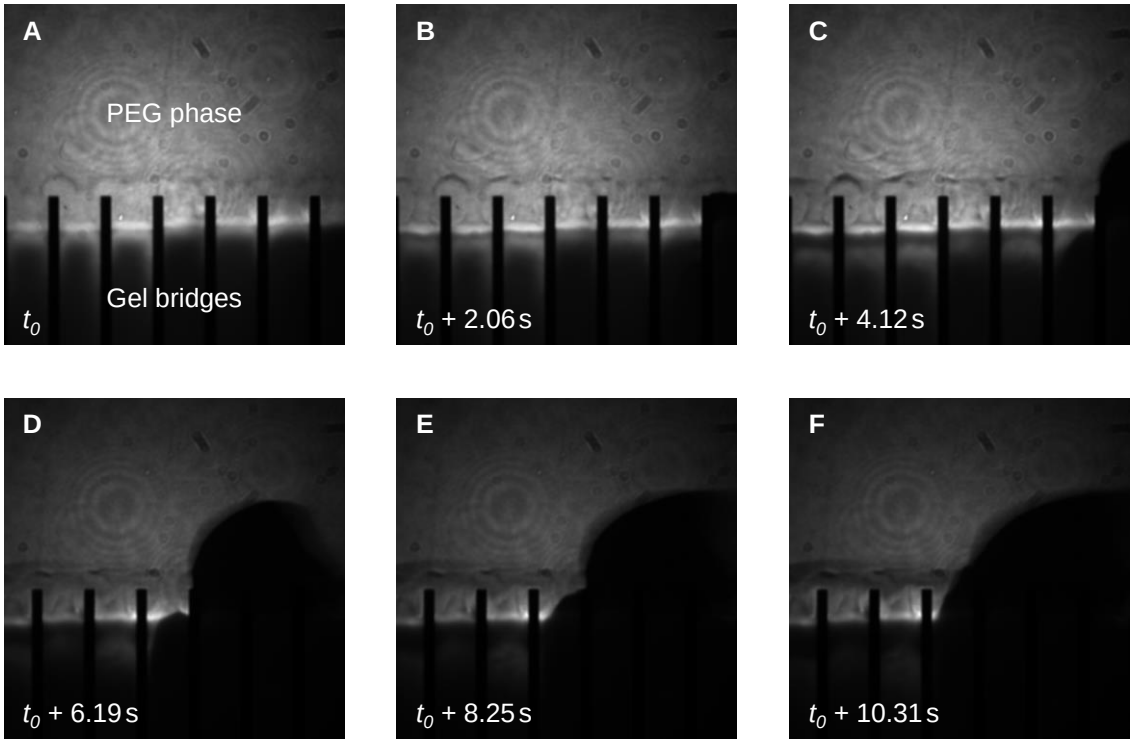

Figure 4.3: Penetration of a third phase from the gel bridges into the bulk of the PEG phase. The different subfigures show how the phase spreads during $\approx 10\,\mathrm{s}$. Between C) and D), the field of view has been shifted slightly to the right to capture more of the third phase. A BES buffer with pH = 7 and $\mathcal{I} = 10\,\mathrm{mM}$ was used here. The flow rate was $\dot{V} = 10\,\mu\mathrm{l/min}$, the applied voltage $U_{app} = 400\,\mathrm{V}$. The images were recorded through a 2x objective.

tions of the phase boundary. For example, instabilities were observed at a flow rate of $\dot{V} = 5\,\mu\mathrm{l/min}$ and an applied voltage of $U_{app} = 1000\,\mathrm{V}$ in an ATPS based on BES buffer with with pH = 8 and $\mathcal{I} = 15\,\mathrm{mM}$, see Figure 4.4. Shortly after the external voltage is applied, the interface is deformed (Subfigure B). The dextran phase begins to bulge into the PEG phase. The bulge continues to grow (Subfigures C and D) until it eventually collapses (Subfigure E). The next two images show the formation of a new, less pronounced bulge (Subfigures F and G), which eventually collapses again (Subfigures H to K). In the last image (Subfigure L), the interface is more or less in the same configuration as at the beginning of the experiment. The subfigures cover a period of ca. 45 s. With the given frame rate, it is difficult to tell at what time intervals the bulges form and collapse again. However, the observations suggest that this process may occur repeatedly, which could be related to the formation of regular wave patterns as shown in Figure 4.2. As before, the results were difficult to reproduce. Therefore, it is not possible to establish a clear correlation between the experimental parameters flow rate and applied voltage on the one hand and the occurrence of instabilities on the other.

Again, some important insights were gained by using fluorescent dextran and epifluorescence microscopy. As the gel bridges repeatedly broke when higher voltages were applied in previous experiments, they were omitted here to avoid any possible negative

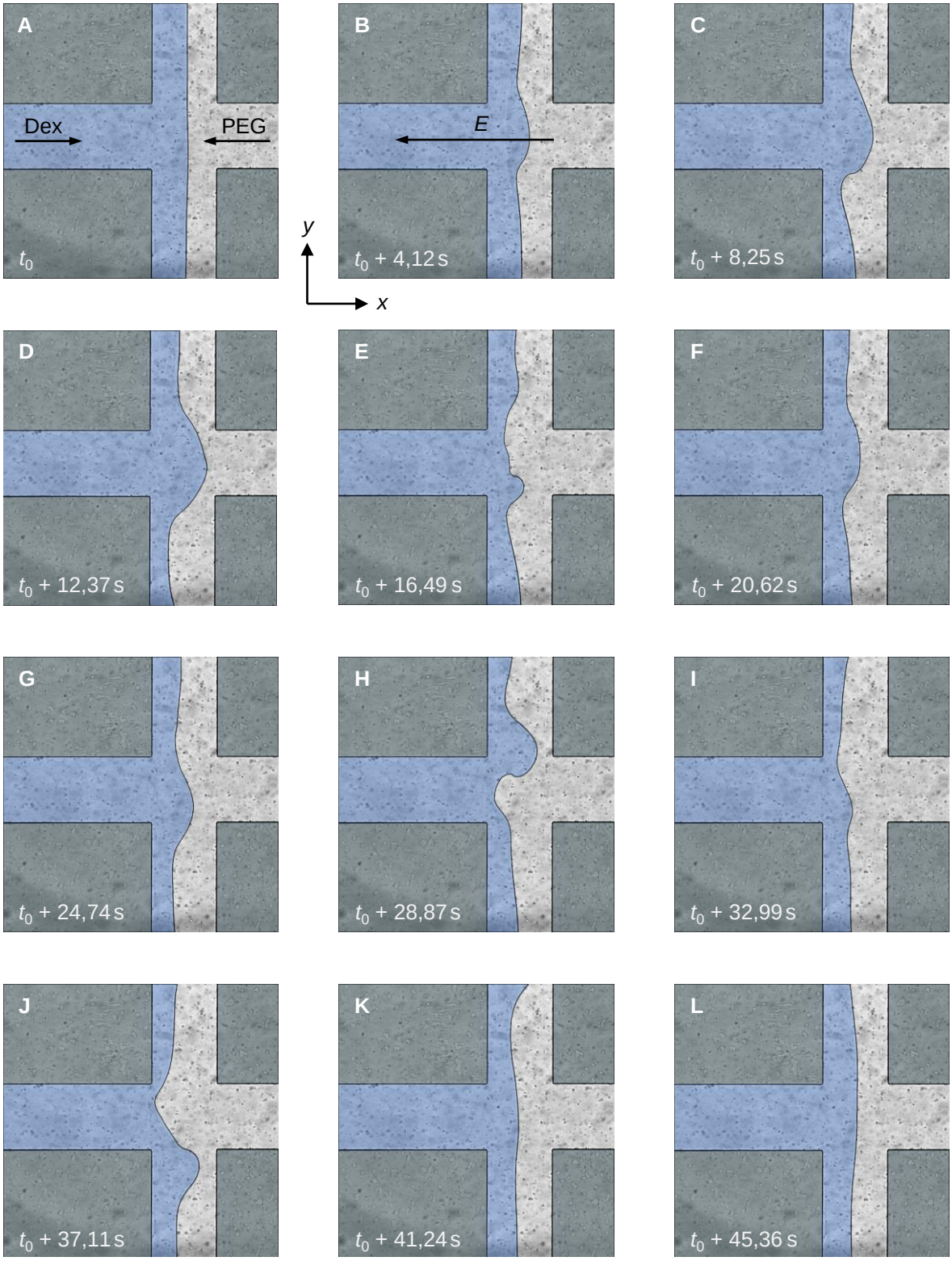

Figure 4.4: Bright-field microscopy images of the interfacial deformation in an ATPS under an electric field in a cross-shaped microchannel. The subfigures represent different times t. At approximately $t = 0$, the voltage has been applied. For visualization purposes, the dextran phase has been colored in blue and the PDMS channel boundaries in dark grey. A BES buffer with pH = 8 and $\mathcal{I} = 15\,\mathrm{mM}$ was used here. The flow rate was $\dot{V} = 10\,\mu\mathrm{l/min}$, the applied voltage $U_{app} = 1000\,\mathrm{V}$. The images were recorded through a 4x objective.

effect on the reproducibility of the tests. Hence, the reservoirs and the main channel were no longer separated. Instead of pure buffer, the reservoirs now contained dextran or PEG phase. Only relatively short periods could be observed with this modification, as the experiments had to be interrupted before bubbles formed at the electrode and disturbed the interface. Again, a variety of flow rates and electric field strengths were used. Regardless of the parameter combination, the development of a third phase was always observed. This was also the case when the positions of the anode and cathode were reversed. The third phase always developed in the phase in which the anode was located. As an example, Figure 4.5 shows the interaction of the third phase with the interface. The red dashed line represents the interface between the PEG phase and the dextran phase.[‡] Subfigure A shows the arrival of the third phase in the field of view from the right. As it reaches the interface, the interface starts to deform, see Subfigures B and C. From this point on, it is increasingly difficult to track the position of the phase boundary, since the third phase partly crosses it and replaces the fluorescent dextran phase. Subfigures D to L show how the interfacial deformation develops over time. Bulges form (Subfigures D and K) an collapse again (Subfigures F to I and L). In between, the interface is more or less in its initial condition (Subfigure J). The image acquisition was stopped after 23 s because bubble formation at the electrodes was expected and because the dextran phase and the PEG phase were no longer clearly distinguishable. Therefore, it is not clear whether the process of bulge formation and collapse was repeated afterwards. Comparing Figure 4.4 and Figure 4.5, it seems likely that the interaction between the third phase and the ATPS phase boundary is the root cause for the interfacial perturbations observed in this kind of experiments. However, not in all cases, especially at lower voltages, the third phase caused instabilities. Instead, it followed the flow of the PEG phase and was withdrawn through one of the outlets. As before, no clear relationship between flow rate and applied voltage on the one hand and the occurrence of instabilities on the other hand was observed because the experiments were again not reproducible.

4.5.3 Observations at the electrode

Faradaic reactions are one possible explanation for the origin of the third phase. If this were the case, the development of the third phase should begin directly at the electrodes. For this reason, images were taken of the area around the anode placed in one of the reservoirs of the cross-shaped microchannel, see Figure 4.6. At the beginning of the experiment, only the anode is visible (Subfigure A). Approximately 2 s later, the third phase is beginning to take shape (Subfigure B). It grows and propagates towards the main channel, see Subfigures C to F. From Subfigure D on, a gas bubble caused by electrode reactions can be observed at the upper edge of the images. In experiments with

[‡]Although the third phase has displaces some of the fluorescent dextran, in most cases the contrast between the dextran phase and the PEG phase is still high enough to detect the interface.

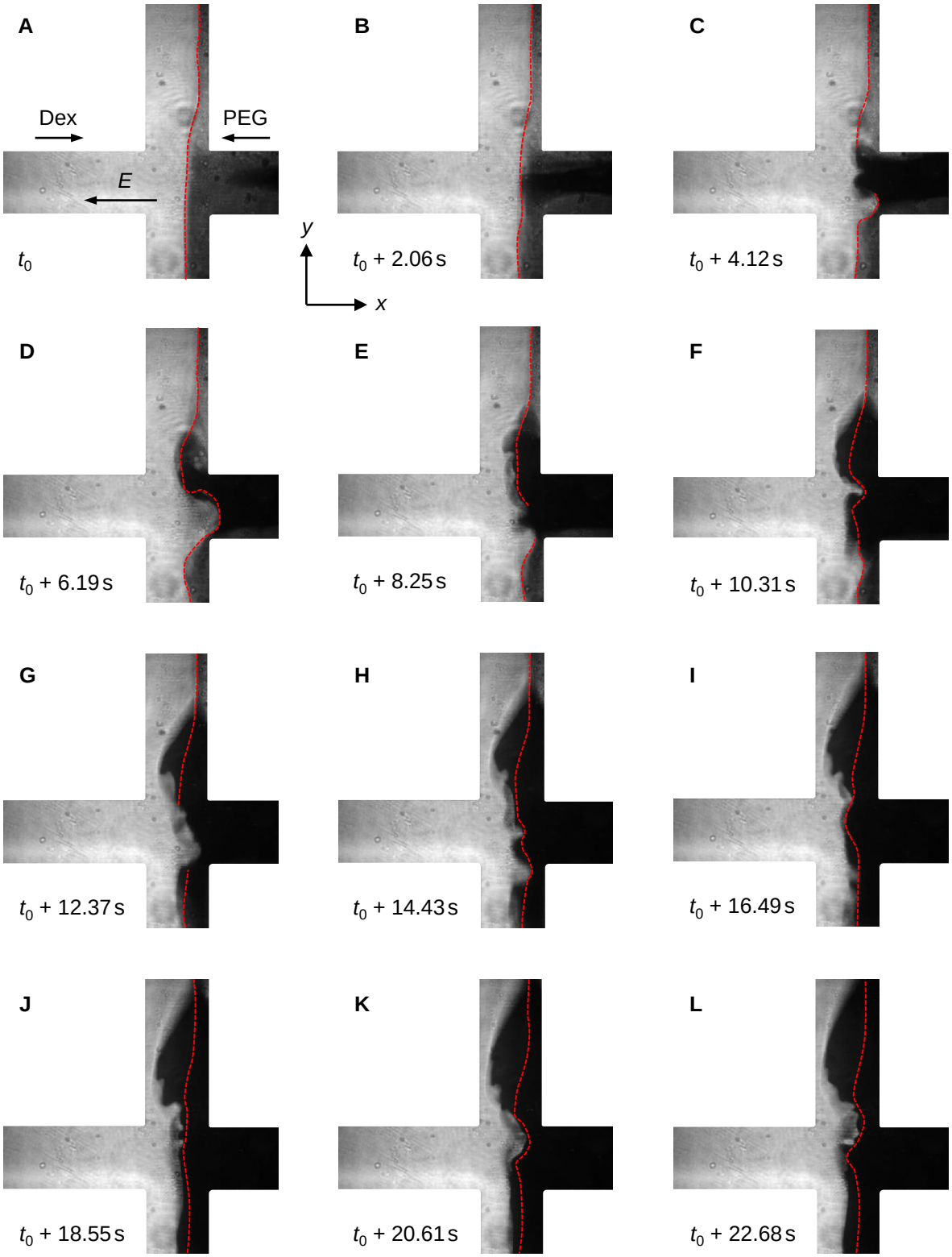

Figure 4.5: Epifluorescence microscopy images of the interaction of the third phase with the ATPS interface. Where possible, a red dashed line was drawn to highlight the position of the interface between the dextran and PEG phase. A phosphate buffer with pH = 7 and $\mathcal{I} = 20\,\mathrm{mM}$ was used here. The flow rate was $\dot{V} = 1\,\mu\mathrm{l/min}$, the applied voltage $U_{app} = 600\,\mathrm{V}$. The images were recorded through a 4x objective.

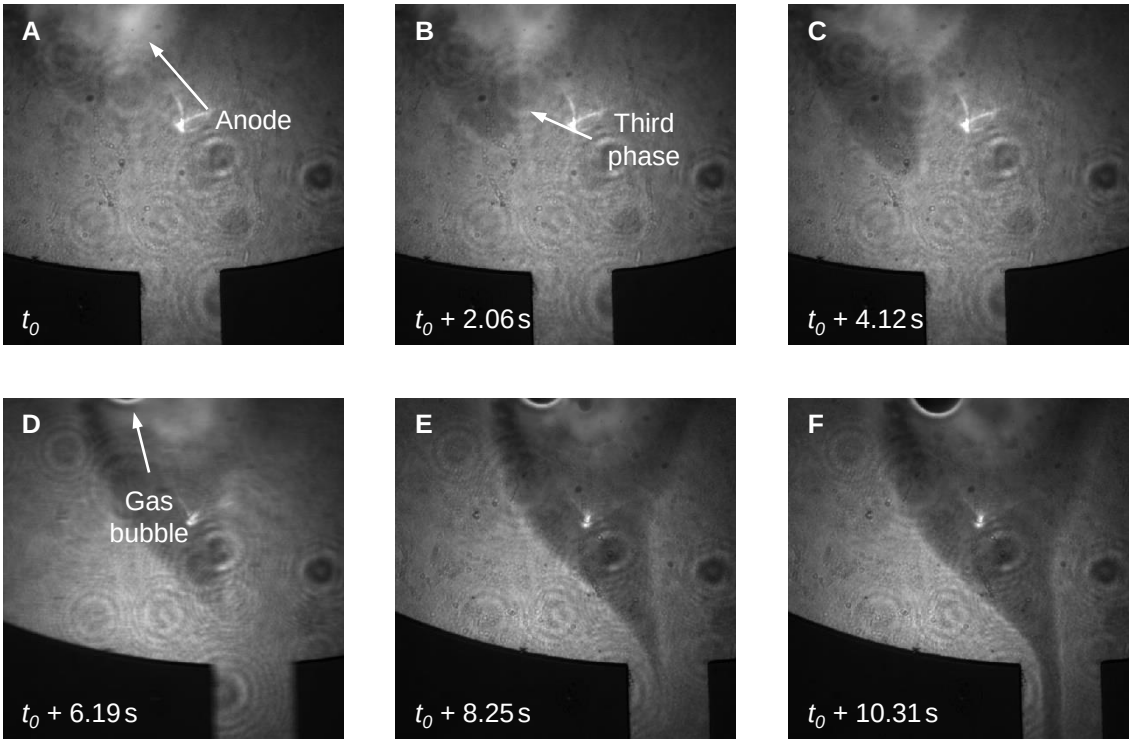

Figure 4.6: Temporal evolution of the third phase at the anode immersed in the PEG phase. A phosphate buffer with pH = 7 and $\mathcal{I} = 20\,\mathrm{mM}$ was used here. The flow rate was $\dot{V} = 1\,\mu\mathrm{l/min}$, the applied voltage $U_{app} = 600\,\mathrm{V}$. The images were recorded through a 4x objective.

different applied voltages, a general trend was observed. The time it takes until the third phase develops increases with decreasing voltage. At lower voltages, the propagation into the main channel also took much longer. Hence, it can be concluded that the electric field is the driving force behind the transport of the third phase towards the interface. Remarkably, when the cathode is observed during the same type of experiments, the evolution of another, less distinct fourth phase can be observed. It was probably not detected earlier because of a different image contrast in the previous experiments.

It seems to be confirmed that the third and fourth phase are the result of Faradaic reactions. However, the type of reaction remains unclear. The third phase was also observed in experiments where the electrodes were dipped in pure buffer solution instead of the dextran or PEG phase. Dextran and PEG are therefore most likely not part of the reaction. Besides, some additional experiments without NaCl were carried out. Since the third and fourth phases were still observed, chloride ions can also be excluded. So it could be that both buffer chemicals, BES and NaH_2PO_4, are involved in electrode reactions. Apart from that, Bockris et al. report that platinum oxidizes and dissolves in electrochemical reactions above a threshold voltage of 1.2 V [209]. In experiments with buffer systems and electric field strengths similar to those used here, Gencoglu et al. demonstrated that platinum electrodes corrode to a significant extent [210]. It is therefore conceivable that the platinum electrodes participate in the formation of the third phase. When graphite electrodes were used instead of platinum electrodes, the

formation of a third and fourth phase was still observed. However, even with voltages up to 1000 V no instabilities were detected in this case when the third phase reached the ATPS interface. The influence of the electrode material on the formation of the third phase and the occurrence of instabilities therefore remains an open question.

4.6 Conclusions and outlook

The original goal of the investigations presented here was to find out in which ranges of flow rate and electric field strength instabilities can be observed at the ATPS phase boundary. But it soon became clear that the results were not reproducible. Therefore, it was not possible to find a clear relationship between the experimental parameters $\dot{V}$ and U_{app} and the occurrence of interfacial perturbations. Nevertheless, some important conclusions can be drawn.

Most likely, Faradaic reactions at the electrodes are responsible for the formation of new components that significantly influence the composition of the ATPS. The reaction products in the form of a third and fourth phase even appear to displace the dextran and PEG phases. However, the investigations suggest that this phenomenon may occur not only in ATPS, but also in other (microfluidic) applications where high electric field strengths are used in electrolyte systems. Therefore, further studies should be carried out that can provide information about the reactions taking place.

If the direct influence of the electric field on the interface and its stability is to be investigated, the formation of the third (and fourth) phase and/or its transport to the ATPS interface must be prevented. Ultimately, this would also make separation processes at the interface more reliable. The use of more robust electrodes could help if the electrode material plays a significant role in the formation of the third phase. However, as long as the influence of the electrode remains unclear, another option seems more promising: By continuously flushing the electrode reservoirs with buffer solution, any reaction products could be removed directly. An alternative chip design incorporating this concept is discussed in Section A of the Appendix.

As a side effect, the above experiments showed that the gel bridges used to dislocate the electrodes from the main channel break easily when exposed to higher electric field strengths. This should be kept in mind for separation processes with particles that require higher field strengths to overcome the transport resistance at the phase boundary. An alternative design of the microfluidic device that does not require gel bridges, but still prevents the migration of gas bubbles resulting from electrode reactions to the interface, would be desirable.

Chapter 5

Detecting isotachophoresis zones hidden in noise using signal processing

5.1 Summary

Lowering the limit of detection in chemical or biochemical analysis is key to extending the application scope of sensing schemes. Usually, this is related to an increased instrumentation effort, which in turn precludes many commercial applications. It is demonstrated that the signal-to-noise ratio of isotachophoresis-based microfluidic sensing schemes can be substantially increased merely by postprocessing of recorded signals. This becomes possible by exploiting knowledge about the physics of the underlying measurement process. The implementation of this new method is based on microfluidic isotachophoresis and fluorescence detection, for which the physics of electrophoretic sample transport and the structure of noise in the imaging process are exploited. By processing only 200 images, the detectable concentration, compared to the detection from a single image, is already lowered by 2 orders of magnitude without any additional instrumentation effort. Furthermore, the signal-to-noise ratio is proportional to the square root of the number of fluorescence images, which leaves room for further lowering of the detection limit. In the future, these results could be relevant for various applications where the detection of minute sample amounts plays a role.

5.2 Contributions, funding and publications related to this project

Work on this project began in 2019 as part of the joint Merck Lab@TU Darmstadt, a research collaboration of Merck KGaA and the Technical University of Darmstadt. Through this collaboration, Merck funded research activities focused on the field of low instrumentation analytics. Since the scheme presented here improves the signal-to-noise ratio of very basic isotachophoretic experiments without any additional instrumentation effort,

it fitted nicely within this scope. After some first promising results were obtained, the development of the new post-processing algorithm was continued even after the funding by Merck KGaA had expired. In 2023, the final results were published in Analyitical Chemistry, a journal of the American Chemical Society [211]. Several people have contributed to this paper. Henning Bonart, Tamal Roy, Benno Liebchen, Steffen Hardt, and the author of this thesis designed the research. The author of this thesis conducted the experiments. Henning Bonart, Lukas Hecht, Tamal Roy, and the author of this thesis developed the post-processing algorithm and analyzed the research data. Henning Bonart, Tamal Roy, Steffen Hardt, and the author of this thesis wrote the paper with contributions from all authors. Henning Bonart and the author of this thesis contributed equally to this work. Some parts of the text of this paper were directly inserted here, others were slightly adjusted. The content of the figures presented below is the same as in the article and its supplementary information. The formatting and some symbols were adjusted to match the style of this thesis.* The raw fluorescence images obtained from the ITP experiments† and a reference implementation of the post-processing algorithm‡ are freely available.

5.3 Introduction

The detection of low-abundance analytes is a persistent challenge in chemical and biological analytics. In many cases, the concentration of the analyte of interest is so low that it falls below the detection limits of the sensing principle employed. In some other cases, the total amount of analyte itself is low, for example when an analyte is extracted from a single cell. The challenge of lowering the detection limits in (bio)chemical analysis has been discussed and emphasized in conjunction with optical biosensors for unlabeled targets in general [212], specific realizations of optical biosensors such as plasmonic [213] or optical waveguide interferometric sensors [214], graphene-based electrochemical sensors [215], aptamer-based electrochemical sensors [216], and nucleic acid-based sensors [217]. Also in context with lateral flow assays the relevance of low detection limits has been highlighted [218]. These examples underpin the pressing need for (bio)sensors with low detection limits.

In practice, all sensor output is superposed by random variations or noise, making the detection of comparatively weak signals difficult. Obviously, reducing the noise, and subsequently increasing the signal-to-noise ratio (SNR), is of great interest. In addition, in applications such as point-of-care diagnostics, it is often the balance between the detection limit on the one hand and the instrumentation effort / analysis times on the other hand

*Reproduced with permission from Anal. Chem. 2023, 95, 19, 7575–7583. Copyright ©2023 American Chemical Society.

†https://doi.org/10.48328/tudatalib-914

‡https://doi.org/10.5281/zenodo.7881096

that counts. Using a simple principle and reaching a detection limit which is comparable to that of highly involved instrumentation or complex assays is often an attractive option.

In this chapter, a novel scheme for improving the *SNR* solely based on the post-processing of multiple fluorescence images of a sample traveling through a microchannel driven by isotachophoresis (ITP) is introduced. ITP is often used for increasing the sample concentration, which is a prerequisite for achieving low detection limits. As mentioned before, using ITP, preconcentration factors between a few thousand and one million have been reported [62, 74–78], which enables sample detection with high sensitivity and low detection limits [79–83]. With the new scheme, scenarios are addressed in which ITP is used as a preconcentration technique, exemplified by recent work on microfluidic ITP [52, 84, 219]. Therefore, in related applications, the task is to detect an ITP zone in a noisy environment rather than superposed to a background signal of deterministic nature.

The new post-processing algorithm works without any additional instrumentation effort by exploiting the existing knowledge about the spatiotemporal characteristics of the signal to be detected. It is presented in detail including a Bayesian detection decision formed under uncertainty of the noisy signal. Using experiments with tiny sample concentrations of a common fluorophore, it is then shown that the scheme works even if the initial *SNR* is much smaller than 1 and the sample would not be detectable. The resulting *SNR* scales with the number of processed images N as $SNR \propto \sqrt{N}$. By processing only 200 images, the detectable concentration, compared to the detection from a single image, is already lowered by two orders of magnitude.

5.4 Concept and theoretical background

The first part of this section serves as a guideline through the rest of this chapter by explaining the basic ideas behind the post-processing scheme that is presented below. The second part explains the fundamentals of the statistical methods that have been incorporated.

5.4.1 Basic principles of the post-processing scheme

The experimental setup used in all experiments is based on a standard microfluidic system in which a fluorophore is transported through a microchannel in peak-mode ITP. Its components are depicted in Figure 5.1.A. A fluorescence microscope equipped with a CCD camera is employed to image the fluorescence signal originating from a section of the microchannel. More details on the experiments will be given in Section 5.5.

When applying an electric field to the microchannel, the different electrophoretic mobilities of LE, TE and sample result in the formation of three spatially distinct zones, with the sample zone bracketed between the LE and TE zones, as described in Section 2.6. If the *SNR* is high enough, fluorescent samples focused with ITP can be detected *via*

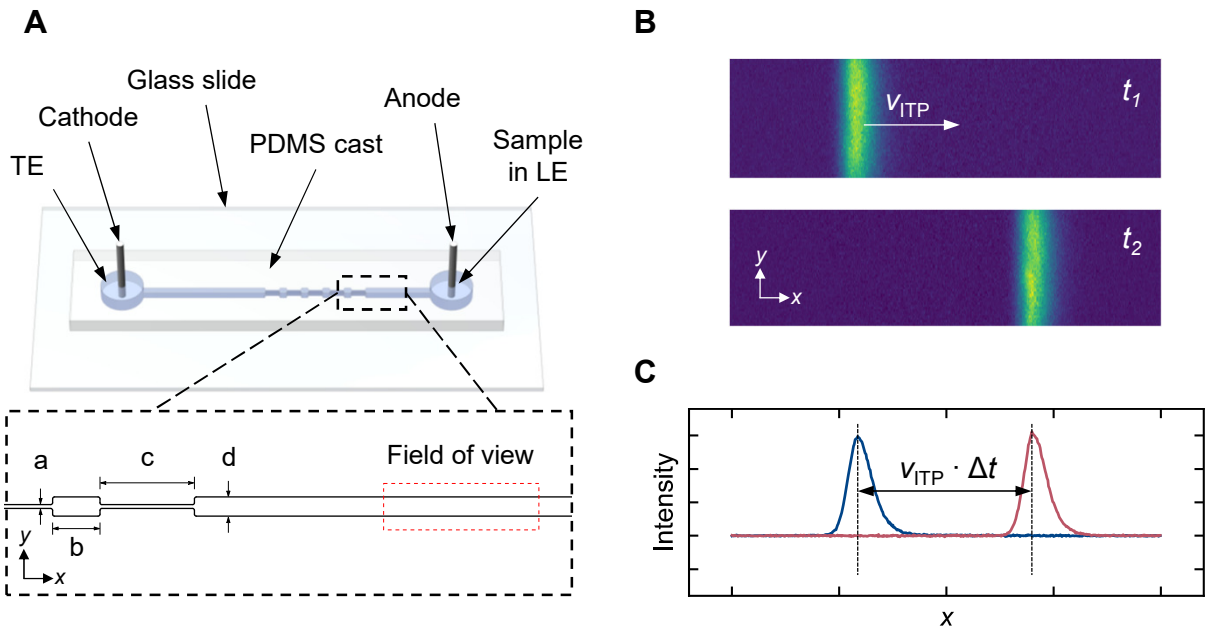

Figure 5.1: Overview of the experimental setup and typical fluorescence images obtained in constant-current ITP. A: Schematic drawing of the microfluidic device used to perform ITP experiments including a close-up of the constricted sections that are used to trace the location of the sample zone and the field of view next to it. The dimensions are $a = 20\,\mu m$, $b = 250\,\mu m$, $c = 500\,\mu m$, and $d = 100\,\mu m$. B: Exemplaric 2D intensity distributions of the ITP sample zone at different times. C: Fluorescence intensities averaged along the y-axis. A) was reproduced with permission from Anal. Chem. 2023, 95, 19, 7575–7583. Copyright ©2023 American Chemical Society.

fluorescence microscopy because the sample zone appears as a blurry fluorescent stripe, as shown in Figure 5.1.B for a high *SNR*. As expected, in peak-mode ITP, the concentration distribution (and hence the fluorescence intensity distribution) averaged over the channel cross section takes the shape of a narrow peak when plotted along the channel axis, see Figure 5.1.C. In constant-current ITP, in contrast to constant-voltage ITP, v_{ITP} is constant over time. Hence, the peak of the intensity distribution is continuously shifted at a constant rate. This is the first information that is used in the newly developed post-processing algorithm presented here. By cross-correlating the averaged intensity distributions of the whole set of images acquired in an experiment, the time-independent sample velocity v_{ITP} can be estimated. The sample velocity can then be used to perform a Galilean transformation on the intensity distributions to align the peaks of all images.

By doing so, a set of quasi-replicate data is generated since the width of the sample zone along the channel axis does not change significantly during an experiment. Again, this is true only for constant-current ITP, where the electric field strength in the LE, TE, and sample zone stays constant during an experiment, see for example Ramachandran and Santiago [11]. Here, time-dependent effects on the sample distribution due to carbon dioxide dissolved in the electrolytes [220], sample dispersion due to electro-osmotic or pressure-driven counter flow [44, 45], or Joule heating [221] are neglected. In Subsec-

tion 5.5.5, evidence will be provided that this is a valid assumption for all experiments presented here.

If the noise corrupting the signal of interest is uncorrelated and has a mean of zero, averaging over a set of replicate data can reduce the noise associated with it. In Subsection 5.6.1, it will be shown that the measured data are superposed by additive white Gaussian noise (AWGN). Therefore, estimating the velocity, aligning the intensity distributions of a set of images, and averaging over the resulting quasi-replicate data will result in an increased *SNR*.

In short, the post-processing algorithm presented here uses knowledge of isotachophoretic sample transport to shift and align multiple images, which is why it is called shifting-and-averaging-multiple-images (short SAMI) method. Ultimately, the goal is to use the SAMI method to simplify the detection of samples in isotachophoretic processes. For this reason, the algorithm is told to make a binary decision whether a sample is present or not based on three criteria. SAMI only gives a positive result if 1) the sample velocity, 2) the width of the sample distribution after averaging, and 3) the *SNR* after averaging are within plausible and meaningful regions. Otherwise, it decides that there is no sample. All three criteria are estimated from the image data by SAMI using Bayesian inference. This incorporates the full uncertainty of estimation into the decision. The SAMI method is described and demonstrated below in more detail.

5.4.2 Statistical methods

As described above, SAMI employs some rather advanced statistical methods, namely Bayesian inference, for uncertainty quantification. Hence, an introduction to Bayesian inference will be given here. Besides, it will be shown how information obtained with Bayesian inference can be used in binary decisions, e.g. if a sample can be detected or not from a set of fluorescence images.

5.4.2.1 Bayesian statistical inference

In the following, the basic principles of Bayesian statistical inference are presented based on explanations by Bertsekas and Tsitsiklis [222]. The term statistical inference generally describes a process in which observations are used to gain information about an unknown variable or model. In Bayesian statistical inference, or just Bayesian inference, in specific, this is done by application of Bayes' rule to combine prior knowledge about unknown quantities with new data to obtain a posterior distribution, representing the updated knowledge about these quantities. Here, unknown quantities are modeled as random variable or finite collection of random variables, denoted as Θ. The prior knowledge about Θ is formulated as prior distribution p_Θ. To update the knowledge about Θ, a collection of related random variables $X = (X_1, X_2, ..., X_n)$, also called observation vector, is related

to Θ via the conditional distribution $p_{X|\Theta}$. Once values x of X have been measured, a posterior distribution of Θ, which is now an updated estimate of the unknown quantities, can be calculated using Bayes' rule. For discrete Θ and X, it is written as

$$p_{\Theta|X}(\theta|x) = \frac{p_\Theta(\theta)p_{X|\Theta}(x|\theta)}{\sum_{\theta'} p_\Theta(\theta')p_{X|\Theta}(x|\theta')}, \tag{5.1}$$

where the denominator, the marginal likelihood, is always positive and independent of θ. Kruschke presents a good explanation of the different parts of this equation [223]. The prior $p_\Theta(\theta)$ expresses the credibility of the θ values without the observed data x. The likelihood $p_{X|\Theta}(x|\theta)$ is the probability that the data x could be described by a given model with parameter value θ. The denominator, also called evidence, can also be referred to as $p_X(x)$. It averages over all possible values of θ weighted by the strength of belief in those parameter values. Thereby, the evidence represents the overall probability of the data according to the model. The posterior, finally, is the credibility of θ values after considering the observed data x. It is a full probabilistic description of the uncertainty regarding the θ values.

For multidimensional unknown random variables, i.e. $\Theta = (\Theta_1, \Theta_2, ..., \Theta_m)$, the marginal posterior distributions of a single component, for example Θ_1, can be calculated by summarizing the posterior distribution over all other components [222]:

$$p_{\Theta_1|X}(\theta_1|x) = \sum_{\theta_2} ... \sum_{\theta_m} p_{\Theta|X}(\theta_1, \theta_2, ..., \theta_m|x). \tag{5.2}$$

The posterior distribution contains all the relevant information that x provides on the unknown quantity Θ. However, often only a point estimate, a single numerical value that represents the best guess of Θ, instead of a whole probability distribution is required. To account for this, the maximum a posteriori probability (MAP) rule can be used to compute the value of θ that maximizes the posterior distribution $p_{\Theta|X}(\theta|x)$ for given values of x [222]:

$$\bar{\theta} = \arg\max_\theta p_{\Theta|X}(\theta|x). \tag{5.3}$$

In this equation, $\bar{\theta}$ is the most probable value of θ. If Θ is symmetric about its mean and unimodal, the maximum of the posterior distribution is found at the mean. Still, one has to bare in mind that $\bar{\theta}$ may also lie quite far from the bulk of the posterior distribution and therefore might not be an accurate estimate of the unknown quantity of interest in all cases.

5.4.2.2 Decision making with regions of practical equivalence

The result of Bayesian inference as described above is the posterior distribution of one or more parameters of interest. This section explains, based on the work of Kruschke [224], how the posterior distribution is used to make a decision about accepting or rejecting the assumption that a parameter falls within a certain interval. Kruschke describes a decision rule based on highest density intervals (HDI) and regions of practical equivalence (ROPE), which is why he calls it HDI+ROPE decision rule. This term will also be used below.

The width of a posterior distribution reflects the uncertainty in the estimated parameter values. Wider distributions indicate that there is a lot of uncertainty in the parameter values, usually because there is little data available. More data by contrast leads to narrower parameter distributions, which means that the certainty of the estimate has increased. The HDI covers the range of most credible parameter values. Thereby, it represents the width of the posterior distribution, i.e. the uncertainty in the parameter estimation. In particular, a 95 % HDI will be used in the following sections, i.e. the probabilities of all parameter values inside the 95 % HDI add up to a total probability of 95 %.

As mentioned above, the goal is to make a decision about the acceptance or rejection of the assumption that a parameter falls within a certain interval. In what follows below, the ROPE represents the range of parameter values that are physically plausible. The HDI+ROPE decision rule now is as follows: If the 95 % HDI falls completely inside the ROPE, the assumption should be accepted. If the 95 % HDI falls completely outside the ROPE, the assumption is rejected. If parts of the 95 % HDI are both inside and outside the ROPE, no decision on the acceptance or rejection of the assumption can be made. Hence, the ROPE marks the decision boundaries for the HDI+ROPE decision rule. Details on the definition of the ROPEs for the relevant parameters isotachophoretic velocity, sample width and signal-to-noise ratio can be found in Subsection 5.5.5.

5.5 Experiments and data processing

This section focuses on the preparation and execution of the ITP experiments. In addition, the post-processing of the experimental data is explained in detail and a reference approach serving as benchmark is introduced.

5.5.1 Buffer and sample preparation

Both LE and TE were baseds on an aqueous solution of 50 mM tris(hydroxymethyl)aminomethane (Tris) and 10 mM $MgCl_2$. The pH of the LE was adjusted to a value of 8.2 by adding HCl, the pH of the TE to 7.8 by adding HEPES (4-(2-hydroxyethyl)-

1-piperazineethanesulfonic acid). To suppress EOF, 0.1 % (w/v) polyvinylpyrrolidone (PVP) was dissolved in both LE and TE. Alexa Fluor 647 carboxylic acid, tris(trimethylamonium) salt (AF647, Thermofisher), a fluorophore that served as sample molecule, was mixed with the LE at concentrations of 10, 1, 0.1, 0.01, and 0.001 ng/l.

5.5.2 Microfluidic devices

All experiments were carried out in a microchannel with a depth of 20 µm and a length of 2 cm, as depicted in Figure 5.1.A. The close-up of the drawing shows that the channel has five constricted sections that result from variations of the channel width between 20 and 100 µm. Polydimethylsiloxane (PDMS) casting was used to fabricate the chips. A 10:1 mixture of PDMS monomer and a cross-linker were degassed and then deposited on a photolithographically structured SU-8 wafer. Subsequently, the PDMS is cured for 3 h at 85 °C. After that, the PDMS cast is peeled off from the wafer, and inlet and outlet holes are punched into it. In a last step, oxygen plasma activation is utilized to bond the PDMS cast to a 1 mm thick glass slide.

5.5.3 Experimental procedure

The first step was to add 20 µl of LE and AF647 to the right reservoir, as shown in Figure 5.1.A. The channel was then filled with the electrolyte solution by creating a vacuum in the left reservoir. Then 20 µl of TE was added to the left reservoir. Once the channel was filled and mounted on the stage of a Nikon Eclipse Ti microscope, platinum electrodes serving as anode and cathode were placed in the reservoirs. The sample was detected using a 10x S-Fluor objective (NA = 0.5, Nikon) and a 639 nm diode laser to excite the fluorophore. To initiate an experiment, a constant current of 5 µA was applied with a Keithley 2470 high voltage source, which simultaneously kept track of the voltage across the channel to track the location of the sample zone. In short, when the sample zone enters an area of reduced channel cross-section, the voltage applied to the microchannel changes abruptly. Using LabVIEW code, the applied voltage was recorded and cross-correlated with a step function to help identify the point at which the sample zone enters a constricted area. This method was inspired by Karsenty et al., who used a similar approach for constant-voltage ITP [225]. In this way, it was possible to determine when the sample zone approximately entered the field of view. LabVIEW then triggered the image acquisition with an Andor iXon+ 897 EMCCD camera in Nikon's NIS Elements software. All images were recorded with an exposure time of 20 ms and a frame rate of 46 fps. To reduce the image size, a region if interest with 152x512 px around the microchannel was defined. The pixel pitch λ_{im}, representing the width of a pixel in metric units, was 1.6 µm/px.

5.5.4 Definition of Bayesian models

As already mentioned in the brief introduction of SAMI, Bayesian inference was used to quantify uncertainty. Here, details about the mathematical expressions used for signal modeling will be explained. Bayesian inference is first used to estimate the sample velocity after cross-correlating the averaged intensity distributions. The likelihood function is given by a descriptive model of the noise-free correlation function and a measurement noise model. The sample distribution in peak-mode ITP can be approximated by a skewed Gaussian function. Cross-correlating two sample distributions of this shape leads to a Gaussian distribution. Therefore, the first part of the model, the noise-free correlation function, can be well described by

$$F_1(x, \alpha, \beta, \gamma, \epsilon) = \alpha \exp\left(-\left(\frac{x-\beta}{\sqrt{2}\gamma}\right)^2\right) + \epsilon, \tag{5.4}$$

where α, β, and γ are the amplitude, center position, and standard deviation of the distribution, respectively. The parameter ϵ is an additive offset. An additive stochastic measurement noise, assumed to be AWGN with zero mean and standard deviation σ, completes the model. These five parameters, α, β, γ, ϵ, and σ, are summarized as a collection of stochastic parameters labeled θ.

The cross-correlated data is used by SAMI to estimate the ITP velocity, which in turn is used to align the uncorrelated data. Subsequently, a second probability model is conditioned on the shifted and averaged intensity distribution. The likelihood function is now given by a descriptive model of the noise-free intensity distribution and a measurement noise model. Here, the noise-free intensity distribution is modeled with a skewed Gaussian distribution

$$F_2(x, \alpha, \beta, \gamma, \delta, \epsilon) = \alpha \exp\left(-\left(\frac{x-\beta}{\sqrt{2}\gamma}\right)^2\right)\left(1 - \operatorname{erf}\left(\delta\frac{x-\beta}{\sqrt{2}\gamma}\right)\right) + \epsilon\,. \tag{5.5}$$

This model resembles the Gaussian distribution above, but contains a term that accounts for a skew in the sample distribution. Hence, δ is the skewness parameter of the sample distribution. As explained by Rubin et al., the sample distribution in peak-mode ITP actually follows a hypergeometric function [41]. However, the skewed Gaussian distribution as presented here represents an approximation to the more complex hypergeometric function. Again, measurement noise is modeled as AGWN with zero mean and standard deviation σ. Together, α, β, γ, δ, ϵ, and σ form the collection of stochastic parameters ϕ.

The priors $p(\theta)$ and $p(\phi)$[§] include all the knowledge about the parameters before any data is obtained, e.g. the scale or ranges of probable values. Fairly uninformative priors

[§]Note that the indices of priors, likelihood distributions, and posterior distributions are omitted in the following.

Parameter	Value in $p(\theta)$	Value in $p(\phi)$
α	$\mathcal{H}(10)$	$\mathcal{H}(10)$
β	$\mathcal{U}(0, 512)$	$\mathcal{U}(0, 512)$
γ	$\mathcal{H}(50)$	$\mathcal{H}(20)$
δ	$-$	$\mathcal{N}(0, 0.1)$
ϵ	$\mathcal{N}(0, 1)$	$\mathcal{N}(0, 0.01)$
σ	$\mathcal{H}(1)$	$\mathcal{H}(1)$

Table 5.1: Overview of the priors used by SAMI for sample detection.

are used mostly to specify upper and lower bounds: a uniform distribution

$$\mathcal{U}(a,b) = \begin{cases} \dfrac{1}{b-a} & \text{for } a \leq x \leq b \\ 0 & \text{for } x < a \text{ or } x > b \end{cases} \tag{5.6}$$

for β, wide half-normal distributions

$$\mathcal{H}(a) = \begin{cases} \dfrac{\sqrt{2}}{a\sqrt{\pi}} \exp\left(-\left(\dfrac{x}{a}\right)^2\right) & \text{for } x \geq 0 \\ 0 & \text{for } x < 0 \end{cases} \tag{5.7}$$

for α, γ, and σ as well as a normal distribution

$$\mathcal{N}(a,b) = \frac{1}{b\sqrt{2\pi}} \exp\left(-\left(\frac{x-a}{b}\right)^2\right) \tag{5.8}$$

for δ and ϵ. A complete overview of the priors is given in Table 5.1.

5.5.5 Definition of ROPEs

The ROPEs for the isotachophoretic velocity v_{ITP} and the sample spread, represented by fit parameter γ, are based on experience gained from experiments performed at high sample concentrations and on the physics underlying the isotachophoretic sample transport. Figure 5.1.C shows that at comparatively high sample concentrations, the sample is clearly visible as a sharp peak in the averaged intensity distribution. Thus, an approximate value for v_{ITP} can be determined by comparing the peak position in two different images recorded with a known time interval, since the sample velocity is constant over time in peak-mode ITP. Besides, in peak-mode ITP, the sample concentration does not affect v_{ITP}. Therefore, it is plausible to base the definition of the ROPE for v_{ITP} on experiments with high sample concentrations. Specifically, the five experiments with a sample concentration of 10 ng/l were used for this purpose. For all pairs of images taken with

ROPE	Description	Value
$ROPE_v$	ROPE of the sample velocity v_{ITP}	[130,190] µm/s
$ROPE_\gamma$	ROPE of the sample spread γ	[4.3,10.7] px
$ROPE_{SNR}$	ROPE of the *SNR*	[3,∞)

Table 5.2: Overview of the ROPEs used by SAMI for sample detection.

$\Delta t = 1\,\text{s}$ in which the full peak of the intensity distribution was visible, a value for v_{ITP} was calculated. The mean value that results from this procedure is $161.48 \pm 7.34\,\mu\text{m/s}$. Next, it is assumed that in subsequent measurements the velocities obey a Gaussian distribution. Based on these results, the ROPE is set to $[130, 190]\,\mu\text{m/s}$.

Next, a skew normal distribution function of the form of 5.5 can easily be fitted to the intensity distribtuins obtained at high sample concentrations. In this way, insights into possible values for the sample spread parameter γ are gained. As an example, the development of γ over a series of 100 images is shown in Figure 5.2.A (blue curve) together with a linear fit (red curve). The slope of the linear fit is rather negligible. On the right, in Figure 5.2.B, the frequency of occurrence of the spread parameter γ derived from the data on the left is depicted in a histogram together with a Gaussian fit. The figure suggests that γ obeys a Gaussian distribution. Summing up, it can be concluded that the spread γ does not increase significantly during the time of observation. The mean spread γ calculated from five experiments is $6.5 \pm 0.75\,\text{px}$. Using a three sigma range, a ROPE of $[4.3, 8.8]\,\text{px}$ is obtained. However, SAMI was observed to deliver slightly larger spreads (probably due to smoothing with a Fourier filter, see below) with an average of approximately 8.5 but practically the same standard deviation. Similar to above, this would lead to a ROPE of $[6.3, 10.7]\,\text{px}$. As a reflection of this uncertainty concerning the spread, the final ROPE is set to $[4.3, 10.7]\,\text{px}$.

The ROPE for the *SNR* was set to $[3, \infty)$, i.e. a one-sided ROPE, since values > 3 result in a sample peak that is clearly distinguishable from the image noise. All these ROPE values are based on experience, but remain subjective to some degree. Wider or narrower ROPEs might also be reasonable. However, the choice of ROPEs will always affect the detection results: Too wide ROPEs can lead to false positives, too narrow ROPEs increase the risk of false negatives. A summary of the ROPEs is given in Table 5.2.

5.5.6 Additional information on the post-processing algorithm

The SAMI algorithm was programmed in Python. Bayesian data analysis was performed using PyMC3 (version 3.11.4) and ArviZ (0.11.4), two Python packages specifically created for this purpose [226, 227]. The posterior distributions of the relevant model parameters were approximated using a No-U-Turn sampler [228]. The code also includes a gradient-free optimizer that determines a set of 200 images (out of a total of 460 images

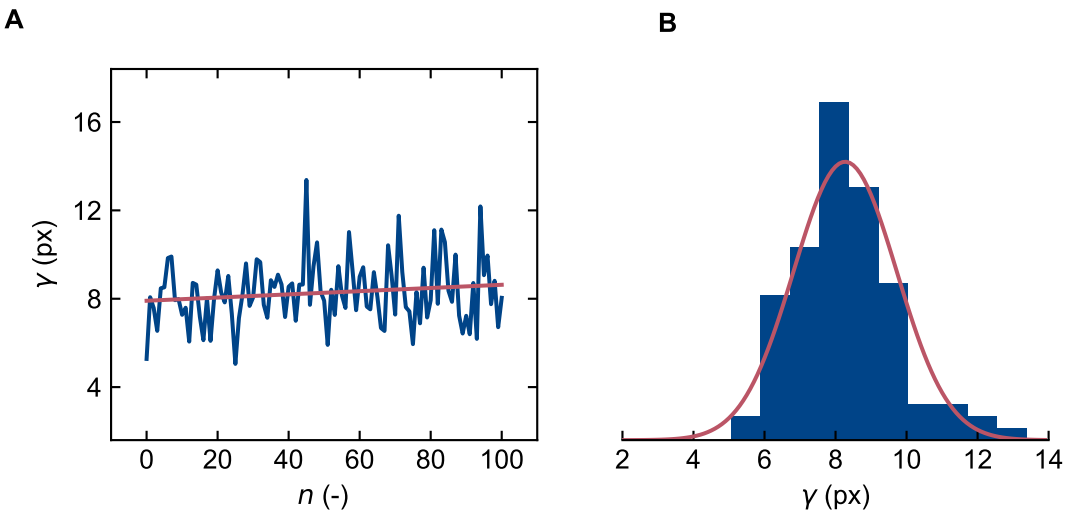

Figure 5.2: Evaluation of the sample spread parameter γ from experimental data obtained at high sample concentrations. A) Temporal evolution of γ derived from a series of 100 images. B) Frequency of occurrence of γ derived from the data in A).

per experiment) with which the estimated HDI of the key parameters v_{ITP} and γ is minimized. The reader is again referred to the reference implementation of the algorithm, which is available from a public repository[¶].

5.5.7 Demonstration of the post-processing algorithm

The SAMI algorithm can be roughly divided into four steps. First, all raw images are pre-processed. In a second step, the sample velocity is estimated. At the end of this step, a first decision takes place. If the estimated velocity is outside a physically plausible range, SAMI will stop with a negative result. Otherwise, the third step follows. Here, the width of the sample distribution and the *SNR* are estimated from the averaged data. Last, in the fourth step, a final detection decision is made. This section elucidates the crucial intermediate steps and outcomes of the data processing using SAMI. In Figure 5.3, the processing of two sets of fluorescence images acquired at comparatively high and low concentrations, namely 10 and 0.01 ng/l, is compared.

5.5.7.1 Pre-processing

Capturing a time series of 2D images of the ITP sample zone progression results in a three-dimensional data array denoted as $I(x, y, n)$, where x and y represent the coordinates along the horizontal and vertical axes of the images, respectively, and n enumerates the images chronologically. To pre-process the raw images, they are first cropped in the y-direction to match the width of the microchannel. After this step, each image had a size of 54x512 px. Subsequently, a background image devoid of any sample is subtracted to

[¶]Link to the repository: https://doi.org/10.5281/zenodo.7881096

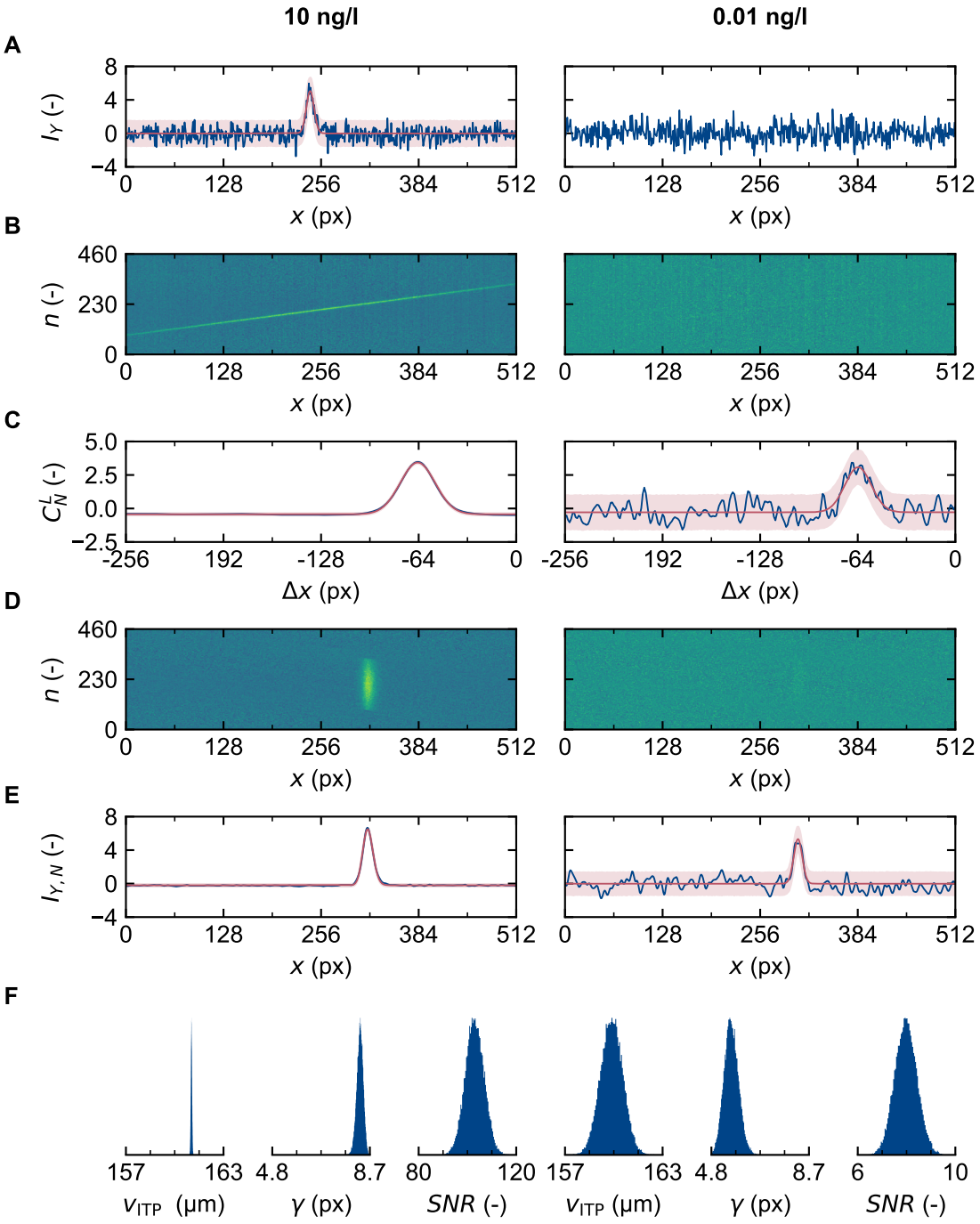

Figure 5.3: Demonstration of the SAMI method comparing images acquired at a high and a low sample concentration (10 and 0.01 ng/l). A) Intensity distribution averaged along the vertical direction of a pre-processed image. B) Spatiotemporal plot obtained by stacking the averaged image data. C) Cross-correlated data with an image lag of $L = 30$ after averaging over all 170 cross-correlation functions. The position of the peak indicates the isotachophoretic velocity. D) Data shifted according to the sample velocity. E) Sample peak after averaging over 200 shifted images. F) Marginal posteriors of the three detection criteria isotachophoretic velocity, sample spread, and signal-to-noise ratio. Reproduced with permission from Anal. Chem. 2023, 95, 19, 7575–7583. Copyright ©2023 American Chemical Society.

eliminate the background fluorescence. If the concentration distribution remains more or less constant along the vertical axis and the noise is uncorrelated, a signal enhancement can be achieved by averaging the intensity values I over y, resulting in a condensed data set denoted as $I_Y(x, n)$. At a high concentration of 10 ng/l, the sample peak can be clearly identified, which is shown on the left side of Figure 5.3.A. The red line is a skew normal function fitted to the intensity distribution together with its 95 % confidence interval. In contrast, at a low concentration of 0.01 ng/l, the sample is completely hidden by noise, which can be seen on the right side of the same figure.

Interesting insights can be obtained by plotting the whole data set $I_Y(x, n)$, which results in a spatiotemporal plot of the propagation of the ITP sample zone, see Figure 5.3.B. As a first step of denoising, a Fourier filter has been applied to the spatiotemporal data. Fourier filters first transform the signal, here the spatiotemporal data, to the frequency domain. The Fourier transform of the signal is then multiplied with a filter or mask that suppresses certain frequencies. In the present investigation, a 2D Gaussian window is used as mask. Afterwards, the filtered signal is transformed back to its original domain. From the left side of Figure 5.3.B, it becomes obvious that the sample indeed travels at a roughly constant velocity. With the lower sample concentration, a faint line is still perceptible. However, this would not be sufficient for a reliable sample detection. Additionally, Figure 5.3.B illustrates that the fluorescence intensity is highest at the image's center, gradually diminishing towards the left and right edges. This discrepancy can be attributed to non-uniform illumination of the detection window in the experimental setup. However, since the sample peak's width remains roughly constant over time (refer to Figure 5.2), it does not affect the functionality of the post-processing algorithm. A complete overview of the spatiotemporal plots obtained by evaluating all experiments with different concentrations is given in Subsection B.1 in the appendix. Ideally, SAMI only averages over images of the ITP sample zone, i.e. it should omit images that do not contain a peak in their intensity distribution, which is why the gradient-free optimizer was integrated.

5.5.7.2 Estimation of the isotachophoretic sample velocity

Theoretically, the isotachophoretic sample velocity could be calculated from experimental parameters like electric current, electrolyte concentrations, electrophoretic mobilities, and the cross-section of the microchannel, as described for example by Ramachandran and Santiago [11]. However, small deviations from the theoretical values of these parameters can lead to relatively large deviations in the calculated velocity. The ITP velocity could also be determined by the slope of the diagonal in Figure 5.3.B. As can already be seen in the right part of the figure, this would only work for rather high initial signal-to-noise ratios. Therefore, this method, as well as the estimation *via* the progression of the sample peak as in Subsection 5.5.5, is not suitable for minute sample concentrations. Instead, SAMI uses a different way to estimate the ITP velocity even in cases where the imaging

noise is dominant over the signal of the low concentration sample. It takes advantage of the fact that the sample velocity and the width of the peak remain more or less constant.

In a first step, the averaged intensity distributions $I_Y(x, n)$ of images n and $n + L$, where L is a pre-specified time lag between two images, are cross-correlated along the x coordinate according to

$$\begin{aligned} C^L(\Delta x, n) = \sum_x I_Y(x, n) I_Y(x + \Delta x, n + L) \\ \forall\ n \in \{1, 2, \ldots, N - L\}. \end{aligned} \tag{5.9}$$

Here, N is the total number of images taken into account, and Δx is the displacement. This first step leads to $N - L$ cross-correlation functions. Due to the constant ITP velocity, they all have a maximum at approximately the same position, and differ mainly by random correlations caused by measurement noise. Hence, averaging over all cross-correlation functions leads to an effective reduction of noise:

$$C_N^L(\Delta x) = \frac{1}{N - L} \sum_{n=1}^{N-L} C^L(\Delta x, n)\ . \tag{5.10}$$

In Figure 5.3.C, the resulting compressed data array $C_N^L(\Delta x)$ is depicted for both high and low concentrations. For 10 ng/l, noise is almost completely removed. Even at 0.01 ng/l, an unambiguous maximum is obtained.

Bayesian inference is then used to accurately and reliably estimate the position of the peak position including its uncertainty from the cross-correlation function. The correlated signal is modeled with a Gaussian function according to Equation 5.4. As an intermediate result, this step delivers the posterior probability $p(\theta|C_N^L)$. Figure 5.3.C shows the resulting posterior means as red lines and the 95 % HDI representing the uncertainty as light-red background. Comparing the two concentrations, it becomes obvious that the uncertainty is much higher for the lower concentration. Nevertheless, the maximum of the averaged cross-correlation functions is still evident.

The ITP velocity can be calculated by fitting 5.4 to the posterior distribution and dividing β, describing the center position of the distribution, by the lag between two images L:

$$v_{\mathrm{ITP}} = \frac{\beta}{L}. \tag{5.11}$$

The result will be a velocity in px/frame. To obtain physically meaningful units, i.e. µm/s, v_{ITP} has to be multiplied with the experimental frame rate f_{im} in fps and the pixel pitch λ_{im} in µm/px. For both concentrations, the final velocity distribution is displayed in the first plot in Figure 5.3.F. Strikingly, the distribution for the lower concentration is much wider than that for the higher concentration.

As mentioned above, a first decision is now being made. SAMI will only continue if the 95 % HDI of the velocity falls completely within the pre-defined ROPE of $[130, 190]$ µm/s. Otherwise, it will stop the data processing at this point and decide that no sample is detectable. See below for more details on the decision-making process. Figure 5.3.F shows that the distributions for both concentrations are within the ROPE.

5.5.7.3 Shifting and averaging multiple images

MAP estimation can now be used to calculate the most probable value of the ITP velocity according to

$$\bar{v}_{\mathrm{ITP}} = \arg\max_{v_{\mathrm{ITP}}} p(v_{\mathrm{ITP}}|C_N^L) \ . \tag{5.12}$$

With $\bar{v}_{\mathrm{ITP}}$ (in px/frame), a Galilean transformation can now be performed on the intensity distributions:

$$I_Y(x', n) = I_Y(x - \bar{v}_{\mathrm{ITP}} n, n) \ . \tag{5.13}$$

In this way, the sample peaks for every instance of n are aligned at the same position, as can be seen in Figure 5.3.D. Again, a Fourier filter is used to further denoise the resulting image. Last, averaging over all images results in the final data array

$$I_{Y,N}(x') = \frac{1}{N} \sum_{n=1}^{N} I_Y(x', n) \ , \tag{5.14}$$

which is represented by the blue lines in Figure 5.3.E. Altogether, the initial image data $I(x, y, n)$ is compressed into the data set $I_{Y,N}(x')$, which does not have an explicit time dependence.

Now, Bayesian inference is used to derive information from $I_{Y,N}(x')$ about the two remaining decision criteria, namely the sample spread γ and the *SNR* after averaging. The model comprises the skewed Gaussian distribution in Equation 5.5 and a model for the measurement noise. As a result, the posterior probability $p(\phi|I_{Y,N}(x'))$ is obtained. The signal-to-noise ratio is defined as $SNR = \alpha/\sigma$. Hence, both *SNR* and γ are obtained by determining the respective marginal posterior distributions from $p(\phi|I_{Y,N}(x'))$. Exemplary mean and HDI values are depicted in Figure 5.3.E as red lines and light-red backgrounds, respectively. Comparing subfigures A and E, the improvement in *SNR* achieved with SAMI becomes obvious, especially in the low concentration case: Initially, no peak could be detected. But after post-processing, the sample is clearly visible, even when including the uncertainty of the estimation.

5.5.7.4 Final decision on sample detection

After the post-processing is completed, SAMI has to decide whether a sample is present or not. For this reason, it compares the HDI of the ITP velocity, the sample spread γ and

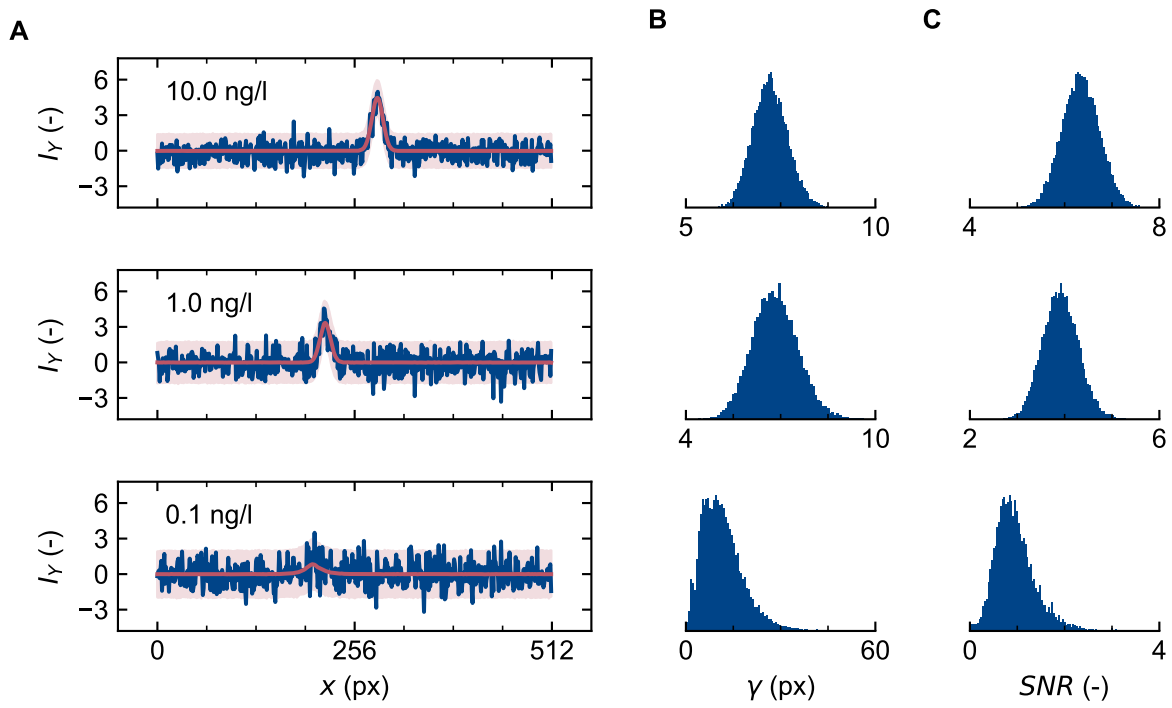

Figure 5.4: Typical results obtained with the single image approach. A) Averaged intensity distributions at different concentrations together with a fit and HDI. B) Posterior distribution of the sample spread γ. C) Posterior distribution of the *SNR*. Reproduced with permission from the SI of Anal. Chem. 2023, 95, 19, 7575–7583. Copyright ©2023 American Chemical Society.

the *SNR* with the pre-defined ROPEs. In this way, not only one single quantity, e.g. the *SNR*, is taken into account, but rather a set of quantities derived from ITP experiments as well as their uncertainties. Figure 5.3.F shows that the 95 % HDIs of all three quantities fall within the respective ROPE for both concentrations. Hence, both samples are clearly detectable with the SAMI method.

5.5.8 Single image approach

The SAMI method combines multiple shifted images to detect samples in microfluidic ITP without any additional instrumentation effort. To evaluate its potential, SAMI is compared with a benchmark approach that aims at detecting samples at different concentrations merely by evaluating the intensity profile of a single image. Above, the intermediate steps and results of SAMI were presented. Here, the focus is on exemplary results obtained with the benchmark process. Note that this approach only estimates γ and *SNR*, since it is not possible to determine v_{ITP} from a single image.

For three different concentrations, namely 10, 1 and 0.1 ng/l, an exemplary averaged intensity distribution is displayed in Figure 5.4.A. By conditioning a probability model (see Equation 5.5) to them, the corresponding means and HDIs are obtained, which are shown in red. In case of the high and medium concentration (top and center row), the sample

is clearly visible as a peak in the intensity distribution. Accordingly, the characteristic quantities γ and SNR are within the ROPEs, meaning that these samples are detectable even without SAMI, see Figure 5.4.B and 5.4.C. Already at a concentration of 0.1 ng/l, the single image approach is not able to detect the sample. Neither is the sample visible as a peak in the intensity distribution, nor do the 95 % HDIs of the detection criteria fall within the ROPE. Note that the best estimates for each concentration were determined by checking several images per experiment. A detailed overview of success and failure with SAMI and the single image approach will be given in the results section.

5.6 Results and discussion

SAMI is based on the assumption that the image data it evaluates are corrupted by additive white Gaussian noise (AWGN). The validity of this assumption is shown in the first part of this section. Afterwards, the performance of SAMI is evaluated in more detail.

5.6.1 Analysis of the image noise

To characterize the noise corrupting the experimental data, images recorded without any sample were analyzed. The histogram in Figure 5.5.A shows the standardized distribution of intensity values from an image chosen as an example. A skewed Gaussian distribution describes the data well (red fitting curve). However, the skew is negligible, as can be seen by comparing the red curve with the blue curve, which represents a Gaussian normal distribution. Figure 5.5.B shows that the power spectral density of an image derived with a Fourier transformation is constant over all frequencies (except for zero frequency). Together with the negligible temporal and spatial autocorrelations, as depicted in Figure 5.5.C and 5.5.D, this indicates that the pixels of the images in all experiments presented in this chapter are uncorrelated. Hence, the assumption of AWGN is justified.

5.6.2 Improvement with SAMI against detection from single images

Above, exemplary results obtained with SAMI and the single image approach were presented. In total, five experiments were carried out for each sample concentration of 0 (control group), 0.001, 0.01, 0.1, 1, and 10 ng/l. Then, the respective images were evaluated using the SAMI and the single image method. Detection decisions were based on the same ROPEs in both cases, while only incorporating two detection criteria in the case of the single image method (since the sample velocity can not be determined from a single image). An overview of the number of correct decisions is given in Figure 5.6. At the highest sample concentration of 10 ng/l and in the control case without sample, the single image approach decides correctly. Still four out of five decisions are correct at

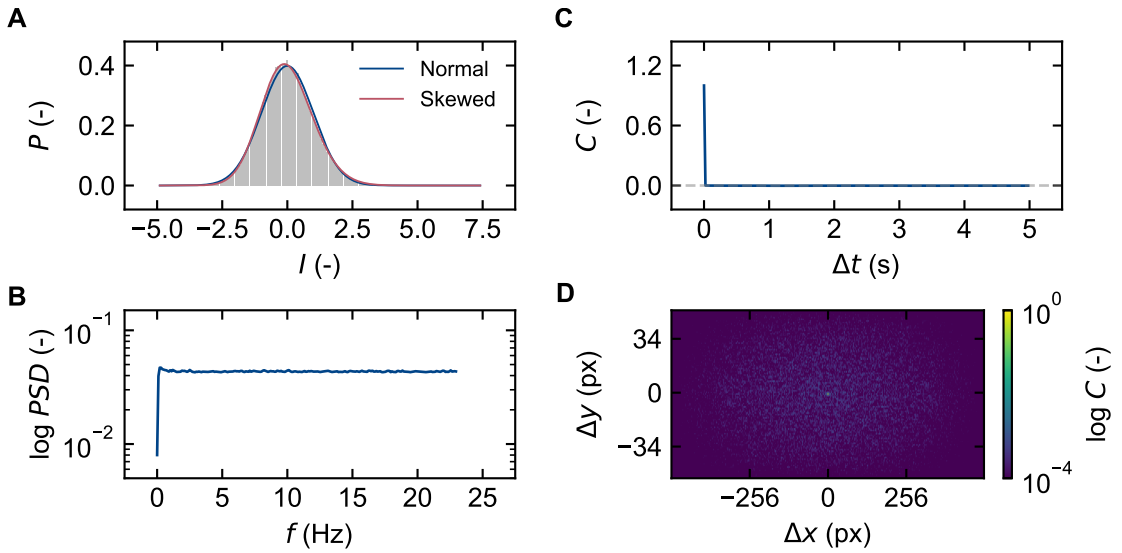

Figure 5.5: Analysis of the image noise. A) Histogram of standardized intensity values from an exemplary image. B) Power spectral density, C) temporal and D) spatial autocorrelation showing that the pixels of the image are uncorrelated. Reproduced with permission from the SI of Anal. Chem. 2023, 95, 19, 7575–7583. Copyright ©2023 American Chemical Society.

1 ng/l. However, below that, it cannot detect any of the samples. The SAMI method, by contrast, is capable of detecting all samples down to a concentration of 0.1 ng/l and four out of five samples at 0.01 ng/l. Only at 0.001 ng/l, it fails completely. In addition, it decides correctly in all cases without any sample. This is an important result, too, since it indicates that SAMI was not misled by a background signal caused by contaminants in experiments with low sample concentrations of 0.1 and 0.01 ng/l. Summarizing, these results suggest that the SAMI method is able to lower the detectable sample concentration by approximately two orders of magnitude compared to the single image approach by using the information of a series of 200 images. A further reduction of the lowest detectable concentration might be achieved by using more images in the SAMI method.

5.6.3 Characteristic quantities determined during sample detection

The previous subsection served as a demonstration of SAMI's capability to detect samples. In this subsection, details about the characteristic quantities forming the foundation of the detection decision will be given. Both approaches deliver a full posterior probability distribution for the the sample spread γ and the *SNR*. In addition, SAMI also includes the sample velocity v_{ITP}. A complete overview of the posterior distributions obtained with SAMI is given in the Appendix, see Subsections B.2 to B.4. Here, however, the estimated most probable values, i.e. the modes, of the three characteristic quantities are presented in Figure 5.7. Additionally, the 95 % HDIs calculated by SAMI to characterize

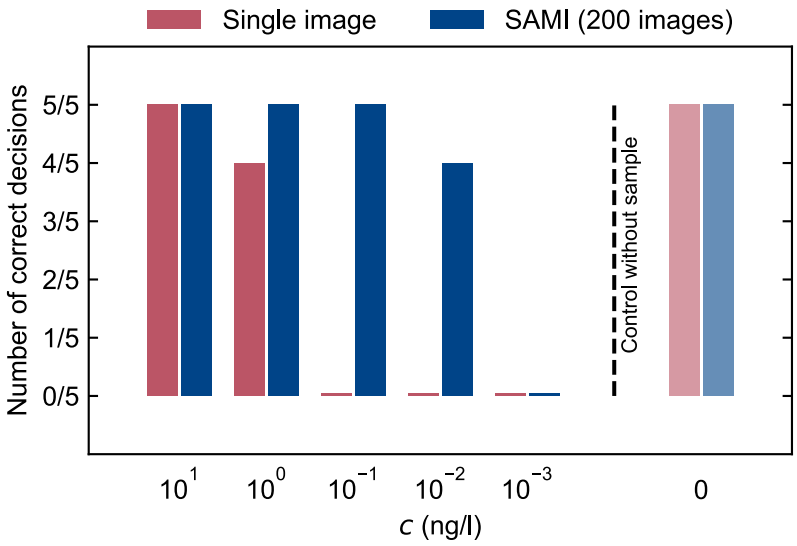

Figure 5.6: Number of correct detection decisions for different sample concentrations obtained with the SAMI method and the benchmark process. Reproduced with permission from Anal. Chem. 2023, 95, 19, 7575–7583. Copyright ©2023 American Chemical Society.

the uncertainty are shown in Figure 5.7.D. All data points are averages from experiments with a given sample concentration in which the sample could be detected.

5.6.3.1 Sample velocity

The mean values of the modes of v_{ITP} are displayed in Figure 5.7.A. The reference values were determined by tracking the peak of the intensity distributions (see Subsection 5.5.5). As expected, the ITP velocity varies only insignificantly with sample concentration. Accordingly, all averaged velocity modes fall within the ROPE from 150 to 170 µm/s. At lower sample concentrations, the standard deviation is increased. Presumably, the accuracy of the estimation method decreases with sample concentration, as the latter directly affects the signal-to-noise ratio. Remarkably, the reference values perfectly match the velocities obtained via SAMI. It can therefore be concluded that SAMI can be used to reliably determine sample velocities even at low sample concentrations.

5.6.3.2 Sample spread

In Figure 5.7.B, all averaged modes of the sample spread γ are in the range between 6 and 9 px. They therefore completely fall within the ROPE of [4.3, 10.7] px. Interestingly, the values at a concentration of 10 ng/l vary significantly between the SAMI and the single-image method. There are two possible explanations for this: On the one hand, SAMI uses a Fourier filter, which slightly smooths the peaks in the intensity distributions. On the other hand, if the estimation of the sample velocity in the previous step is even slightly inaccurate, the sample peaks will not be perfectly aligned. Hence, averaging will result in a broadened peak. Another observation stands out: It seems like the estimated

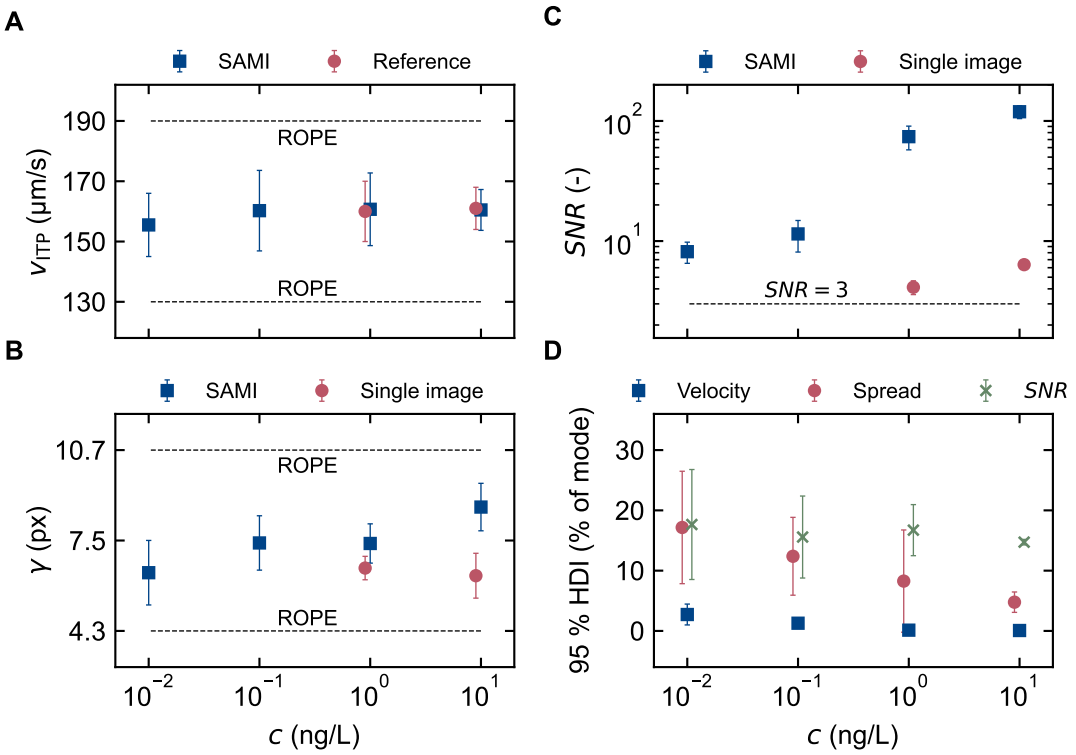

Figure 5.7: Results of the characteristic quantities used for sample detection, namely A) isotachophoretic velocity, B) sample spread, and C) signal-to-noise ratio. All data points are averages of the modes of the respective posterior probability distributions. Only experiments where a sample was successfully detected were considered. The error bars represent the standard deviation of the respective values. In D), the mean 95 % HDI determined with SAMI is shown relative to the mode values of the corresponding characteristic quantity together with its standard deviation. Reproduced with permission from Anal. Chem. 2023, 95, 19, 7575–7583. Copyright ©2023 American Chemical Society.

sample spread increases with the sample concentration. This would contradict the theory as described for example by Rubin et al. [41], according to which the width of the sample distribution, and therefore the width of the corresponding intensity distribution, is independent of the sample concentration in peak-mode isotachophoresis. However, since the sample concentrations are comparatively low, inaccuracies during the experiments or during image processing are the more likely explanation, especially since this trend is not found with the single image approach.

5.6.3.3 Signal-to-noise ratio

The expectation is that as the amount of sample increases, so should the SNR. This is confirmed by Figure 5.7.C for both methods. Notably, at the two highest concentrations, SAMI achieves more than ten times higher SNR values than the single-image method. In this way it is possible to see a clear peak in most cases even at a very low concentration of 0.01 ng/l, since the *SNR* is greater than 3. See B.5 in the Appendix for all averaged sample peaks resulting from SAMI.

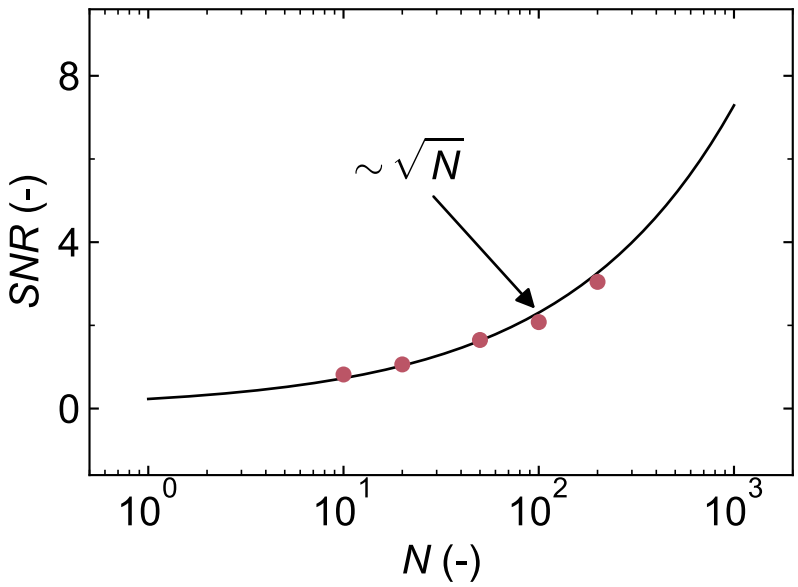

Figure 5.8: Dependence of the signal-to-noise ratio on the number of images N included in the averaging. The SAMI method was applied without Fourier filtering, as this causes slight correlations between images. Reproduced with permission from Anal. Chem. 2023, 95, 19, 7575–7583. Copyright ©2023 American Chemical Society.

5.6.3.4 Highest density interval

For each of the characteristic quantities v_{ITP}, γ and SNR, an average width of the corresponding 95 % intervals can be determined. In Figure 5.7.D, they are depicted relative to the respective mean mode values. They increase with falling sample concentrations in almost all cases, showing that SAMI is less accurate at lower sample concentrations. However, especially for the sample velocity, the HDIs are very narrow, which again underlines the capability of SAMI to determine v_{ITP} even at low sample concentrations.

5.6.4 Improvement of the signal-to-noise ratio with the number of images

As shown above, an improvement of SNR can be achieved by averaging over a series of quasi-replicate measurements. It is well-known that averaging over a number of replicate measurements corrupted by AWGN leads to an increase in SNR proportional to the square root of the number of measurements. Consequently, the SNR obtained with the SAMI method should be proportional to $\sqrt{N}$, where N is the total number of images that serve as input to the post-processing algorithm. All results presented above were computed with a series of 200 images. To gain insight into the dependence of the SNR on the number of quasi-replicate measurements, N was sequentially reduced down to 10 images.

Exemplary results for a comparatively low concentration of 0.1 ng/l are presented in Figure 5.8. Note that since the Fourier filtering applied by SAMI causes slight correlations

between images and therefore degrades the square root dependence, this step has been omitted from the calculation of the results here. As expected, smaller values of N lead to a lower *SNR*. Below $N = 200$, the *SNR* is even below the critical value of 3, marking the threshold for sample detection in SAMI. Compared to $N = 10$, the *SNR* at $N = 200$ is about 4 times higher, which renders the low concentration sample detectable. The curve fitted to the data points clearly supports the assumption that the *SNR* is proportional to $\sqrt{N}$. Thus, the depicted *SNR* values are slightly lower than they would be if the filters were included.

The observed relation between N and *SNR* highlights a very important feature of SAMI: in theory, even extremely low concentration samples should be detectable if the number of images used as input to SAMI is large enough. Naturally, experimental factors such as measurement time on the one hand and camera sensitivity and maximum frame rate on the other hand will limit the capacity of SAMI. It is important to notice that SAMI will only perform well if AWGN is the dominant source of noise. For example, especially at very low exposure times, shot noise is often dominant. In this case, the measurement process, and therefore the likelihood function of the noise, must be modeled with a Poisson distribution instead of a Gaussian distribution. But as long as the noise is uncorrelated or random, SAMI's ensemble averaging will effectively reduce it. Since these limits are all case-specific, it can be said from the current results that knowledge about the physics underlying a detection process can be used to generate a large number of quasi-replicate measurements and thereby significantly reduce the detection limits of that process.

5.7 Conclusions and outlook

In this chapter, a strategy based on performing a large number of quasi-replicate measurements to increase the *SNR* in microfluidic sensing applications was presented. This is made possible by exploiting knowledge of the physical processes underlying the measurement process. The usefulness of this approach for fluorescence detection over a wide range of sample concentrations was demonstrated using an implementation for ITP named the *shifting-and-averaging-multiple-images* method (SAMI). In comparison to single image detection, SAMI could reduce the detectable concentration by two orders of magnitude using 200 images. Experimental data showed that this method follows the well known signal processing proportionality $SNR \propto \sqrt{N}$, where N is the number of images. Thus, by increasing N, there is room to further reduce the detection limits. Obviously, any such attempt will have to take into account the trade-off between measurement time, detector sensitivity and detector response time.

The SAMI method achieves significant improvements of the *SNR* only based on software, i.e. without any additional instrumentation effort. It could therefore be a good

alternative other detection schemes relying on elaborate or expansive hardware. Capillary zone electrophoresis and ITP experiments are often carried out with point detectors (or cameras as effective point detectors), which leads to a spatiotemporal convolution of the intensity peaks. In this way, the *SNR* can too be improved without a major instrumentation effort. However, the SAMI method could still be a straightforward alternative to these approaches, since it results in additional information: it accurately estimates the ITP sample velocity and the spatial sample distribution. These two quantities can then be included in detection decisions. Another approach without averaging multiple images, albeit less straight-forward then the SAMI method, could be based on pattern recognition algorithms using machine learning to minute samples. However, such studies are left for future work.

As an alternative to the SAMI method, counterflow ITP could be utilized as a method to increase the *SNR* by keeping the sample velocity rather low or even stopping the sample [59, 66, 75, 101] and increasing the exposure time or averaging over multiple images of a stationary sample zone. Of course, this comes at the expense of additional instrumentation effort. In contrast to counterflow ITP, the SAMI method is even suitable for applications where the sample zone is dynamic. This enables lowering the detection limits without increasing the time span of the ITP protocol. In addition, counterflow ITP results in sample dispersion and a corresponding reduction of the sample concentration [45], which can be largely suppressed for moving sample zones.

Another aspect to consider is that many real-world assays use ITP to detect an increase of a fluorescence signal relative to a background signal, for example caused by reactions between a target molecule and a fluorescent probe, which usually autofluoresces to some degree [48, 89]. These detection schemes are limited by the signal-to-background ratio rather than by the signal-to-noise ratio. Hence, the extent to which the SAMI method can improve these assays is limited. SAMI could still be applied to reduce the random variations in the signal and make both the background and the increased signal more accurately visible. Furthermore, if target-probe hybrids on the one hand and excess probe molecules causing a background signal on the other hand can be separated prior to or during the isotachophoretic process [59, 67, 229], the SAMI method will still be applicable.

Finally, it should be emphasized that the SAMI method is merely an implementation of a general principle for sample detection. Using insights into the physics underlying a measurement process to perform a large number of quasi-replicate measurements should have great potential for many other sensing applications in (bio)chemical analysis. For example, it should be possible to apply the SAMI principle to capillary electrophoresis (CE). However, different from the ITP-based sample transport discussed in this work, in CE protocols, a significant sample dispersion along a capillary or microchannel is observed due to molecular diffusion and other factors [230]. In this case, an extension of SAMI

would require to not only estimate the velocity to shift the sample zone along a capillary or channel, but also compressing the zone to reverse the sample dispersion. However, the proof of this hypothesis must be provided in future work.

Chapter 6

Isotachophoresis with oscillating sample zones to control the mixing of co-focused species

6.1 Summary

Microfluidic isotachophoresis (ITP) is a powerful technique that can significantly increase the reaction rate of chemical species by co-focusing them in a narrow sample zone. Correspondingly, ITP has been utilized to reduce the reaction time in various bioanalytical assays. However, in conventional ITP, it is hardly possible to control the reaction rate in real time, i.e., speeding up or slowing down a reaction on demand. Here a new mode of ITP is experimentally demonstrated that enables controlling the overlap of two ITP zones over time, which is a first step toward controlling reaction rates. Two non-reactive samples are initially focused and separated by a spacer using a DC electric field. By superimposing an oscillating field component with sufficiently high amplitude to the DC field, the spatial overlap of their concentration profiles, i.e. their mixing, is temporarily increased due to electromigration dispersion. The time average of this overlap can be precisely controlled by varying the frequency and amplitude of the oscillation. It is proposed that this scheme can be transferred to chemical reactions between ionic species with sufficiently different electrophoretic mobilities. Tuning the parameters of the oscillatory electric field should allow to directly control the corresponding reaction rate.

6.2 Contribuitons and publications related to this project

This chapter is based on an article published in 2024 in Analyitical Chemistry, a journal of the American Chemical Society [231]. Several people have contributed to this paper in addition to the author of this thesis. Henning Bonart, Steffen Hardt, and the author

of this thesis designed the research. Tamal Roy, Tobias Meckel, and the author of this thesis planned the experiments. The author of this thesis conducted the experiments. Henning Bonart and the author of this thesis analyzed the experimental data. Henning Bonart, Steffen Hardt, and the author of this thesis wrote the manuscript with input from all authors. Some parts of the text of this paper were directly inserted here, others were slightly adjusted. The content of the figures presented below was reproduced from the article and its supplementary information. The formatting and some symbols were adjusted to match the style of this thesis.* The raw fluorescence images obtained from the ITP experiments and the code used to quantify the time-dependent overlap of two oscillating ITP zones are freely available†.

6.3 Introduction

The rate of chemical reactions between two or more species depends on the concentration of the reactants, among others. Microfluidic ITP is therefore particularly suitable for enhancing reaction rates, as it allows to increase the local concentration of ionic species by several orders of magnitude [62, 74–78]. As mentioned before, this offers great potential for chemical reactions, especially if at least one of the reactants is present only at a low concentration. Despite the clear advantages of ITP, little attention has been paid to the control of chemical reactions after the reactants have been preconcentrated. In their review on ITP and biochemical reactions, Eid and Santiago discuss the potential of ITP to control reactions [98]. However, in this context "control" usually means the initiation of a reaction by co-focusing and thereby mixing two samples in a single ITP zone. What is missing are approaches for slowing down, speeding up, interrupting, and resuming reactions at any time during an ITP-based assay. The common scheme to control reaction rates (and therefore the progress of a reaction) is based on regulating the temperature or pressure in a reactor. However, this is usually challenging or undesired in microfluidic ITP.

Therefore, the focus in this chapter is on a third parameter that has a direct impact on the reaction rate: the degree of mixing of the reactants. A a new approach is presented in which two samples are initially separated by a spacer zone. Using a DC electric field, they are preconcentrated and transported through a microchannel. Then, an oscillating component is superimposed on the DC field, which leads to a time-dependent overlap of the concentration distributions of the two samples. In this way, it is possible to mix (and demix) the two samples in a controlled manner. This has the potential to introduce a new level of controllability to ITP-based (homogeneous) reaction processes.

*Reproduced with permission from Anal. Chem. 2024, 96, 11, 4446–4454. Copyright ©2024 American Chemical Society.

†https://doi.org/10.48328/tudatalib-1359

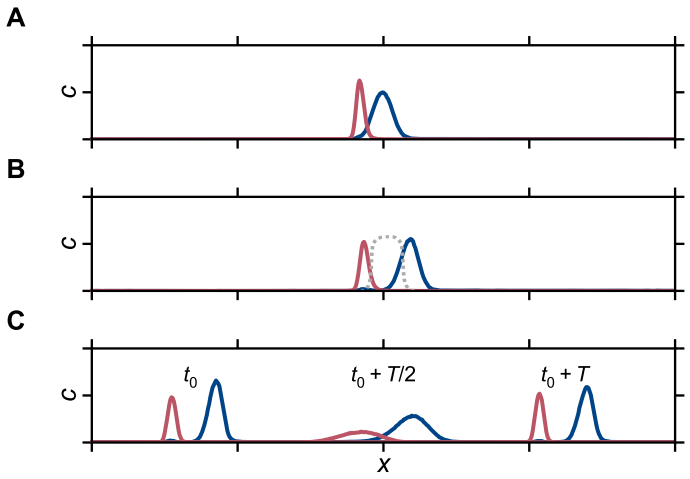

Figure 6.1: Concept of controlling the overlap of ITP zones. A) Two co-focused species without spacer. The overlap of their concentration distributions is determined by the electrophoretic mobilities of the two species and stays roughly constant over time. B) Two species separated by a spacer (gray dotted line). The gap between the sample zones is determined by the amount of spacer ions. C) Two species separated by a spacer under an oscillating electric field with a DC offset. Their overlap varies with time. The data presented here was obtained in experiments where the intensity distribution of two fluorescent samples focused by ITP was measured. Because of the linear relationship between sample concentration and fluorescence intensity, the concentration distribution directly corresponds to the intensity distribution. The gray dotted line in B) represents the spacer distribution and is only symbolic, since the spacer does not fluoresce and therefore cannot be observed. Reproduced with permission from Anal. Chem. 2024, 96, 11, 4446–4454. Copyright ©2024 American Chemical Society.

6.4 Concept for controlling ITP zones

When two samples are co-focused in two subsequent ITP zones, the overlap of their concentration distributions is determined by their electrophoretic mobilities, as has been discussed in detail by Rubin et al. [41]. If their electrophoretic mobilities are identical, they completely overlap. If they differ, however, the center and width of the respective distributions are not identical, as depicted in Figure 6.1.A. In any case, co-focusing two reactive species in two subsequent ITP zones allows to increase the reaction rate significantly.[‡] However, as soon as two species are co-focused in this way, it is difficult to control the spatial overlap of their distributions and hence the progress of their reaction. Therefore, a new method to control the time-averaged overlap of the concentration profiles of two species, which utilizes a spacer between the two samples and an oscillatory electric field with a DC offset, is suggested.

A spacer zone with ions having an electrophoretic mobility between those of the two samples allows to separate their concentration profiles, see Figure 6.1.B. Here, the spacer distribution is represented by the gray dotted line. The distance between the two sample

[‡]Besides, Rubin et al. have shown that for asymmetric concentration profiles, the optimum reaction rate is not obtained for perfectly overlapping sample distributions [41].

zones is determined by the amount of spacer ions. For comparatively broad spacer zones, the two samples hardly overlap, and hence possible reactions occur only at a low rate.

In the new approach that is presented here, two samples are first focused and separated by a spacer. To do so, a DC electric field is applied as it is usually done in ITP. Then, an oscillatory component with temporal period T is superimposed on the DC field, with an amplitude higher than the DC offset. This yields a time-dependent overlap of the concentration distributions of the two samples, see Figure 6.1.C. At times t_0 and $t_0 + T$, the two samples are barely in contact. By contrast, at $t_0 + T2$, the sample distributions are widened and therefore partially overlap. As will be shown below, by varying the amplitude and frequency of oscillation, the time-averaged overlap can be precisely controlled. To do so, experiments were carried out with two different fluorophores, namely Fluorescein and Alexa Fluor 647 (AF647), being focused in separate sample zones. Besides, experiments are presented that provide insights in the time evolution of the sample distributions under oscillation.

6.5 Experiments and data processing

This section documents the preparation of the LE and TE, including samples and spacers. Next, details on the experimental set-up and parameters are presented. Last, the image processing and the methods to evaluate the sample overlap are explained.

6.5.1 Buffer and sample preparation

A solution of 50 mM HEPES, 100 mM bis-tris methane (Bis-Tris), and 1 % (w/v) PVP (MW 40,000) for suppression of electro-osmotic flow served as TE. Its pH was approximately 7.3. The LE consisted of 100 mM HCl, 200 mM Bis-Tris, 1 % (w/v) PVP, and different amounts of 2-(N-morpholino)ethanesulfonic acid (MES), which focuses between LE and TE as spacer. The pH of the LE was approximately 6.6. The buffers were designed using the CAFES online simulation tool [232]. A first series of experiments was carried out to demonstrate the time evolution of the sample distribution over one period of oscillation. They were done with vanishing spacer concentration and only with AF647. Next, experiments to demonstrate the time evolution of the overlap of two sample distributions were conducted with a spacer concentration of 200 µM and both fluorophores. The last group of experiments served to quantify the influence of the amplitude and frequency of oscillation on the overlap of the sample distributions. Here, the spacer concentration was 500 µM.

Fluorescein sodium salt (Carl Roth) was added to the TE with a concentration of 60 µg/l, Alexa Fluor 647 carboxylic acid, tris(trimethylamonium) salt (Thermofisher) to the LE with a concentration of 150 µg/l. Rather high fluorophore concentrations were chosen to achieve a high signal-to-noise ratio, which allows a better identification of the

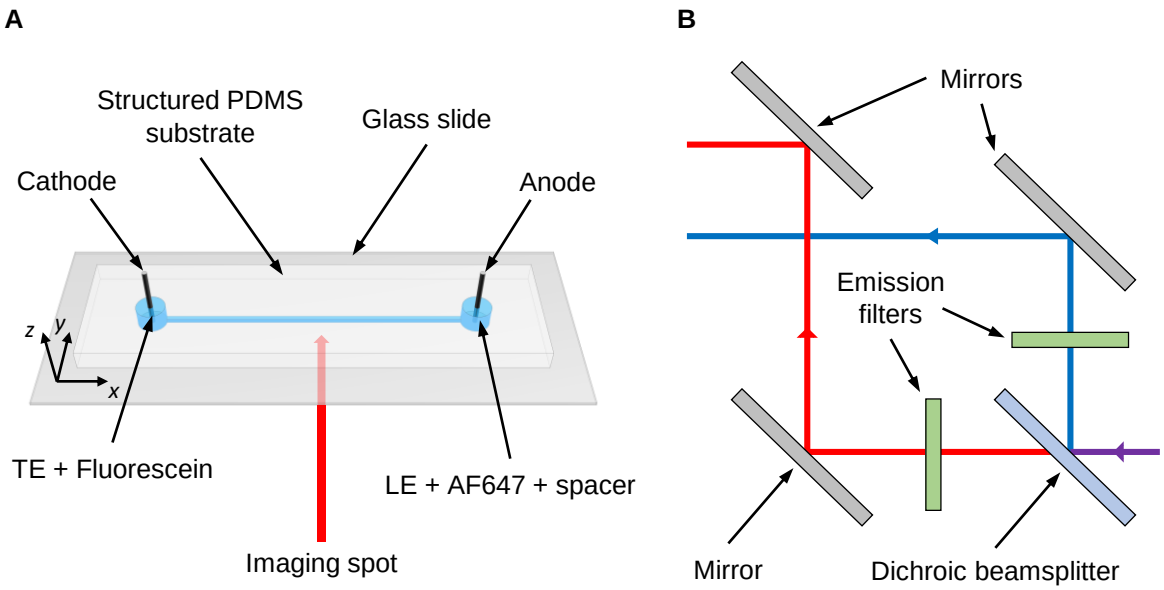

Figure 6.2: Experimental setup used in the experiments on oscillating ITP zones. A) Schematic drawing of the microfluidic device. B) Schematic drawing of the path that the light emitted by the fluorophores takes inside the image splitter. Reproduced with permission from the SI of Anal. Chem. 2024, 96, 11, 4446–4454. Copyright ©2024 American Chemical Society.

sample distributions. Fluorescein was chosen since its electrophoretic mobility shows a rather strong pH dependence [233]. With the specific pH values of TE and LE given above, Fluorescein and AF647 focus behind and in front of the spacer zone, respectively.

6.5.2 Experimental setup and procedure

Simple 20 µm wide, 16 µm deep and 30 mm long microchannels as schematically shown in Figure 6.2 were used for all experiments. They were fabricated according to the protocol explained in Subsection 5.5.2. As shown in Figure 6.2.A, the right reservoir of the microchannel was filled with 20 µl of LE with AF647 and spacer. Using a syringe, a vacuum was created in the left reservoir for 5 s to fill the channel with the mixture. Afterwards, 20 µl of TE with Fluorescein were added to the left reservoir. Then, the microchannel was mounted on the stage of a Nikon Eclipse Ti microscope, and platinum electrodes were placed in the reservoirs.

A 10× Plan Fluor objective (NA = 0.3, Nikon) was used to detect the samples. To excite the fluorophore, the field of view was illuminated with an Intensilight C-HGFI mercury fiber illuminator (Nikon). A triple band filter for FITC, Cy3 and Cy5 to filter the excitation and emission light entering and leaving the microscope, respectively, was used. Besides, an Optosplit image splitter (Cairn Research) was placed between microscope and camera. It uses a dichroic mirror to split the emission light of different wavelengths into two light paths and projects each path on one half of the sensor of the camera. In Figure 6.2.B, the path of the emitted light inside the image splitter is depicted schemat-

ically. Here, a 633 nm dichroic as well as a 525/50 nm and a 700/75 nm emission filter were used. In this way, light with a wavelength of 525 nm was projected on the upper half of the sensor, and light of 700 nm on the lower half. Thereby, it was possible to observe both samples simultaneously but spatially separated with only one camera without color sensor. All images were recorded with an Andor iXon+ 897 EMCCD camera. The exposure time was 23 ms, and the frame rate was 40 fps. The positioning of the optical setup relative to the microfluidic chip is indicated with a red arrow in Figure 6.2.A.

6.5.3 Voltage settings

All experiments were controlled and monitored *via* LabVIEW. To start an experiment, a voltage of 500 V was applied between the electrodes with a HVS448 6000 D high voltage sequencer (Labsmith). After 40 s of preconcentration, LabVIEW set the voltage to a) an oscillating voltage with a DC offset or b) to a constant voltage. 5 s after the preconcentration phase had ended, the image acquisition was started manually in Nikon's NIS Elements software.

In experiments with an oscillating electring field, a time-dependent voltage

$$U(t) = A\sin(2\pi ft) + U_{DC} \tag{6.1}$$

was applied after the preconcentration phase. The amplitude A was set to either 1000, 1500, 2000 or 2500 V. The frequency f was set to values of 0.5, 1, 2, or 4 Hz, respectively. The DC offset U_{DC}, which was set to 500 V, results in a sample migration along the channel (positive x direction, see also Figure 6.2.A) with a decreasing speed over time. However, the speed is quasi-constant during the time of observation. In addition, some experiments with a rectangular instead of a sinusoidal waveform were carried out. If not explicitly stated otherwise, all results presented below were obtained with a sinusoidal waveform. For reference, experiments without an oscillatory electric field component were conducted. In these experiments, a constant voltage of $U_{DC} = 500$ V or $U_{DC} = 100$ V was applied after the preconcentration phase.

6.5.4 Image processing

All image data was processed and evaluated using the programming language Python. In a first step, the full images were split in an upper and a lower half containing the fluorescence signals originating from wavelengths of 525 nm and 700 nm, respectively. In the experiments using only AF647, the upper half of the image was discarded. Next, each half was cropped to the width of the microchannel. Then, the background fluorescence was removed and a flatfield correction was carried out to compensate for inhomogeneous illumination of the images.

As a result, two data arrays $I_{FL}(x, y, n)$ and $I_{AF}(x, y, n)$ containing the intensity distributions of the Fluorescein and AF647 samples, respectively, were obtained. Here, x and y are the coordinates in a frame-of-reference attached to the bottom left corner of an image, and n is the image number, corresponding to the time when an image was taken. For demonstration purposes, the data sets were averaged along the y-axis to obtain $I_{Y,FL}(x, n)$ and $I_{Y,AF}(x, n)$. Again, for experiments in which only AF647 is used, only one data array $I_{Y,AF}(x, n)$ was obtained.

6.5.5 Quantifying the spatial overlap of the intensity distributions of the two fluorophores

Since the fluorescence data is superposed by noise, it was smoothed by fitting a function of the form

$$F(x) = \alpha \exp\left(-\left(\frac{x-\beta}{\gamma}\right)^2\right)\left(1 - \operatorname{erf}\left(\delta\left(\frac{x-\beta}{\gamma}\right)\right)\right) + \epsilon \tag{6.2}$$

(similar to Equation 5.4) to each row (along the y coordinate) of the two data arrays $I_{FL}(x, y, n)$ and $I_{AF}(x, y, n)$. The parameters α, β, γ, and δ represent the amplitude, position of the center, width, and skew of the sample distribution, respectively. In addition, ϵ accounts for an offset that results from a residue of background fluorescence. It was subtracted from the fitted data. The result of this operation are two sets of smoothed data that will be referred to as $\tilde{I}_{FL}(x, y, n)$ and $\tilde{I}_{AF}(x, y, n)$, respectively. This smoothing step also eliminates unwanted intensity peaks caused by crosstalk of fluorescence emission or by contaminating ions, as described in Subsection C.1 in the Appendix.

Next, the two sets of smoothed data were multiplied elementwise according to

$$R(x, y, n) = \tilde{I}_{FL}(x, y, n)\tilde{I}_{AF}(x, y, n). \tag{6.3}$$

In this way, the 2D intensity distributions of the two samples for different points in time were multiplied. The letter R was chosen as a reference to the reaction rate, which is, for second-order reactions between two species, proportional to the product of the reactant concentrations. To obtain a measure for the spatial overlap of the sample distributions or an indicator for the total reaction rate, R was summed over x and y:

$$R_{X,Y}(n) = \sum_{x=1}^{X}\sum_{y=1}^{Y} R(x, y, n). \tag{6.4}$$

Here, X and Y are the total number of pixels in the x and y direction, respectively. Their values are $X = 512$ and $Y = 10$. Subsequently, a time-average of $R_{X,Y}$ was calculated by

$$\bar{R} = \frac{1}{N} \sum_{n=1}^{N} R_{X,Y}(n), \tag{6.5}$$

where N is the number of images recorded during one period of oscillation (i.e. $N = 80$ for $f = 0.5\,\mathrm{Hz}$, $N = 40$ for $f = 1\,\mathrm{Hz}$, etc. with a frame rate of 40 fps). For the reference case without oscillation, $N = 10$ was chosen. All values of $\bar{R}$ were then normalized with $\bar{R}_{ref}$, which is an average $\bar{R}$ obtained from five experiments with $U_{DC} = 500\,\mathrm{V}$ and without oscillation, i.e. $A = 0\,\mathrm{V}$:

$$R^* = \frac{\bar{R}}{\bar{R}_{ref}}. \tag{6.6}$$

6.6 Results and discussion

In the following, the experimental results are presented. First, spatiotemporal plots show how oscillating ITP zones propagate through a microchannel. Then, the time-evolution of the sample distribution of a single sample focused between LE and TE is evaluated. In the following two subsections, the focus is on both the time-dependent and the time-averaged overlap of two oscillating sample zones separated by a spacer. This section ends with some remarks on the possibilities to control the overlap by simply adjusting a DC electric field without an oscillatory component.

6.6.1 Spatiotemporal propagation of an oscillating ITP zone

In a first step, only one single sample, namely AF647 focused between LE and TE, was considered. By representing the intensity distribution $I_Y(x, n)$ as a colormap, spatiotemporal plots of the propagation of the sample zone were obtained, as depicted in Figure 6.3. Note that the image number n directly corresponds to the time t *via* $n = tf_{\mathrm{im}}$ with the frame rate f_{im}. The first subfigure shows the reference case of ITP with $U_{DC} = 500\,\mathrm{V}$ and $A = 0\,\mathrm{V}$. Here, the sample velocity is almost constant over the time of observation. The fluorescence intensity of the sample zone decreases slightly from the left to the right. This is most likely an artifact of an imperfect flatfield correction.

Subfigures B to D show the propagation of an oscillating sample zone with different values of amplitude A and frequency f. Due to the DC offset, the sample is still transported through the channel with an on-average constant velocity. However, the position of the sample zone oscillates around an imaginary diagonal line that coincides with the trace visible in Figure 6.3.A. The phase where the sample moves faster (more slowly) than the average sample velocity will be referred to as the advancing (receding) phase. While oscillating, the width of the sample zone changes continuously. The plots in Figure 6.3

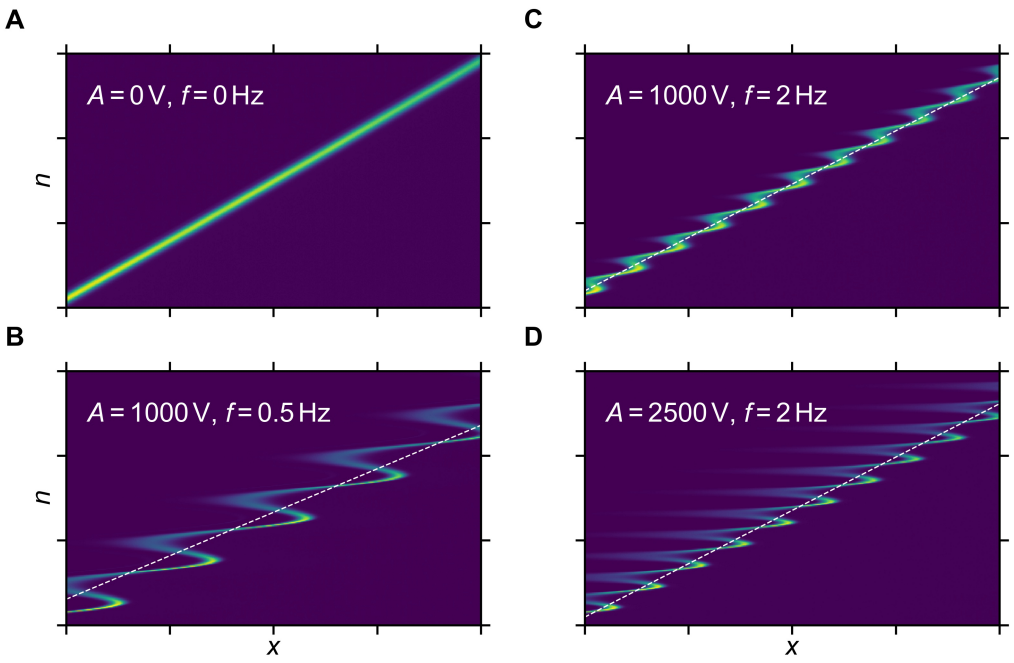

Figure 6.3: Spatiotemporal plot of the propagation of a single sample zone with AF647 driven by an oscillating electric field with sinusoidal waveform. In A), the sample was transported using a DC electric field. In B) to D), an oscillatory component was superimposed on the DC field. The dashed white line represents the imaginary trajectory around which the sample zone oscillates. The scaling of both abscissa and ordinate is the same in every plot. Reproduced with permission from Anal. Chem. 2024, 96, 11, 4446–4454. Copyright ©2024 American Chemical Society.

already indicate that the displacement from the diagonal line and the broadening of the sample distributions significantly depend on the parameters of oscillation: the higher A and the lower f, the more pronounced the displacement and the broadening of the sample.

Four combinations of A and f were tested together with a rectangular waveform in experiments with Fluorescein and AF647 separated by a spacer. The spatiotemporal plots of this variant are shown in Figure 6.4. The plots depict the propagation of AF647 focused between LE and spacer. As expected, the rectangular waveform leads to a sharp transition between phases where the sample zone moves in the positive x direction and phases where it moves in the negative x direction. Again, the frequency and amplitude of oscillation of the electric field determine the displacement and broadening of the sample peak.

6.6.2 Development of the sample distribution over time

A detailed representation of the development of the sample distribution over one period of oscillation is given in Figure 6.5. The combinations of A and f are the same as in Figure 6.3. Each column in the figure shows one combination, whereas each row represents a different point in time. The starting point t_0 marks the transition between receding and

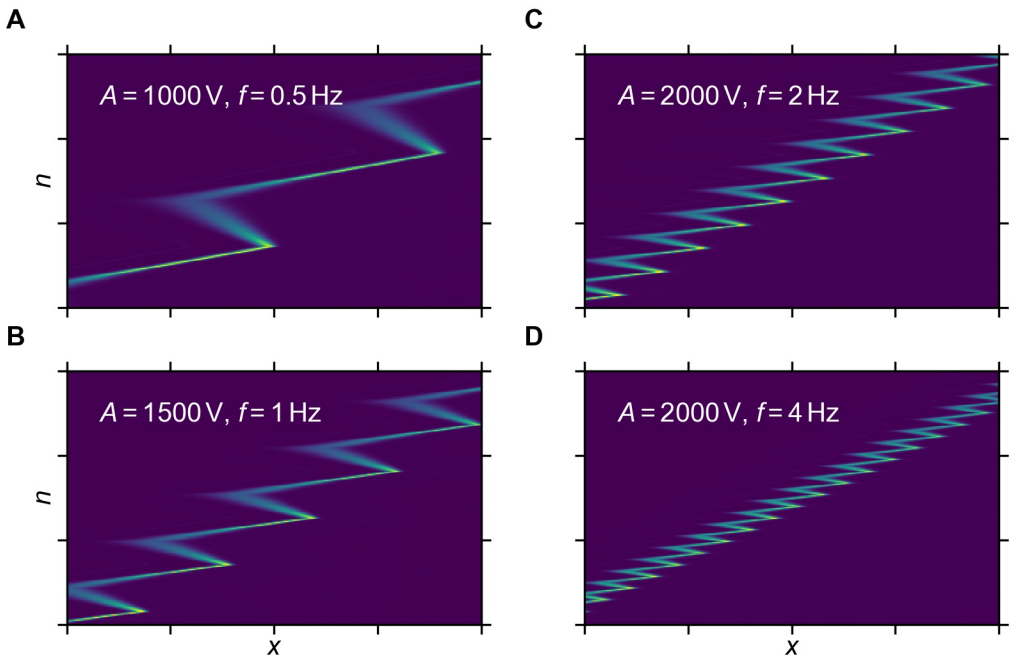

Figure 6.4: Spatiotemporal plot of the propagation of a single sample zone with AF647 driven by an oscillating electric field with rectangular waveform. The scaling of both abscissa and ordinate is the same in every plot. Reproduced with permission from the SI of Anal. Chem. 2024, 96, 11, 4446–4454. Copyright ©2024 American Chemical Society.

advancing phase. In Figure 6.5, the quasi-constant velocity caused by the DC offset was subtracted. In other words, the sample distributions are shown in a frame-of-reference moving with the average sample velocity. The coordinate $\bar{x}$ on the abscissa represents the distance from the origin of the corresponding coordinate system along the x-axis.

At $t_0+T/4$, the sample zone is at its maximum displacement in the positive $\bar{x}$ direction. Only with $A = 2500\,\mathrm{V}$ and $f = 2\,\mathrm{Hz}$ it is narrower than at t_0. For the other two parameter combinations, the width and height of the peak are not significantly different. Between $t_0 + T/4$ and $t_0 + 3T/4$, the displacement of the sample distribution relative to $\bar{x} = 0$ decreases. The maximum displacement in the negative $\bar{x}$ direction is reached at $t_0+3T/4$. During the receding phase, the zone broadens. However, its maximum width is reached before $t_0+3T/4$, see below. From $t_0+3T/4$ on, the zone is shifted in the positive $\bar{x}$ direction again. At $t_0 + T$, it is more or less of the same shape and at the same position $\bar{x}$ as at t_0. The sample distribution at $t_0 + T/2$ differs from that at the beginning and end of the period, both in displacement and width. Therefore, the phase where the sample is shifted in positive $\bar{x}$ direction is not simply an inversion of the phase where it is shifted in the negative $\bar{x}$ direction. This is due to the fact that during the advancing phase, the sample zone is compressed, whereas it is broadened during the receding phase. In addition, when the electric field is inverted, the sample is dispersed due to electromigration dispersion, see below.

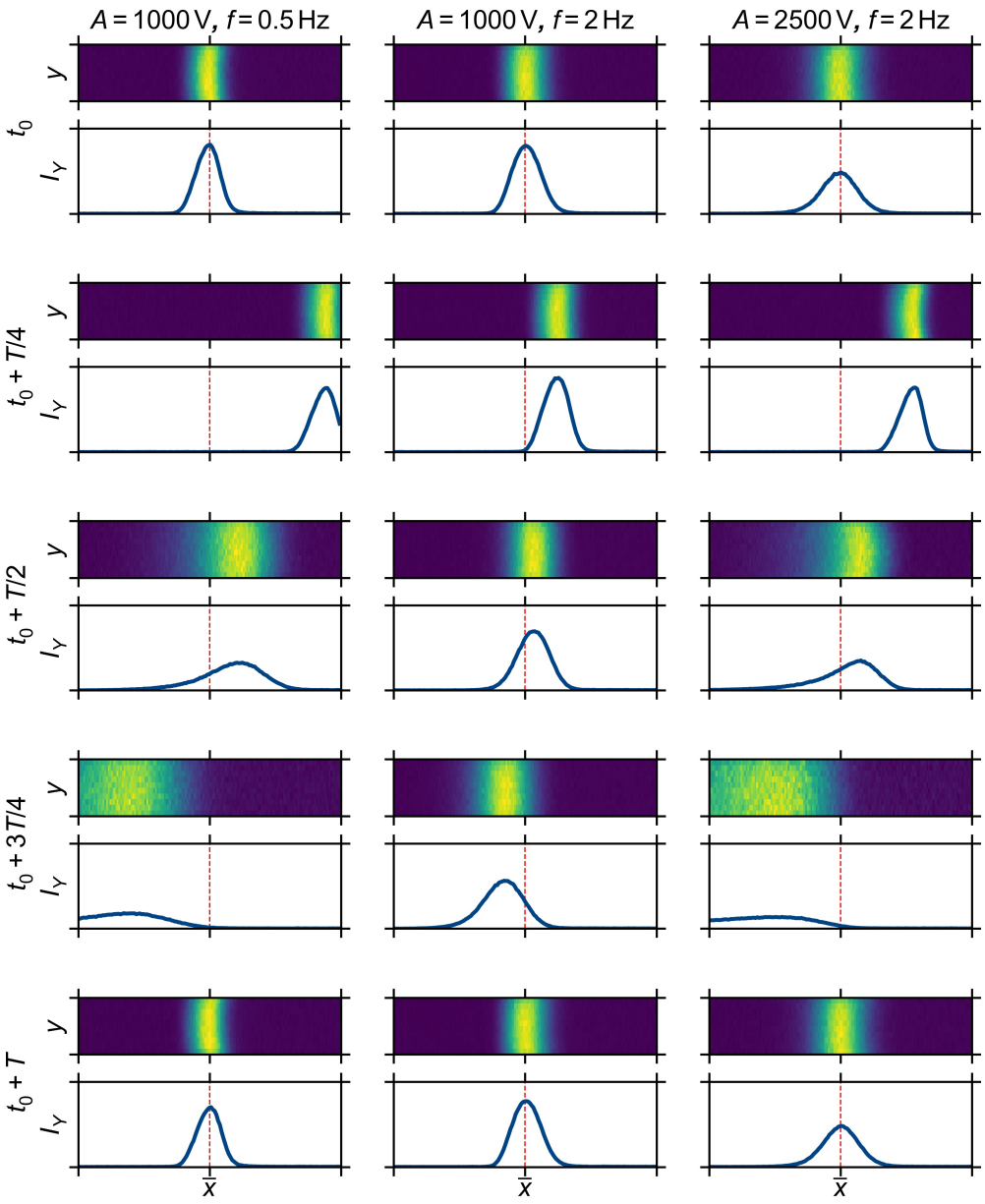

Figure 6.5: Oscillation of a single sample zone (AF647) shown in a frame of reference moving with constant velocity over one period of oscillation. Each column represents a different combination of amplitude A and frequency f of the oscillatory component of the applied electric field. Each row represents a different point in time. The first plot for each combination of A, f and t shows the 2D intensity distributions of AF647, the second one the same intensity distributions averaged along the y-axis. The scaling of the abscissa is the same for every plot. Besides, in all I_Y plots, the scaling of the ordinate is the same. Reproduced with permission from Anal. Chem. 2024, 96, 11, 4446–4454. Copyright ©2024 American Chemical Society.

Fundamentally, the displacement and broadening (or narrowing) of the sample zone could also be achieved if the amplitude of oscillation was lower than or equal to U_{DC}. However, $A > U_{DC}$ is important if the goal is to increase the time-averaged overlap of two sample distributions separated by a spacer. When $U(t) < 0$, the direction of the electric field is inverted and electromigration dispersion occurs. In the literature on capillary zone electrophoresis (CZE), electromigration dispersion is a well-described phenomenon [234–

238]. CZE is used to separate charged analytes based on their electrophoretic mobility. Driven by an electric field, each analyte migrates in its own analyte zone. If its concentration is high enough, the electrical conductivity of the background electrolyte is affected. As a consequence, there is a locally inhomogeneous electric field, leading to dispersion of the analyte zone. Ramachandran and Santiago transfer the concept of electromigration dispersion to ITP [11]: The high-mobility anions of the LE migrate towards the TE (or spacer) zone and quickly invade it. On the other hand, the low-mobility anions of the TE penetrate into the region originally occupied by LE (or spacer). Consequently, TE and LE (and spacer) are mixed. This also leads to a heavy broadening of the sample zones.

In addition to electromigration dispersion, other dispersion mechanisms can occur. Some of the 2D sample distributions in Figure 6.5 show a slight curvature, see for example the plot for $A = 1000\,\mathrm{V}$ and $f = 0.5\,\mathrm{Hz}$ at t_0. This might be caused by residual EOF or minor pressure differences between the reservoirs. As a consequence, the intensity distribution is slightly inhomogeneous in the y direction.[§] Therefore, the overlap is calculated by multiplying the 2D intensity distributions $I(x, y, n)$ instead of the averaged intensity distributions $I_Y(x, n)$. In the following, however, it is assumed that there are no major deviations in the z direction. This must be kept in mind for all quantitative arguments that are presented.

An example of the quantitative development of the width, the height, and the center position of the sample peak over one period of oscillation is presented in Figure 6.6 for $A = 1000\,\mathrm{V}$ and $f = 0.5\,\mathrm{Hz}$. Figure 6.6.A shows the progression of the sample by plotting the position of the maximum (the center position) of its intensity distribution over time. Between $t_0 + T/4$ and $t_0 + T/2$, the curve has a local maximum, between $t_0 + T/2$ and $t_0 + 3T/4$ a local minimum. In Figure 6.6.B, the quasi-constant velocity component caused by the DC offset has been subtracted. Hence, the position of the intensity maximum is plotted in a frame-of-reference moving with a constant velocity. The local maximum and minimum in Figure 6.6.A have therefore been shifted slightly to the left and right, respectively, and are now an absolute maximum and minimum, respectively. In Figure 6.6.C, the development of the width and the maximum value of the intensity distribution over time are shown. The width has been derived from the intensity distribution by fitting a function of the form of equation 2 of the main text to it. Here, γ^* is computed by normalizing the values of the width parameter γ of the fit function with its value at t_0. The width stays constant until approximately $t_0 + 3T/8$, where the local maximum in Figure 6.6.A is found. Then it increases continuously until

[§]More pronounced inhomogeneities were observed in preliminary tests on ITP with oscillating sample zones in capillaries with a width of 100 µm and a height of 20 µm. In those experiments, the sample distribution was highly asymetric with respect to the center line of the channel above certain threshold values for both amplitude and frequency of oscillation. This suggests that depending on the channel geometry, additional dispersion mechanisms may occur that were not further examined at that time. As a consequence, however, the channel width was reduced to 20 µm, which helped to mitigate those dispersion effects that cause inhomogeneities along the y-axis.

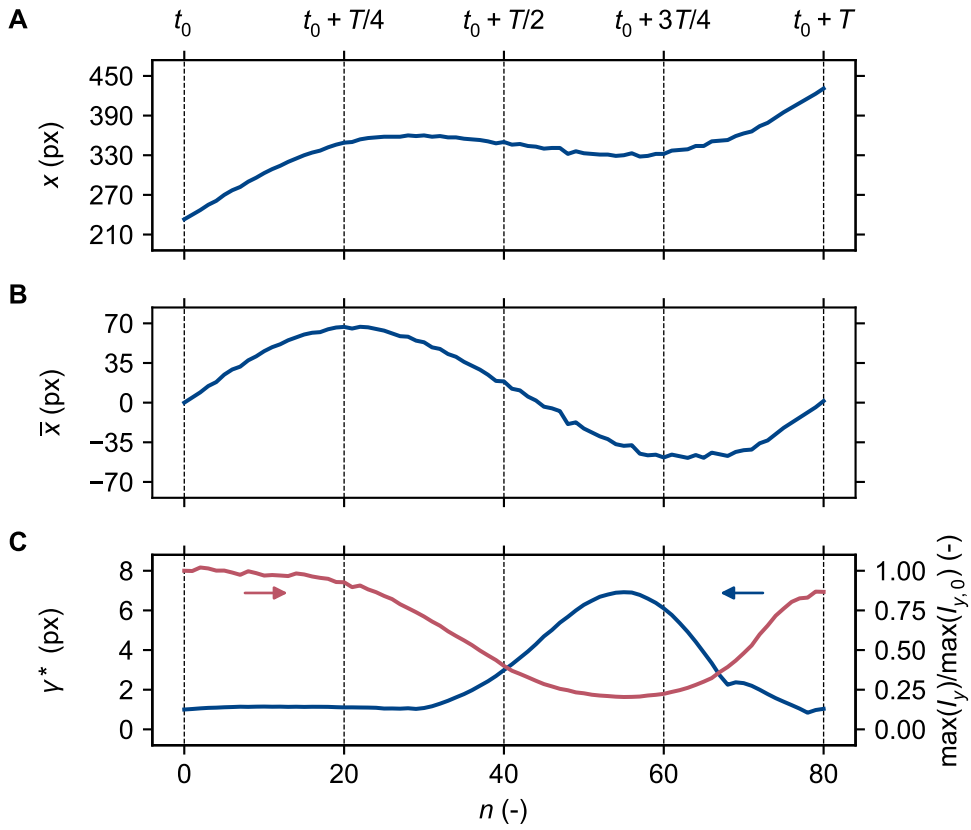

Figure 6.6: Development of the width and maximum value of the intensity distribution of AF647 focused between TE and LE, with $A = 1000\,\mathrm{V}$ and $f = 0.5\,\mathrm{Hz}$. A) shows the position of the center of the averaged intensity distribution I_Y over time. B) shows the position of the center of the averaged intensity distribution over time after subtracting the quasi-constant velocity component caused by the DC offset of the electric field. C) shows the normalized width γ^* and maximum value of the averaged intensity distribution I_Y over one period of oscillation. Both the width and the maximum value were normalized with the value at the beginning of the period. The red and blue arrows indicate the y-axis corresponding to the red and blue curve, respectively. Reproduced with permission from the SI of Anal. Chem. 2024, 96, 11, 4446–4454. Copyright ©2024 American Chemical Society.

it reaches its maximum between $t_0 + T/2$ and $t_0 + 3T/4$. This maximum occurs roughly at the same time as the local minimum in Figure 6.6.A. Afterwards, γ^* decreases again and eventually takes approximately the same value as at the beginning of the period of oscillation. The maximum value of the intensity distribution develops more or less in the opposite way. It is roughly constant during most of the first quarter of the oscillation. Then it decreases continuously and reaches a minimum. The minimum approximately coincides with the maximum of γ^*. During the last quarter of the oscillation, it increases again and finally is of approximately the same value as at the beginning. Note that again, each maximum value has been normalized with the one obtained at t_0.

6.6.3 Development of the spatial overlap over time

In analogy to Figure 6.5, Figure 6.7 shows the oscillation of two sample zones separated by a spacer (initial concentration of 200 µM) during one period of oscillation. Here, however, the velocity component caused by the DC offset of the electric field was not subtracted. Hence, the net migration of the samples in positive x direction can be observed. For all considered values of A and f, the distance between the centers of the sample distributions of AF647 and Fluorescein does not change significantly over time. At $t_0 + T/2$ and $t_0 + 3T/4$, an increased overlap of the intensity distributions of AF647 and Fluorescein can clearly be observed, which is caused by the broadening of the sample zones. Compared to $A = 1000\,\mathrm{V}$ and $f = 2\,\mathrm{Hz}$ (center column), both lowering the frequency (left column) and increasing the amplitude (right column) of oscillation lead to an improved mixing at these points in time.

To quantify the development of the spatial overlap, i.e. the mixing of the two samples over one period of oscillation, experiments with an initial spacer concentration of 500 µM and a large variety of values for A and f were conducted. In Figure 6.8, only a limited number of combinations of A and f is displayed. For a larger variety of parameter combinations, the reader is referred to Subsection C.2 in the Appendix. Figure 6.8.A shows the reference case without oscillation. As expected, $R_{X,Y}$ stays constantly close to zero. Note that the data points represent the average from five experiments, the error bars indicate the corresponding standard deviation. For reasons of comparability, the image number n has been normalized with the total number of images N that were acquired during one period of oscillation. Subfigures B to D show $R_{X,Y}$ for different oscillation parameters. Independent of A and f, $R_{X,Y}$ is close to zero during a large part of the oscillation period. All plots show a clear peak around $n^* \approx 0.75$, indicating a temporary increase in sample overlap. The amplitude of the peaks in subfigures B to D is clearly related to the amplitude and frequency of oscillation, confirming the previous observations: The higher A and the lower f, the more pronounced is the overlap represented by $R_{X,Y}$ and hence the mixing of the two species.

In Figures 6.7 and 6.8, the development of the overlap of the sample distributions of AF647 and Fluorescein over time is investigated both on a qualitative and a quantitative level. However, the relation between the different phases of oscillation and the overlap is not shown in detail. Instead, this relation is illustrated in Figure 6.9. First, Figure 6.9.A shows the center position of the intensity distributions of Fluorescein (red curve) and AF647 (blue curve) over one period of oscillation with $A = 1000\,\mathrm{V}$ and $f = 0.5\,\mathrm{Hz}$. Most of the time, the two curves are parallel, i.e. Fluorescein and AF647 anions are transported with the same velocity. However, between $t_0 + T/2$ and $t_0 + 3T/4$, the gap between the two curves increases. Figure 6.9.B, where the quasi-constant velocity caused by the DC offset of the electric field has again been subtracted, supports this observation. During this time interval, Fluorescein is first displaced from $\bar{x}$ more strongly. But then, the gap

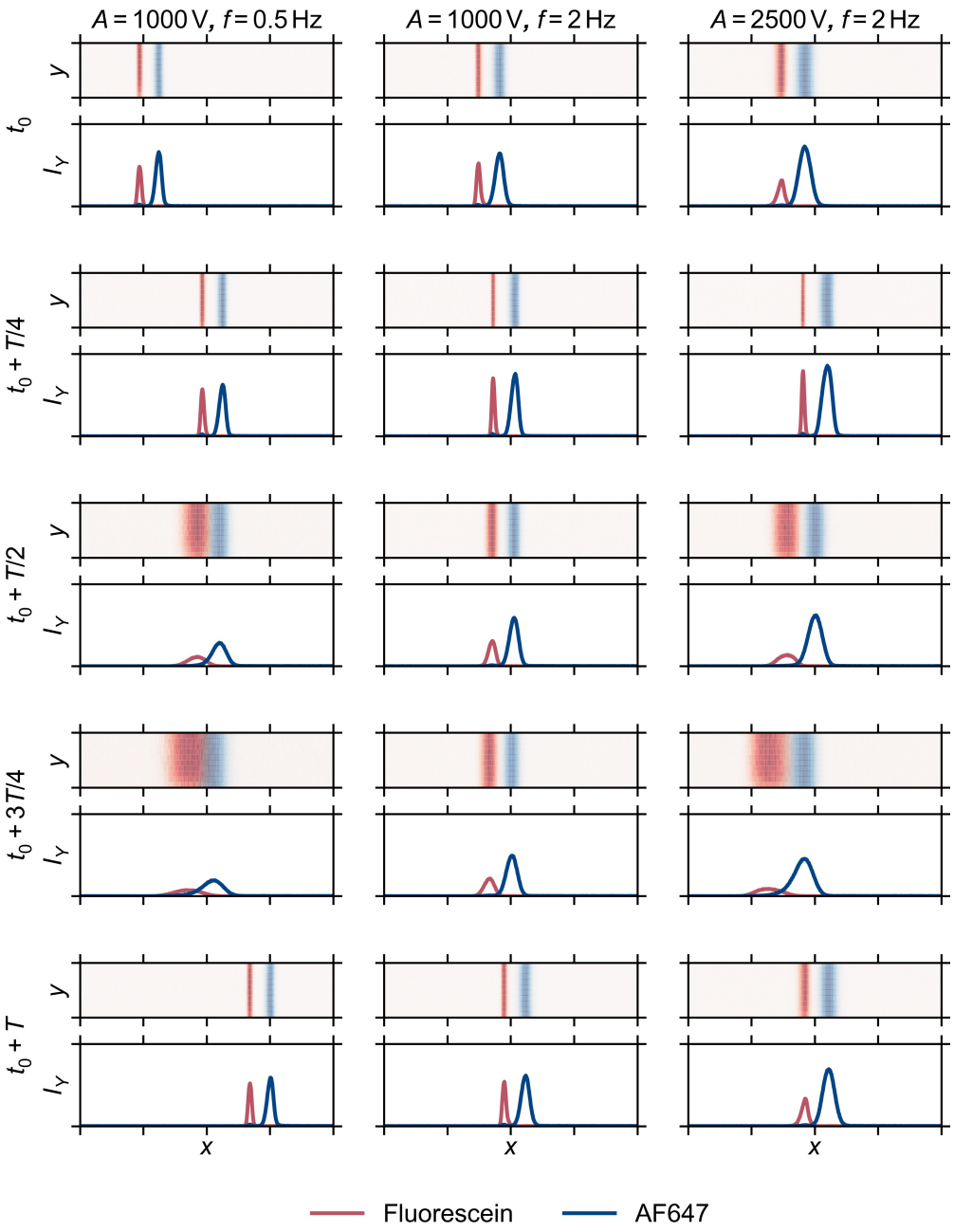

Figure 6.7: Overlap of two sample zones over one period of oscillation. Each column represents a different combination of amplitude A and frequency f of the oscillatory component of the applied electric field. Each row represents a different point in time. The first plot for each combination of A, f and t shows the 2D intensity distributions of both Fluorescein and AF647, the second one the same intensity distributions averaged along the y-axis. The scaling of the abscissa is the same for every plot. Besides, in all I_Y plots, the scaling of the ordinate is the same. Reproduced with permission from Anal. Chem. 2024, 96, 11, 4446–4454. Copyright ©2024 American Chemical Society.

between the two peaks shrinks until the two curves are parallel again. This observation was repeatedly made for different values of A and f. However, without a detailed analysis of the spatiotemporal evolution of the electric field, this phenomenon is difficult to explain.

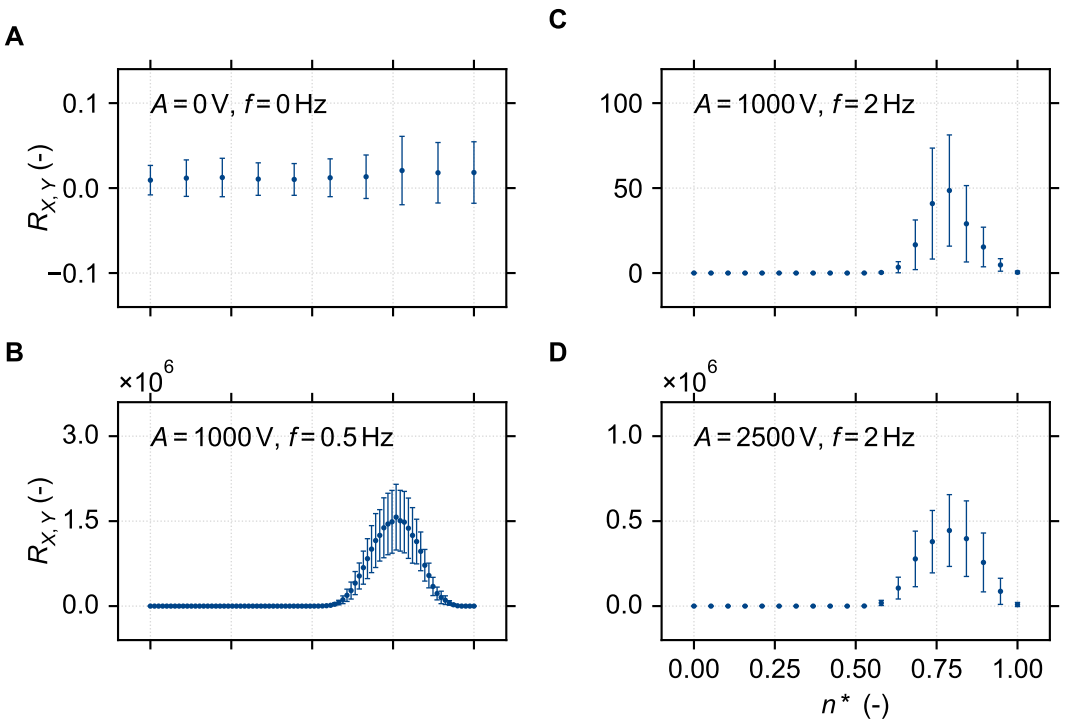

Figure 6.8: Overlap of the intensity distributions of two samples over one oscillation period for varying amplitude and frequency. $R_{X,Y}$ is the product of the smoothed 2D intensity distributions of AF647 and Fluorescein, integrated over x and y, n^* is the image number n normalized with the total number of images N that were acquired during one period of oscillation. The data points represent the average from five experiments, the error bars indicate the corresponding standard deviation. Note that the y-axis is scaled differently in each subfigure. Reproduced with permission from Anal. Chem. 2024, 96, 11, 4446–4454. Copyright ©2024 American Chemical Society.

Interestingly, the overlap of the two sample distributions, measured by $R_{X,Y}$, is maximal when their center-to-center distance is greatest. It is concluded that the broadening of the sample distributions, which should also be at its maximum at this point according to Figure 6.6, compensates for the growing distance. During those phases where the distance between the two zones stays roughly constant, the overlap of the intensity distributions is close to zero.

Figure 6.10 shows $R_{X,Y}$ over n^* with a rectangular oscillation waveform. Here, the transition between increasing and decreasing values of $R_{X,Y}$ is much sharper than with a sinusoidal waveform. Besides, the standard deviations are lower than with a sinusoidal waveform. Just as with a sinusoidal waveform, $R_{X,Y}$ increases with increasing amplitude and decreasing frequency of oscillation. Comparing Figures 6.10 and C.10 (Appendix), it becomes obvious that for the same combinations of A and f, the peak of $R_{X,Y}$ is higher with a rectangular waveform than with a sinusoidal one.

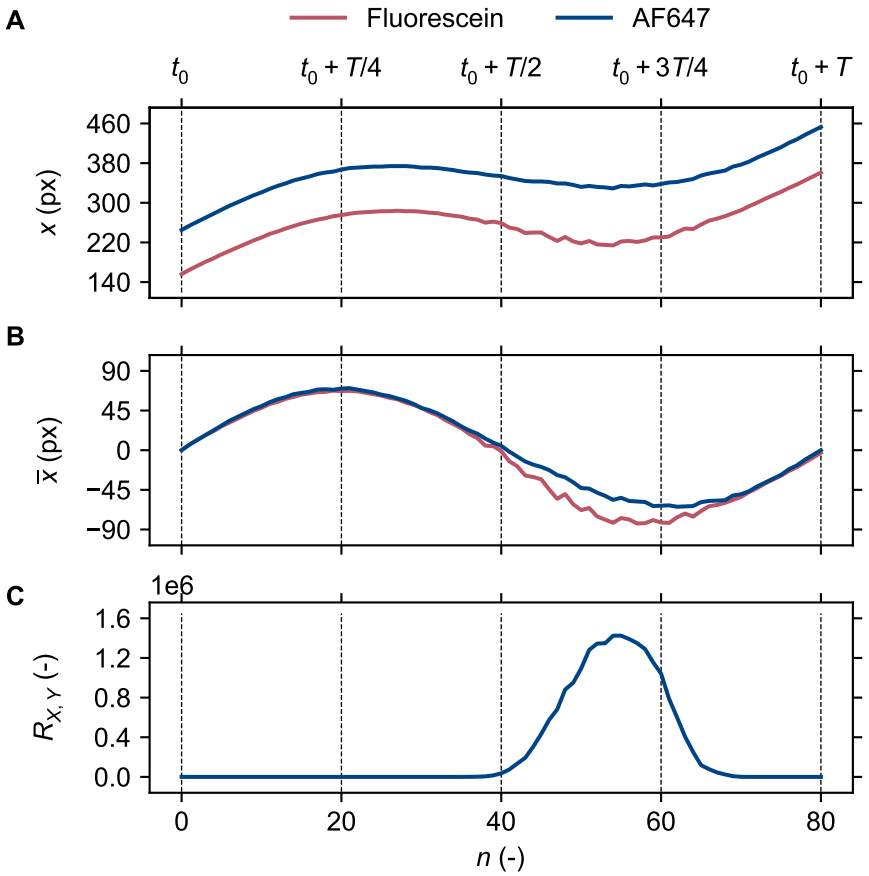

Figure 6.9: Development of the spatial overlap of the AF647 and Fluorescein intensity profiles over time during one period of oscillation with $A = 1000\,\mathrm{V}$ and $f = 0.5\,\mathrm{Hz}$. A) shows the position of the centers of the two intensity distributions over time. B) shows the same after subtracting the constant velocity caused by the DC offset of the electric field. C) shows the overlap of the intensity distributions of the two samples over one period of oscillation. Reproduced with permission from the SI of Anal. Chem. 2024, 96, 11, 4446–4454. Copyright ©2024 American Chemical Society.

6.6.4 Time-averaged overlap for different oscillation parameters

In a last step, the time-averaged, normalized overlap R^* is evaluated. Figure 6.11.A shows R^* for every combination of A and f that has been tested with a sinusoidal waveform. Combinations of $f = 0.5\,\mathrm{Hz}$ with $A = 2000\,\mathrm{V}$ and $A = 2500\,\mathrm{V}$, respectively, have not been tested since the field of view was not wide enough to cover one complete period of oscillation. Each data point represents the mean value from five experiments together with the corresponding standard deviation, indicated by error bars. The plot shows two clear trends. First, for a fixed value of f, R^* increases with A. Second, for a fixed value of A, R^* increases with decreasing f. This is in good agreement with the results presented before. The error bars tend to increase with f. This has a simple explanation: The higher f, the fewer images can be acquired during one oscillation period. Fewer images

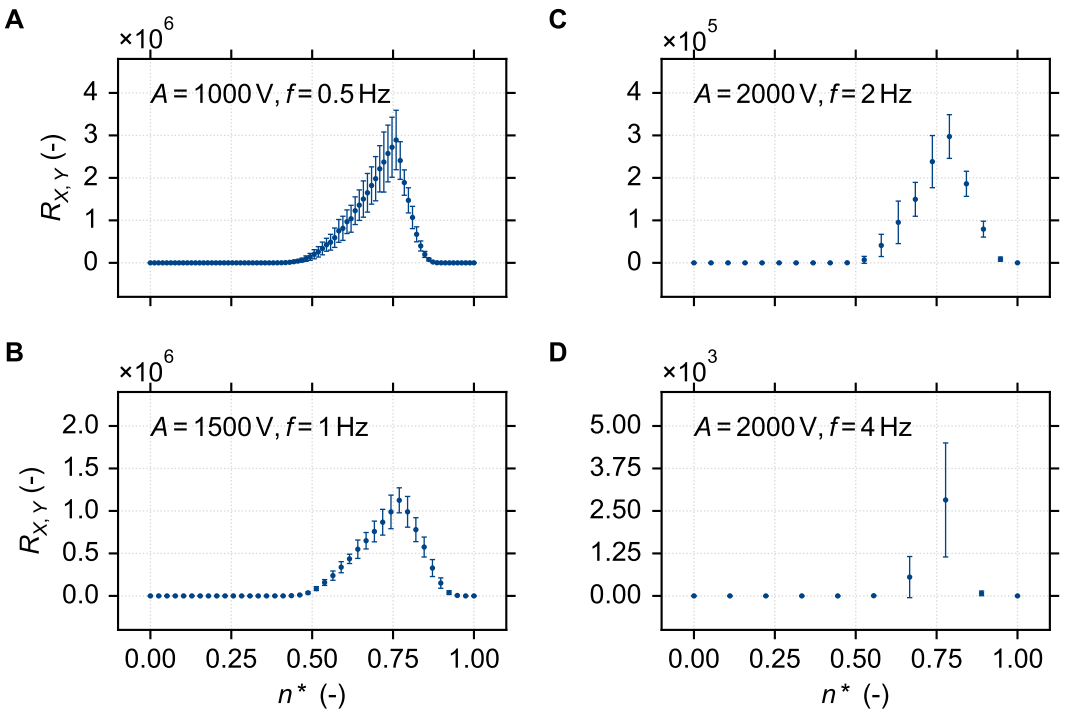

Figure 6.10: Overlap of the intensity distributions of the two samples over one period of oscillation for different amplitudes and frequencies, based on a rectangular oscillation waveform. The data points represent the average from five experiments, the error bars indicate the corresponding standard deviation. Note that the y-axis is scaled differently in each subfigure. Reproduced with permission from the SI of Anal. Chem. 2024, 96, 11, 4446–4454. Copyright ©2024 American Chemical Society.

per oscillation directly lead to a less accurate observation of the overlap of the two sample distributions over time.

In Figure 6.11.B, R^* is plotted over A/f. The blue data points are the same as in Figure 6.11.A. Additional data obtained with a rectangular waveform of oscillation is shown in red. The data points obtained with a sinusoidal waveform collapse on one curve, indicating that the time-averaged overlap only depends on the parameter combination A/f. The mean value of R^* strictly increases with A/f. However, the last two data points suggest that R^* could reach a plateau for $A/f > 3\,\mathrm{kVs}$. The data points obtained with a rectangular waveform show a similar trend. At $A/f = 0.5\,\mathrm{kVs}$, R^* is approximately one order of magnitude higher than with a sinusoidal waveform. However, for larger values of A/f, the data points corresponding to the two waveforms approach each other.

The results shown in Figure 6.11 indicate that the time-averaged product of two sample concentrations can be tuned over several orders of magnitude. Translating the sample overlap to a chemical reaction rate, this suggests that the proposed scheme offers far-reaching options to control the progress of a chemical reaction occurring between two samples focused by ITP.

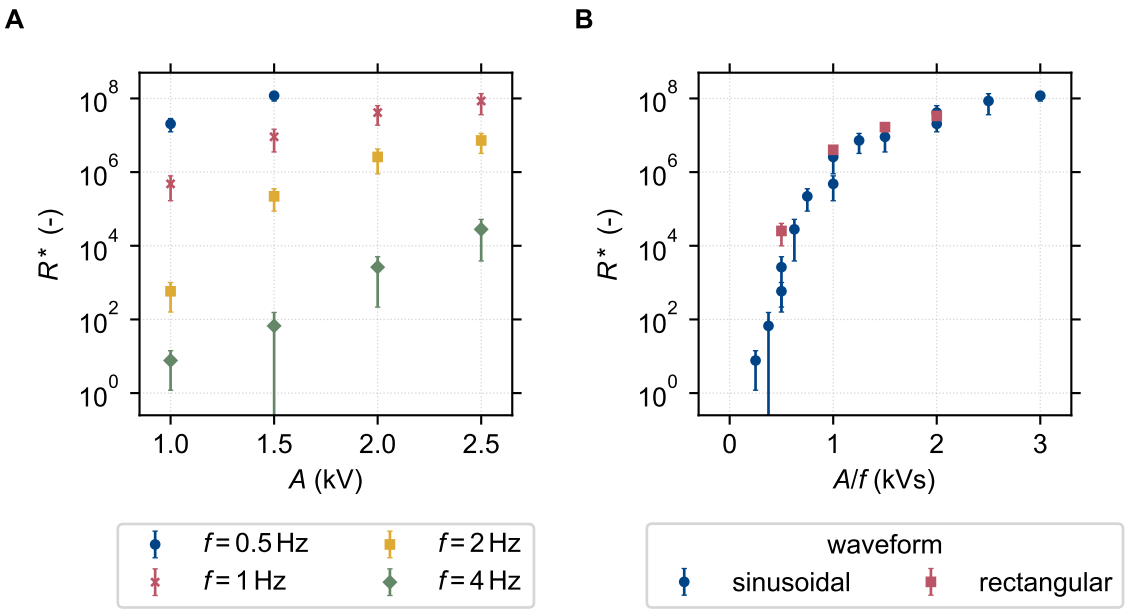

Figure 6.11: Time-averaged and normalized overlap of the intensity distributions of the two samples. A) R^* for different values of A and f, where the oscillatory component of the electric field has a sinusoidal waveform. B) R^* as a function of A/f. Blue (red) data points represent a sinusoidal (rectangular) waveform of the oscillatory electric field component. For $A = 1.5\,\text{kV}$ and $f = 4\,\text{Hz}$ ($A/f = 0.375\,\text{kVs}$), the standard deviation is higher than the mean value. Reproduced with permission from Anal. Chem. 2024, 96, 11, 4446–4454. Copyright ©2024 American Chemical Society.

6.6.5 Creating overlap with a DC voltage

The width of a sample zone in ITP strongly depends on the applied electric field strength. Higher field strengths lead to narrower sample zones and *vice versa*. Therefore, a simple way to deliberately broaden two ITP sample zones and hence to increase their overlap is to work with a tunable DC voltage without AC component. To prove this, experiments were conducted where the samples were first preconcentrated with a constant voltage of 500 V for 40 s. Then, the voltage was lowered to a constant value of 100 V. The result can be seen in Figure 6.12. Figure 6.12.A shows the averaged intensity distributions of Fluorescein and AF647 transported with a constant voltage of 500 V without oscillation, which is the reference case for all experiments. By contrast, Figure 6.12.B shows what happens when the voltage is lowered. The distance between the centers of the peaks is roughly the same in both plots. However, in Figure 6.12, the peaks are significantly wider. In this way, the overlap of the sample distributions is increased. With this configuration, an average R^* of $1.01 \cdot 10^8$ is obtained, which is of the same order of magnitude as the value obtained with a sinusoidal oscillation and $A/f = 3\,\text{kVs}$. Therefore, high values of R^* can also be obtained simply by lowering U_{DC} and without any oscillation. Correspondingly, increasing U_{DC} goes along with a reduction of R^*. While solely working with a tunable DC voltage to control the sample overlap and thus the progress of chemical reactions may

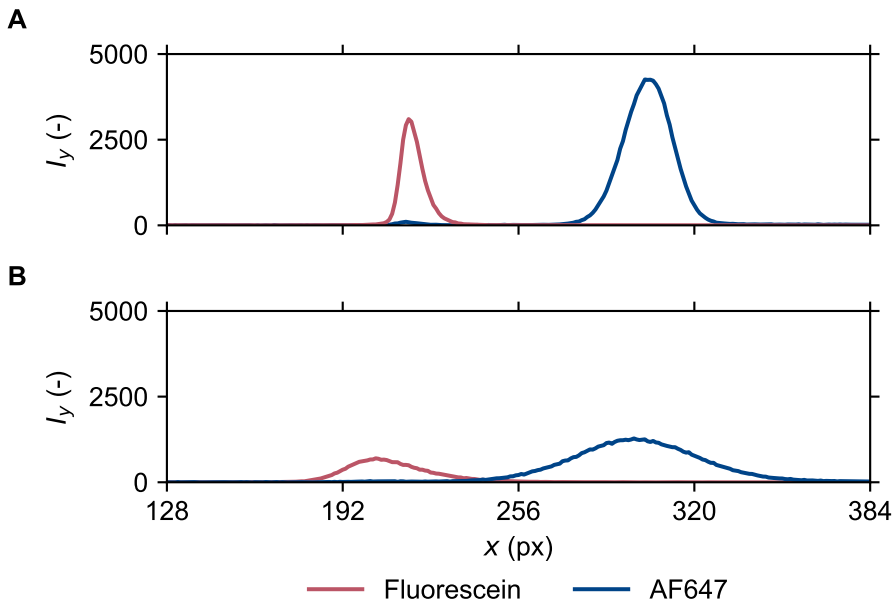

Figure 6.12: Overlap of averaged Fluorescein and AF647 intensity profiles with a spacer concentration of 500 µM and a DC voltage of A) 500 V and B) 100 V. In both cases, the sample was transported by a DC electric field without oscillatory component. Reproduced with permission from the SI of Anal. Chem. 2024, 96, 11, 4446–4454. Copyright ©2024 American Chemical Society.

be a viable option in some cases, such a scheme does not offer the flexibility of using superposed DC and AC voltages. Only being able to tune U_{DC} means that the sample overlap and the sample velocities (translating to their residence time in the microchannel) are affected simultaneously. By contrast, superposed DC and AC voltages allow tuning the sample overlap and the residence time independently.

Note that U_{DC} always must be > 0. If $U_{DC} = 0$, the average voltage is zero, too, which is equivalent to switching off the voltage completely. In this case, the sample will no longer be focused. To test this, experiments were carried out in which a sample was focused with a voltage of 500 V until it arrives in the field of view. Then it is oscillated with $A = 1000\,\mathrm{V}$ and $f = 4\,\mathrm{Hz}$ or $A = 500\,\mathrm{V}$ and $f = 10\,\mathrm{Hz}$, respectively, but without any DC offset. The dispersion the peaks experience is roughly the same as in the reference case where the voltage was switched off completely.

6.7 Conclusions and outlook

In this chapter, a new approach to conduct isotachophoresis using superposed DC and AC electric fields was presented. This scheme allows to control the mixing of two co-focused samples separated by a spacer. In a first step, the effect of an oscillatory field component on the propagation of an ITP zone and the corresponding sample distribution was demonstrated. The DC offset of the electric field determines the time-averaged sample velocity.

For large enough AC admixtures, the propagation of the sample zone can be divided into an advancing and a receding phase, corresponding to compression and broadening of the sample. During the receding phase, the sample zone significantly broadens. The displacement and broadening of the sample strongly depend on the amplitude and frequency of oscillation.

The temporary broadening of a sample zone can be used to increase the overlap of two sample zones and hence to control their mixing. In phases when the electric field is inverted, two co-focused samples separated by a spacer show a significant overlap, while they can be almost completely separated when the electric field points in a direction to focus the samples. By adjusting the amplitude A and frequency f of oscillation, the time-averaged overlap of the sample distributions can be precisely controlled, where A/f was identified as the parameter that determines the overlap. A control of sample overlap can also be achieved by solely employing a tunable DC voltage (without superposed AC component), however, at the expense of reduced controllability compared to superposed DC and AC voltages.

It is suggested that these findings can be transferred to reactions between species focused by ITP. Any two (or more) species with sufficiently different electrophoretic mobilities can be separated by spacers. By switching on an oscillatory electric field, their mixing can be controlled. This can be used to start a reaction at any given time during an ITP protocol. By switching back to a DC electric field without oscillatory component, the samples can be separated again, terminating the reaction. In between, the time-averaged reaction rate can be tuned via the control parameter A/f. This could significantly expand the scope of ITP-based reaction systems by enabling an unprecedented real-time control over the course of a reaction.

Chapter 7

Concluding remarks

This final chapter summarizes the contributions of the studies presented above to the field of microfluidic electrophoresis. In addition, an outlook is given for each chapter, indicating possible next steps. The thesis began with an introduction to the fundamental equations of fluid dynamics and electrokinetics in microfluidics in Chapter 2. Each of the following chapters then had its own focus.

Chapter 3 dealt with the electric field-driven accumulation and separation of bioparticles at liquid-liquid interfaces in microfluidic ATPS. Using two model proteins, BSA and BγG, this study has shown that, in principle, different types of proteins can be fractionated at the phase boundary due to their different adsorption-desorption behavior. It was shown that a large proportion of both proteins accumulated at the three-phase contact line formed between the two phases of the ATPS and the microchannel walls, presumably due to a recirculating flow pattern caused by EOF. Until this work was published in 2021 [103], a similar approach had only been used to separate DNA molecules [106, 107]. Moreover, preliminary tests have shown that it should also be possible to isolate exosomes from proteins in microfluidic ATPS. At relatively high electric field strengths, most BSA molecules crossed the phase boundary, while exosomes with a mean size of about 110 nm were mainly retained. Future work will need to validate whether this method can be used to reliably purify exosomes. In addition, it should also be investigated whether it is also possible to fractionate extracellular vesicles of different types and sizes in the same way. This could be particularly interesting as there is not yet an established method used by the majority of researchers working with extracellular vehicles for diagnostic purposes [110].

However, Chapter 4 suggests that Faradayic reactions occur at the electrodes during electrophoretic separation operations in ATPS. The corresponding reaction products can cause instabilities if they are transported to the interface and interact with it, especially at higher electric field strengths. To ensure a reliable separation process, this effect should be prevented, e.g. by continuous flushing the electrode reservoirs. A proposal for how this could be achieved in practice is given in Section A in the Appendix.

Chapter 5 shifted the focus to the detection of low concentration samples focused with ITP. By cross-correlating, aligning and averaging a series of images, the SAMI algorithm was able to significantly increase the detectability of ITP sample zones hidden in noise. This new method has two main strengths: First, it does not require any additional hardware and is therefore easy to implement. Second, it uses Bayesian inference and therefore also incorporates uncertainty into the final decision as to whether or not a sample is present. In the future, the SAMI method should be used, for example, to detect fluorescent sample molecules with biomedical relevance in order to demonstrate its suitability for practical applications.

The research presented in Chapter 6 was also based on isotachophoresis. Two fluorescent dyes, which served as model species, were concentrated in ITP sample zones separated by a spacer. It was then shown that an oscillating electric field with DC offset can be used to precisely control the time-averaged overlap of the two sample distributions *via* the amplitude and frequency of the oscillatory electric field component. In other words, two samples can be mixed and unmixed under controlled conditions throughout an isotachophoretic process. Since the mixing of two reactive species has a direct effect on the rate of the corresponding reaction, it suggests itself that ITP with oscillating sample zones can be used to influence the course of chemical reactions. The next step would be to validate this claim using two reactive species that can be separated by a spacer.

To summarize, this thesis has contributed to the advancement of electrophoretic techniques in microfluidics. In particular, the accumulation, separation, mixing, and detection of charged species have been discussed in detail. May the results of this thesis contribute to the realization of Whiteside's vision - mentioned in the introduction of this thesis - that microfluidics will sooner or later play a major role in the analysis and synthesis of molecules - and other particles.

Acknowledgements

I want to express my appreciation to Prof. Dr. Steffen Hardt for the opportunity to conduct my studies at his institute and complete them with this dissertation. He consistently maintained an open-door policy, offering valuable guidance and constructive feedback that played an important role in my academic journey. I truly enjoyed the freedom he granted me to contribute my own ideas to various research projects. Next, I am grateful for all my former and current colleagues at the Institute of Nano- and Microfluidics — our exchanges have been incredibly valuable. Special thanks to Dr. Johannes Hartmann, who helped me to start my experimental work and collaborated with me on my first paper. I also want to acknowledge the insightful discussions with my fellow experimentalists: Dr. Sebastian Dehe, Dr. Maximilian Hartmann, Salar Farrokhi, Steffen Bißwanger, and Lisa Bauer. In this context, I would also like to mention my student assistants Alexander May and Sonja Kemmerer, who supported me in my research work. Besides, I want to acknowledge the collaborative spirit of Dr. Henning Bonart, whose contributions consistently provided fresh perspectives to our joint work. He, Dr. Tobias Baier, and Aaron Ratschow helped me a lot by providing their valuable feedback to the draft of my thesis. I would also like to thank Corinna Neumann for her administrative support over the years. And a nod to my office colleague, Jörg Bültemann, for the amusing Thursday morning breakfasts — I will remember those with a smile. There were so many other people I worked with at the Institute of Nano- and Microfluidics who contributed to a positive working atmosphere: Maximilian Schür, Dr. Mostafa Shojaeian, Frank Plückebaum, Dr. Michael Eigenbrod, Dr. Nico Sinn, Dr. Sattarupa Dutta, Dr. Rajkumar Sarma, Dr. Doyel Pandey, Dr. Pramodt Srinivasula, Dr. Arman Sadeghi and Alexander Wagner. Thanks to all of you!

During my PhD studies, I also had the opportunity to work with many other people, from Technische Universität Darmstadt, but also from other universities and from industry. Therefore, I would like to acknowledge my external collaborators. First, I want to thank Merck KGaA for their financial support. Special mention goes to Suman Kumar Metya and Dr. Henry Hess from the Merck Innovation Center, as well as my colleagues at the Merck Lab@TU Darmstadt, particularly Dr. Uta Clerkin, Dr. Gerhard Schwall, Dr. Dieter Spiehl, and Klaus Villforth. A heartfelt thanks to Dr. Tobias Meckel, whose unwavering support with optical setups - even beyond the Merck Lab - has been instrumental in my work. I am also grateful to Prof. Dave Carter and Dr. Genevieve Melling from

Oxford Brookes University, UK, who provided exosomes for my studies. The collaboration with Lukas Hecht and Prof. Dr. Benno Liebchen was indispensable in advancing the work on improved sample detection using isotachophoresis. Besides, I want to appreciate the preliminary work and feedback from Dr. Tamal Roy, a former group member, which significantly contributed to the progress of my work. Special thanks to Klaus-Dieter Voss from IMNS Darmstadt, who introduced me to the fabrication of SU-8 coated wafers. To all mentioned collaborators and contributors, your collective efforts have played a crucial role in the success of this work. Thank you! In addition, I want to express my gratitude to Prof. Dr. Moran Bercovici from Technion Haifa in Israel, who agreed to be the second reviewer of my thesis.

Next, I would like to thank my family and friends. I would not be who I am today without the influence of my parents, Uli and Heiko. Even though neither of them ever went to university, they gave me a lot of guidance that I have benefited from along the way. As a child, they encouraged my curiosity and were there for me when I needed them. They taught me the value of perseverance and hard work, but also showed me that there are more important things in life than my performance at school or my academic achievements. My brothers and my friends have always accompanied me on my journey, making both my personal and professional life much more enjoyable. A huge thank you goes to my wife. Especially in the last few months, she has given me a lot of freedom and support, which allowed me to complete my dissertation. When I was down, she cheered me up. Lena, this would not have been possible without you. I am blessed to have you by my side.

Finally, as a Christian, I would like to thank God, from whom I believe all good things come and without whom I can do nothing. As a scientist, I always strive to learn and to gain new insights. Even if my future is not at a university, that is unlikely to change. At the same time, I believe that there are things that can never be understood by the human mind, but which make your life so much richer.

Appendix

A Alternative chip design for particle separation in aqueous two-phase systems

As shown in Chapter 3, bioparticles can be effectively separated in microfluidic ATPS. In a next step, flow-through operation of such separation processes would be desirable. Thereby, the throughput can be increased compared to the operation under quiescent condition as described before. However, there would be two major challenges associated with flow-through operation: First, the position of the interface must be kept constant over a relatively long period of time. In principle, the position of the interface can be controlled *via* the volume flow rates of the dextran and PEG phase [239]. In practice, however, slight variations in the flow rate, e.g. due to fluctuations caused by the syringe pumps used to generate a continuous flow, can slightly shift the phase boundary. Therefore, it might be difficult to reliably separate the two phases at the outlet of the microfludic device. In systems based on an aqueous and an organic phase, characterised by a high interfacial tension, the position of the interface can be easily fixed using phase guides, see for example [240, 241]. Here, the phase boundary can pin to guide structures, making it less susceptible to fluctuations in the flow rate. With ATPS, however, pinning of the interface is not easily achieved. Therefore, the position of the interface has to be stabilised using other methods. Second, in microfluidic devices for flow-through operation, there is usually a conflict between throughput and residence time. Due to the small channel volumes, relatively high flow rates will result in a short residence time, which can affect the efficiency of the separation process. In response to these challenges, an alternative chip design is suggested, see Figure A.1.

This new chip design differs from the one presented in Figure 3.4 in a few details. First, it has two outlets, allowing the two phases to be split at the end of the channel. Ideally, one phase contains the particles that have accumulated at the interface, and the other contains the particles that have been able to cross the interface. With two outlets, each phase can be withdrawn individually for further processing steps or an offline analysis. Second, the reservoirs are closed. This allows to continuously flush the electrode reservoirs, which should remove any by-products from Faradaic reactions and prevent the formation

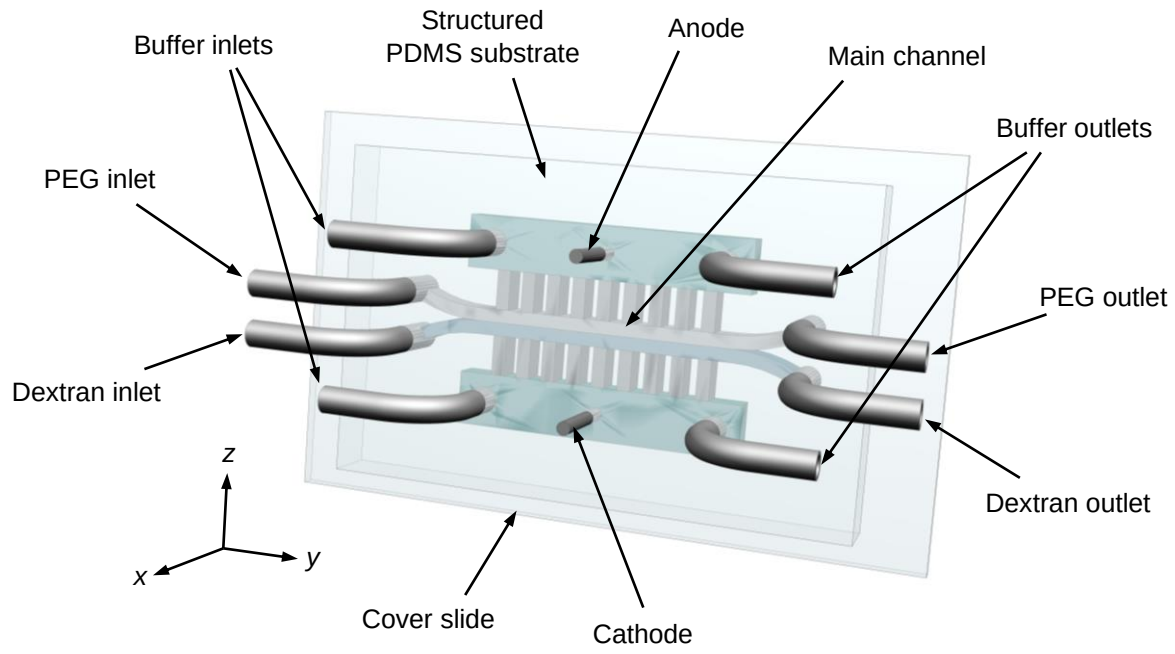

Figure A.1: Schematic drawing of an alternative chip design for bioparticle separation. The two phases of the ATPS are stacked according to their density. For orientation: Gravity acts in the negative z-direction.

of additional phases as observed in Chapter 4. Next, the goal was to design a chip that allows density based stacking of the two ATPS phases. As the chip is completely closed, it can be rotated so that the PEG phase is inserted above the dextran phase. With the previous design, the two phases flowed side by side, not on top of each other. Last, the cross-section of the main channel of this alternative chip design is 2 mm x 2 mm (while the length is 20 mm). In this way, the capacity of the chip is increased, which allows to achieve higher throughputs and residence times, respectively. Due to the relatively large width and height of the main channel, the chip is no longer a microfluidic device. This should support the stabilization of the interface through density-based stacking, since interfacial tension forces should play only a subordinate role. In principle, this modification should make it easier to control the position of the interface *via* the inlet volume flow rates. The purpose of this section is to evaluate the functionality of the alternative chip design.

A.1 Experiments

The newly developed chip is fabricated in a similar way to that described above. However, there are some significant changes to the fabrication protocol that are explained here. Some details of the experimental procedure for testing the new device are also given.

Device fabrication

The chips were fabricated using the soft lithography protocol as described in Subsection 3.5.3. Instead of a SU-8 coated silicon wafer, a 3D printed master structure was used. Due to the increased channel height, it was not possible to create a finer comb structure between the reservoirs and the main channel. With finer lamellae, the PDMS cast was damaged each time it was detached from the master structure. Therefore, the width of the PDMS lamellae and the gel bridges, respectively, was increased to 1 mm.

In consequence, the protocol for polymerizing the gel bridges in Subsection 3.5.3 had to be modified. As before, the chips were filled with acrylamide solution. Everything but the comb structure was covered with a lithography mask. After 20 s of exposure to UV light, the light source was switched off to prevent the polymerization reaction from spreading to the main channel or the reservoirs. However, this relatively short exposure time was not sufficient to polymerize all of the acrylamide. Only at the coverslide, a thin layer of polymerized acrylamide was formed. Hence, the chip was flushed with isoporpanol, refilled with acrylamide solution and again exposed to UV light for 20 s. This process was repeated six to eight times. In this way, during each cycle a layer of acrylamide was added until the gel bridges tightly separated the reservoirs from the main channel. The chip was exposed to UV light alternately from the glass side and the PDMS side.

Flow-through experiments

To test the functionality of the alternative channel design, a 20 mM phosphate buffer solution (pH = 7) was used. In a first step, the reservoirs were filled with buffer. The buffer was then continuously exchanged using a peristaltic pump connected to a larger reservoir. Next, buffer solution was introduced to the main channel using two syringe pumps. The ultimate goal would be to fill the main channel with an ATPS. However, since dextran is rather expensive, first tests were carried out with buffer only. Preliminary tests in a channel similar to the one shown in Figure A.1, but without reservoirs and gel bridges, have shown that it is principally possible to stack the two phases based on their density. It was possible to keep the position of the interface stable for about 30 min at ~50 µl/min in both phases by repeatedly adjusting the flow rate slightly during the test run. Here, however, only pure buffer solution was used. Once the chip was completely filled, a voltage of 10 or 100 V was applied.

Temperature measurement

In narrow microchannels, heat generated by Joule heating (or reactions) can be removed relatively quickly *via* thermal conduction through the confining channel walls. Here, however, the characteristic length scales of the chip are significantly larger. Therefore, in a variation of the experiments described above, the temperature in the center of the main

channel and the reservoirs was measured. To do so, small holes were punched through the PDMS channel walls and thermocouples were inserted. In this way, it was possible to monitor the temporal evolution of the temperature in the chip after a voltage was applied.

A.2 Experimental results

The following is a best practice for filling the main channel and flushing the electrode reservoirs. It is accompanied by some comments on the stability of the gel bridges and the temperature evolution inside the chip.

Choosing the right flow rates

When the main channel is filled at the beginning of an experiment, there is usually some air in the tubes connected to the inlet. At low initial flow rates, this air is transported into the main channel and usually forms bubbles that adsorb to the channel walls. Only at high initial flow rates of 25 ml/min or more it is possible to remove these bubbles. This is important as bubbles can interfere with the interface and negatively affect separation processes. After the main channel is filled, the flow rate can be reduced to values of 100 µl/min or lower.

When a voltage is applied between the electrodes, Faradaic reactions occur, resulting in the formation of bubbles. The higher the applied voltage, the higher the rate at which bubbles form. These bubbles have a tendency to adsorb to the channel walls or electrodes, ultimately reducing the current and hence the separation efficiency. Therefore, the volume flow rate in the reservoirs has to be increased until all bubbles reliably be removed. However, this is only possible at a relatively high volume flow rate between 150 and 200 ml/min, close to the maximum rate of the peristaltic pump. The volume of the reservoirs is approximately 175 µl. Assuming a flow rate of 150 ml/min, the buffer in the reservoirs is exchanged more than 14 times per second. This should be sufficient to prevent the formation of additional phases that could eventually interfere with the interface as described in Chapter 4.

Stability of the gel bridges

Choosing the right flow rates is a delicate task. As described above, lower flow rates may not be sufficient to remove bubbles from the channel walls and electrodes. However, at higher flow rates, the gel bridges might not be sufficient to separate the main channel from the reservoirs. At the flow rates described above, they normally prevent buffer from leaking from the main channel into the reservoirs or *vice versa*. In some experiments, however, a significant flow of buffer across the gel bridges was observed. It is assumed that the gradual fabrication process described above is more likely to lead to defects compared to the establish process described in Subsection 3.5.3. As a consequence, the

gel bridges break easily when the pressure in the main channel or reservoirs becomes too high.

In addition, especially at an applied voltage of 100 V, bubble formation in the main channel close to the gel bridges was observed. One possible explanation for this is that smaller bubbles that have formed at the electrodes are not retained by the gel bridges. They then accumulate and coalesce in the main channel to form larger bubbles. Due to the relatively low flow rate (~100 µl/min after the initial filling process), these larger bubbles are not removed, but adsorb to the channel walls or disturb the interface, which should be avoided.

Development of temperature over time

In a first step, the temporal evolution of the temperature inside the chip was tested in flow-through mode. The flow rate inside the main channel was 100 µl/min, the flow rate in the reservoirs ~200 ml/min (the maximum rate of the peristaltic pump). The temperature was measured inside the main channel and in the cathode reservoir. At an applied voltage of 100 V, the temperature increase in the main channel (cathode reservoir) was approximately 1.5 K (1.9 K), which should not have a negative effect on interfacial separation processes. This test was then repeated under quiescent conditions, i.e. with no volume flow in or out of the chip. The voltage was again set to 100 V. After 2 min, there was no buffer left in the reservoirs because it was replaced by gas formed in Faradaic reactions at the electrodes. Until then, the temperature in the main channel has increased by approximately 8 K. This again underlines the importance of flow-through operation: On the one hand, convective heat transport will prevent major temperature increases. On the other hand, fresh buffer solution will be transported to the reservoirs, which will keep the process running.

A.3 Simulation of the electric field distribution

In addition to the experiments presented above, the electric field distribution in the chip shown in Figure A.1 was simulated. All experiments were performed by Alexander May, the author's student assistant, with input from Dr. Tobias Baier. Alexander May gave permission to use his results in this thesis.

Using Comsol Multiphysics 6.0, a set of three equations was solved. First, the conservation of current was described as

$$\nabla \cdot \vec{i} = Q, \tag{A.1}$$

where i is the current density and Q is a source term. Next, the current density can be expressed as the product of the electrical conductivity and the electric field:

$$\vec{i} = \kappa \vec{E}. \tag{A.1}$$

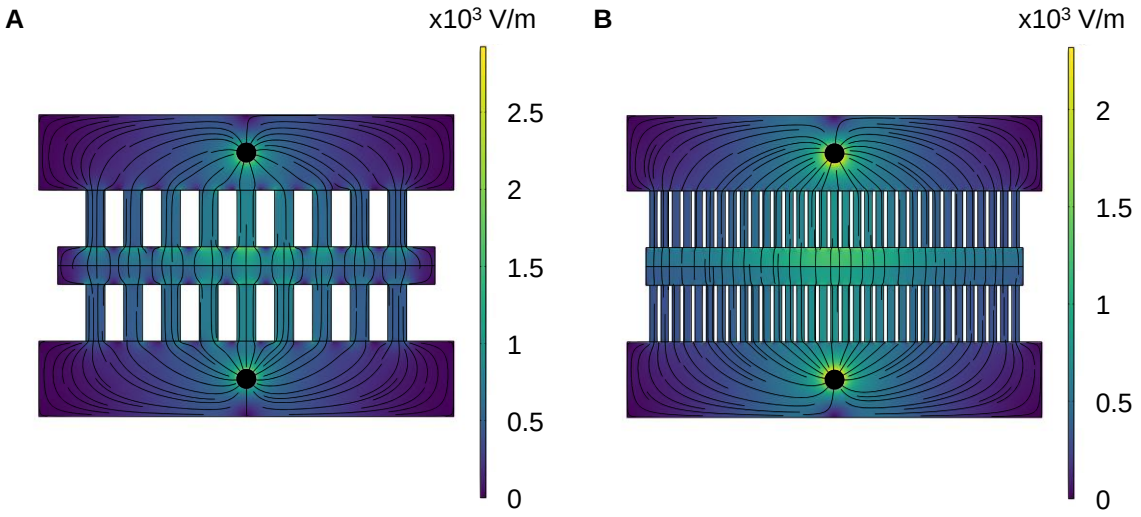

Figure A.2: 2D simulation of the electric field distribution with the alternative chip design. A) shows the electric field distribution in a chip as presented in Figure A.1. In B), the number (width) of the gel bridges separating the reservoirs from the main channel has been increased (decreased). The electric field lines are represented by black curves in both plots.

The last equation describes the connection between the electric field and the electric potential:

$$\vec{E} = -\nabla\varphi. \tag{A.1}$$

The boundary conditions were defined as follows: At the cathode, the potential was set to 0 V, at the anode to 10 V. In addition, there is no electric field component normal to the channel walls. Together with these boundary conditions, the above equations were solved in a model domain representing a simplified version of the newly developed chip in 2D. To account for different electrical conductivities in the dextran phase, PEG phase, buffer rerservoirs, and gel bridges, different regions were defined within this domain. The conductivity in the dextran (PEG) phase was set to $\kappa_{dex} = 1.226\,\mathrm{mS/cm}$ ($\kappa_{PEG} = 1.699\,\mathrm{mS/cm}$), which corresponds to the values measured in an ATPS based on a 10 mM BES buffer solution (pH = 8) as described in Subsection 3.5.1. Likewise, the conductivity in pure buffer was determined to be $\kappa_{buf} = 3.160\,\mathrm{mS/cm}$. This value was used for both the reservoirs and, for simplicity, the gel bridges.

The resulting electric field distribution is shown in Figure A.2.A. The colormap represents the electric field strength, the black curves the electric field lines. Obviously, the electric field is very inhomogeneously distributed. In the main channel, the field strength decreases from the center towards the outlets and inlets, respectively. Besides, it is locally increased in regions around the edges of the gel bridges. Inhomogeneous electric field distributions are undesired since they will lead to a non-uniform particle transport towards the interface. Besides, as explained in Subsection 3.4.4, the interfacial transport resistance in separation processes depends on the potential distribution at the phase

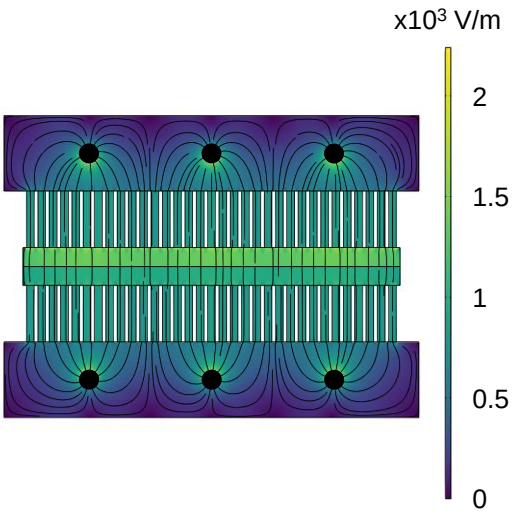

Figure A.3: 2D simulation of the electric field distribution with the alternative chip design with six electrodes and an increased number of gel bridges. The electric field lines are represented by black curves.

boundary. Therefore, a more homogeneous electric field distribution will also lead to a more uniform transport resistance.

To achieve an improved electric field distribution, two measures were tested in subsequent simulations. In a first step, the number (width) of gel bridges separating the reservoirs from the main channel was increased (decreased). As shown in Figure A.2.B, the electric field strength still decreases from the center of the main channel towards the outlets and inlets with this modification, but in contrast to Figure A.2.A, it decreases more smoothly. If the difficulties in producing the gel bridges on the millimeter scale described in Subsection A.1 can be overcome, it would therefore make sense to transfer these findings to the experimental setup.

In a third simulation, the number of electrodes was increased. Three anodes and three cathodes, respectively, were placed in the respective reservoirs. The voltage at the anodes (cathodes) was set to 10 V (0 V). As a result, the electric field is now homogeneously distributed across the main channel, see Figure A.3. Therefore, this electrode configuration should be used in particle separation experiments. It is reasonable to assume that similar results would be obtained by using a single electrode extending from the buffer inlet to the corresponding outlet.

A.4 Conclusions and outlook

A few conclusions can be drawn from the investigations presented above. The gel bridges are a major weak point of the system. The larger channel dimensions make it more difficult to fabricate them, which makes them less robust. Liquids can cross them at higher flow rates. Besides, they seem to be permeable for smaller gas bubbles. Therefore, they do not

completely separate the reservoirs from the main channel, which is a key requirement for reliable electric field-driven separation processes. In addition, they may also be damaged at higher field strengths, as shown in Chapter 4. Summing up, it would be best to find another way to separate the reservoirs and the main channel. Otherwise, the chip should be scaled down again to facilitate the polymerisation process and increase the robustness of the gel bridges. As this issue remains unresolved, it has not yet been tested whether an ATPS can be inserted into the main channel of the newly developed chip in flow-through mode.

Using a peristaltic pump, the electrode reservoirs can be continuously flushed at a high flow rate. This reliably removes gas bubbles, allowing the system to operate continuously. At low reservoir volumes, the buffer is exchanged several times per second, which should eliminate a potential source of interfacial instabilities: The formation of additional phases through electrode reactions as observed in Chapter 4. Besides, flow-through operation contributes positively to the removal of heat created by Joule heating.

Last, to obtain a homogeneous electric field distribution, more than one electrode should be placed in each reservoir. The simulations above show that three electrodes on each side of the chip should be sufficient. In addition, many narrow gel bridges are preferable to a few wide ones. A more homogeneous electric field ensures more uniform transport of sample ions to the interface. Likewise, a more homogeneous potential distribution at the phase boundary will also result in a more uniform interfacial transport resistance.

B Sample detection using isotachophoresis

B.1 Vertically averaged and stacked data

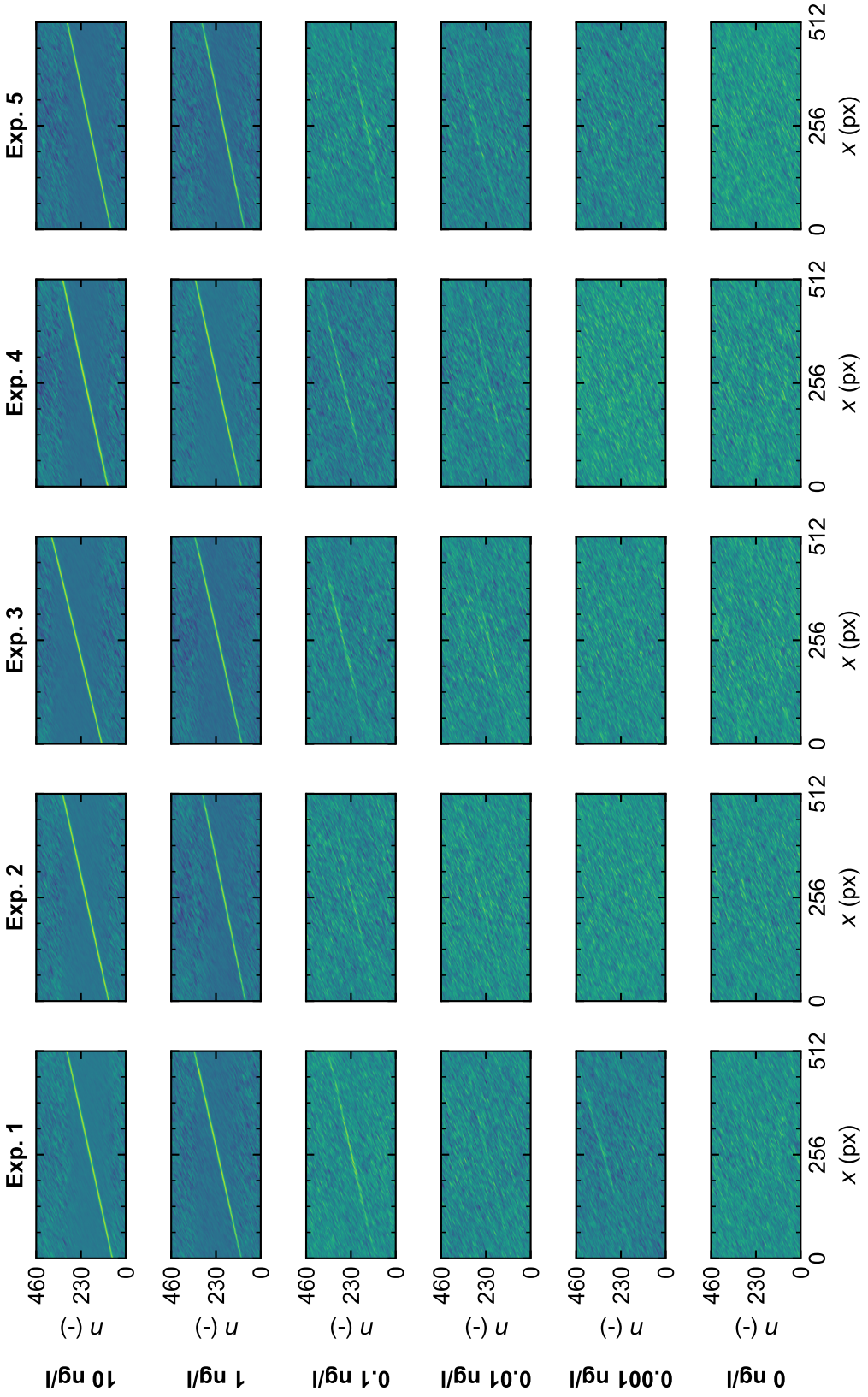

Figure B.4: Image data after being vertically averaged, stacked, and filtered by SAMI for different concentrations.

B.2 Marginal posteriors of the sample velocity

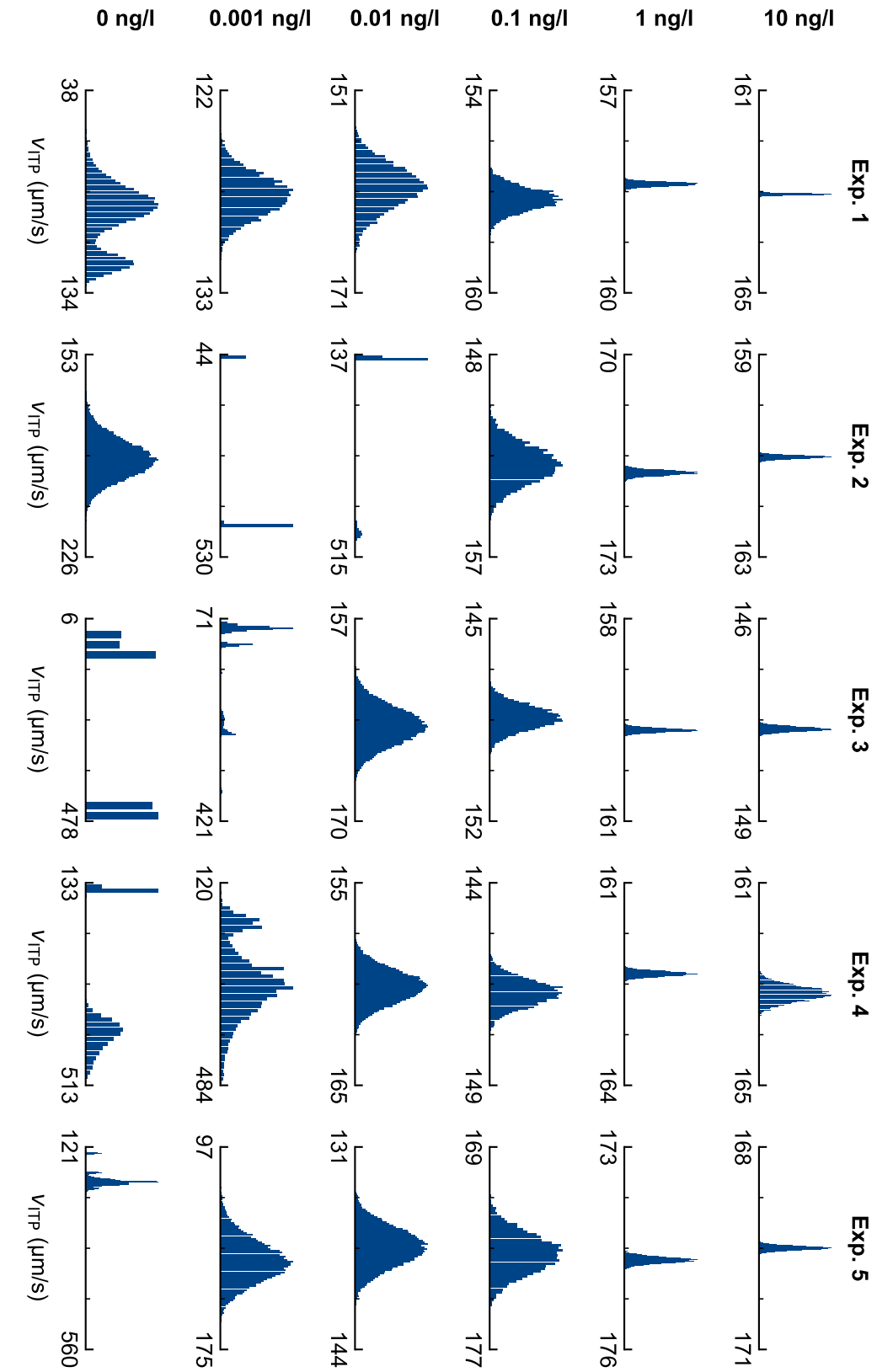

Figure B.5: Marginal posteriors of v_{TTP} computed by SAMI for different concentrations.

B.3 Marginal posteriors of the sample spread

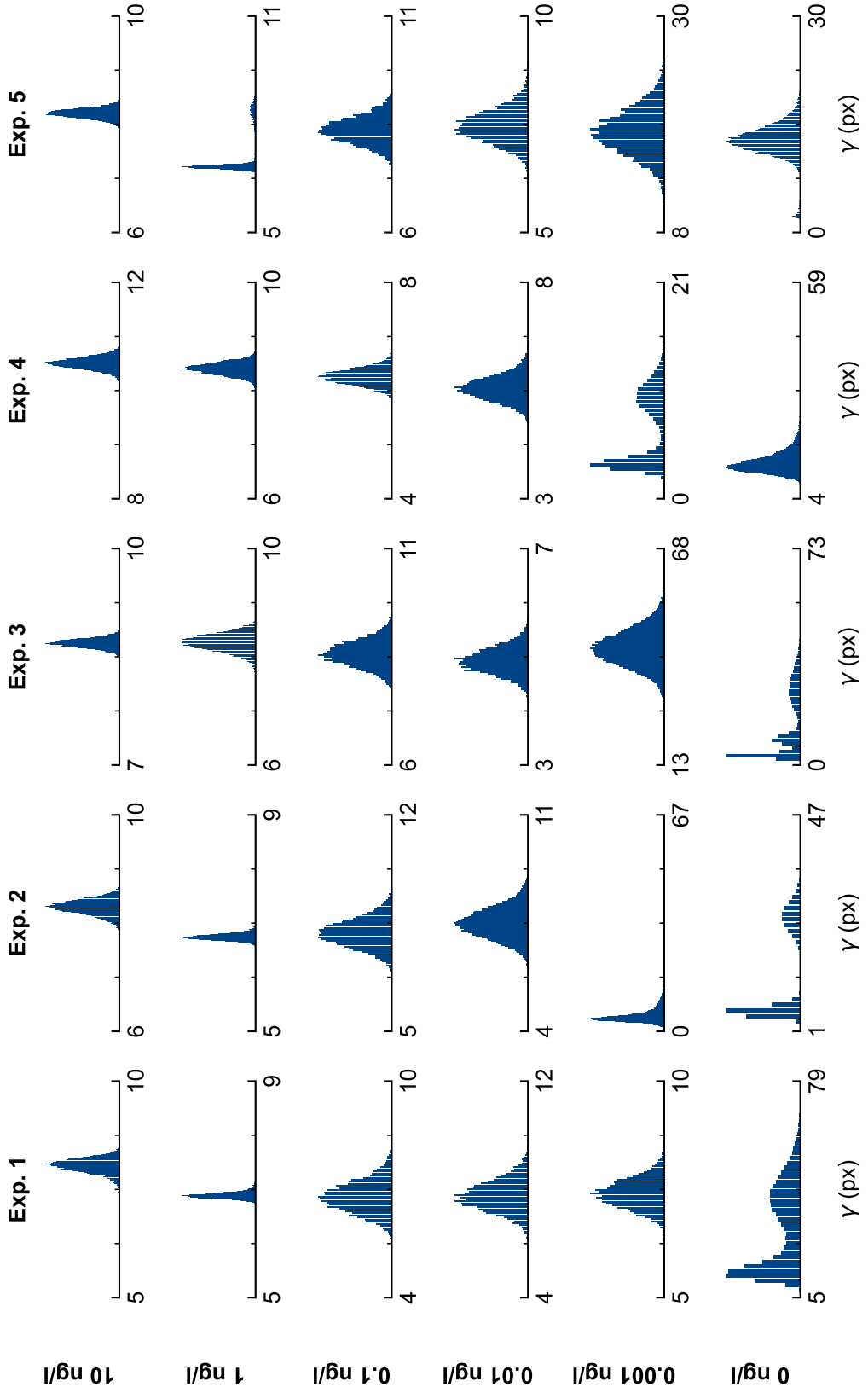

Figure B.6: Marginal posteriors of the sample spread γ computed by SAMI for different concentrations.

B.4 Marginal posteriors of the *SNR*

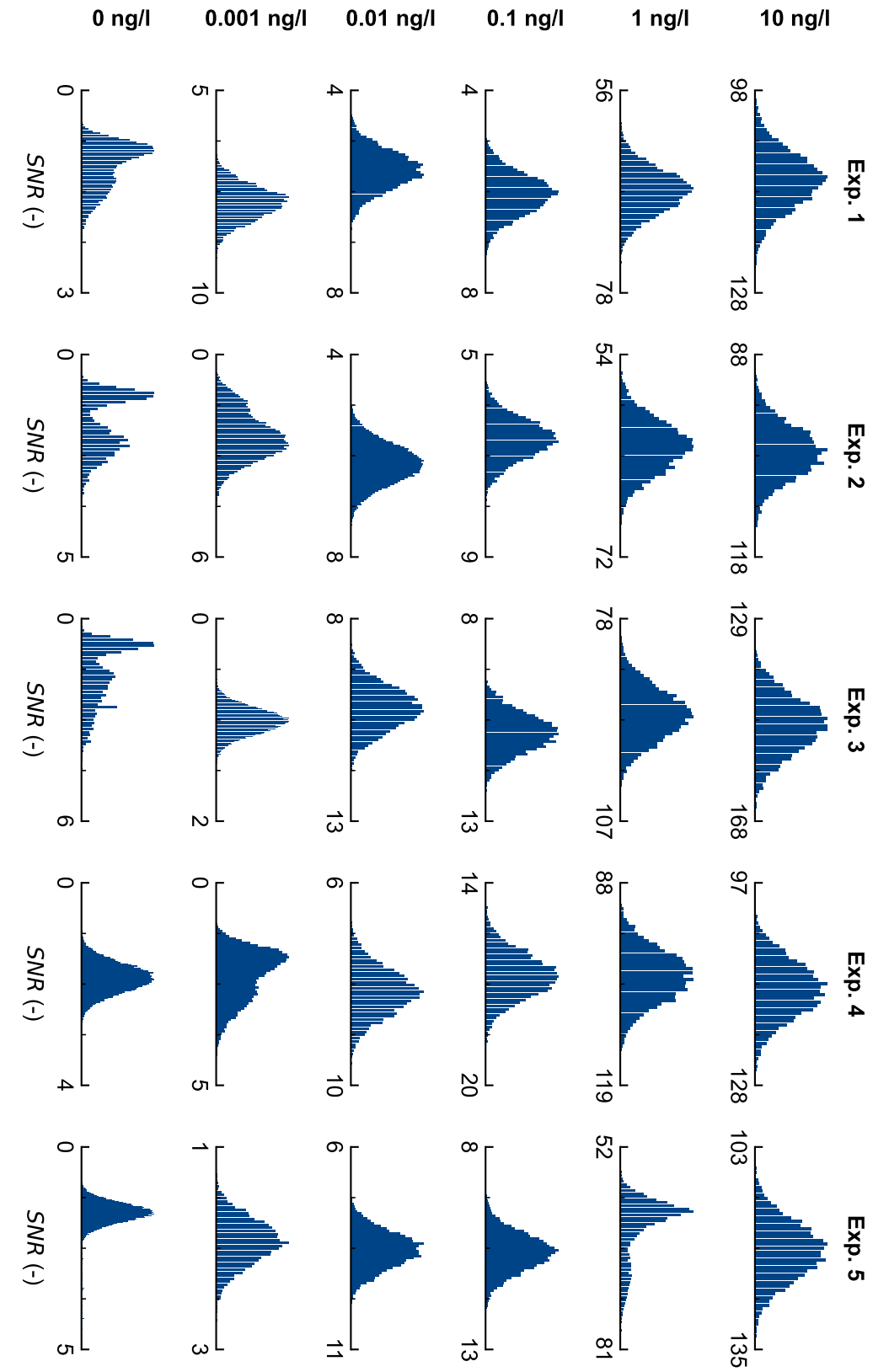

Figure B.7: Marginal posteriors of the *SNR* computed by SAMI for different concentrations.

B.5 Sample peaks

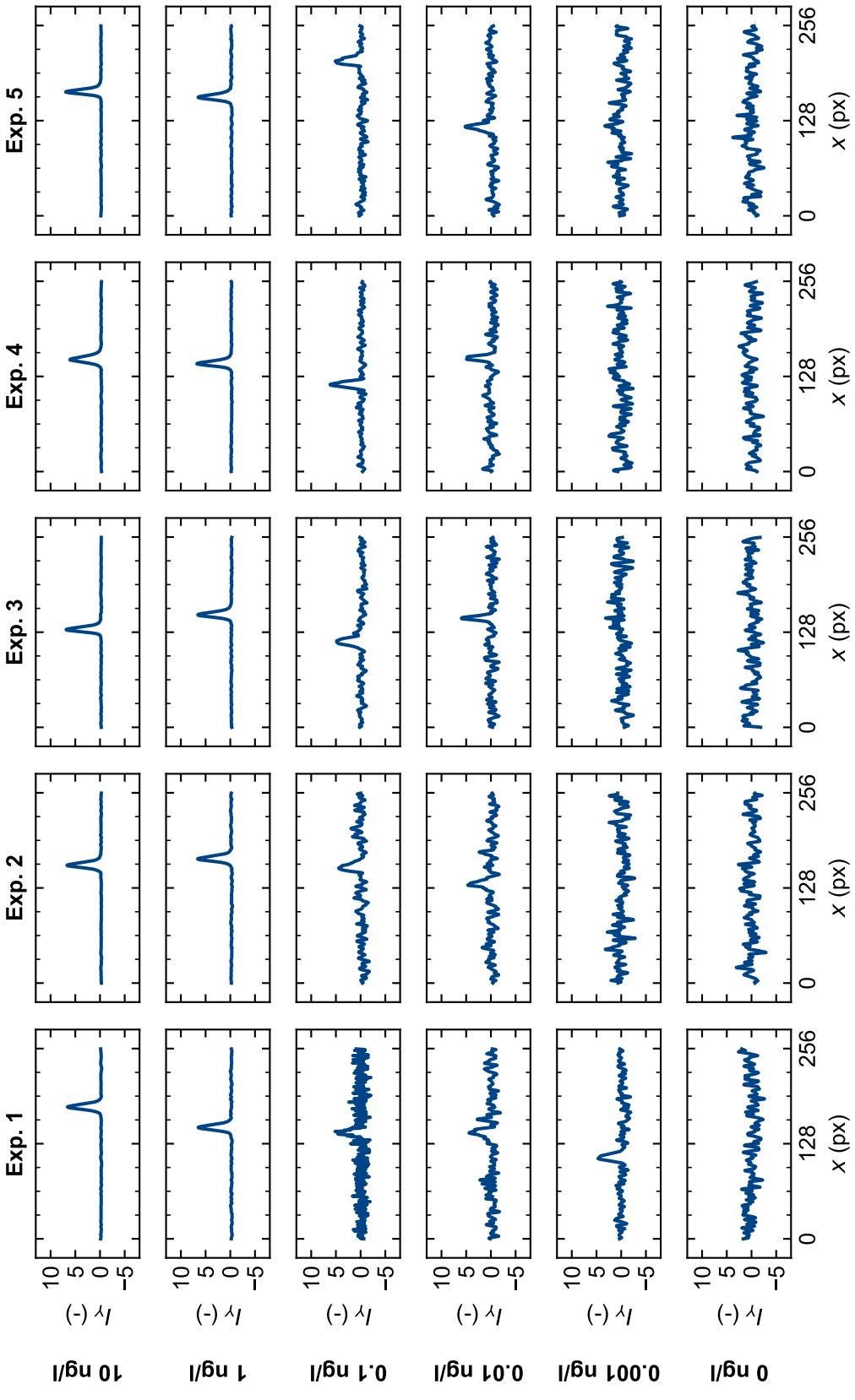

Figure B.8: Sample peaks after being shifted and averaged by SAMI for different concentrations.

C ITP with oscillating sample zones

C.1 Analysis of crosstalk and possible contaminations

In a quantitative analysis of fluorescence intensities originating from two different fluorophores as presented in the main text, crosstalk often has a negative influence. Crosstalk occurs when the emission spectra of two fluorophores partly overlap and hence their emitted light cannot be completely separated with a dichroic mirror as depicted in Figure 6.2. Besides, ITP is a powerful technique for increasing the concentration of species of interest, but it often also focuses impurities. If these impurities fluoresce to a significant degree, they corrupt the signal of interest. Therefore, an analysis of these possible sources of error is presented here. Experiments were conducted with spacer and a) no sample, b) only AF647, and c) only Fluorescein. A DC electric field corresponding to a voltage of 500 V was used. The results are shown in Figure C.9. The first plot in each subfigure represents the upper half of the image, where emission light with a wavelength of ~525 nm is detected. The second plot represents the lower half, where emission light with a wavelength of ~700 nm is collected. Note that neither a background nor a flatfield correction were carried out here. Each experiment was conducted in a new microchannel to avoid cross contamination between two experiments.

Figure C.9.A shows the results obtained without any sample. At the center of the first plot, a small peak can be detected. Since neither AF647 nor Fluorescein are present, it must result from contaminating ions that are either present at a low concentration or fluoresce only weakly. It is impossible to determine whether these contaminants focus between LE and spacer or between spacer and LE, as there is no second peak left or right of the first one in neither of the two plots. The height of the peak is hardly distinguishable from the image noise and can therefore be neglected. By smoothing the data array $I_{FL}(x, y, n)$ during the quantitative analysis as described in the main text, it will be eliminated.

Figure C.9.B, several peaks can be seen. The highest one, which can be found in the second plot, stems from the part of the fluorescence spectrum of AF647 that is actually to be detected. In the first plot, there are two peaks. The right one coincides with the peak in the second plot. Hence, it is likely caused by crosstalk. The left one could be the equivalent of the peak in the first plot in Figure C.9.A. This would mean that it is caused by contamination, but it is not possible to determine this unequivocally. However, the peaks in the first plot are again hardly distinguishable from the image noise and will be eliminated by smoothing the data. The inset in the second plot is a close-up of the region along the x-axis where the left peak occurs in the first plot. No peak can be observed here.

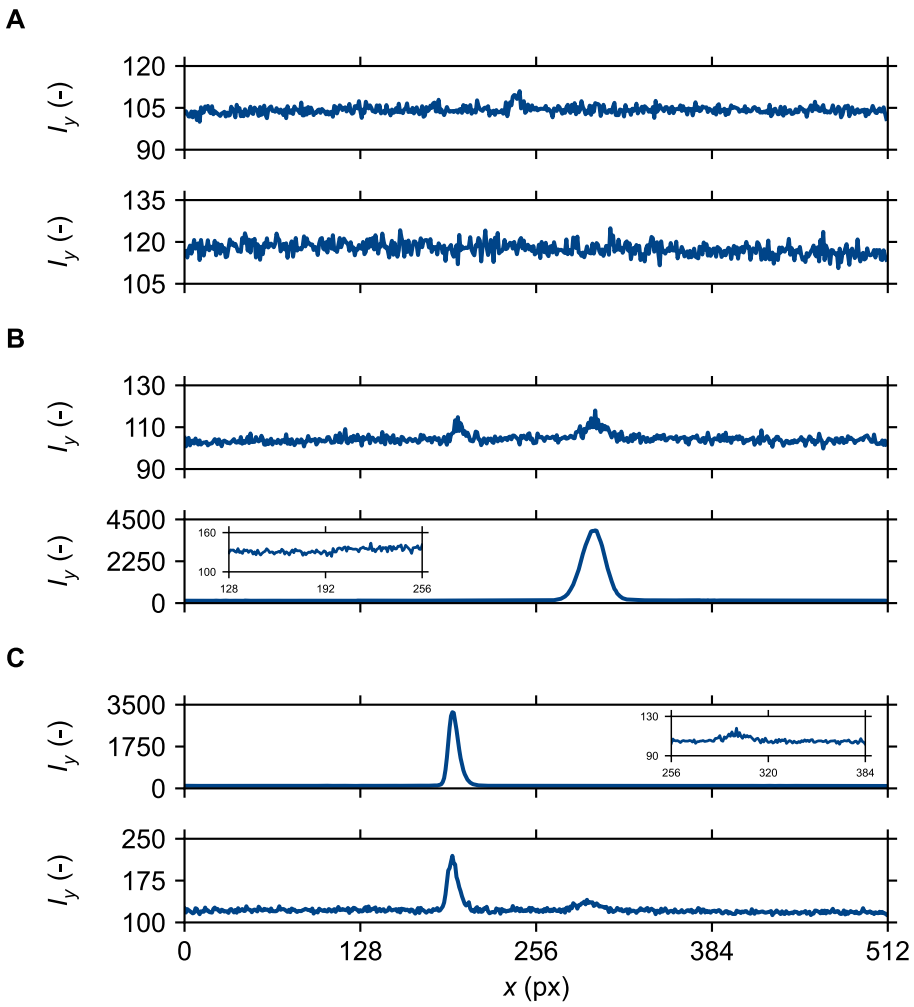

Figure C.9: Analysis of crosstalk and possible contaminations. The first plot in each subfigure shows the averaged fluorescence intensity in the upper part of the image (where light with a wavelength of ~525 nm is detected), the second one shows the averaged fluorescence intensity from the lower part of the image (where light with a wavelength of ~700 nm is detected). A) shows the averaged intensities from an experiment without Fluorescein or AF647. In B) and C), the averaged intensities from experiments with only AF647 and Fluorescein, respectively, are depicted. The insets are close-ups of relevant sections along the x-axis with a different y-axis scaling. Reproduced with permission from the SI of Anal. Chem. 2024, 96, 11, 4446–4454. Copyright ©2024 American Chemical Society.

As in Figure C.9.B, in Figure C.9.C, several peaks can be seen. Again, the highest peak, this time in the first plot, is what is to be observed, since it represents major parts of the light emitted by Fluorescein. At the same position along the x-axis in the second plot, there is also a significant peak. Most likely, it can be attributed to crosstalk. It is much higher than the other peaks caused by crosstalk or contamination that have been described above. In experiments with Fluorescein and AF647, it will appear next to the high peak caused by AF647. However, its height is still one order of magnitude lower than that of the AF647 peak shown in the second plot of Figure C.9.B. Therefore, it can still be eliminated by smoothing the intensity data as described in Subsection 6.5.5. Between

$x = 256\,\text{px}$ and $x = 384\,\text{px}$, a rather insignificant peak can be detected in both plots (see the inset in the first plot). It is difficult to attribute the lower one to contaminations since there is no equivalent in the second plot in Figure C.9.A. One possible explanation is that Fluorescein dissociates to some degree. The products of this dissociation could partly be focused in the sample zone between LE and spacer and emit light with a different emission spectrum than Fluorescein. However, this is only a hypothesis. The true reason for the two lower peaks in the right half of the two plots is not evident. Anyway, also they can be eliminated by smoothing the fluorescence data.

C.2 Overlap as a function of time with different oscillation parameters

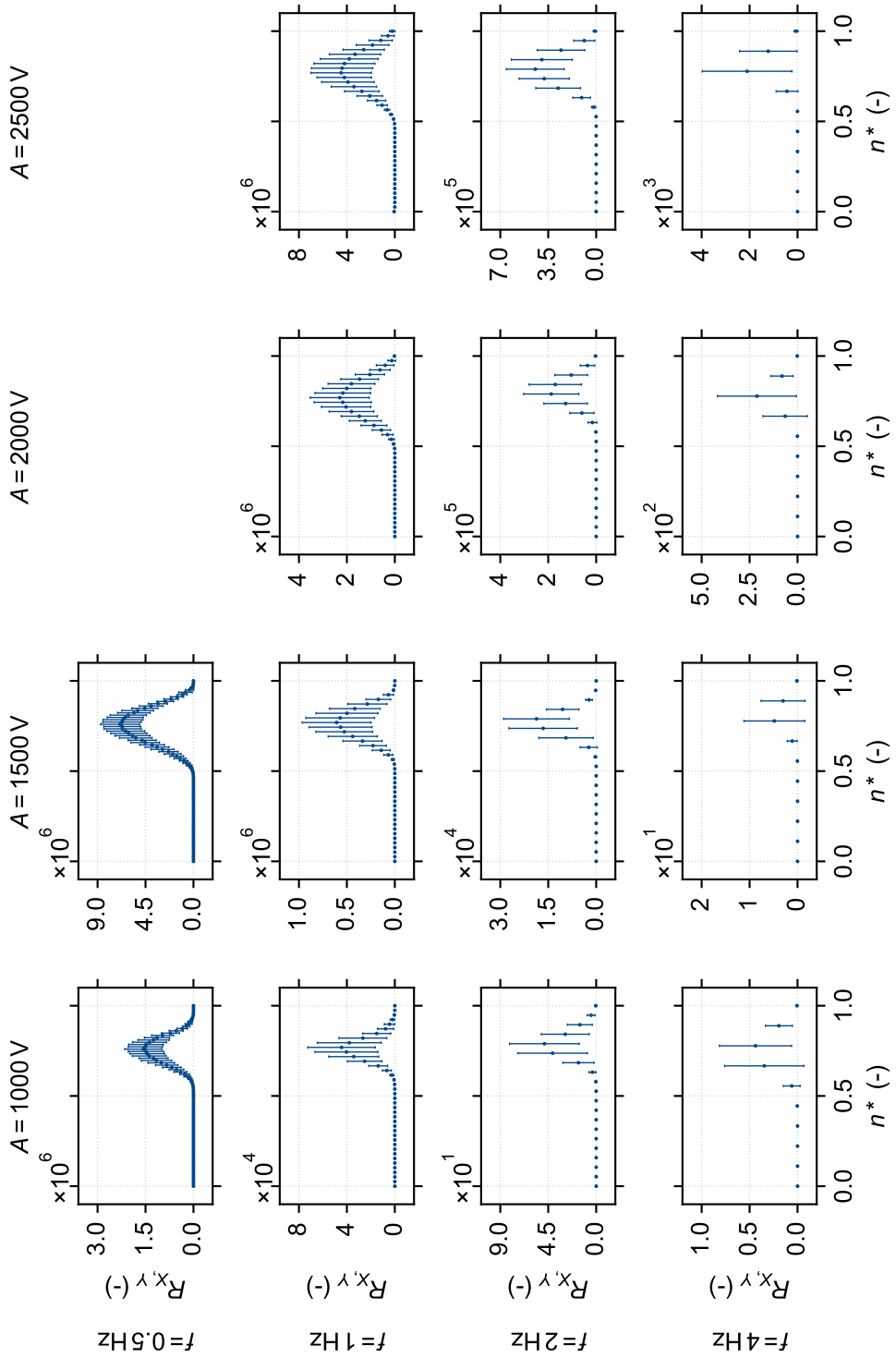

Figure C.10: Overlap of the intensity distributions of the two samples over one period of oscillation with varying amplitude and frequency. Each column represents one value of the amplitude A, and each row represents one value of the frequency f. The data points represent the average from five experiments, the error bars indicate the corresponding standard deviation. Note that the y-axis is scaled differently in each subfigure. Reproduced with permission from the SI of Anal. Chem. 2024, 96, 11, 4446–4454. Copyright ©2024 American Chemical Society.

Bibliography

[1] G. M. Whitesides. "The origins and the future of microfluidics". In: *Nature* **442**, 7101 (2006), pp. 368–373. DOI: 10.1038/nature05058.

[2] D. J. Beebe, G. A. Mensing, and G. M. Walker. "Physics and applications of microfluidics in biology". In: *Annual Review of Biomedical Engineering* **4** (2002), pp. 261–286. DOI: 10.1146/annurev.bioeng.4.112601.125916.

[3] E. K. Sackmann, A. L. Fulton, and D. J. Beebe. "The present and future role of microfluidics in biomedical research". In: *Nature* **507**, 7491 (2014), pp. 181–189. DOI: 10.1038/nature13118.

[4] J. K. Nunes and H. A. Stone. "Introduction: Microfluidics". In: *Chemical Reviews* **122**, 7 (2022), pp. 6919–6920. DOI: 10.1021/acs.chemrev.2c00052.

[5] H. Stone, A. Stroock, and A. Ajdari. "Engineering Flows in Small Devices: Microfluidics Toward a Lab-on-a-Chip". In: *Annual Review of Fluid Mechanics* **36**, 1 (2004), pp. 381–411. DOI: 10.1146/annurev.fluid.36.050802.122124.

[6] T. M. Squires and S. R. Quake. "Microfluidics: Fluid physics at the nanoliter scale". In: *Reviews of Modern Physics* **77**, 3 (2005), pp. 977–1026. DOI: 10.1103/RevModPhys.77.977.

[7] J. P. Landers, ed. *Handbook of Capillary and Microchip Electrophoresis and Associated Microtechniques*. 3. Edition. Boca Raton, FL, USA: CRC Press, 2008.

[8] R. T. Turgeon and M. T. Bowser. "Micro free-flow electrophoresis: theory and applications". In: *Analytical and Bioanalytical Chemistry* **394** (2009), pp. 187–198. DOI: 10.1007/s00216-009-2656-5.

[9] N. W. Frost, M. Jing, and M. T. Bowser. "Capillary Electrophoresis". In: *Analytical Chemistry* **82**, 12 (2010), pp. 4682–4698. DOI: 10.1021/ac101151k.

[10] S. S. Bahga and J. G. Santiago. "Coupling isotachophoresis and capillary electrophoresis: a review and comparison of methods". In: *The Analyst* **138**, 3 (2013), pp. 735–754. DOI: 10.1039/C2AN36150G.

[11] A. Ramachandran and J. G. Santiago. "Isotachophoresis: Theory and Microfluidic Applications". In: *Chemical Reviews* **122**, 15 (2022), pp. 12904–12976. DOI: 10.1021/acs.chemrev.1c00640.

[12] R. B. Bird, W. E. Stewart, and E. N. Lightfoot. *Transport phenomena*. 2. Edition. Hoboken, NJ, USA: John Wiley & Son,s Inc., 2007.

[13] J. H. Masliyah and S. Bhattacharjee. *Electrokinetic and Colloid Transport*. Hoboken, NJ, USA: JohnWiley & Sons, Inc., 2006. DOI: 10.2307/2690024.

[14] R. F. Probstein. *Physicochemical Hydrodynamics*. 2. Edition. Hoboken, NJ, USA: John Wiley & Sons, Inc., 1994. DOI: 10.1002/0471725137.

[15] H. Helmholtz. "Ueber einige Gesetze der Vertheilung elektrischer Ströme in körperlichen Leitern mit Anwendung auf die thierisch-elektrischen Versuche". In: *Annalen der Physik und Chemie* **165**, 6 (1853), pp. 211–233. DOI: 10.1002/andp.18531650603.

[16] H. Helmholtz. "Studien über electrische Grenzschichten". In: *Annalen der Physik und Chemie* **243**, 7 (1879), pp. 337–382. DOI: 10.1002/andp.18792430702.

[17] L. G. Gouy. "Sur la constitution de la charge électrique à la surface d'un electrolyte". In: *Journal de Physique Théorique et Appliquée* **9**, 1 (1910), pp. 457–468.

[18] D. L. Chapman. "A contribution to the theory of electrocapillarity". In: *The London, Edinburgh, and Dublin Philosophical Magazine and Journal of Science* **25**, 148 (1913), pp. 475–481. DOI: 10.1080/14786440408634187.

[19] O. Stern. "Zur Theorie der elektrolytischen Doppelschichten". In: *Zeitschrift für Elektrochemie und angewandte physikalische Chemie* **30**, 21-22 (1924), pp. 508–516. DOI: 10.1002/bbpc.192400182.

[20] B. J. Kirby and E. F. Hasselbrink. "Zeta potential of microfluidic substrates: 1. Theory, experimental techniques, and effects on separations". In: *Electrophoresis* **25**, 2 (2004), pp. 187–202. DOI: 10.1002/elps.200305754.

[21] B. J. Kirby and E. F. Hasselbrink. "Zeta potential of microfluidic substrates: 2. Data for polymers". In: *Electrophoresis* **25**, 2 (2004), pp. 203–213. DOI: 10.1002/elps.200305755.

[22] D. C. Grahame. "The Electrical Double Layer and the Theory of Electrocapillarity." In: *Chemical Reviews* **41**, 3 (1947), pp. 441–501. DOI: 10.1021/cr60130a002.

[23] S. Trasatti. "Effect of the nature of the metal on the dielectric properties of polar liquids at the interface with electrodes. A phenomenological approach". In: *Journal of Electroanalytical Chemistry and Interfacial Electrochemistry* **123**, 1 (1981), pp. 121–139. DOI: 10.1016/S0022-0728(81)80047-2.

[24] E. Gongadze, U. Rienen, and A. Iglič. "Generalized stern models of the electric double layer considering the spatial variation of permittvity and finite size of ions in saturation regime". In: *Cellular and Molecular Biology Letters* **16**, 4 (2011), pp. 576–594. DOI: 10.2478/s11658-011-0024-x.

[25] E. Hückel. "Die Kataphorese der Kugel". In: *Physikalische Zeitschrift* **25** (1924), pp. 204–210.

[26] D. C. Henry. "The cataphoresis of suspended particles. Part I.—The equation of cataphoresis". In: *Proceedings of the Royal Society of London A* **133**, 821 (1931), pp. 106–129. DOI: 10.1098/rspa.1931.0133.

[27] A. Persat, M. E. Suss, and J. G. Santiago. "Basic principles of electrolyte chemistry for microfluidic electrokinetics. Part II: Coupling between ion mobility, electrolysis, and acid-base equilibria". In: *Lab on a Chip* **9**, 17 (2009), pp. 2454–2469. DOI: 10.1039/b906468k.

[28] B. Jachimska and A. Pajor. "Physico-chemical characterization of bovine serum albumin in solution and as deposited on surfaces". In: *Bioelectrochemistry* **87** (2012), pp. 138–146. DOI: 10.1016/j.bioelechem.2011.09.004.

[29] W. Friedl, J. C. Reijenga, and E. Kenndler. "Ionic strength and charge number correction for mobilities of multivalent organic anions in capillary electrophoresis". In: *Journal of Chromatography A* **709**, 1 (1995), pp. 163–170. DOI: 10.1016/0021-9673(95)00159-K.

[30] D. Li, S. Fu, and C. A. Lucy. "Prediction of Electrophoretic Mobilities. 3. Effect of Ionic Strength in Capillary Zone Electrophoresis". In: *Analytical Chemistry* **71**, 3 (1999), pp. 687–699. DOI: 10.1021/ac980843x.

[31] J.-L. Viovy. "Electrophoresis of DNA and other polyelectrolytes: Physical mechanisms". In: *Reviews of Modern Physics* **72**, 3 (2000), pp. 813–872. DOI: 10.1103/RevModPhys.72.813.

[32] T. Kaneta, T. Ueda, K. Hata, and T. Imasaka. "Suppression of electroosmotic flow and its application to determination of electrophoretic mobilities in a poly(vinylpyrrolidone)-coated capillary". In: *Journal of Chromatography A* **1106**, 1-2 (2006), pp. 52–55. DOI: 10.1016/j.chroma.2005.08.062.

[33] D. Milanova, R. D. Chambers, S. S. Bahga, and J. G. Santiago. "Effect of PVP on the electroosmotic mobility of wet-etched glass microchannels". In: *Electrophoresis* **33**, 21 (2012), pp. 3259–3262. DOI: 10.1002/elps.201200336.

[34] D. A. MacInnes and L. G. Longsworth. "Transference Numbers by the Method of Moving Boundaries." In: *Chemical Reviews* **11**, 2 (1932), pp. 171–230. DOI: 10.1021/cr60039a001.

[35] F. Kohlrausch. "Ueber Concentrations-Verschiebungen durch Electrolyse im Inneren von Lösungen und Lösungsgemischen". In: *Annalen der Physik und Chemie* **298**, 10 (1897), pp. 209–239. DOI: 10.1002/andp.18972981002.

[36] E. B. Dismukes and R. A. Alberty. "Weak Electrolyte Moving Boundary Systems Analogous to the Electrophoresis of a Single Protein". In: *Journal of the American Chemical Society* **76**, 1 (1954), pp. 191–197. DOI: 10.1021/ja01630a050.

[37] T. M. Jovin. "Multiphasic Zone Electrophoresis. I. Steady-State Moving-Boundary Systems Formed by Different Electrolyte Combinations". In: *Biochemistry* **12**, 5 (1973), pp. 871–879. DOI: 10.1021/bi00729a014.

[38] V. Hruška and B. Gaš. "Kohlrausch regulating function and other conservation laws in electrophoresis". In: *Electrophoresis* **28**, 1-2 (2007), pp. 3–14. DOI: 10.1002/elps.200600513.

[39] T. K. Khurana and J. G. Santiago. "Sample Zone Dynamics in Peak Mode". In: *Analytical Chemistry* **80**, 16 (2008), pp. 6300–6307.

[40] C. Eid and J. G. Santiago. "Influx and production rates in peak-mode isotachophoresis". In: *Analytical Chemistry* **88**, 23 (2016), pp. 11352–11357. DOI: 10.1021/acs.analchem.6b03467.

[41] S. Rubin, O. Schwartz, and M. Bercovici. "Sample distribution in peak mode isotachophoresis". In: *Physics of Fluids* **26**, 012001 (2014). DOI: 10.1063/1.4861399.

[42] F. Schönfeld, G. Goet, T. Baier, and S. Hardt. "Transition zone dynamics in combined isotachophoretic and electro-osmotic transport". In: *Physics of Fluids* **21**, 092002 (2009). DOI: 10.1063/1.3222866.

[43] T. Baier, F. Schönfeld, and S. Hardt. "Analytical approximations to the flow field induced by electroosmosis during isotachophoretic transport through a channel". In: *Journal of Fluid Mechanics* **682** (2011), pp. 101–119. DOI: 10.1017/jfm.2011.250.

[44] G. Garcia-Schwarz, M. Bercovici, L. A. Marshall, and J. G. Santiago. "Sample dispersion in isotachophoresis". In: *Journal of Fluid Mechanics* **679** (2011), pp. 455–475. DOI: 10.1017/jfm.2011.139.

[45] S. Bhattacharyya, P. P. Gopmandal, T. Baier, and S. Hardt. "Sample dispersion in isotachophoresis with Poiseuille counterflow". In: *Physics of Fluids* **25**, 022001 (2013). DOI: 10.1063/1.4789967.

[46] N. GanOr, S. Rubin, and M. Bercovici. "Diffusion dependent focusing regimes in peak mode counterflow isotachophoresis". In: *Physics of Fluids* **27**, 072003 (2015). DOI: 10.1063/1.4927230.

[47] J. Kendall and E. D. Crittenden. "The Separation of Isotopes". In: *Proceedings of the National Academy of Sciences* **9**, 3 (1923), pp. 75–78. DOI: 10.1073/pnas.9.3.75.

[48] M. Bercovici et al. "Rapid detection of urinary tract infections using isotachophoresis and molecular beacons". In: *Analytical Chemistry* **83**, 11 (2011), pp. 4110–4117. DOI: 10.1021/ac200253x.

[49] C. M. Han et al. "Simultaneous RNA purification and size selection using on-chip isotachophoresis with an ionic spacer". In: *Lab on a Chip* **19**, 16 (2019), pp. 2741–2749. DOI: 10.1039/C9LC00311H.

[50] F. Duša, D. Moravcová, and K. Šlais. "DNA purification and concentration by isotachophoresis in nonwoven fabric strip". In: *Analytica Chimica Acta* **1117** (2020), pp. 41–47. DOI: 10.1016/j.aca.2020.04.029.

[51] A. T. Bender et al. "HIV detection from human serum with paper-based isotachophoretic RNA extraction and reverse transcription recombinase polymerase amplification". In: *Analyst* **146**, 9 (2021), pp. 2851–2861. DOI: 10.1039/d0an02483j.

[52] L. Chen, J. M. Cabot, and B. Paull. "Thread-based isotachophoresis for DNA extraction and purification from biological samples". In: *Lab on a Chip* **21**, 13 (2021), pp. 2565–2573. DOI: 10.1039/d1lc00179e.

[53] A. Persat and J. G. Santiago. "MicroRNA profiling by simultaneous selective isotachophoresis and hybridization with molecular beacons". In: *Analytical Chemistry* **83**, 6 (2011), pp. 2310–2316. DOI: 10.1021/ac103225c.

[54] M. Bercovici, C. M. Han, J. C. Liao, and J. G. Santiago. "Rapid hybridization of nucleic acids using isotachophoresis". In: *Proceedings of the National Academy of Sciences* **109**, 28 (2012), pp. 11127–11132. DOI: 10.1073/pnas.1205004109.

[55] C. M. Han, E. Katilius, and J. G. Santiago. "Increasing hybridization rate and sensitivity of DNA microarrays using isotachophoresis". In: *Lab on a Chip* **14**, 16 (2014), pp. 2958–2967. DOI: 10.1039/C4LC00374H.

[56] M. Karsenty, S. Rubin, and M. Bercovici. "Acceleration of Surface-Based Hybridization Reactions Using Isotachophoretic Focusing". In: *Analytical Chemistry* **86**, 6 (2014), pp. 3028–3036. DOI: 10.1021/ac403838j.

[57] N. Ostromohov, O. Schwartz, and M. Bercovici. "Focused upon Hybridization: Rapid and High Sensitivity Detection of DNA Using Isotachophoresis and Peptide Nucleic Acid Probes". In: *Analytical Chemistry* **87**, 18 (2015), pp. 9459–9466. DOI: 10.1021/acs.analchem.5b02547.

[58] R. Vilensky, M. Bercovici, and E. Segal. "Oxidized Porous Silicon Nanostructures Enabling Electrokinetic Transport for Enhanced DNA Detection". In: *Advanced Functional Materials* **25**, 43 (2015), pp. 6725–6732. DOI: 10.1002/adfm.201502859.

[59] T. Rosenfeld and M. Bercovici. "Amplification-free detection of DNA in a paper-based microfluidic device using electroosmotically balanced isotachophoresis". In: *Lab on a Chip* **18**, 6 (2018), pp. 861–868. DOI: 10.1039/c7lc01250k.

[60] A. T. Bender et al. "Semiquantitative Nucleic Acid Test with Simultaneous Isotachophoretic Extraction and Amplification". In: *Analytical Chemistry* **90**, 12 (2018), pp. 7221–7229. DOI: 10.1021/acs.analchem.8b00185.

[61] H. Cui, P. Dutta, and C. F. Ivory. "Isotachophoresis of proteins in a networked microfluidic chip: Experiment and 2-D simulation". In: *Electrophoresis* **28**, 7 (2007), pp. 1138–1145. DOI: 10.1002/elps.200600525.

[62] J. Wang et al. "Exceeding 20 000-fold concentration of protein by the on-line isotachophoresis concentration in poly(methyl methacrylate) microchip". In: *Electrophoresis* **30**, 18 (2009), pp. 3250–3256. DOI: 10.1002/elps.200900111.

[63] R. Khnouf, G. Goet, T. Baier, and S. Hardt. "Increasing the sensitivity of microfluidics based immunoassays using isotachophoresis". In: *Analyst* **139**, 18 (2014), pp. 4564–4571. DOI: 10.1039/C4AN00545G.

[64] S. Arshavsky-Graham et al. "On Chip Protein Pre-Concentration for Enhancing the Sensitivity of Porous Silicon Biosensors". In: *ACS Sensors* **2**, 12 (2017), pp. 1767–1773. DOI: 10.1021/acssensors.7b00692.

[65] F. Paratore et al. "Isotachophoresis-Based Surface Immunoassay". In: *Analytical Chemistry* **89**, 14 (2017), pp. 7373–7381. DOI: 10.1021/acs.analchem.7b00725.

[66] S. C. Phung et al. "Counter-pressure-assisted ITP with electrokinetic injection under field-amplified conditions for bacterial analysis". In: *Analytical and Bioanalytical Chemistry* **407**, 23 (2015), pp. 6995–7002. DOI: 10.1007/s00216-015-8838-4.

[67] S. C. Phung et al. "Isotachophoretic Fluorescence in Situ Hybridization of Intact Bacterial Cells". In: *Analytical Chemistry* **89**, 12 (2017), pp. 6513–6520. DOI: 10.1021/acs.analchem.7b00598.

[68] S. Guo et al. "Paper-based ITP technology: An application to specific cancer-derived exosome detection and analysis". In: *Biosensors and Bioelectronics* **164** (2020), p. 112292. DOI: 10.1016/j.bios.2020.112292.

[69] V. Datinská et al. "Recent progress in nucleic acids isotachophoresis". In: *Journal of Separation Science* **41**, 1 (2018), pp. 236–247. DOI: 10.1002/jssc.201700878.

[70] R. Khnouf and C. Han. "Isotachophoresis-Enhanced Immunoassays: Challenges and opportunities". In: *IEEE Nanotechnology Magazine* **14**, 2 (2020), pp. 6–17. DOI: 10.1109/MNANO.2020.2966028.

[71] G. Goet, T. Baier, and S. Hardt. "Transport and separation of micron sized particles at isotachophoretic transition zones". In: *Biomicrofluidics* **5**, 1 (2011), pp. 1–16. DOI: 10.1063/1.3555194.

[72] H. Shintaku, J. W. Palko, G. M. Sanders, and J. G. Santiago. "Increasing Hybridization Rate and Sensitivity of Bead-Based Assays Using Isotachophoresis". In: *Angewandte Chemie International Edition* **53**, 50 (2014), pp. 13813–13816. DOI: 10.1002/anie.201408403.

[73] G. Goet, T. Baier, S. Hardt, and A. K. Sen. "Isotachophoresis with emulsions". In: *Biomicrofluidics* **7**, 4 (2013), p. 044103. DOI: 10.1063/1.4816347.

[74] B. Jung, R. Bharadwaj, and J. G. Santiago. "On-Chip Millionfold Sample Stacking Using Transient Isotachophoresis". In: *Analytical Chemistry* **78**, 7 (2006), pp. 2319–2327. DOI: 10.1021/ac051659w.

[75] M. C. Breadmore and J. P. Quirino. "100 000-Fold Concentration of Anions in Capillary Zone Electrophoresis Using Electroosmotic Flow Controlled Counterflow Isotachophoretic Stacking under Field Amplified Conditions". In: *Analytical Chemistry* **80**, 16 (2008), pp. 6373–6381. DOI: 10.1021/ac8007835.

[76] D. Bottenus et al. "10 000-fold concentration increase of the biomarker cardiac troponin I in a reducing union microfluidic chip using cationic isotachophoresis". In: *Lab on a Chip* **11**, 5 (2011), pp. 890–898. DOI: 10.1039/c0lc00490a.

[77] X. F. van Kooten, M. Truman-Rosentsvit, G. V. Kaigala, and M. Bercovici. "Focusing analytes from 50 μL into 500 pL: On-chip focusing from large sample volumes using isotachophoresis". In: *Scientific Reports* **7**, 10467 (2017). DOI: 10.1038/s41598-017-10579-5.

[78] S. M. Friedrich et al. "Molecular rheotaxis directs DNA migration and concentration against a pressure-driven flow". In: *Nature Communications* **8**, 1 (2017), p. 1213. DOI: 10.1038/s41467-017-01214-y.

[79] J. Reijenga, T. Verheggen, and F. Everaerts. "Fluorescence emission and fluorescence quenching as detection methods in isotachophoresis". In: *Journal of Chromatography A* **283** (1984), pp. 99–111. DOI: 10.1016/S0021-9673(00)96245-9.

[80] R. Jarofke. "Determination of histamine in biological fluids by capillary isotachophoresis and fluorescence". In: *Journal of Chromatography A* **390**, 1 (1987), pp. 161–167. DOI: 10.1016/S0021-9673(01)94371-7.

[81] D. Kaniansky et al. "Photometric detection at 405 nm in trace analysis by capillary isotachophoresis". In: *Journal of Chromatography A* **390**, 1 (1987), pp. 51–60. DOI: 10.1016/S0021-9673(01)94359-6.

[82] D. Kaniansky and J. Marák. "On-line coupling of capillary isotachophoresis with capillary zone electrophoresis". In: *Journal of Chromatography A* **498** (1990), pp. 191–204. DOI: 10.1016/S0021-9673(01)84247-3.

[83] F. Foret, E. Szökő, and B. L. Karger. "Trace analysis of proteins by capillary zone electrophoresis with on-column transient isotachophoretic preconcentration". In: *Electrophoresis* **14**, 1 (1993), pp. 417–428. DOI: 10.1002/elps.1150140167.

[84] J. D. Spitzberg, X. F. Van Kooten, M. Bercovici, and A. Meller. "Microfluidic device for coupling isotachophoretic sample focusing with nanopore single-molecule sensing". In: *Nanoscale* **12**, 34 (2020), pp. 17805–17811. DOI: 10.1039/d0nr05000h.

[85] A. Persat, L. A. Marshall, and J. G. Santiago. "Purification of Nucleic Acids from Whole Blood Using Isotachophoresis". In: *Analytical Chemistry* **81**, 22 (2009), pp. 9507–9511. DOI: 10.1021/ac901965v.

[86] R. B. Schoch, M. Ronaghi, and J. G. Santiago. "Rapid and selective extraction, isolation, preconcentration, and quantitation of small RNAs from cell lysate using on-chip isotachophoresis". In: *Lab on a Chip* **9**, 15 (2009), pp. 2145–2152. DOI: 10.1039/b903542g.

[87] T. Jacroux et al. "Cationic isotachophoresis separation of the biomarker cardiac troponin I from a high-abundance contaminant, serum albumin". In: *Electrophoresis* **35**, 14 (2014), pp. 2029–2038. DOI: 10.1002/elps.201400009.

[88] H. Shintaku et al. "On-Chip Separation and Analysis of RNA and DNA from Single Cells". In: *Analytical Chemistry* **86**, 4 (2014), pp. 1953–1957. DOI: 10.1021/ac4040218.

[89] A. Ramachandran et al. "Electric field-driven microfluidics for rapid CRISPR-based diagnostics and its application to detection of SARS-CoV-2". In: *Proceedings of the National Academy of Sciences* **117**, 47 (2020), pp. 29518–29525. DOI: 10.1073/pnas.2010254117.

[90] C. C. Park et al. "Controlling data quality and reproducibility of a high-sensitivity immunoassay using isotachophoresis in a microchip". In: *Analytical Chemistry* **80**, 3 (2008), pp. 808–814. DOI: 10.1021/ac701709n.

[91] T. Kawabata, H. G. Wada, M. Watanabe, and S. Satomura. "Electrokinetic Analyte Transport Assay for α-fetoprotein immunoassay integrates mixing, reaction and separation on-chip". In: *Electrophoresis* **29**, 7 (2008), pp. 1399–1406. DOI: 10.1002/elps.200700898.

[92] A. Persat and J. G. Santiago. "On-chip device for isothermal, chemical cycling polymerase chain reaction". In: *Proc. μTAS2008, 12th Int. Conf. Miniaturized Systems for Chemistry and Life Sciences*. San Diego, CA, USA, 2008, pp. 1081–1083.

[93] G. Goet, T. Baier, and S. Hardt. "Micro contactor based on isotachophoretic sample transport". In: *Lab on a Chip* **9**, 24 (2009), pp. 3586–3593. DOI: 10.1039/b914466h.

[94] S. S. Bahga, C. M. Han, and J. G. Santiago. "Integration of rapid DNA hybridization and capillary zone electrophoresis using bidirectional isotachophoresis". In: *Analyst* **138**, 1 (2013), pp. 87–90. DOI: 10.1039/c2an36249j.

[95] C. Eid, G. Garcia-Schwarz, and J. G. Santiago. "Isotachophoresis with ionic spacer and two-stage separation for high sensitivity DNA hybridization assay". In: *Analyst* **138**, 11 (2013), pp. 3117–3120. DOI: 10.1039/c3an00374d.

[96] O. Schwartz and M. Bercovici. "Microfluidic assay for continuous bacteria detection using antimicrobial peptides and isotachophoresis". In: *Analytical Chemistry* **86**, 20 (2014), pp. 10106–10113. DOI: 10.1021/ac5017776.

[97] C. Eid, J. W. Palko, E. Katilius, and J. G. Santiago. "Rapid Slow Off-Rate Modified Aptamer (SOMAmer)-Based Detection of C-Reactive Protein Using Isotachophoresis and an Ionic Spacer". In: *Analytical Chemistry* **87**, 13 (2015), pp. 6736–6743. DOI: 10.1021/acs.analchem.5b00886.

[98] C. Eid and J. G. Santiago. "Isotachophoresis applied to biomolecular reactions". In: *Lab on a Chip* **18**, 1 (2017), pp. 11–26. DOI: 10.1039/c7lc00852j.

[99] B. Y. Moghadam, K. T. Connelly, and J. D. Posner. "Isotachophoretic Preconcenetration on Paper-Based Microfluidic Devices". In: *Analytical Chemistry* **86**, 12 (2014), pp. 5829–5837. DOI: 10.1021/ac500780w.

[100] L. Chen et al. "Thread-based isotachophoresis coupled with desorption electrospray ionization mass spectrometry for clean-up, preconcentration, and determination of alkaloids in biological fluids". In: *Analytica Chimica Acta* **1193** (2022), p. 338810. DOI: 10.1016/j.aca.2021.338810.

[101] F. Everaerts, J. Vaci´k, T. P. Verheggen, and J. Zuska. "Isotachophoresis: Experiments with electrolyte counterflow". In: *Journal of Chromatography A* **60** (1971), pp. 397–405. DOI: 10.1016/S0021-9673(00)95577-8.

[102] F. Gebhard. "Purification and separation of proteins at liquid/liquid interfaces of aqueous two-phase systems". Master's thesis. Technische Universität Darmstadt, 2019.

[103] F. Gebhard, J. Hartmann, and S. Hardt. "Interaction of proteins with phase boundaries in aqueous two-phase systems under electric fields". In: *Soft Matter* **17**, 14 (2021), pp. 3929–3936. DOI: 10.1039/d0sm01921f.

[104] G. Münchow, S. Hardt, J. P. Kutter, and K. S. Drese. "Electrophoretic partitioning of proteins in two-phase microflows". In: *Lab on a Chip* **7**, 1 (2007), pp. 98–102. DOI: 10.1039/B612669N.

[105] G. Münchow, F. Schönfeld, S. Hardt, and K. Graf. "Protein Diffusion Across the Interface in Aqueous Two-Phase Systems". In: *Langmuir* **24**, 16 (2008), pp. 8547–8553. DOI: 10.1021/la800956j.

[106] T. Hahn and S. Hardt. "Size-dependent detachment of DNA molecules from liquid–liquid interfaces". In: *Soft Matter* **7**, 13 (2011), pp. 6320–6326. DOI: 10.1039/c1sm05309d.

[107] T. Hahn and S. Hardt. "Concentration and Size Separation of DNA Samples at Liquid–Liquid Interfaces". In: *Analytical Chemistry* **83**, 14 (2011), pp. 5476–5479. DOI: 10.1021/ac201228v.

[108] R. Hatti-Kaul. "Aqueous Two-Phase Systems: A General Overview". In: *Molecular Biotechnology* **19**, 3 (2001), pp. 269–278. DOI: 10.1385/MB:19:3:269.

[109] J. A. Asenjo and B. A. Andrews. "Aqueous two-phase systems for protein separation: Phase separation and applications". In: *Journal of Chromatography A* **1238** (2012), pp. 1–10. DOI: 10.1016/j.chroma.2012.03.049.

[110] C. Théry et al. "Minimal information for studies of extracellular vesicles 2018 (MISEV2018): a position statement of the International Society for Extracellular Vesicles and update of the MISEV2014 guidelines". In: *Journal of Extracellular Vesicles* **7**, 1 (2018). DOI: 10.1080/20013078.2018.1535750.

[111] C. Théry, L. Zitvogel, and S. Amigorena. "Exosomes: composition, biogenesis and function". In: *Nature Reviews Immunology* **2**, 8 (2002), pp. 569–579. DOI: 10.1038/nri855.

[112] Y. Jia, Z. Ni, H. Sun, and C. Wang. "Microfluidic Approaches Toward the Isolation and Detection of Exosome Nanovesicles". In: *IEEE Access* **7** (2019), pp. 45080–45098. DOI: 10.1109/ACCESS.2019.2907123.

[113] S. Lin et al. "Progress in Microfluidics-Based Exosome Separation and Detection Technologies for Diagnostic Applications". In: *Small* **1903916** (2019), pp. 1–18. DOI: 10.1002/smll.201903916.

[114] M. Iqbal et al. "Aqueous two-phase system (ATPS): an overview and advances in its applications". In: *Biological Procedures Online* **18**, 1 (2016), pp. 1–18. DOI: 10.1186/s12575-016-0048-8.

[115] Y. Chao and H. C. Shum. "Emerging aqueous two-phase systems: From fundamentals of interfaces to biomedical applications". In: *Chemical Society Reviews* **49**, 1 (2020), pp. 114–142. DOI: 10.1039/c9cs00466a.

[116] P. Å. Albertsson. "Partition of Proteins in Liquid Polymer–Polymer Two-Phase Systems". In: *Nature* **182**, 4637 (1958), pp. 709–711. DOI: 10.1038/182709a0.

[117] P.-Å. Albertsson. "Particle fractionation in liquid two-phase systems - The composition of some phase systems and the behaviour of some model particles in them - Application to the isolation of cell walls from microorganisms". In: *Biochimica et Biophysica Acta* **27** (1958), pp. 378–395. DOI: 10.1016/0006-3002(58)90345-7.

[118] H.-O. Johansson, G. Karlström, F. Tjerneld, and C. A. Haynes. "Driving forces for phase separation and partitioning in aqueous two-phase systems". In: *Journal of Chromatography B* **711**, 1-2 (1998), pp. 3–17. DOI: 10.1016/S0378-4347(97)00585-9.

[119] J. A. Asenjo and B. A. Andrews. "Aqueous two-phase systems for protein separation: A perspective". In: *Journal of Chromatography A* **1218**, 49 (2011), pp. 8826–8835. DOI: 10.1016/j.chroma.2011.06.051.

[120] R. M. de Oliveira et al. "Liquid—Liquid Equilibrium of Aqueous Two-Phase Systems Containing Poly(ethylene) Glycol 4000 and Zinc Sulfate at Different Temperatures". In: *Journal of Chemical & Engineering Data* **53**, 4 (2008), pp. 919–922. DOI: 10.1021/je700493t.

[121] E. Atefi, D. Fyffe, K. B. Kaylan, and H. Tavana. "Characterization of Aqueous Two-Phase Systems from Volume and Density Measurements". In: *Journal of Chemical and Engineering Data* **61**, 4 (2016), pp. 1531–1539. DOI: 10.1021/acs.jced.5b00901.

[122] P. Vázquez-Villegas et al. "A microdevice assisted approach for the preparation, characterization and selection of continuous aqueous two-phase systems: from micro to bench-scale". In: *Lab on a Chip* **16**, 14 (2016), pp. 2662–2672. DOI: 10.1039/C6LC00333H.

[123] H. Bakhshi and P. Mobalegholeslam. "Phase equilibria calculations of electrolyte solutions containing water-polymer-salt using a new thermodynamic model, applicable in aqueous two phase systems". In: *Fluid Phase Equilibria* **434** (2017), pp. 222–232. DOI: 10.1016/j.fluid.2016.11.033.

[124] P. Selvakumar, T. C. Ling, S. Walker, and A. Lyddiatt. "Redefinition of working aqueous two-phase systems: A generic description for prediction of the effective phase chemical composition for process control and biorecovery". In: *Journal of Chromatography B* **878**, 21 (2010), pp. 1784–1790. DOI: 10.1016/j.jchromb.2010.05.004.

[125] G. Johansson and A. Hartman. "A Quantitative Model for Partition in Aqueous Multiphase Systems". In: *European Journal of Biochemistry* **63**, 1 (1976), pp. 1–8. DOI: 10.1111/j.1432-1033.1976.tb10199.x.

[126] C. R. Mace et al. “Aqueous Multiphase Systems of Polymers and Surfactants Provide Self-Assembling Step-Gradients in Density”. In: *Journal of the American Chemical Society* **134**, 22 (2012), pp. 9094–9097. DOI: 10.1021/ja303183z.

[127] Y. Liang et al. “Aqueous four-phase system of SDS/DTAB/PEG/NaBr/H2O”. In: *Colloids and Surfaces A: Physicochemical and Engineering Aspects* **454** (2014), pp. 152–158. DOI: 10.1016/j.colsurfa.2014.04.012.

[128] C. Silva Abreu et al. “Aqueous three-phase systems formed by poly(vinylpyrrolidone) + poly(ethyleneglycol) + lithium sulfate + water: Phase behavior and partition data”. In: *Journal of Molecular Liquids* **355** (2022), p. 118959. DOI: 10.1016/j.molliq.2022.118959.

[129] J. A. Asenjo, S. L. Mistry, B. A. Andrews, and J. C. Merchuk. “Phase separation rates of aqueous two-phase systems: Correlation with system properties”. In: *Biotechnology and Bioengineering* **79**, 2 (2002), pp. 217–223. DOI: 10.1002/bit.10273.

[130] K. S. M. S. Raghavarao, R. M. Stewart, and P. Todd. “Electrokinetic Demixing of Two-Phase Aqueous Polymer Systems. II. Separation Rates of Polyethylene Glycol–Maltodextrin Mixtures”. In: *Separation Science and Technology* **26**, 2 (1991), pp. 257–267. DOI: 10.1080/01496399108050470.

[131] K. S. M. S. Raghavarao, R. M. Stewart, S. R. Rudge, and P. Todd. “Electrokinetic Demixing of Aqueous Two-Phase Systems. 3. Drop Electrophoretic Mobilities and Demixing Rates”. In: *Biotechnology Progress* **14**, 6 (1998), pp. 922–930. DOI: 10.1021/bp9800889.

[132] N. Nagaraj, S. Chethana, and K. S. M. S. Raghavarao. “Electrokinetic demixing of aqueous two-phase polymer/salt systems”. In: *Electrophoresis* **26**, 1 (2005), pp. 10–17. DOI: 10.1002/elps.200406122.

[133] M. C. Madhusudhan, S. Chethana, and K. S. M. S. Raghavarao. “Electrokinetic Demixing of Polymer/Salt Systems Containing Biomolecules”. In: *Separation Science and Technology* **46**, 5 (2011), pp. 727–733. DOI: 10.1080/01496395.2010.529098.

[134] H. Passos, A. Luís, J. A. Coutinho, and M. G. Freire. “Thermoreversible (Ionic-Liquid-Based) Aqueous Biphasic Systems”. In: *Scientific Reports* **6**, 20276 (2016). DOI: 10.1038/srep20276.

[135] H.-O. Johansson, G. Karlstroem, and F. Tjerneld. “Experimental and theoretical study of phase separation in aqueous solutions of clouding polymers and carboxylic acids”. In: *Macromolecules* **26**, 17 (1993), pp. 4478–4483. DOI: 10.1021/ma00069a012.

[136] H.-O. Johansson, G. Karlström, and F. Tjerneld. "Temperature-induced phase partitioning of peptides in water solutions of ethylene oxide and propylene oxide random copolymers". In: *Biochimica et Biophysica Acta - General Subjects* **1335**, 3 (1997), pp. 315–325. DOI: 10.1016/S0304-4165(96)00150-X.

[137] H.-O. Johansson, J. Persson, and F. Tjerneld. "Thermoseparating water/polymer system: A novel one-polymer aqueous two-phase system for protein purification". In: *Biotechnology and Bioengineering* **66**, 4 (1999), pp. 247–257. DOI: 10.1002/(SICI)1097-0290(1999)66:4<247::AID-BIT6>3.0.CO;2-5.

[138] B.-U. Moon et al. "Evaporation-Driven Water-in-Water Droplet Formation". In: *Langmuir* **36**, 47 (2020), pp. 14333–14341. DOI: 10.1021/acs.langmuir.0c02683.

[139] W. Guo et al. "Non-associative phase separation in an evaporating droplet as a model for prebiotic compartmentalization". In: *Nature Communications* **12**, 1 (2021), p. 3194. DOI: 10.1038/s41467-021-23410-7.

[140] A. May, J. Hartmann, and S. Hardt. "Phase separation in evaporating all-aqueous sessile drops". In: *Soft Matter* **18**, 34 (2022), pp. 6313–6317. DOI: 10.1039/D2SM00613H.

[141] J. B. Boreyko, P. Mruetusatorn, S. T. Retterer, and C. P. Collier. "Aqueous two-phase microdroplets with reversible phase transitions". In: *Lab on a Chip* **13**, 7 (2013), p. 1295. DOI: 10.1039/c3lc41122b.

[142] K. Mayolo-Deloisa, J. Benavides, and M. Rito-Palomares. "General Concepts and Definitions of Aqueous Two-Phase Systems". In: *Aqueous Two-Phase Systems for Bioprocess Development for the Recovery of Biological Products*. Ed. by M. Rito-Palomares and J. Benavides. Cham, CH: Springer Cham, 2017, pp. 1–18. DOI: 10.1007/978-3-319-59309-8_1.

[143] Y. Liu, R. Lipowsky, and R. Dimova. "Concentration dependence of the interfacial tension for aqueous two-phase polymer solutions of dextran and polyethylene glycol". In: *Langmuir* **28**, 8 (2012), pp. 3831–3839. DOI: 10.1021/la204757z.

[144] R. H. Tromp, M. Vis, B. H. Erné, and E. M. Blokhuis. "Composition, concentration and charge profiles of water-water interfaces". In: *Journal of Physics Condensed Matter* **26**, 46 (2014). DOI: 10.1088/0953-8984/26/46/464101.

[145] M. Vis et al. "Interfacial Tension of Phase-Separated Polydisperse Mixed Polymer Solutions". In: *Journal of Physical Chemistry B* **122**, 13 (2018), pp. 3354–3362. DOI: 10.1021/acs.jpcb.7b09967.

[146] I. Ziemecka et al. "Monodisperse hydrogel microspheres by forced droplet formation in aqueous two-phase systems". In: *Lab on a Chip* **11**, 4 (2011), pp. 620–624. DOI: 10.1039/C0LC00375A.

[147] D. Lai, J. P. Frampton, H. Sriram, and S. Takayama. "Rounded multi-level microchannels with orifices made in one exposure enable aqueous two-phase system droplet microfluidics". In: *Lab on a Chip* **11**, 20 (2011), p. 3551. DOI: 10.1039/c1lc20560a.

[148] B.-U. Moon et al. "Water-in-Water Droplets by Passive Microfluidic Flow Focusing". In: *Analytical Chemistry* **88**, 7 (2016), pp. 3982–3989. DOI: 10.1021/acs.analchem.6b00225.

[149] M. Mastiani, S. Seo, B. Mosavati, and M. Kim. "High-Throughput Aqueous Two-Phase System Droplet Generation by Oil-Free Passive Microfluidics". In: *ACS Omega* **3**, 8 (2018), pp. 9296–9302. DOI: 10.1021/acsomega.8b01768.

[150] A. Pfennig, A. Schwerin, and J. Gaube. "Consistent view of electrolytes in aqueous two-phase systems". In: *Journal of Chromatography B* **711**, 1-2 (1998), pp. 45–52. DOI: 10.1016/S0378-4347(97)00593-8.

[151] F. G. Donnan. "The Theory of Membrane Equilibria." In: *Chemical Reviews* **1**, 1 (1924), pp. 73–90. DOI: 10.1021/cr60001a003.

[152] A. Philipse and A. Vrij. "The Donnan equilibrium: I. On the thermodynamic foundation of the Donnan equation of state". In: *Journal of Physics: Condensed Matter* **23**, 19 (2011), p. 194106. DOI: 10.1088/0953-8984/23/19/194106.

[153] M. Vis, V. F. D. Peters, R. H. Tromp, and B. H. Erné. "Donnan Potentials in Aqueous Phase-Separated Polymer Mixtures". In: *Langmuir* **30**, 20 (2014), pp. 5755–5762. DOI: 10.1021/la501068e.

[154] E. Verwey and K. Niessen. "XL. The electrical double layer at the interface of two liquids". In: *The London, Edinburgh, and Dublin Philosophical Magazine and Journal of Science* **28**, 189 (1939), pp. 435–446. DOI: 10.1080/14786443908521199.

[155] C. Gavach, P. Seta, and B. D'epenoux. "The double layer and ion adsorption at the interface between two non miscible solutions. Part I. Interfacial tension measurements for the water-nitrobenzene tetraalkylammonium bromide systems". In: *Journal of Electroanalytical Chemistry and Interfacial Electrochemistry* **83**, 2 (1977), pp. 225–235. DOI: 10.1016/S0022-0728(77)80168-X.

[156] G. Torrie and J. Valleau. "Double layer structure at the interface between two immiscible electrolyte solutions". In: *Journal of Electroanalytical Chemistry and Interfacial Electrochemistry* **206**, 1-2 (1986), pp. 69–79. DOI: 10.1016/0022-0728(86)90257-3.

[157] B. Su, N. Eugster, and H. H. Girault. "Simulations of the adsorption of ionic species at polarisable liquid|liquid interfaces". In: *Journal of Electroanalytical Chemistry* **577**, 2 (2005), pp. 187–196. DOI: 10.1016/j.jelechem.2004.11.030.

[158] G. Luo et al. "Ion Distributions near a Liquid-Liquid Interface". In: *Science* **311**, 5758 (2006), pp. 216–218. DOI: 10.1126/science.1120392.

[159] H. Hartounian, S. Sandler, and K. Eric. "Aqueous Two-Phase Systems. 1. Salt Partitioning". In: *Industrial Engineering Chemistry Research* **33** (1994), pp. 2288–2293.

[160] M. Vis et al. "Decreased Interfacial Tension of Demixed Aqueous Polymer Solutions due to Charge". In: *Physical Review Letters* **115**, 078303 (2015). DOI: 10.1103/PhysRevLett.115.078303.

[161] P. A. Rosa, A. M. Azevedo, and M. R. Aires-Barros. "Application of central composite design to the optimisation of aqueous two-phase extraction of human antibodies". In: *Journal of Chromatography A* **1141**, 1 (2007), pp. 50–60. DOI: 10.1016/j.chroma.2006.11.075.

[162] M. Vargas et al. "Purification of IgG and albumin from human plasma by aqueous two phase system fractionation". In: *Biotechnology Progress* **28**, 4 (2012), pp. 1005–1011. DOI: 10.1002/btpr.1565.

[163] P. Selvakumar, T. C. Ling, S. Walker, and A. Lyddiatt. "Partitioning of haemoglobin and bovine serum albumin from whole bovine blood using aqueous two-phase systems". In: *Separation and Purification Technology* **90** (2012), pp. 182–188. DOI: 10.1016/j.seppur.2012.02.032.

[164] M. V. Quental et al. "Enhanced extraction of proteins using cholinium-based ionic liquids as phase-forming components of aqueous biphasic systems". In: *Biotechnology Journal* **10**, 9 (2015), pp. 1457–1466. DOI: 10.1002/biot.201500003.

[165] A. M. Ferreira et al. "Improving the extraction and purification of immunoglobulin G by the use of ionic liquids as adjuvants in aqueous biphasic systems". In: *Journal of Biotechnology* **236** (2016), pp. 166–175. DOI: 10.1016/j.jbiotec.2016.08.015.

[166] S. C. Ribeiro, G. A. Monteiro, J. M. S. Cabral, and D. M. F. Prazeres. "Isolation of plasmid DNA from cell lysates by aqueous two-phase systems". In: *Biotechnology and Bioengineering* **78**, 4 (2002), pp. 376–384. DOI: 10.1002/bit.10227.

[167] K. A. Moreira et al. "Extraction of Dengue 2 Plasmid DNA Vaccine (pD2) from Cell Lysates by Aqueous Two-Phase Systems". In: *Biotechnology* **6**, 4 (2007), pp. 520–526. DOI: 10.3923/biotech.2007.520.526.

[168] F. Luechau, T. C. Ling, and A. Lyddiatt. "Selective partition of plasmid DNA and RNA in aqueous two-phase systems by the addition of neutral salt". In: *Separation and Purification Technology* **68**, 1 (2009), pp. 114–118. DOI: 10.1016/j.seppur.2009.04.016.

[169] P. Malmström et al. "Separation of rat leukocytes by countercurrent distribution in aqueous two-phase systems". In: *Cellular Immunology* **37**, 2 (1978), pp. 409–421. DOI: 10.1016/0008-8749(78)90209-5.

[170] R. Hamamoto, M. Kamihira, and S. Iijima. "Specific separation of animal cells using aqueous two-phase systems". In: *Journal of Fermentation and Bioengineering* **82**, 1 (1996), pp. 73–76. DOI: 10.1016/0922-338X(96)89458-X.

[171] A. Kumar et al. "Type-specific separation of animal cells in aqueous two-phase systems using antibody conjugates with temperature-sensitive polymers". In: *Biotechnology and Bioengineering* **75**, 5 (2001), pp. 570–580. DOI: 10.1002/bit.10080.

[172] M. González-González and M. Rito-Palomares. "Application of affinity aqueous two-phase systems for the fractionation of CD133 + stem cells from human umbilical cord blood". In: *Journal of Molecular Recognition* **28**, 3 (2015), pp. 142–147. DOI: 10.1002/jmr.2374.

[173] J. Benavides et al. "Rotavirus-like particles primary recovery from insect cells in aqueous two-phase systems". In: *Journal of Chromatography B* **842**, 1 (2006), pp. 48–57. DOI: 10.1016/j.jchromb.2006.05.006.

[174] L. Hammar and G. Gilljam. "Extraction of HIV-1 in Aqueous Two-Phase Systems To Obtain a High Yield of gp120". In: *AIDS Research and Human Retroviruses* **6**, 12 (1990), pp. 1379–1388. DOI: 10.1089/aid.1990.6.1379.

[175] K. S. Vijayaragavan, A. Zahid, J. W. Young, and C. L. Heldt. "Separation of porcine parvovirus from bovine serum albumin using PEG–salt aqueous two-phase system". In: *Journal of Chromatography B* **967** (2014), pp. 118–126. DOI: 10.1016/j.jchromb.2014.07.025.

[176] C. Ladd Effio et al. "Downstream processing of virus-like particles: Single-stage and multi-stage aqueous two-phase extraction". In: *Journal of Chromatography A* **1383** (2015), pp. 35–46. DOI: 10.1016/j.chroma.2015.01.007.

[177] J. Kim et al. "Isolation of High-Purity Extracellular Vesicles by Extracting Proteins Using Aqueous Two-Phase System". In: *PLOS ONE* **10**, e0129760 (2015). DOI: 10.1371/journal.pone.0129760.

[178] H. Shin et al. "High-yield isolation of extracellular vesicles using aqueous two-phase system". In: *Scientific Reports* **5**, 13103 (2015). DOI: 10.1038/srep13103.

[179] H. Shin et al. "Aqueous two-phase system to isolate extracellular vesicles from urine for prostate cancer diagnosis". In: *PLOS ONE* **13**, e0194818 (2018). DOI: 10.1371/journal.pone.0194818.

[180] O. K. Kırbaş et al. "Optimized Isolation of Extracellular Vesicles From Various Organic Sources Using Aqueous Two-Phase System". In: *Scientific Reports* **9**, 19159 (2019). DOI: 10.1038/s41598-019-55477-0.

[181] S. Hardt and T. Baier. "Non-equilibrium electric double layers at the interface between two electrolytes". In: **arXiv:1105** (2011). DOI: https://doi.org/10.48550/arXiv.1105.0249.

[182] S. Hardt and T. Hahn. "Microfluidics with aqueous two-phase systems". In: *Lab on a Chip* **12**, 3 (2012), pp. 434–442. DOI: 10.1039/c1lc20569b.

[183] Y. Song, A. Sauret, and H. Cheung Shum. "All-aqueous multiphase microfluidics". In: *Biomicrofluidics* **7**, 6 (2013), p. 061301. DOI: 10.1063/1.4827916.

[184] M. Přibyl. "Separation efficiency of parallel flow microfluidic extractors with transport enhanced by electric field". In: *Separation and Purification Technology* **221** (2019), pp. 311–318. DOI: 10.1016/j.seppur.2019.03.089.

[185] K. Mařík, L. Tichá, L. Vobecká, and M. Přibyl. "Theoretical study on enzyme synthesis of cephalexin in a parallel-flow microreactor combined with electrically driven ATPS microextraction". In: *Reaction Chemistry and Engineering* **5**, 3 (2020), pp. 570–583. DOI: 10.1039/c9re00482c.

[186] L. Sauer et al. "Effects of aqueous systems and stabilization membranes on the separation of an antibiotic precursor in a microextractor". In: *Separation and Purification Technology* **292** (2022), p. 121050. DOI: 10.1016/j.seppur.2022.121050.

[187] B. H. Han et al. "Isolation of extracellular vesicles from small volumes of plasma using a microfluidic aqueous two-phase system". In: *Lab on a Chip* **20**, 19 (2020), pp. 3552–3559. DOI: 10.1039/D0LC00345J.

[188] G. Münchow, S. Hardt, J. P. Kutter, and K. S. Drese. "Protein Transport and Concentration by Electrophoresis in Two-phase Microflows". In: *Journal of Laboratory Automation* **11**, 6 (2006), pp. 368–373. DOI: 10.1016/j.jala.2006.08.006.

[189] T. Hahn, G. Münchow, and S. Hardt. "Electrophoretic transport of biomolecules across liquid-liquid interfaces". In: *Journal of Physics Condensed Matter* **23**, 27 (2011). DOI: 10.1088/0953-8984/23/27/279502.

[190] S. Hardt, J. Hartmann, S. Zhao, and A. Bandopadhyay. "Electric-Field-Induced Pattern Formation in Layers of DNA Molecules at the Interface between Two Immiscible Liquids". In: *Physical Review Letters* **124**, 64501 (2020). DOI: 10.1103/PhysRevLett.124.064501.

[191] T. Hahn. "Interfacial elektrokinetic transport phenomena and their impact on DNA electrophoresis in microfluidics". Dissertation. Technische Universität Darmstadt, 2011.

[192] A. Sinha, A. K. Mollah, S. Hardt, and R. Ganguly. "Particle dynamics and separation at liquid–liquid interfaces". In: *Soft Matter* **9**, 22 (2013), pp. 5438–5447. DOI: 10.1039/c3sm00120b.

[193] M. Li and D. Li. "Bidirectional transfer of particles across liquid-liquid interface under electric pulse". In: *Journal of Colloid and Interface Science* **560** (2020), pp. 436–446. DOI: 10.1016/j.jcis.2019.10.091.

[194] M. Li, D. Li, Y. Song, and D. Li. "Tunable particle/cell separation across aqueous two-phase system interface by electric pulse in microfluidics". In: *Journal of Colloid and Interface Science* **612** (2022), pp. 23–34. DOI: 10.1016/j.jcis.2021.12.140.

[195] C. D. M. Campos et al. "Membrane-free electroextraction using an aqueous two-phase system". In: *RSC Advances* **4**, 90 (2014), pp. 49485–49490. DOI: 10.1039/c4ra09246e.

[196] I. Axelsson. "Characterization of proteins and other macromolecules by agarose gel chromatography". In: *Journal of Chromatography A* **152**, 1 (1978), pp. 21–32. DOI: 10.1016/S0021-9673(00)85330-3.

[197] M. E. Flatté, A. A. Kornyshev, and M. Urbakh. "Understanding voltage-induced localization of nanoparticles at a liquid-liquid interface". In: *Journal of Physics Condensed Matter* **20**, 7 (2008). DOI: 10.1088/0953-8984/20/7/073102.

[198] S. Kemmerer. "Experimental analysis of the effect of electric fields on the stability of interfaces in aqueous two-phase systems". Bachelor's thesis. Technische Universität Darmstadt, 2022.

[199] M. H. Oddy, J. G. Santiago, and J. C. Mikkelsen. "Electrokinetic Instability Micromixing". In: *Analytical Chemistry* **73**, 24 (2001), pp. 5822–5832. DOI: 10.1021/ac0155411.

[200] C.-H. Chen, H. Lin, S. K. Lele, and J. G. Santiago. "Convective and absolute electrokinetic instability with conductivity gradients". In: *Journal of Fluid Mechanics* **524** (2005), pp. 263–303. DOI: 10.1017/S0022112004002381.

[201] J. D. Posner and J. G. Santiago. "Convective instability of electrokinetic flows in a cross-shaped microchannel". In: *Journal of Fluid Mechanics* **555** (2006), pp. 1–42. DOI: 10.1017/S0022112005008542.

[202] J. D. Posner, C. L. Pérez, and J. G. Santiago. "Electric fields yield chaos in microflows". In: *Proceedings of the National Academy of Sciences* **109**, 36 (2012), pp. 14353–14356. DOI: 10.1073/pnas.1204920109.

[203] A. O. El Moctar, N. Aubry, and J. Batton. "Electro-hydrodynamic micro-fluidic mixer". In: *Lab on a Chip* **3**, 4 (2003), pp. 273–280. DOI: 10.1039/b306868b.

[204] S. Dutta, A. Ghosh, P. S. G. Pattader, and D. Bandyopadhyay. "Electric field mediated von Kármán vortices in stratified microflows: transition from linear instabilities to coherent mixing". In: *Journal of Fluid Mechanics* **865** (2019), pp. 169–211. DOI: 10.1017/jfm.2018.1023.

[205] S. Dehe and S. Hardt. "Deformation modes of an oil-water interface under a local electric field: From Taylor cones to surface dimples". In: *Physical Review Fluids* **6**, 123702 (2021). DOI: 10.1103/PhysRevFluids.6.123702.

[206] S. Dehe, M. Hartmann, A. Bandopadhyay, and S. Hardt. "Controlling the electrostatic Faraday instability using superposed electric fields". In: *Physical Review Fluids* **7**, L082002 (2022). DOI: 10.1103/PhysRevFluids.7.L082002.

[207] S. Dehe, M. Hartmann, A. Bandopadhyay, and S. Hardt. "The spatial structure of electrostatically forced Faraday waves". In: *Journal of Fluid Mechanics* **939**, A6 (2022). DOI: 10.1017/jfm.2022.163.

[208] L. Vobecká et al. "Electric field driven addressing of ATPS droplets in microfluidic chips". In: *Microfluidics and Nanofluidics* **21**, 3 (2017), p. 51. DOI: 10.1007/s10404-017-1891-x.

[209] J. O. Bockris, A. K. Reddy, and M. E. Gamboa-Aldeco. *Modern Electrochemistry 2A: Fundamentals of Electrodics*. 2. Edition. New York, NY, USA: Kluwer Academic Publishers, 2000.

[210] A. Gencoglu and A. Minerick. "Chemical and morphological changes on platinum microelectrode surfaces in AC and DC fields with biological buffer solutions". In: *Lab on a Chip* **9**, 13 (2009), pp. 1866–1873. DOI: 10.1039/b820126a.

[211] H. Bonart et al. "Detecting Isotachophoresis Zones Hidden in Noise Using Signal Processing". In: *Analytical Chemistry* **95**, 19 (2023), pp. 7575–7583. DOI: 10.1021/acs.analchem.3c00321.

[212] X. Fan et al. "Sensitive optical biosensors for unlabeled targets: A review". In: *Analytica Chimica Acta* **620**, 1-2 (2008), pp. 8–26. DOI: 10.1016/j.aca.2008.05.022.

[213] J. N. Anker et al. "Biosensing with plasmonic nanosensors". In: *Nature Materials* **7**, 6 (2008), pp. 442–453. DOI: 10.1038/nmat2162.

[214] P. Kozma et al. "Integrated planar optical waveguide interferometer biosensors: A comparative review". In: *Biosensors and Bioelectronics* **58** (2014), pp. 287–307. DOI: 10.1016/j.bios.2014.02.049.

[215] S. Kumar et al. "Electrochemical Sensors and Biosensors Based on Graphene Functionalized with Metal Oxide Nanostructures for Healthcare Applications". In: *ChemistrySelect* **4**, 18 (2019), pp. 5322–5337. DOI: 10.1002/slct.201803871.

[216] L. Wang et al. "Recent advances in the development of electrochemical aptasensors for detection of heavy metals in food". In: *Biosensors and Bioelectronics* **147** (2020), p. 111777. DOI: 10.1016/j.bios.2019.111777.

[217] Y. Y. Zhang et al. "Evolution of nucleic acids biosensors detection limit III". In: *Analytical and Bioanalytical Chemistry* **414**, 2 (2022), pp. 943–968. DOI: 10.1007/s00216-021-03722-9.

[218] V.-T. Nguyen, S. Song, S. Park, and C. Joo. "Recent advances in high-sensitivity detection methods for paper-based lateral-flow assay". In: *Biosensors and Bioelectronics* **152** (2020), p. 112015. DOI: 10.1016/j.bios.2020.112015.

[219] A. Shebindu et al. "A fully integrated isotachophoresis with a programmable microfluidic platform". In: *Talanta* **225** (2021), p. 122039. DOI: 10.1016/j.talanta.2020.122039.

[220] T. K. Khurana and J. G. Santiago. "Effects of carbon dioxide on peak mode isotachophoresis: Simultaneous preconcentration and separation". In: *Lab on a Chip* **9**, 10 (2009), pp. 1377–1384. DOI: 10.1039/b815460k.

[221] A. Terzis, A. Ramachandran, J. Kang, and J. G. Santiago. "Simultaneous optical and infrared thermal imaging of isotachophoresis". In: *Analytica Chimica Acta* **1131** (2020), pp. 9–17. DOI: 10.1016/j.aca.2020.07.014.

[222] D. P. Bertsekas and J. N. Tsitsiklis. *Introduction to Probability*. 2. Edition. Belmont, MA, USA: Athena Scientific, 2008.

[223] J. K. Kruschke. *Doing Bayesian data analysis*. 2. Edition. Boston, MA, USA: Academic Press, 2015.

[224] J. K. Kruschke. "Rejecting or Accepting Parameter Values in Bayesian Estimation". In: *Advances in Methods and Practices in Psychological Science* **1**, 2 (2018), pp. 270–280. DOI: 10.1177/2515245918771304.

[225] M. Karsenty, T. Rosenfeld, K. Gommed, and M. Bercovici. "Current monitoring in a microchannel with repeated constrictions for accurate detection of sample location in isotachophoresis". In: *Analytical Chemistry* **87**, 1 (2015), pp. 388–393. DOI: 10.1021/ac5036346.

[226] J. Salvatier, T. V. Wiecki, and C. Fonnesbeck. "Probabilistic programming in Python using PyMC3". In: *PeerJ Computer Science* **2016**, 4 (2016), pp. 1–24. DOI: 10.7717/peerj-cs.55. arXiv: 1507.08050.

[227] R. Kumar, C. Carroll, A. Hartikainen, and O. Martin. "ArviZ a unified library for exploratory analysis of Bayesian models in Python". In: *Journal of open source software* **4**, 33 (2019), p. 1143. DOI: 10.21105/joss.01143.

[228] M. D. Hoffman and A. Gelman. "The no-U-turn sampler: Adaptively setting path lengths in Hamiltonian Monte Carlo". In: *Journal of Machine Learning Research* **15**, 2008 (2014), pp. 1593–1623.

[229] C. Crosnier de Lassichère, T. Duc Mai, and M. Taverna. "Antibody-free detection of amyloid beta peptides biomarkers in cerebrospinal fluid using capillary isotachophoresis coupled with mass spectrometry". In: *Journal of Chromatography A* **1601** (2019), pp. 350–356. DOI: 10.1016/j.chroma.2019.05.006.

[230] S. Ghosal. "Electrokinetic Flow and Dispersion in Capillary Electrophoresis". In: *Annual Review of Fluid Mechanics* **38** (2006), pp. 309–338. DOI: 10.1146/annurev.fluid.38.050304.092053.

[231] F. Gebhard et al. "Isotachophoresis with Oscillating Sample Zones to Control the Spatial Overlap of Co-focused Species". In: *Analytical Chemistry* **96**, 11 (2024), pp. 4446–4454. DOI: 10.1021/acs.analchem.3c04606.

[232] A. S. Avaro et al. "Web-Based Open-Source Tool for Isotachophoresis". In: *Analytical Chemistry* **93**, 47 (2021), pp. 15768–15774. DOI: 10.1021/acs.analchem.1c03925.

[233] D. Milanova, R. D. Chambers, S. S. Bahga, and J. G. Santiago. "Electrophoretic mobility measurements of fluorescent dyes using on-chip capillary electrophoresis". In: *Electrophoresis* **32**, 22 (2011), pp. 3286–3294. DOI: 10.1002/elps.201100210.

[234] F. Mikkers, F. Everaerts, and T. Verheggen. "High-performance zone electrophoresis". In: *Journal of Chromatography A* **169** (1979), pp. 11–20. DOI: 10.1016/0021-9673(75)85029-1.

[235] V. Šustáček, F. Foret, and P. Boček. "Selection of the background electrolyte composition with respect to electromigration dispersion and detection of weakly absorbing substances in capillary zone electrophoresis". In: *Journal of Chromatography A* **545**, 2 (1991), pp. 239–248. DOI: 10.1016/S0021-9673(01)88716-1.

[236] P. Gebauer and P. Boček. "Predicting Peak Symmetry in Capillary Zone Electrophoresis: The Concept of the Peak Shape Diagram". In: *Analytical Chemistry* **69**, 8 (1997), pp. 1557–1563. DOI: 10.1021/ac960796d.

[237] P. Gebauer, J. Caslavska, W. Thormann, and P. Boček. "Prediction of zone patterns in capillary zone electrophoresis with conductivity detection. Concept of the zone conductivity diagram". In: *Journal of Chromatography A* **772**, 1-2 (1997), pp. 63–71. DOI: 10.1016/S0021-9673(97)00103-9.

[238] B. Gaš and E. Kenndler. "Dispersive phenomena in electromigration separation methods". In: *Electrophoresis* **21**, 18 (2000), pp. 3888–3897. DOI: 10.1002/1522-2683(200012)21:18<3888::AID-ELPS3888>3.0.CO;2-D.

[239] Y. Lu, Y. Xia, and G. Luo. "Phase separation of parallel laminar flow for aqueous two phase systems in branched microchannel". In: *Microfluidics and Nanofluidics* **10**, 5 (2011), pp. 1079–1086. DOI: 10.1007/s10404-010-0736-7.

[240] M. Tokeshi et al. “Continuous-flow chemical processing on a microchip by combining microunit operations and a multiphase flow network”. In: *Analytical Chemistry* **74**, 7 (2002), pp. 1565–1571. DOI: 10.1021/ac011111z.

[241] J. W. Schoonen et al. “Continuous-flow microelectroextraction for enrichment of low abundant compounds”. In: *Analytical Chemistry* **86**, 16 (2014), pp. 8048–8056. DOI: 10.1021/ac500707v.

List of Figures

Symbols

Latin symbols

Symbol	Description
a	Particle radius
A	Amplitude of oscillatory electric field component
c, c_i	Molar concentration (of species i)
C	Cross-correlation
$c_{i,0}$	Bulk concentration of species i
C^L	Cross-correlation function with time lag L
C_N^L	Cross-correlation function with time lag L after averaging over all $N - L$ cross-correlation functions C^L
d	Distance from the interface of an ATPS
D	Diffusion coefficient
e	Elementary charge
$E, \vec{E}$	Electric field
E_{ext}	External electric field
f	Frequency of oscillatory electric field component
$\vec{f}$	Force per unit volume
F	Faraday constant
$\vec{F}_d$	Drag force on a particle
$\vec{F}_{el}$	Force on a charged particle caused by an electric field
f_{im}	Frame rate
ΔG_{mix}	Gibbs free energy of mixing
ΔH_{mix}	Enthalpy of mixing
$i, \vec{i}$	Electric current density
I	Fluorescence intensity
I^*	Normalized fluorescence intensity
$I_{X,Y}$	Fluorescence intensity averaged along the x and y direction
I_Y	Fluorescence intensity averaged along the y direction

$I_{Y,N}$	Fluorescence intensity averaged along the y direction and over all N images
$\mathcal{I}$	Ionic strength
j, $\vec{j}$	Molar flux density
K, K_i	Partition coefficient (of species i)
k_B	Boltzmann constant
l	Charactertic length scale
L	Time lag between two images in cross-correlation function
L_{int}	Characteristic width of an ITP interface
L_S	Characteristic width of an ITP sample zone
n	Dimensionless number, for example an image number
n_S	Number of accumulated sample molecules per unit area
N	Total Number of a dimensionless quantity
N_S	Total number of focused sample molecules
P	Pressure
q	Charge of a particle
R	Product of intensity distributions of two samples focused *via* ITP
$\bar{R}$	Time-averaged overlap of sample distributions
$\hat{R}$	Universal gas constant
R^2	Coefficient of determination
$R_{X,Y}$	Overlap of sample distributions: R integrated over y and x
R^*	Normalized and time-averaged overlap of sample distributions
ΔS_{mix}	Entropy difference between mixed and phase-separated state
t	Time
T	Period of oscillation
u, $\vec{u}$	Velocity
$\vec{u}_b$	Bulk velocity
U	Voltage
U_{app}	Applied voltage
D_{DC}	DC offset of oscillating electric field
w_A	Alberty function
w_K	Kohlrausch regulating function
w_J	Jovin function

Greek symbols

Symbol	Description
α	Fit parameter: rate constant of desorption in chapter 3; amplitude of signal distribution in chapter 5 and chapter 6
β	Fit parameter: scaling factor of normalized intensity distribution in chapter 3; center position of signal distribution in chapter 5 and chapter 6
γ	Fit parameter: width of signal distribution
δ	Fit parameter: skewness parameter of signal distribution
ϵ	Fit parameter: additive offset of singal distribution
ε	Dielectric permittivity
ζ	ζ potential
η	Dynamic viscosity
θ	Value of random variable Θ and collection of parameters estimated in Bayesian inference, respectively
Θ	Random variable modeling unknown parameter
ϑ	Absolute temperature
κ	Electrical conductivity
λ_D	Debye length
λ_{im}	Pixel pitch (describes the width of a pixel in µm/px)
μ, μ_i	Electrophoretic mobility (of species i)
ν, ν_i	Charge number / valence (of species i)
ρ	Mass density
ρ_e	Charge density
σ	Standard deviation
$\boldsymbol{\tau}$	Viscous stress tensor
ϕ	Collection of parameters estimated in Bayesian inference
φ	Electrostatic potential
φ_0	Electrostatic potential at a wall or another system boundary
ω	Mass fraction

Abbreviations

Abbreviation	Meaning
AF647	Alexa Fluor 647 carboxylic acid, tris(trimethylamonium) salt
ATPS	Aqueous two-phase system
BES	N,N-bis[2-hydroxyethyl]-2-aminoethanesulfonic acid
BSA	Bovine serum albumin
Bis-Tris	Bis-tris methane
BγG	Bovine γ-globulin
CZE	Capillary zone electrophoresis
Dex	Dextran phase
EDL	Electric double layer
EOF	Electro-ostmotic flow
EV	Extracellular vesicle
fps	Frames per second
HEPES	4-(2-hydroxyethyl)-1-piperazineethanesulfonic acid
HDI	Highest density interval
ITP	Isotachophoresis
LE	Leading electrolyte
MAP	Maximum a posteriori probability
MES	2-(N-morpholino)ethanesulfonic acid
NA	Numerical apperture
PBS	Phosphate-buffered saline
PDMS	Polydimethylsiloxane
PEG	Polyethylene glycol
PVP	Polyvinylpyrrolidone
Re	Reynolds number
ROPE	Region of practical equivalence
SAMI	Shifting and averaging multiple images
SNR	Signal-to-noise ratio
TE	Trailing electrolyte
Tris	Tris(hydroxymethyl)aminomethane